

University of Windsor

Scholarship at UWindor

Electronic Theses and Dissertations

Theses, Dissertations, and Major Papers

3-2-2021

Behaviour of Wrinkled Energy Pipes Subjected to Axial Cyclic Induced Fatigue Failure

Habeeb Boluwatife Sobanke
University of Windsor

Follow this and additional works at: <https://scholar.uwindsor.ca/etd>

Recommended Citation

Sobanke, Habeeb Boluwatife, "Behaviour of Wrinkled Energy Pipes Subjected to Axial Cyclic Induced Fatigue Failure" (2021). *Electronic Theses and Dissertations*. 8537.
<https://scholar.uwindsor.ca/etd/8537>

This online database contains the full-text of PhD dissertations and Masters' theses of University of Windsor students from 1954 forward. These documents are made available for personal study and research purposes only, in accordance with the Canadian Copyright Act and the Creative Commons license—CC BY-NC-ND (Attribution, Non-Commercial, No Derivative Works). Under this license, works must always be attributed to the copyright holder (original author), cannot be used for any commercial purposes, and may not be altered. Any other use would require the permission of the copyright holder. Students may inquire about withdrawing their dissertation and/or thesis from this database. For additional inquiries, please contact the repository administrator via email (scholarship@uwindsor.ca) or by telephone at 519-253-3000ext. 3208.

Behaviour of Wrinkled Energy Pipes Subjected to Axial Cyclic Induced Fatigue Failure

By

Habeeb Sobanke

A Thesis

Submitted to the Faculty of Graduate Studies
through the Department of Civil and Environmental Engineering
in Partial Fulfillment of the Requirements for
the Degree of Master of Applied Science
at the University of Windsor

Windsor, Ontario, Canada

2020

© 2020 Habeeb Sobanke

Behaviour of Wrinkled Energy Pipes Subjected to Axial Cyclic Induced Fatigue Failure

by

Habeeb Sobanke

APPROVED BY:

N. Kar

Department of Electrical and Computer Engineering

H. Ghaednia

Department of Civil and Environmental Engineering

S. Das, Advisor

Department of Civil and Environmental Engineering

December 14, 2020

AUTHOR'S DECLARATION OF ORIGINALITY

I hereby certify that I am the sole author of this thesis and that no part of this thesis has been published or submitted for publication.

I certify that, to the best of my knowledge, my thesis does not infringe upon anyone's copyright nor violate any proprietary rights and that any ideas, techniques, quotations, or any other material from the work of other people included in my thesis, published or otherwise, are fully acknowledged in accordance with the standard referencing practices. Furthermore, to the extent that I have included copyrighted material that surpasses the bounds of fair dealing within the meaning of the Canada Copyright Act, I certify that I have obtained a written permission from the copyright owner(s) to include such material(s) in my thesis and have included copies of such copyright clearances to my appendix.

I declare that this is a true copy of my thesis, including any final revisions, as approved by my thesis committee and the Graduate Studies office, and that this thesis has not been submitted for a higher degree to any other University or Institution.

ABSTRACT

The energy industry has since been faced with the issue of development of wrinkle defect on buried pipelines located in vicious environment. Although, there have been different literatures on how to assess the integrity of pipelines with structural defects such as; corrosion, dents, buckles and welds, limited research data or guideline(s) are available on how to assess the severity of small wrinkle defects. Failure to assess the severity of these wrinkle defects, especially in buried pipelines located in the regions prone to geotechnical movement and extreme seasonal temperature variation, may lead to shutdown of the pipeline operations, and as result lead to loss of revenue. Therefore, this current study is focused on investigating the failure and behaviour of wrinkled pipes with varying wrinkle geometry, when they are subjected to axial cyclic loads representative of extreme seasonal temperature variation and cyclic freeze-thaw. This research program was conducted using both experimental method and finite element analysis (FEA) based approach.

This study shows that a pipe with a wrinkle defect subjected to displacement-controlled axial cyclic loading, may fail by fatigue and result to fracture at the crest of the wrinkle due to localized stress and strain concentration. Additionally, the fatigue life of a wrinkled pipe is dependent on the magnitude of internal pressure applied and the type of cyclic loading applied. A methodology based on the strain life approach used in this study, was considered sufficient in analysing the remaining life of wrinkled pipes subjected to displacement-controlled axial cyclic loading.

DEDICATION

This thesis is dedicated to almighty God, whom in his utmost benevolence granted me the mental and physical strength to complete this research. To my beloved family, Mr. Salmon Shobanke, Mrs. Olatundun Shobanke and Nofisat Sobanke, who I remained in their thoughts and prayers and never failed to check on my well being. Also, to the peaceful protesters who lost their lives fighting against police brutality and bad governance in Nigeria on the 20th of October 2020.

ACKNOWLEDGMENTS

Firstly, I wish to express my sincere gratitude towards Dr. S. Das for providing me the rare opportunity to work with him and his research team on this research project. Dr. Das devoted his time, resources and sincere effort to provide all necessary facilities for this research. I would also like to acknowledge the contributions from my committee members, Dr. N. Kar, Dr. H. Ghaednia and Dr. S. Das for their constructive suggestions to improve this thesis.

I also greatly appreciate the technical support from Dr. J. Zohrehheydariha, and Dr. J. Dhanapal rendered in the setup of instrumentation and data acquisition system. Additionally, I recognise the time and patience endured by Mr. M. St. Louis and Mr. J. Finnerty when providing me with technical assistance in the University of Windsor's Structural Engineering Laboratory.

Furthermore, I would like to appreciate the contributions from my friends and colleagues who aided me during the experimental program and made the experience worthwhile. Specifically, I would like to thank Mr. A. Adesina, Mr. N. Singh, Mr. B. Van Boxtel, Mr. S. Ehikhuenmen, Mr. S. Mitra, Mr. S. Sharma, Mr. I. Stephen and Mr. B. Hajimohammadi

Lastly, I would like to thank my family for the support, confidence and encouragement that they have given me during this entire program.

TABLE OF CONTENTS

AUTHOR’S DECLARATION OF ORIGINALITY	iii
ABSTRACT.....	iv
DEDICATION.....	v
ACKNOWLEDGMENTS	vi
LIST OF TABLES	xiii
LIST OF FIGURES	xiv
LIST OF ABBREVIATIONS / SYMBOLS.....	xxi
CHAPTER 1	1
INTRODUCTION	1
1.1 General	1
1.2 Statement of Problem.....	2
1.3 Objectives and Scope	3
1.4 Organization of thesis.....	3
CHAPTER 2	5
LITERATURE REVIEW	5
2.1 General	5
2.2 Local Buckling	5
2.2.1 Geotechnical Movement	6
2.2.1.1 Slope Movement	6
2.2.1.2 Frost Heave and Thaw Settlement.....	8
2.2.2 Parameters Affecting Local Buckling and Wrinkling	9
2.3 Failure Modes of Buckled Pipes	15
2.3.1 Collapse.....	15
2.3.2 Rupture.....	15

2.3.3	Fracture	16
2.4	Factors Affecting Fracture in Pipelines.....	16
2.4.1	Internal Pressure.....	17
2.4.2	Mean stress.....	17
2.4.3	Stress Amplitude.....	18
2.4.4	Wrinkle Amplitude	18
2.5	Fracture and Rupture Failure Under Different Load Combinations	19
2.5.1	Axial Cyclic Loads	19
2.5.2	Lateral Loads	20
2.5.3	Pressure Cyclic Loads.....	20
2.6	Assessment of Fatigue Life	21
2.6.1	Stress Life Approach.....	21
2.6.2	Strain Life Approach.....	24
2.6.3	Energy Based Approach	28
2.7	Current Codes and Standards	29
2.7.1	CSA Z662-19	29
2.7.2	ASME Code for Pressure Pipping, B31.....	31
2.7.3	DNV GL (DNV-OS-F101).....	34
2.8	Summary	36
CHAPTER 3		54
EXPERIMENTAL PROGRAM.....		54
3.1	General	54
3.2	Phase 1 – Initiation of Wrinkle Defect.....	55
3.2.1	Selection of Specimen.....	55
3.2.2	Selection of Wrinkle Defect Profile.....	56

3.2.3	Boundary Conditions	56
3.2.4	Preparation of Specimen	57
3.2.5	Specimen Designation	58
3.2.6	Test Setup for Monotonic Loading.....	58
3.2.7	Instruments and Instrumentation for Phase 1.....	59
3.2.7.1	Strain Gauges	59
3.2.7.2	LVDT (Linear Variable differential transformer).....	60
3.2.7.3	Pressure Pump.....	60
3.2.7.4	Collars	60
3.2.7.5	Pressure Transducer	61
3.2.7.6	Hydraulic Cylinder and Load cell.....	61
3.2.7.7	Data Acquisition System.....	61
3.2.7.8	Contour Gauge	62
3.2.8	Monotonic Loading Procedure	62
3.3	Phase 2 – Axial Cyclic Loading.....	64
3.3.1	Selection of Axial Cyclic Range.....	64
3.3.2	Preparation of Specimen	64
3.3.3	Test Setup for Axial Cyclic Loading	65
3.3.4	Instrumentation for Phase 2	66
3.3.4.1	Strain Gauges	66
3.3.4.2	LVDT	66
3.3.5	Axial Cyclic Loading Procedure.....	66
3.4	Determination of Material Properties.....	67
CHAPTER 4		80
EXPERIMENTAL RESULTS AND DISCUSSION		80

4.1	General	80
4.2	Phase 1 – Initiation of Wrinkle Defect.....	80
4.2.1	Discussion on Behaviour of Group 1 Specimens	81
4.2.1.1	Load vs. Global Deformation Behaviour.....	81
4.2.1.2	Load vs. Local Strain Behaviour	82
4.2.1.3	Discussion on Wrinkle Defect	82
4.2.2	Discussion on Behaviour of Group 2 Specimens	83
4.2.2.1	Load vs. Global Deformation Behaviour.....	83
4.2.1.2	Load vs. Local Strain Behaviour	84
4.2.2.3	Discussion on Wrinkle Defect	84
4.3	Phase 2 – Axial Cyclic Loading.....	85
4.3.1	Discussion on Behaviour of Group 1 Specimens	85
4.3.1.1	Cycles to Failure	85
4.3.1.2	Load vs. Deformation Behaviour.....	86
4.3.1.3	Hysteresis Loop Energy	87
4.3.1.4	Load vs. Local Strain Behaviour	88
4.3.1.5	Failure Patterns and Visual Observations	89
4.3.2	Discussion on Behaviour of Group 2 Specimens	90
4.3.2.1	Cycles to Failure	90
4.3.2.2	Load vs. Deformation Behaviour.....	91
4.3.2.3	Hysteresis Loop Energy	92
4.3.2.4	Load vs. Local Strain Behaviour	93
4.3.2.5	Failure Patterns and Visual Observations	94
4.4	Material Tests.....	94
4.5	Summary	95

CHAPTER 5	120
FINITE ELEMENT MODELLING (FEM).....	120
5.1 General	120
5.2 Finite Element Model.....	121
5.2.1 Phase 1: Initiation of Wrinkle Defect	121
5.2.1.1 Assembly.....	121
5.2.1.2 Interaction	122
5.2.1.3 Loads and Boundary Conditions.....	123
5.2.1.4 Material Properties.....	123
5.2.1.5 Element Selection	125
5.2.1.6 Mesh Convergence Study	126
5.2.1.7 Load Histories.....	128
5.2.2 Phase 2: Axial Cyclic Loading	129
5.2.2.1 Element and Mesh Selection.....	129
5.2.2.3 Material Properties.....	130
5.2.2.4 Load Histories.....	130
5.2.2.5 Solution Strategies	131
5.2.3 Material Property Verification.....	132
CHAPTER 6	142
VALIDATION OF FINITE ELEMENT MODEL	142
6.1 General	142
6.2 Phase 1 – Initiation of Wrinkle Defect.....	142
6.2.1 Discussion on Group 1 Specimens	143
6.2.1.1 Comparison for Load-Displacement Behaviour	143
6.2.2 Discussion on Group 2 Specimens	143

6.2.2.1	Comparison for Load-Displacement Behaviour	143
6.2.3	Comparison of Wrinkled Shape.....	144
6.3	Phase 2 – Axial Cyclic Loading.....	144
6.3.1	Comparison of Cyclic Load vs. Local Strain Behaviour	144
6.4	Strain-Life Fatigue Assessment	145
6.5	Numerical Quantification of Strain Values.....	147
6.6	Correlation of Number of Cycles to Failure.....	148
6.7	Summary	149
CHAPTER 7		165
SUMMARY, CONCLUSIONS AND RECOMMENDATIONS.....		165
7.1	Summary	165
7.2	Conclusions	166
7.3	Recommendations	167
REFERENCES		169
APPENDICES		175
Appendix A - Relationship Between Load, Strain and Displacement for All Tested Specimens		175
Appendix B - Wrinkle Profile Measurement Log.....		186
Appendix C - Pictures of Tested Specimens		188
Appendix D - Copyright Clearances.....		191
VITA AUCTORIS		227

LIST OF TABLES

Table 3.1: Wrinkle Defect Profile Measurements	68
Table 3.2: Text Matrix for Experimental Program	68
Table 4.1: Critical Loads and Displacements During Wrinkle Initiation Phase for Group 1 (0.3py) Specimens	97
Table 4.2: Maximum Local Compressive Strain Values for Group 1 (0.3py) Specimens Under Monotonic Loading.....	97
Table 4.3: Critical Loads and Displacements During Wrinkle Initiation Phase for Group 2 (0.6py) Specimens	98
Table 4.4: Maximum Local Compressive Strain Values for Group 2 (0.6py) Specimens Under Monotonic Loading.....	98
Table 4.5: Cyclic Test Results (Phase 2)	99
Table 4.6: Maximum Compressive and Tensile Load at Initial and Final Cycle for All Specimens	100
Table 4.7: Material Properties from Tension Test on Coupon 6	101
Table 5.1: Plastic Material Properties Used for The Pipe Model	134
Table 5.2: Effect of Mesh Density on the Accuracy and Duration of Analysis	134
Table 5.3: Workstation System Configuration Details	135
Table 6.1: Summary of Experimental and FEA Results for Group 1 Specimens.....	150
Table 6.2: Summary of Experimental and FEA Results for Group 2 Specimens.....	151
Table 6.3: Summary of Comparison of Results from Strain Life Fatigue Models for Group 1 Specimens	152

LIST OF FIGURES

Figure 1.1: Fractured Field Pipeline of Wascana Energy Inc. (Courtesy of Wascana Energy Inc.)	4
Figure 1.2: Fractured Field Pipeline of Husky Energy Inc. (Courtesy of Husky Energy Inc.)	4
Figure 1.3: Fractured Field Pipeline of WestCoast Energy Inc. (Courtesy of WestCoast Energy Inc.)	4
Figure 2.1: Pipeline Industry Performance Report (CEPA 2019)	38
Figure 2.3: Differential Frost Heave of Buried Pipeline (Nixon et al., 2002)	39
Figure 2.4: Differential Thaw Settlement of Buried Pipeline (Nixon et al., 2002)	39
Figure 2.5: UOE Forming Process (Kashani et al., 2018)	40
Figure 2.6: Axial Profiles of Radial Tube Displacement Recorded at Different Average strain levels During Monotonic Compression of a Specimen that Shows the Evolution of the Wrinkle (Jiao and Kyriakides, 2011)	40
Figure 2.7: Collapsed Form of a Defected Specimen Subjected to Cyclic Axial Loads (Zeinoddini et al., 2015).....	41
Figure 2.8: Accordion-type FAilure of Wrinkled Pipe (Das et al., 2007a)	42
Figure 2.9: Rupture Failure of Wrinkled Pipe (Nazemi et al., 2009)	42
Figure 2.10: Fracture Failure of Wrinkled Pipe (Das et al. 2007a)	42
Figure 2.11: Peak Circumferential Strain vs Number of Cycles for Three Different Pressurized tubes (Jiao and Kyriakides 2011).....	43
Figure 2.12(a): Peak Axial Strain vs Number of Cycles to Failure for Tested Tubes of Same Pre-strain and Internal Pressure (Jiao and Kyriakides 2011)	43
Figure 2.12(b): Peak Circumferential Strain vs Number of Cycles to Failure for Tested Tubes of Same Pre-strain and Internal Pressure (Jiao and Kyriakides 2011).....	44
Figure 2.13: Strain at Clip Gauge vs Global Strain (Das et al., 2007a).....	44
Figure 2.14: Final Deformed Shape of Specimens (Nazemi et al., 2009)	45

Figure 2.15: Picture of the Specimen Showing Strain Gauges and Repair Location (Alexander and Kulkarni 2009)	45
Figure 2.16: S-N Curves for Tubular Connections (API RP2A, 2002)	46
Figure 2.17: Nomograph RELating H/L to Design Life and Years of Service Using REsults With and Without Composite Reinforcement (Alexandre et al., 2009)	47
Figure 2.18(a): Fatigue Test Result against Theoretical S-N Curves for 5% Dent Depths (Cunha et al., 2009)	47
Figure 2.18(b): Fatigue Test Result Against Theoretical S-N Curves for 10% Dent Depths (Cunha et al., 2009).....	47
Figure 2.19(a): Effect of Pipe Grade on D/t and SCF (Durowoju et al., 2016).....	48
Figure 2.19(b): Effect of Pressure Cyclic Load Range on D/t and SCF (Durowoju et al., 2016)	49
Figure 2.20: Schematics of Four-point Experimental Test Setup (Dama et al., 2007).....	49
Figure 2.21: Denting Setup for Pipe Specimen (Pournara et al., 2015).....	50
Figure 2.22: Monotonic and Cyclic Bending Setup for Dented Pipe Specimen (Pournara et al., 2015)	50
Figure 2.23: Cyclic Bending Setup for Strip Specimen (Pournara et al., 2015).....	51
Figure 2.24: Strip Specimens Cut from Pipes (Das et al., 2007b).....	51
Figure 2.25: Details of Strip Specimens Cut from Pipes (Das et al., 2007b)	52
Figure 2.26(a): Recommended Maximum Allowable Ripples, Wrinkles and Buckles for Steel Pipe (CSA Z662, 2019).....	52
Figure 2.26(b): Geometric Measurement of Wrinkle Profile Parameters.....	53
Figure 3.1: Pipe Specimen with Four Straight Bars	69
Figure 3.2: Geometric Measurement of Wrinkle Profile Parameters	69
Figure 3.3: Cut Pipe Specimens with Appropriate Markings and Straight Bars	70
Figure 3.4(a): Schematics of Specimen Bottom Plate	70
Figure 3.4(b): Schematics of Specimen Top Plate.....	71

Figure 3.5: Test Setup for Monotonic Loading Stage.....	71
Figure 3.6: Schematics of Test Setup for Monotonic Test	72
Figure 3.7: Schematics of Support Base Top Plate.....	72
Figure 3.8: Schematics of Strain Gauge Configuration	73
Figure 3.9: Sprague Air-driven Hydrostatic Pressure Pump	73
Figure 3.10: Picture of a Steel Collar.....	74
Figure 3.11: Wrinkle Profile Measurement using Contour Gauge	74
Figure 3.12: Mean Monthly Soil Temperature at 0.3 m Depth at Different Locations Around Pipelines Located in Southern Alberta (Naeth et al., 1993)	75
Figure 3.13: Test Setup for Axial Cyclic Loading Stage.....	75
Figure 3.14: Schematics of Test Setup for Axial Cyclic Test.....	76
Figure 3.15(a): Load Cell – Pipe Specimen Connecting-Plate	76
Figure 3.15(b): Load Cell – Connecting Plate Connecting Rod.....	77
Figure 3.16(a): Strain Gauge Configuration on Wrinkled Pipe.....	77
Figure 3.16(b): Schematics of Strain Gauge Configuration for Wrinkled Pipe	78
Figure 3.17: Axial Cyclic Test Amplitude Data for Five Cycles	78
Figure 3.18: Six Pipe Coupon Specimens.....	79
Figure 3.19: Coupon Specimen under MTS Universal Testing Machine.....	79
Figure 4.1: Load vs. Global Displacement Behaviour for Group 1 Specimens	101
Figure 4.2: Load vs. Local Strain Behaviour for Specimen IP30WA10.5	102
Figure 4.3: Load vs. Local Strain Behaviour for All Group 1 Specimens Near the Wrinkle Crest	102
Figure 4.4: Deformed Shape of Group 1 (0.3py) Specimens	103
Figure 4.5: Load vs. Global Displacement Behaviour for Group 2 Specimens	103
Figure 4.6: Load vs. Local Strain Behaviour for Specimen IP60WA8	104

Figure 4.7: Load vs. Local Strain Behaviour for All Group 2 Specimens Near the Wrinkle Crest	104
Figure 4.8: Deformed Shape of Group 2 (0.6py) Specimens	105
Figure 4.9: Relationship Between Wrinkle Amplitude Ratio and No. of Cycles to Failure for Group 1 (0.3py) Specimens	105
Figure 4.10: Load vs. Displacement Hysteresis curve for IP30WA4.....	106
Figure 4.11: Relationship Between HLE and Number of Cycles for Group 1 (0.3py) Specimens	106
Figure 4.12: Relationship Between Total Hysteresis Loop Energy and Wrinkle Amplitude Ratio for Group 1 (0.3py) Specimens	107
Figure 4.13: Strain Movement Around the Wrinkle Region During Axial Cyclic Loading	107
Figure 4.14(a): Relationship Between Local Longitudinal Strain and Applied Load at Wrinkle Crest for Specimen IP30WA4	108
Figure 4.14(b): Relationship Between Local Longitudinal Strain and Applied Load at Wrinkle Crest for Specimen IP30WA6	108
Figure 4.15(a): Relationship Between Local Longitudinal Strain and Applied Load at Wrinkle Crest for Specimen IP30WA8	109
Figure 4.15(b): Relationship Between Local Longitudinal Strain and Applied Load at Wrinkle Crest for Specimen IP30WA10.5	109
Figure 4.16: Relationship Between Local Hoop Strain and Applied Load at Wrinkle Crest for Specimen IP30WA4.....	110
Figure 4.17: Relationship Between Local Longitudinal Strain at Wrinkle Feet and Applied Load for Specimen IP30WA4.....	110
Figure 4.18(a): Visible Crease at Wrinkle Crest for Specimen IP30WA10.5	111
Figure 4.18(b): Visible Notch at Wrinkle Crest for Axial Cyclically Loaded Wrinkled Pipes (Das et al. 2007a).....	111
Figure 4.19: Visible Circumferential Fracture at Wrinkle Crest for Specimen IP30WA8.....	112

Figure 4.20: Relationship Between Wrinkle Amplitude Ratio and No. of Cycles to Failure for Group 2 (0.6py) Specimens	112
Figure 4.21: Relationship Between Wrinkle Amplitude Ratio and No. of Cycles to Failure for All Specimens	113
Figure 4.22: Load vs. Displacement Hysteresis curve for IP60WA4.....	113
Figure 4.23: Relationship Between HLE and Number of Cycles for Group 2 (0.6py) Specimens	114
Figure 4.24: Relationship Between Total Hysteresis Loop Energy and Wrinkle Amplitude Ratio for Group 2 (0.6py) Specimens	114
Figure 4.25: Relationship Between Local Longitudinal Strain and Applied Load at Wrinkle Crest for Specimen IP60WA4.....	115
Figure 4.26(a): Relationship Between Local Longitudinal Strain and Applied Load at Wrinkle Crest for Specimen IP60WA6	115
Figure 4.26(b): Relationship Between Local Longitudinal Strain and Applied Load at Wrinkle Crest for Specimen IP60WA8	116
Figure 4.26(c): Relationship Between Local Longitudinal Strain and Applied Load at Wrinkle Crest for Specimen IP60WA10.5	116
Figure 4.27: Relationship Between Local Hoop Strain and Applied Load at Wrinkle Crest for Specimen IP60WA4.....	117
Figure 4.28: Relationship Between Local Longitudinal Strain and Applied Load at Wrinkle Feet for Specimen IP60WA4.....	117
Figure 4.29: Visible Flat Appearance at Wrinkle Crest for Specimen IP60WA10.5	118
Figure 4.30: Visible Longitudinal Fracture at Wrinkle Crest for Specimen IP60WA6	118
Figure 4.31: Nominal Stress and Strain Behaviour of API 5L X42 Pipe Material.....	119
Figure 5.1: General Pipe Assembly	135
Figure 5.2: Nominal Stress and Strain Behaviour of API 5L X42 Pipe Material from Coupon 6	136

Figure 5.3: True Stress and True Plastic Strain Behaviour till Fracture.....	136
Figure 5.4: Load vs. Global Displacement Behaviour for Specimen IP30WA4 with Varying Mesh Densities.....	137
Figure 5.5: Load at Maximum Displacement vs. Varying Mesh Density for Specimen IP30WA4.....	137
Figure 5.6: von Mises Stress at Wrinkle Crest vs. Mesh Density for Specimen IP30WA4.....	138
Figure 5.7(a): Typical Pipe Mesh	138
Figure 5.7(b): Typical Endplate Mesh.....	139
Figure 5.8: Meshing of Imported Deformed Pipe Geometry.....	139
Figure 5.9: Element Selection and Meshing for Coupon 6 FE Model.....	140
Figure 5.10: Schematics of Boundary Conditions Associated with Coupon 6 FE Model.....	140
Figure 5.11: API 5L X42 Elastic-plastic Material Verification.....	141
Figure 6.1: Comparison for Load vs Displacement Plot Between Experimental and FEA Results for Specimen IP30WA10.5.....	153
Figure 6.2: Comparison for Load vs Displacement Plot Between Experimental and FEA Results for Specimen IP30WA8.....	153
Figure 6.3: Comparison for Load vs Displacement Plot Between Experimental and FEA Results for Specimen IP30WA6.....	154
Figure 6.4: Comparison for Load vs Displacement Plot Between Experimental and FEA Results for Specimen IP30WA4.....	154
Figure 6.5: Comparison for Load vs Displacement Plot Between Experimental and FEA Results for Specimen IP60WA10.5.....	155
Figure 6.6: Comparison for Load vs Displacement Plot Between Experimental and FEA Results for Specimen IP60WA8.....	155
Figure 6.7: Comparison for Load vs Displacement Plot Between Experimental and FEA Results for Specimen IP60WA6.....	156

Figure 6.8: Comparison for Load vs Displacement Plot Between Experimental and FEA Results for Specimen IP60WA4.....	156
Figure 6.9: Comparison of Deformed Shape for Specimen IP30WA10.5	157
Figure 6.10: Comparison of Deformed Shape for Specimen IP30WA8	158
Figure 6.11: Comparison of Deformed Shape for Specimen IP30WA6	158
Figure 6.12: Comparison of Deformed Shape for Specimen IP30WA4	158
Figure 6.13a: Relationship Between Local Longitudinal Strain and Applied Load at Wrinkle Crest Obtained from FEA for Specimen IP30WA4	159
Figure 6.13b: Relationship Between Local Longitudinal Strain and Applied Load at Wrinkle Crest Obtained from Experiment for Specimen IP30WA4	159
Figure 6.14: First Cycle Comparison for the Relationship Between Local Longitudinal Strain and Applied Load at Wrinkle Crest for Specimen IP30WA4	160
Figure 6.15: First Cycle Comparison for the Relationship Between Local Longitudinal Strain and Applied Load at Wrinkle Crest for Specimen IP30WA6	160
Figure 6.16: First Cycle Comparison for the Relationship Between Local Longitudinal Strain and Applied Load at Wrinkle Crest for Specimen IP30WA8	161
Figure 6.17: First Cycle Comparison for the Relationship Between Local Longitudinal Strain and Applied Load at Wrinkle Crest for Specimen IP30WA10.5	161
Figure 6.18a: Fatigue Strain-Life Curve (Dowling, 2013).....	162
Figure 6.18b: Cycle-Dependent Relaxation of Mean Stress for an AISI 1045 Steel (Dowling, 2013).....	162
Figure 6.19: FEA Results for Maximum Principal Strain After One Cycle for Specimen IP30WA8	163
Figure 6.20: Maximum Principal Strain Along Wrinkled Region Obtained from FEA Analysis	163
Figure 6.21: Comparison of Cycles to Failure Obtained from Strain Model and Experiment...	164

LIST OF ABBREVIATIONS / SYMBOLS

Abbreviations

AC	Alternating Current
AISI	American Iron and Steel institute
API	American Pipeline Institute
APPW	Armor Plate Pipe Wrap
ASTM	American Society for Testing and Materials
ASME	American Society of Mechanical Engineers
BPVC	Boiler and Pressure Vessel Code
CAE	Computer-Aided Engineering
CEPA	Canadian Energy Pipeline Association
CSA	Canadian Standards Association
DAQ	Data Acquisition System
DIC	Digital Image Correlation
DNVGL	Det Norske Veritas Group
DOF	Degree of Freedom
ECA	Engineering Critical Assessment
ERW	Electric Resistance Weld
FE	Finite Element
FEA	Finite Element Analysis
FFS	Fitness-for-Service
FRP	Fibre Reinforced Polymer
GEOPIG	Geometry Pipeline Intervention Gadget

HCF	High Cycle Fatigue
HLE	Hysteresis Loop Energy
LCF	Low Cycle Fatigue
LVDT	Linear Differential Transformer
MAOP	Maximum Allowable Operating Pressure
NPS	Nominal Pipe Size
PC	Personal Computer
PIG	Pipeline Intervention Gadget
RAM	Random Access Memory
RP	Reference point
SAF	Sandvik Austenite-Ferrite
SAE	Society of Automotive Engineers
SCF	Stress Concentration Factor
SEL	Structural Engineering Laboratory
SMYS	Specified Minimum Yield Strength
SNCF	Strain Concentration Factor
SNG	Southern Natural Gas
VI	Virtual Instrument

Latin Symbols

A_s	Cross-sectional area of the pipe
b	Fatigue strength exponent
B	non-dimensional dent geometric parameters
c	Fatigue ductility exponent

C_e	Thrust load due to the endplate
C_t	Thermal expansion/contraction load
C_v	Poisson's ratio plane strain constraint load
d	Dent depth
d/D	dent depth-to-pipe diameter ratio
D	Nominal diameter of pipe
D_F	Damage factor
D_o	Outer diameter of pipe specimen
D/t	Nominal diameter-to-thickness ratio
E	Young's Modulus
h	height of wrinkle crest to trough
h/L	Wrinkle height-to-wrinkle length ratio
K_f	Fatigue stress concentration factor
K_t	Theoretical stress concentration factor
L	Length of pipe or tube
L/D	Length-to-nominal diameter ratio or pipe specimens' slenderness ratio
M_b	Resultant bending moment
M_i	In-plane bending moment
M_o	Out-of-plane bending moment
M_t	Torsional moment
N_f	Number of cycles that causes failure
p_y	Internal pressure causing yielding in the pipe

P_s	Net load applied on the pipe specimen
P_u	Ultimate load
P_y	Yield load
R_i	Internal radius of pipe specimen
R_o	Outer radius of the pipe
S	Stress range
S_b	Resultant bending stress
S_e	Endurance limit
S_E	Thermal expansion range
S_t	Torsional stress, MPa
S_u	Ultimate tensile strength
S_{30}	The total hysteresis loop energy required to fail Group 1 wrinkled pipe specimens
S_{60}	The total hysteresis loop energy required to fail Group 2 wrinkled pipe specimen
$S - N$	Stress fatigue curve
t	Thickness of pipe
T	Temperature factor
U_o	Hysteresis Loop Energy obtained from the first cycle of hysteresis loop
ν	Poisson's ratio
Z	Section modulus of pipe

Greek Symbols

α	Coefficient of linear thermal expansion for the pipe material
----------	---

δ_x^p	Change in longitudinal length of pipe or tube
δ_x^p/L	Peak axial strain
ε_e	Elastic strain
ε_p	Plastic strain
$\varepsilon_{\theta p}$	Peak circumferential strain
ε_f'	Fatigue ductility coefficient
$\varepsilon - N$	Strain fatigue curve
σ_a	Alternating stress
σ_m	Mean stress
σ_{max}	Maximum stress
σ_{min}	Minimum stress
σ_f'	Fatigue strength coefficient
σ_h	Hoop stress in the pipe wall due to applied internal pressure
σ_y	Yield strength of the pipe material
Δ_u	Global ultimate displacement
Δ_y	Global yield displacement
$\Delta\varepsilon_{max}$	Maximum strain variation
$\Delta\varepsilon_{nom}$	Nominal strain variation
ΔL	Change in length of pipe
ΔT	Temperature difference

CHAPTER 1

INTRODUCTION

1.1 General

The oil and gas industry are an essential part of the growing Canadian economy and has solidified its place in the global energy industry as the sixth largest producer of oil and natural gas in the world. This sector contributes about 10% to Canada's GDP, which pays about 20 billion dollars per year in taxes, royalties and fees to the government (NRCAN, 2019). These oil, natural gas and petroleum products are transported from where they are produced to where they are needed primarily by using steel pipelines. The majority of these pipelines run underground; thus, they are called buried pipelines. Pipelines have been commissioned in Canada since 1853, with about 119,000 km underground network, transporting up to 3.8 million barrels of crude oil per day and 14.2 billion cubic feet of natural gas per day (NRCAN 2019). Although pipelines have been proven to be the most reliable means of natural oil and gas transport, operators are charged with the responsibility of anticipating, preventing and mitigating potentially dangerous conditions associated with their pipelines.

Notwithstanding the fact that most pipelines are designed for a life cycle of 50 – 100 years, most of the buried pipelines reach their service life before the age of 50 years, and 8% of that failure is caused by geotechnical failure (CEPA, 2019). Basically, 30% of the pipelines in Alberta; which is Canada's largest oil and gas producing province, are more than 25 years old, and 5% are more than 50 years old. Considering these circumstances, most of these buried pipelines are more vulnerable to failure, when subjected to vicious environment. The increasing demand to explore the natural oil and gas deposits located in remote areas of the Canada, has fostered the exploration of oil and gas in the complex topographical terrains of the arctic and sub-arctic regions of Canada. Pipelines are compelled to be buried along mountains, river crossings, discontinuous permafrost and unstable slopes. One of the most prominent problem experienced by operators is slope movement, which introduces large deformation on the pipe wall. The local deformation of the pipe wall often results in local buckling of the pipe called wrinkling, which is due to the combination of internal pressure, lateral loads and axial loads.

Wrinkled pipelines may possess some ductility reserve after the formation of wrinkle defect, and as such, do not pose an immediate threat to the integrity and safety of pipeline systems (Das et al., 2007a). However, further subjugation of wrinkled pipelines to seasonal temperature variation and cyclic freeze-thaw may induce the effect of fatigue, and thus cause the pipeline to fracture in the region where stress and strain is concentrated. Failure of the wrinkled pipelines may cause leak or rupture which leads to lingering environmental impacts, loss of revenue, and attract regulatory fines and related litigation.

1.2 Statement of Problem

In order to harness the immense economic opportunities, the oil and gas sector presents to Canada, it is inevitable to pass pipeline structures along routes that face geotechnical challenges. Despite geotechnical design considerations, wrinkled field pipelines experience large cyclic displacements which lead to an eventual leak or rupture of the pipe walls, due to fatigue. This fatigue failure on wrinkled pipelines have been visible during operator field investigation. Figure 1.1, Figure 1.2 and Figure 1.3 all present pictures of segments cut from field pipelines used for transportation of oil and gas but fractured due wrinkle defects which developed as a result of geotechnical movements.

Currently, pipeline operators have limited information on how to assess the severity of a wrinkle defect subjected to axial cyclic loading, since limited research data or guidelines are available. Various codes and standards such as; CSA Z662 (CSA Z662, 2019), ASME 31.4 (ASME 31.4, 2016), SME 31.8 (ASME 31.8, 2018) and DNV-OS-F101 (DNV-OS-F101, 2013), either do not discuss this issue or simply provide a conservative approach to remove or repair the segments of the pipeline where wrinkle defects are identified. In order to avoid the risk failure of the pipe wall has on the environment, operators enact costly and often unnecessary removal or repair actions. These precautionary measures may lead to an undesirable shutdown of pipeline operations, and as a result lead to loss of revenue for pipeline operator and interrupt the supply of oil and gas to downstream industries, businesses, and homeowners.

It is alleged that operators may not always have to remove or repair wrinkle defect, depending on the geometry of the wrinkle profile. Therefore, it is necessary to develop a defect assessment guideline that pipeline operators could utilize to assess both the possibility of failure of small wrinkle defect, and the remaining life associated with a wrinkled pipe.

1.3 Objectives and Scope

The present research work was initiated to provide the information regarding the behaviour of buried wrinkled steel pipe when subjected to axial cyclic loads, as a result of seasonal temperature variation or cyclic freeze-thaw. Consequently, the following issues are the primary objectives of this research project.

1. To investigate the failure and behaviour of wrinkled pipes with varying pipe and wrinkle geometry which are subjected to axial cyclic loading, representative of extreme seasonal temperature variation and cyclic freeze and thaw.
2. To provide methodology that is suitable to develop a numerical tool for estimating remaining life of wrinkled field pipelines subjected to axial load cycles, using the strain life approach.

The scope of this project was limited to investigation of 8-inch (211.3 mm) Nominal Pipe Size (NPS8), Schedule 10 (SCH10) of API 5L X42 (API 5L, 2018) steel linepipe. Specifically, only pipes with geometric properties conforming to diameter-to-thickness ratio (D/t) of approximately 50 were tested. A total of eight full-scale tests and eight numerical models having the above-mentioned material and geometric properties were analyzed to investigate the effect of axial cyclic loads on wrinkled pipe specimens. The numerical simulations of the full-scale tests were executed using ABAQUS/CAE, a commercially available general-purpose finite element code capable of simulating non-linear materials and geometries. The primary goal of the numerical simulation was to extract the maximum principal strains associated with the deformed geometry within the wrinkle segment.

1.4 Organization of thesis

This thesis is divided into five major chapters and two smaller chapters: the first chapter is the Introduction and the very last chapter (Chapter 8) is the Summary, Conclusions and Recommendations. Chapter 2 summarizes the findings of previous researchers obtained from the literature and existing codes/standard on wrinkle formation, axial cyclic loading and established fatigue life prediction models. Chapters 3 and 4 discuss the experimental test program as well as results obtained. In the following two chapters (Chapter 5 and 6), numerical modelling of full-scale tests and coupon tests are validated with the results obtained from the experimental program.



Figure 1.1: Fractured Field Pipeline of Wascana Energy Inc. (Courtesy of Wascana Energy Inc.)



Figure 1.2: Fractured Field Pipeline of Husky Energy Inc. (Courtesy of Husky Energy Inc.)



Figure 1.3: Fractured Field Pipeline of WestCoast Energy Inc. (Courtesy of WestCoast Energy Inc.)

CHAPTER 2

LITERATURE REVIEW

2.1 General

This literature review aims at summarizing the previous research, current practices, and guidelines on wrinkled oil and gas pipelines subjected to axial cyclic loads. This review emphasizes the previous works on the local behavior of oil and gas pipelines installed in vicious environments. This review focuses on the consequences of the exposure of pipe walls to stresses and strains, the factors that initiate the subsequent defects, and the limitations of pipelines with a wrinkle defect. In addition, this review discusses the effect of several load combinations including the effects of fatigue on oil and gas pipes with variable wrinkled pipe parameters. There is also a focus on the previous works completed on the factors that propel fatigue in pipelines and the assessment of the remaining life of wrinkled pipelines. However, guidelines for pipeline systems integrity management are available in the current codes and standards pertaining to fatigue and wrinkle initiation. This literature review corroborates researchers' view, that the approach in these codes and standards may be too conservative.

According to various codes and standards, a wrinkle defect that has been evaluated to surpass the allowable limits need to be removed or repaired. Clause 10.10.8.2 of Canadian standard, CSA Z662 states that ripples, wrinkles, and buckles that has been identified as a defect, if not removed or repaired, shall be periodically monitored (CSA Z662, 2019). The wrinkled pipe may either be replaced or be repaired using a steel pressure-containment repair sleeve as discussed in Table 10.2 of CSA Z662-19. However, American codes, ASME 31.8 (ASME 31.8, 2018) and ASME 31.4 (ASME 31.4, 2016) support wrinkle defect repair by using steel pressure-containment encirclement sleeve, reinforcing type-full encirclement sleeve, mechanical bolt-on clamps or the total removal of the defected pipe. Furthermore, reducing the pressure to 80% of the operating pressure experienced by the defect at the time of discovery is also recommended before repair or removal, as discussed in paragraph 851.4.2 of ASME B31.8 (ASME B31.8, 2018).

2.2 Local Buckling

Field observations and Engineering critical assessment (ECA) of buried energy pipelines have indicated that over time the subsurface geotechnical movement with or without thermal loads may produce extreme stresses, strains, curvatures, and deformation on pipe walls (Wilkie and Doblanko

2001, Yoosef-Ghodsi et al. 1995). These combined loadings in conjunction with pipeline construction practices creates a phenomenon described as local buckling which is facilitated by the interaction between soil and pipe walls.

Local buckling which is accompanied by external loads produce large forces and/or displacement that subsequently lead to localization of stresses and strains in the pipe wall at the region of imperfection, i.e. where stress is concentrated. Although pipelines are designed for a lifecycle of 50 to 100 years, most of the pipelines fail before the age of 50 years. According to CEPA 2019 pipeline industry performance report (CEPA, 2019), the major causes of pipeline failure are corrosion, external interference, geotechnical movement, construction practices and operational problems (Figure 2.1). Since, the geotechnical movement largely influences wrinkle initiation, growth and associated failure, the following subsection focuses on the discussions pertaining to geotechnical movements.

2.2.1 Geotechnical Movement

Pipeline-soil interaction in conjunction with pipeline construction practices can stimulate a phenomenon described as local buckling in the pipe wall (also known as a wrinkle defect), when field pipelines are buried in a geotechnically active area which is susceptible to various geotechnical activities and movements. Geotechnical movement of buried pipelines can be due to several natural phenomenon, few of which are: slope movement, landside, frost heave and thaw settlement.

2.2.1.1 Slope Movement

Wilkie et al. (2001) reported the inspection and replacement of buried pipelines, built in the winters of 1983 to 1984, which were used for transporting crude oil from Norman Wells in Sahtu region of Northwest territories to Zama, Alberta in Canada. It was reported that this buried pipeline runs through a discontinuous permafrost region that subjects the pipeline to frozen and unfrozen interfaces. This results in the differential movement of soil around the buried linepipe causing development of localized strains and curvatures. The pipeline of 323 mm outer diameter with 6.91 mm wall thickness (diameter-to-thickness ratio or D/t of 47) was designed for arctic regions to cause little or no disturbance to the environment. The pipes were designed to withstand primary and secondary loads such as live weight, dead weight, internal pressure, and thermal expansion. These loads may induce longitudinal tensile strains limited to 0.5% and longitudinal compressive

strains limited to 0.75%. The pipeline also traverses many slopes whose movement induces structural response. For this reason, “slope 92”, one of the critical slopes out of the 869 km long pipeline was used as a case study since the detection of strain growth by inline inspection (ILI) tool called “Geopig”. The practice of pipeline monitoring program annually led to the use of the Geopig in 1989 to detect pipe movement associated with slope instability and differential freeze and thaw. A strain growth of 0.2% was noticed, which led to exploratory dig to confirm the data from the Geopig run, which was found to be accurate as shown in Figure 2.2. The wrinkle formed beside a girth weld which is a location of stress concentration. Review of the annual Geopig data in 1997 depicted the evolution of a wrinkle was the result of combined internal pressure, axial loads, and bending load caused by the operating pressure, ground movement, and slope instability, respectively. The characteristics that indicated that a wrinkle had formed are as follows:

- a) A high value of the compressive bending strain.
- b) An increase in the internal diameter of the pipe at the same location.

In February 1998, a team of experts visited the site for investigative dig for verifying the existence of the wrinkle, performing complete nondestructive examination near the wrinkle and installing monitoring instrumentation on the slope and pipe. The team found that the Geopig data were accurate as it confirmed the results of the site investigation. Subsequently, the growth of pipe strain and movement of slope was monitored until the pipe section with the wrinkle defect was replaced in February 1999. Laboratory testing was done on the pipe sections excavated out of the ground; however, no discussion was provided by Wilkie et al. (2001).

In the year 2000, Bidwell et al. (2010) undertook a field study to determine the effect of permafrost and slope movement on the section of the linepipe that runs in between Norman wells in Northwest territories to Zama in Alberta. Various strain and slope movement data were collected from the instruments installed on pipe sections located in slopes 44 and 45, crossing between Tulita and Wrigley, NT. The study concluded that the shear plane of the ongoing ground movement crosses the pipeline along the slope, which may cause excessive strain or deformation in the pipe wall.

An Engineering Critical Assessment (ECA) using finite element (FE) method was conducted to assess the effect of a rapid large magnitude slope movement on the structural integrity of the pipeline by applying a large displacement and nonlinear pipe soil interaction. Commercially available FE software, ABAQUS (Dassault Systemes, 2007) was used in the ECA. The thermistor

cables installed during the site investigation showed that the permafrost is 3.8 to 4.3 m deep within that period, and the trend for permafrost deepening (slope movement) will continue for a long-term. The slope inclinometers measured slope movement, which varied along the depth of the ground. The displacement vs. time data collected from the data points in the field showed a relatively uniform rate of movement of about 1.6 mm/month. All the data from these instruments were used to model the properties and interactions between the soil and pipelines in the FE model. The validated FE model was then used to determine both current slope movement and worst-case large magnitude sudden slope movement. It was concluded that it was unlikely to exceed the strain capacity of the pipeline in slopes 44 and 45 if there was a sudden large magnitude slope movement. Although, a continuous slope movement may cause a simultaneous strain on the length of pipe walls that may lead to wrinkling or tensile failure of the pipe wall.

2.2.1.2 Frost Heave and Thaw Settlement

The frost heave and thaw settlement are one of the several reasons for bending deformation and associated local buckling (wrinkling) of the buried pipelines in permafrost regions. The interaction between the buried pipeline and the frozen soil can be a dynamic and complex interaction process.

Frost heave occurs when the mean annual temperature of unfrozen soils falls below 0°C, and ice lenses begin to form within the surrounding soil (Li et al., 2018; Oswell, 2011). The formation of thick ice lenses leads to upward swelling of the soil, which vertically displaces the buried pipeline upward. A schematic of this phenomenon is shown in Figure 2.3 creating bending of the pipe segment. Frost heave requires three basic conditions to form ice lenses: a freezing temperature in unfrozen soils, a source of water to migrate from the warm side to the freezing front, and frost-susceptible soils that permit free water to migrate through the freezing soils. Obstruction of any of these conditions progressively diminishes frost heaving (Li et al., 2018). Frost heave alone does not pose a threat to the structural integrity of buried onshore pipelines, but rather it is the differential frost heave that poses a concern and forms the basis for pipeline design. Differential frost heave could result from change in soil type (textural transition) or change from frozen soil to unfrozen soil (thermal transition). However, the thermal transition usually forms a more extreme design case, because the frozen soil on the stable side forms a stiffer restraint (Nixon et al., 2002).

Thaw settlement occurs when the ice content of a frozen soil is high enough to cause the settlement of the soil grains during ice melting. When the melting of frozen soils occurs at a rapid rate, excess

pore water pressures are generated, which subsequently reduces the bearing capacity of the soils beneath the pipeline. Additional buoyancy forces surrounding the pipeline thereby instigates the settlement of the pipe (Li et al., 2018). Induced gravity loads from the backfill soil leads to downward settlement of the pipe in the unstable soil, generating curvatures and strains on the pipe walls (Figure 2.4). However, thaw settlement alone does not pose a threat to the structural integrity of pipelines, but rather the differential settlement of the pipe over a short distance induces large structural stresses and strain curvatures (Nixon et al., 2002).

In summary, the interaction between buried pipelines, and both frost heave and thaw settlement may induce longitudinal compressive or tensile forces and thermal stresses. These stresses alongside pipelines operating pressure, causes buried pipelines to suffer axial, lateral and vertical movements, as well as local buckling and wrinkling (Li et al., 2018 ; Oswell, 2011; Bidwell et al., 2010; Nixon et al., 2002). However, if the freeze-thaw interaction poses a threat to a pipeline, mitigation procedures are instigated. These procedures include increasing the burial depth of pipelines, increasing the strength of pipelines by increasing the wall thickness, applying insulation measures around and under the pipeline, and altering the operating temperature of the pipe.

2.2.2 Parameters Affecting Local Buckling and Wrinkling

Murray (1997) summarized various studies carried out at the University of Alberta, addressing the behavior of buried pipelines subjected to curvatures, wrinkle defects, and deformations beyond their limit points. These previous studies were carried out with the possibility of assessing the suitability of pipelines passing through regions of discontinuous permafrost. The identified localization of strains causes subsequent development of local deformation or buckling within the region of softening (load decrease with deformation increase). Monotonic compressive load test, also known as stub-column test was performed on pipes of various lengths, and similar characteristics were noticed for all the wrinkling behaviors as follows:

- All the tests developed a single wrinkle extending over only a small part of the length.
- As the wrinkling amplifies in the post-buckling zone, its capacity to carry load decreases and consequently, the load-deformation relationship softens.
- While the strain around the wrinkle continues to increase, the strain in regions away from the wrinkle decreases.

- Stress-strain relationships for gauge lengths that span the region of strain localization are length dependent and do not represent properties of material and cross-section.

The increment of these stresses and localization of strains may lead to the formation of a ‘wrinkle’ on the pipe wall. The wrinkle amplifies as softening in the pipe material occurs in the post-buckling zone.

There are several factors that may affect local buckling (Kashani et al., 2018; Fatemi and Kenny 2017; Das et al., 2007a; Murray 1997; Yoosef-Ghodsi et al., 1995), these factors include the following:

- I. Pipeline Operational Loading Conditions
- II. Pipe Construction Practices
- III. Pipe Geometry
- IV. Pipe Material Properties

The effect of these parameters on local buckling and wrinkling were studied earlier and is reviewed to further have some knowledge on how localization of strain lead to local buckling and ultimately lead to wrinkle formation and growth. A wrinkle is a type of defect that can be responsible for the initiating ductile fracture of an oil and gas pipe.

I. Pipeline Operational Loading Conditions

When all other parameters that affect local buckling are unchanged, the increase of the axial tensile load on a pressurized pipe increases its ultimate moment strength and compressive strain capacity. However, the increase of the axial compressive load applied on a pressurized pipe decreases its ultimate compressive strength and strain capacity (Fatemi and Kenny 2017).

Using finite element method, Zhou and Murray (1995) investigated the post-buckling behavior of linepipes subjected to combined loadings. The analysis was carried out on 13 specimens of Grade XL65 pipe with D/t ratio of 104 (API 5L 2018), where the axial loads and internal pressure were kept unchanged and the bending moment was varied. This was done for adequate prediction of the post-buckling behavior of the buckled segment along the deformed pipe to be achieved. It was deemed necessary to define the quantities based on longitudinal deformations and cross-sectional deformations. Longitudinal deformations were mainly described by average curvatures and average strains at centroid of the cross section while cross-sectional deformations were represented

by diametric differential, diametric expansion and radius differential. The action of combined loadings increased the deformation linearly, as hardening occurred beyond the elastic range. As material softening commenced in the post-buckling region, deformation localizes in the buckled segment to form a “wrinkle” which grows as applied axial and bending loads increase. The wrinkles formed took different buckling shapes and they are either a diamond shape or a bulging shape depending on the magnitude of the internal pressure. The absence of internal pressure (or presence of very low internal pressure) and presence of axial and bending loads caused a diamond shape. The bulging shape is dominant under the effect of high or medium internal pressure, and presence of axial and bending loads. It was found that when the bending load dominates, the wrinkle is confined to the compressive side of the flexural deformation, and when the axial load dominates, the wrinkle extends along entire circumference of the buckling segment.

The behavioral response of buried pipelines to applied external loads and introduction of internal pressure have been analyzed in the previous studies. The application of combined loads has been highlighted to influence wrinkle shape and growth. Significantly, the importance of internal pressure is compelling.

II. Pipeline Construction Practices

Pipes undergo different processes in pipeline construction before they become fully operational and ready to transport natural oil and gas. Because of these processes, it is almost impossible not to introduce imperfections on linepipes. These imperfections may cause defects that can be amplified by the impact of anchors, rocks or other heavy objects in the case of offshore pipelines, and by excavation equipment (Cunha et al., 2009). During pipeline construction to interconnect individual pipe joints, girth welds are produced (Fatemi and Kenny, 2017). Girth welds may create a weak spot because of mismatch of cross-section at the connection or misalignment of pipes during welding (Yoosef-Ghodsi, 1995). Wrinkle bends (cold bends) are also introduced for pipeline alignment in regions with complex topography and as a result lead to stress concentration.

Yoosef-Ghodsi et al. (1995) compared the experimental results extracted from the behavior of wrinkled girth welded pipes to the results of the behavior of wrinkled virgin pipes (pipes with no girth weld). The specimens were subjected to constant internal pressure, constant axial load and monotonically increasing curvature. Three 12-inch (305 mm) long segments of the linepipe with variable internal pressure were compared with four 20-inch (508 mm) long segments with variable

internal pressure. The experiment was controlled by un-pressurizing, half-pressurizing, and fully pressurizing the pipeline specimens. Contrary to the development of wrinkle in the girth-welded region of all the 12-inch (305 mm) long pipeline specimens, the wrinkle developed in the segment close to the end plates when the 20-inch (508 mm) long pipelines were fully pressurized. The moment versus curvature curves were similar to that of the virgin pipes (pipes with no girth weld). As originally observed that the pipe behaves as an elastic-plastic material due to its low elasticity and significant plasticity. It was observed that the internal pressure has a significant effect on the local buckling, as moment resistance decreased, and ductility increased on pressurizing both girth-welded pipes and virgin pipes. However, the ultimate strength and ductility of the virgin pipes was higher than that of girth welded pipes. It was also recommended that the limit strains (onset of wrinkling) for girth-welded pipes to be about 60% of the limit strains for virgin pipes. These results have confirmed that a girth-weld is a weak spot because of the following:

- There may be a mismatch of the cross-sections at the connection
- Possible misalignment of pipes during welding process
- Residual stresses can be generated in the longitudinal and circumferential axis due to thermal contraction of the pipe walls during welding
- Possible generation of geometry imperfections due to thermal contraction of the pipe walls.

A collaborative study was undertaken jointly at Memorial University of Newfoundland and Carleton University (Fatemi and Kenny 2017). A parametric study was carried out on high strength linepipes of grade X80 (API 5L 2018). The specimens were subjected to local buckling to highlight the effect of different parameters (D/t and slenderness ratio) on ultimate moment capacity and compressive strain capacity of pipelines. The effect of girth weld offset misalignment on local buckling was studied. It was observed that that an increase in the amplitude of the girth weld offset misalignment led to a decrease in ultimate moment capacity and strain capacity of the linepipes.

The study on wrinkling of virgin pipes and girth welded pipelines when subjected to combined axial load, internal pressure, and bending loads was discussed by Murray (1997). The study observed the relationship between localization of strains or buckling on the pipe walls and the shape of the wrinkle. It was observed that for fully pressurized virgin pipes, there was a formulation of a periodic wave pattern (ripples) on the pipe wall as compression load increased. However, all ripples disappeared except one which grew into a wrinkle defect as the load-deformation curve

softened. This was not the case for girth welded pipes, as a secondary wrinkle with a smaller amplitude grew near the primary wrinkle which was observed in the test and finite element analysis.

It is important to note that natural gas pipes are formed from flat steel plates by first forming a U-shape by using a U-ing die, which is bent to an almost O-shape before the joints are welded together. The resulting pipe is then radially expanded (E) using a mechanical expander into the plastic range deformation and then released to unload the radial pressure, this process is known as the UOE forming process (Figure 2.5). Kashani et al. (2018) developed a detailed finite element model to determine the effect of residual stresses that arise from the UOE pipe production process on buckling strains of pipes. The results of the detailed finite element analysis of pipes subjected to the forming process and combined-curvature moment load and internal pressure, was compared to analysis of pipes under combined loading without the effect of residual stresses. In all the cases considered (pressurized and unpressurized), the study showed that residual stresses developed as a result of the UOE forming process, and significantly reduced the buckling strains and material yield strength of the detailed model. The stress-strain relationship observed after the forming process also differ from the stress-strain relationship observed in tension test conducted on the flat steel plates.

Wrinkle bending practices were used in pipeline construction up until 1955. Wrinkle bending is a process of conforming steel pipe to the surrounding topography by forcefully compressing the pipe to obtain pipeline alignment. Alexander and Kulkarni (2009) studied wrinkle bends of El Paso pipeline when subjected to internal pressure cyclic loads. It was concluded that the presence of wrinkle bends in a pipeline induces stress concentration, which reduces its fatigue life.

III. Pipe Geometry

The diameter-to-thickness ratio (D/t) determines the bending stiffness of natural gas pipes as well as provides a means of characterization of longitudinal stress distribution along the pipe cross-section (Fatemi and Kenny, 2017). Fatemi and Kenny (2017) conducted a parametric study on linepipes of grade 550 (X80) subjected to local buckling. The study was done to determine the effect of different parameters (pipe geometry, pipe material and operational loading conditions) on ultimate moment capacity and compressive strain capacity of pipelines. The study concluded

that increase in the D/t ratio of linepipes decreased the ultimate moment capacity and the compressive strain capacity of the pipes.

Using commercially available non-linear finite element analysis tool ABAQUS, Nazemi et al. (2009) performed a parametric study on the behavior of X60 grade steel pipelines at the University of Windsor. The specimens were subjected to combined axial load, lateral load, and internal pressure under a constant internal pressure and fixed diameter to thickness ratio (D/t). It was observed that grade X60 wrinkled steel pipes with D/t ratio of 90 and higher do not fail in tearing rupture mode under the influence of combined loadings. However, wrinkled steel pipes with D/t ratio of 60 or lower fails in tearing rupture mode irrespective of the magnitude of internal pressure applied. Whereas, wrinkled pipes with D/t ratio of range 60 to 90 failed either by tearing rupture mode or excessive deformation, depending on the internal pressure applied.

IV. Pipe Material Properties

The longitudinal stress-strain behavior of pipe material may differ from circumferential stress-strain behavior and this is known as material anisotropy. Anisotropy is characterized by the mechanical properties of a material which is direction dependent. Corona et al. (2006) analyzed the results from set of bending tests completed on Aluminum alloy tubes by Kyriakides and Ju (1992). The results of the bending tests predicted using isotropic deformation theory, showed significant variance as compared to experimental results in the pre-buckling and post-buckling response of the linepipes. The predicted onset of wrinkling was later than the observed onset of wrinkling in the experiment and the predicted wrinkle wave lengths were larger than those observed in the experiment for all ranges of D/t examined. However, on incorporating anisotropy in the constitutive models used in pre-buckling and post-buckling analyses, it was observed the predicted wrinkle wavelength values reduced towards the values measured from the experiment. The predicted onset of wrinkling was more accurate compared to the analysis carried out assuming that the material yields isotropically. Results of the parametric study carried out on the anisotropic parameters (yield strength in longitudinal and circumferential direction) concluded that the bifurcation curvature is insensitive to yield strength in the longitudinal direction. However, the curvature increased with increase in yield strength in the circumferential direction. Also, wrinkle wavelength increased as yield strength in the circumferential direction reduced but a significant increase in the yield strength in the longitudinal direction caused an increase in wrinkle wavelength.

2.3 Failure Modes of Buckled Pipes

2.3.1 Collapse

Jiao and Kyriakides (2011) carried out axisymmetric monotonic and axial cyclic loading on circular stainless-steel tubes of D/t of 28 at the University of Texas, Austin. The tests were conducted under variable internal pressure, stress amplitude, and mean stress of axial stress cycles, which are predicted to be major influencing factors on pipe failure. A total of 13 tests were carried out on SAF2507 (ASTM A479 2006) stainless steel tubes. The test section had an outer diameter of 57.2 mm, a length of 102 mm and a thickness of 1.98 mm. The specimens were tested under variable internal pressure within the range of $0p_y$, $0.22p_y$, $0.49p_y$ and $0.6p_y$, where p_y is the internal yield pressure. The tubes were first monotonically compressed to wrinkle amplitudes represented by average pre-strain levels of 1%, 1.7%, 2% and 2.5%. Figure 2.6 shows the wrinkle amplitude and average pre-strain growth for one of the specimens pressurized up to $0.6p_y$, in which w is the height of the wrinkle, R is the radius of the outer diameter of the tube, and $x/2L$ represents the length of the tube. Further exposure of the wrinkle to monotonic and axial cyclic load led to the collapse of the tube at the wrinkle region, at which pipe can no longer serve its purpose. Zeinoddini et al. (2015) applied same loading sequence on similar specimen geometry as Jiao and Kyriakides (2011), however, in this study dent defect was considered. The test conducted at University of Technology in Tehran showed that the wrinkling in defected tubes was non-axisymmetric, compared to axisymmetric wrinkle formed in virgin tubes (non-defected tubes). However, as number of cyclic loading increased, a second wrinkle formed in the damaged part which led to collapse of defected pipe (see Figure 2.7).

The study of post-wrinkling behavior, limit strains, and failure modes of axi-symmetrically wrinkled Grade X52 NPS12 pipes with diameter of 305 mm and D/t of 45 was discussed by Das et al. (2007a). A monotonically increasing axial load was applied on two out of the eight specimens tested under realistic constant internal pressure. Observations from this study showed that the wrinkled pipe specimens tested, exhibited extreme ductile behavior in their post-wrinkling stage. The wrinkled specimens did not fail by fracture, but rather a deformation type failure developed due to formation of multiple wrinkles called accordion failure (Figure 2.8).

2.3.2 Rupture

Ruptures are common failure modes in operating pipelines. Ruptures lead to containment loss of transported products which is usually because of the presence of defect in pipes. Ghaednia et al.

(2017) subjected dent-crack defected pipe specimens to monotonically increasing internal pressure to determine the burst strength of the pipes with dent-crack defect. From this study, it was concluded that a pipe's mode of failure is influenced by the crack length, provided the crack defect is confined within the dent defect. A larger crack length tends to result in a leaking failure, and a smaller crack length tends to cause a violent rupture failure. Nazemi et al. (2009) also carried out full-scale test on NPS X60 grade pipes to study the type of wrinkle and rupture produced by the action of combined axial load, lateral load, and internal pressure. It was observed that the rupture in wrinkled region was confined to one segment of the wrinkled pipe, which was caused by the propagation of visible cracks at the foot or crest of the wrinkle. Further pressurizing of the pipe to simulate the resumption of pipeline operation after shutdown led to failure by tearing rupture mode (Figure 2.9), thereby compromising the structural integrity of the pipes.

2.3.3 Fracture

In fatigue analysis, fracture surfaces are flat and perpendicular to the predominant stress axis. Studies carried out on steel pipes show that wrinkled pipes subjected to cyclic loads initiates fatigue in the region of stress concentration. The orientation of fracture is dependent on the maximum principal stress experienced by the wrinkled pipe (Durowoju et al. 2019; Alexander and Kulkarni 2009; Das et al., 2007a). Same approach applies to fatigue of dented pipes (Cunha et al., 2009; de Carvalho Pinheiro et al., 2009;), as discussed by several earlier studies. Figure 2.10 shows a typical fracture failure as observed in the experimental tests conducted by Das et al. (2007a), to simulate failure mode in field pipelines exposed to temperature variation and cyclic freeze-thaw.

2.4 Factors Affecting Fracture in Pipelines

Fracture in continuum mechanics is a failure mode that occurs when surface or volume discontinuities are created within a crystalline material under the influence of applied stresses. The two basic mechanisms of fracture are brittle fracture and ductile fracture. Ductile fracture arises from the instability that occur when local plastic deformation arises in the region of crystalline defects. In the region of defect, the particle crystals, which are generally less ductile in a matrix of homogenous material, causes large plastic deformations. These deformations produce an instability which leads to the decohesion at the interface, thus initiating a crack. Pipeline construction practices and loading conditions' initiation of imperfections on pipes is almost inevitable. Further subjugation to aggressive environment when the pipe is buried may also lead to the fracture failure phenomenon as described above in Section 2.3. The mechanics of fracture

failure of buried oil and gas pipes have been discussed by various researchers and experts. The available knowledge on the growth of fracture in pipes, are found to be affected by the discussed factors from field observations, experimental tests, and finite element analysis.

2.4.1 Internal Pressure

Fatemi and Kenny (2017) conducted a parametric study on pipelines of grade 550 (X80) (high strength steel pipes) with diameters of 609 mm, 914 mm, and 1219 mm, and thickness of 15.23 mm subjected to local buckling. These pipe specimens had diameter-to-thickness ratios of 40, 60, and 80, respectively. This was done to highlight the effect of different parameters on ultimate moment capacity and compressive strain capacity of pipelines. These parameters were chosen to study the effect of D/t (40, 60, 80) and L/D (3.5, 5, 7, and 12) on the local buckling response of high strength line pipe subjected to combined state of loading. The L/D is the pipe segment's length-to-nominal diameter ratio or pipe specimens' slenderness ratio. When moment was applied to pressurized pipes, it was observed that with the increase in operating pressure the compressive strain capacity of the pipe increased, thereby delaying possible failure by fracture.

Jiao and Kyriakides (2011) used specimens made from grade SAF2507 stainless-steel tubes with D/t (outer diameter of 60 mm and thickness of 4 mm) ratio of 28. The tube specimens were subjected to axial load to form wrinkle with same initial compressive pre-strain. It was observed that increasing the internal pressure tends to lower the compressive strength of the pipe under combined internal pressure and uniaxial loading. On further application of axis-symmetric axial cyclic loads, increase in pressure increased the rate of circumferential ratchetting, and led to reduction in the number of cycles to failure (see Figure 2.11). Figure 2.11 shows the behavior of different pressurized tubes ($0.22p_y$, $0.49p_y$, and $0.6p_y$) wrinkled to same initial compressive pre-strain (2.5%) and subjected to axial cyclic loads of similar stress amplitude of 386 MPa (56000 psi). The figure is the graphical representation of peak circumferential strains, obtained from strain gauges in the hoop direction of the wrinkle crest every fourth cycle, against the number of cycles to failure.

2.4.2 Mean stress

Zeinoddini et al. (2014) investigated the influence of dent depth on the strain ratchetting of X42 and X56 steel tubes with D/t ratio of 12 (outer diameter of 59.4 mm and thickness 5 mm). An axial monotonic compressive loading was applied on the dented tubes, with dent depth-to-diameter ratio

(X/D) of 6%, 12% and 18% to an initial compressive pre-strain of 1% and 1.5% to form a wrinkle defect. After denting, each specimen was first monotonically loaded to the plastic zone, under uniaxial compression and strain control scheme, to reach a desired initial pre-strain. Stress controlled uniaxial cycles were then applied to the wrinkled specimens to study the effect of dent depths, mean stress, and initial compressive pre-strain. Results indicated that the increase in the mean stress increased the mean plastic ratchetting strain rate which thereby led to an early pipeline failure.

2.4.3 Stress Amplitude

Premise to the discussion in Subsection 2.3.1, Jiao and Kyriakides (2011) applied axial cyclic loads at different stress amplitudes (414 MPa, 441 MPa, 469 MPa) on various wrinkled tubes with similar initial compressive pre-strain level (2.0%) at a constant internal pressure ($0.59P_y$). It was concluded that increasing stress amplitude increased the rate of axial ratchetting which thereby reduced the number of cycles to collapse. However, increase in the stress amplitude had no effect on the circumferential ratchetting. Ratchetting in this study is described as the progressive plastic strain accumulation that occurred due to axial cycling of the tube about a non-zero mean stress. Figure 2.12(a) shows a plot of peak axial strain (δ_x^p/L) against number of cycles to failure (N), where δ_x^p is the change in longitudinal length of the tube and L is the initial length of tube. Figure 2.12(b) shows a plot of peak circumferential strain ($\varepsilon_{\theta p}$) against number of cycles to failure, where $\varepsilon_{\theta p}$ is measured from the strain gauges attached to the wrinkle crest and foot.

Zeinoddini et al. (2014) used similar specimens as Jiao and Kyriakides (2011) to investigate the influence of dent depth on the strain ratchetting of steel tubes. The dented tubes were compressed to an initial compressive pre-strain by applying axial monotonic compressive loading. Furthermore, the tubes were subjected to stress controlled uniaxial cycles to study the effect of dent depths, stress amplitudes and initial compressive pre-strain. Results indicated that although initial compressive pre-strain has the most significant effect on dented pipe ratchetting behavior, the increase in the stress amplitude increased the rate of strain ratcheting which led to an early pipeline failure.

2.4.4 Wrinkle Amplitude

Although, the shape of the post-buckling configuration that develops as the wrinkling is amplified is sensitive to the shape of the pre-buckling imperfections, Das et al. (2007a) observed that

inception of axial load cycling at an early post-wrinkling stage required a higher number of cycles to fracture and vice versa. Also, on compressing a pipe up to a certain plastic strain, to form a wrinkle at a constant internal pressure, Jiao and Kyriakides (2011) observed that further ratchetting of the wrinkled pipe with increasing wrinkle amplitude increased the rate of ratchetting and thereby reduced the number of cycles to failure. Both studies, however, did not base the studies on precise length measurement of the wrinkle profile, instead the studies observed the limit strain capacity of the wrinkle profile.

2.5 Fracture and Rupture Failure Under Different Load Combinations

2.5.1 Axial Cyclic Loads

Pipelines in their post-wrinkling stage exhibit high ductile behavior and do not fracture under monotonically increasing axisymmetric axial loads alone. A deformation failure mode (Accordion failure) caused by the development of multiple wrinkles is achieved instead (Das et al., 2007a). However, ratcheting of the pipe walls under low or high cycle fatigue caused by predominant axial and pressure cyclic loadings may lead to the fracture of the pipes.

Jiao and Kyriakides (2011), and Paquette and Kyriakides (2006) at the University of Texas at Austin studied the post-wrinkling behavior of SAF2507 stainless-steel tubes with a D/t ratio of 28 beyond the critical strain. Critical strain here is defined as the strain at the onset of wrinkling. The tests were carried out under axial stress cycles with variable internal pressure ($0p_y$, $0.22p_y$, $0.49p_y$ and $0.6p_y$), stress amplitude (414 MPa, 441 MPa and 469 MPa) and mean stress (155 MPa, 287 MPa and 327 MPa). The studies found that these factors are the major influencing failure factors. It was observed that the strain value at collapse, when a monotonic compressive load is applied to a wrinkled pipe, is similar to the strain value at collapse when an axial cyclic load is applied to the wrinkled pipe. This observation remains inconclusive for fracture failure, as the tested specimens in these studies failed by collapse. Moreover, axis-symmetric cyclic loads applied on wrinkled stainless-steel tubes in this study were stress-controlled.

Das et al. (2007a) completed a study to determine the post-wrinkling behavior, limit strains, and failure modes of axi-symmetrically wrinkled Grade X52 NPS12 pipes. A total of eight specimens were tested. Six specimens were tested under monotonically increasing axial loads, constant internal pressure, and cyclic axial loads. Figure 2.13 is a graphical representation of the relationship between the global strain values and local strain values. Global strain values were

obtained as the stroke of the MTS loading machine was divided by the original specimen length. The local strain values were obtained from the clip gauge attached after the wrinkle started forming at point H1 (see Figure 2.13). The movement of the local strain values from compression to tension is due to the loading and unloading of the MTS loading machine. This confirms the observation that mechanics of strain reversal occurred at the crest of the wrinkle on application of cyclic axisymmetric axial loads which led to the failure of the pipe walls by fracture (see Figure 2.10). However, the pipe still possessed some substantial ductility reserve in the post-wrinkling stage, but the ductility diminished as cycles of axial loadings increased. Depending on how early in the post-wrinkling stage the axisymmetrical axial cyclic loading commenced, the number of cycles to failure increased and vice versa. This observation further went to show that the life expectancy of wrinkled pipelines is highly dependent on the ductility reserve remaining in the wrinkled portion of the pipes.

2.5.2 Lateral Loads

Nazemi et al. (2009) carried out full-scale tests on NPS X60 grade pipes with D/t ratio of 23, to study the type of wrinkle and rupture produced by the action of combined axial, lateral, and internal pressure loads under variable boundary conditions. The wrinkles were developed under monotonically increasing axial loads with constant lateral loads and internal pressure. The boundary conditions were varied to suitably replicate the deformed shape of field pipelines subjected to similar combined loadings. It was observed that rupture in wrinkled region was confined to one segment of the wrinkled pipe, which led to the propagation of visible cracks at the foot or crest of the wrinkle (see Figure 2.14). The study concluded that the pressurizing of the pipe due to the resumption of pipeline operation after shutdown led to failure by tearing rupture mode, thereby compromising the structural integrity of the pipes.

2.5.3 Pressure Cyclic Loads

Natural oil and gas pipelines that are without defects, but subjected to normal pipeline operating pressure, will have no danger of failure within the design fatigue life. However, pipelines with pre-service or service defects subjected to pressure cyclic loading initiated a fracture of the pipe wall (Durowoju et al., 2019; Alexander and Kulkarni, 2009; Cunha et al., 2009).

Alexander and Kulkarni (2009) carried out full-scale tests on three field pipe segments with D/t ranging from 50 to 100, with each pipe specimen consisting of two wrinkle bends. The wrinkle

bends ranged from h/L of 0.05 to 0.5, where h is the height of wrinkle crest to trough, and L is the longitudinal length covering wrinkle region (crest and two feet). Wrinkle bend-corrosion combined defect was simulated by removing 40% of the wall thickness on both wrinkle bends in one of the pipe specimens of grade X52, where one wrinkle was repaired using a composite material, and the other was left unrepaired (see Figure 2.15). Another pipe specimen of grade X42 with wrinkle bend-weld combined defect, was repaired on one wrinkle bend and unrepaired at the other. The third specimen, also of grade X42 had wrinkle bends repaired on one bend and unrepaired at the other. An Armor plate pipe wrap (APPW), 14.3 mm (0.563 in) thick and 50 mm (2 ft) long was used for the composite repair of the wrinkle bend on one end of the pipe (see Figure 2.15). Such that one-third of the composite repair 4.8 mm (0.188 in) thick was laid in the hoop direction, another one-third of similar thickness in the axial direction and the final top layer of similar thickness was applied in the hoop direction. The pipes were then subjected to cyclic internal pressure within the range of 100 psi or 0.689 MPa (8% of SMYS) to 858 psi or 5.9 MPa (approximately 72% of SMYS) until a fracture induced failure occurred. A strain study was undertaken. The strain study observed maximum strain values were recorded in the corroded pipes which led to apparent decreases in the remaining life of the pipes. A reduction in strain value of the rehabilitated wrinkled pipes was observed, which resulted in an approximately two times increase in the remaining life of the rehabilitated wrinkled pipes when compared to unreinforced wrinkled pipes. It was also observed that even though the wrinkled region of the pipe has undergone plasticity, the rehabilitated wrinkled region responded elastically to continuous pressure cyclic loading.

2.6 Assessment of Fatigue Life

2.6.1 Stress Life Approach

The stress life approach is applicable for situations involving primarily elastic deformation. Under elastic deformation, the material is expected to have a long life, usually higher than 10^4 cycles which is in the high cycle fatigue (HCF) range. Alexander and Kulkarni (2009) estimated the remaining life of pipelines with wrinkle bends with combined defect of corrosion and wrinkle bends along with girth welds under pressure cyclic loads. The finite element software, ABAQUS, was used to determine maximum axial stresses at the wrinkle tip, which was then used to calculate the stress concentration factors associated with the wrinkle. The stress concentration factors (SCFs) calculated relative to the wrinkle geometry profile h/L (wrinkle height-to-wrinkle length

ratio) and diameter-to-thickness ratio (D/t) were then used to predict the remaining life of the pipes with combined wrinkle bend-corrosion defect, combined wrinkle bend-weld defect and wrinkle bend defect. These SCFs are associated with anomalies due to stress risers that lead to the premature failure of the pipelines. The fatigue life assessment curve in API RP2A (API 2012) shows the relationship between stress range and the number of cycles to failure (see Figure 2.16). This fatigue curve was used to develop an empirical expression for cycles to failure as shown in Equation 2.1.

$$N = C \times \Delta S^{-m} \quad (2.1)$$

In Equation 2.1, N is number of cycles to failure, the constants C and m are material dependent empirically derived values and S is the stress range. Using Equation 2.1, it was observed that an increase in the stress range reduced the fatigue life by a factor of 16. According to the wrinkle geometry profile relationship, it was observed that an increase in h/L or D/t led to a reduction in the remaining life of the pipelines (see Figure 2.17).

Cunha et al. (2009) proposed a methodology to assess the fatigue life of steel tubes with dent defect that had dent depths of 5% and 10% of the pipe diameter. The tests were carried out at Rio de Janeiro state University, Brazil. The tube specimens had nominal diameter of 73 mm and wall thickness of 3.05 mm and hence, a D/t ratio of 24. The grade of the tube materials was SAE/AISI 1020 (ASTM A29, 2015). The study adopted the high cycle fatigue theory. Experimental tests were performed to validate the proposed assessment methodology. Following the high cycle fatigue theory, S-N curves were generated using Gerber criterion which was found to be more reliable compared to the Goodman criteria to account for the mean stress effect (see Figures 2.18(a) to (c)). Finite element analysis tool was used to simulate experimental indentation process and internal pressure cyclic loading on pipes of same material properties, but variable D/t ratios and dent geometries. This was done to generate stress concentration factors around the dent region. Numerical expressions based on non-dimensional dent geometric parameters (B) were then developed as shown in Equation 2.2. This relationship was then used to estimate theoretical SCFs using results of the finite element analysis.

$$B = \left(\frac{D}{t}\right)^{0.78} \left(\frac{d}{D}\right)^{0.70} \quad (2.2)$$

In Equation 2.2, D is the tube external diameter, d is the dent depth, and t is the tube wall thickness. The non-dimensional dent geometric parameter (B) was then used to determine the fatigue stress concentration factor (K_f), which is usually the same value as theoretical stress concentration factor (K_t) if the notch sensitivity factor is 1 (see Equations 2.3 and 2.4);

$$K_t = 1 + 1.854B \quad (2.3)$$

$$K_f = K_t \quad (2.4)$$

K_f is then used to calculate Fatigue endurance limit (S_e). S_e , however, is then used to estimate the number of stress cycles to failure (N). The expressions for N and S_e are given in Equations 2.5 and 2.6.

$$N = \left(\frac{\sigma_a}{c \left(1 - \left(\frac{\sigma_m}{S_u} \right)^2 \right)} \right)^{1/b} \quad (2.5)$$

$$S_e = S'_e \frac{k_a}{K_f} \quad (2.6)$$

where;

$$C = S_u + 354 \quad (2.7)$$

$$b = \frac{1}{6} \log_{10} \left(\frac{S_e}{C} \right) \quad (2.8)$$

$$\sigma_a = \left[1 - \left(\frac{\sigma_m}{S_u} \right)^2 \right] C N^b \quad (2.9)$$

The parameters C and b are defined as the S-N curve parameters, σ_a is the alternating stress, σ_m is the mean stress, and S_u is the ultimate tensile strength. The estimated expression for SCFs was incorporated into the Gerber criterion to predict the number of stress cycles required to cause failure of tubes with plain dents. This approach was found to be in good correlation with results obtained from the experiments.

Durowoju et al. (2016) at the University of Newcastle in UK used finite element analysis based parametric study on natural gas pipelines with dent defect to predict fatigue life. The parameters considered in this study are; pipe geometry (D/t) ranging from 18 to 90, dent geometry (d/D or dent depth-to-pipe diameter ratio) ranging from 2 to 10, pipe material (API 5L grades of X65, X80, X100), and pressure cyclic loading within the range of 50% and 72% SMYS. A non-linear kinematic hardening model was used to define the cyclic plastic behavior of the pipes with a dent when subjected to pressure cyclic loading. SCFs associated with different dent geometries were then obtained from the maximum principal stresses in the most critical part of the dent region. These SCFs were obtained for different dent geometries, different pipe geometries, and various material properties using FE software, ANSYS (ANSYS 216). The ANSYS software was used to study the behavior of various pipes with dent defect. The results of this study showed that the relationship between material strength of pipes with similar dent defect and pipe geometry (D/t) is directly proportional to SCFs (see Figure 2.19(a)). Also, the SCFs increased as the pressure cyclic loading range decreased (see Figure 2.19(b)). However, pipes with lower diameter-to-thickness ratio (D/t) produced higher SCFs around the dent region (see Figure 2.19(a)).

2.6.2 Strain Life Approach

The strain-based approach is widely used to estimate fatigue life for notched specimens. It is deemed accurate for estimating either low-cycle fatigue (LCF) or high-cycle fatigue (HCF) life (Dowling 2007). However, when the applied stresses are high enough, plastic strain accumulates and the service life of a material decreases, often less than 10^4 , which is considered to be in the LCF range. Strain life approach can be used for estimating LCF. A collaborative research was undertaken jointly by University of Thessaly in Greece and Delft University of Technology in

Netherlands (Dama et al. 2007). This study used values of maximum local strain range computed numerically to predict the number of cycles to failure using the Coffin-Manson/Basquin fatigue formula. Three full-scale tests were conducted on 12 m long pipes with 24 in (610 mm) diameter (hence, a D/t ratio of 77) by applying a cyclic bending loading under a constant internal pressure on pipes. The loading sequence was performed in two different stages. In stage 1, a four-point monotonic bending was applied on a plain pipe to form a globally bent pipe, thereby creating a localized buckle. In stage 2, a cyclic bending load was applied on the bent pipe. Schematics of test set up is shown in Figure 2.20. The strain concentration factors (SNCF) associated with the critical region of the buckling area were generated using FEA (finite element analysis) tool, ABAQUS. These SNCFs were used to assess the remaining fatigue life of the bent pipes by using Equation 2.10.

$$\text{SNCF} = \frac{\Delta\varepsilon_{\max}}{\Delta\varepsilon_{\text{nom}}} \quad (2.10)$$

In this relationship, $\Delta\varepsilon_{\max}$ is the maximum strain variation at the bent region in a specific direction and $\Delta\varepsilon_{\text{nom}}$ is the corresponding nominal strain variation. The $\Delta\varepsilon_{\max}$ values were obtained from FEA and then substituted into the Coffin-Manson/Basquin fatigue formula given by Equation 2.11.

$$\frac{\Delta\varepsilon_{\max}}{2} = \frac{\sigma'_f}{E} (2N)^b + \varepsilon'_f (2N)^c \quad (2.11)$$

In Equation 2.11, σ'_f is a fatigue strength coefficient, which is equal to the ultimate strength of the steel material, ε'_f is the fatigue ductility coefficient, which is equal to the ultimate strain. The fatigue exponent b and c were taken as -0.81 and -0.7, respectively.

The nominal strain variation range ($\Delta\varepsilon_{\text{nom}}$) at the middle section due to displacement variation Δ_u at the loading points can be readily calculated from strength of materials as follows:

$$\Delta\varepsilon_{\text{nom}} = \frac{3D}{L_1(2L_1 + 3L)} \Delta_u \quad (2.12)$$

where, D is the nominal diameter of the pipe, L_1 is the distance between A(A') and B(B') and L is the distance between B and B', as shown in Figure 2.20.

The number of cycles to failure (N) derived from Equation 2.11 was then compared with the number of cycles to failure obtained using Milner's rule. This rule uses the concept of damage factor as shown in Equation 2.13.

$$D_F = \sum_{i=1}^{N_p} \frac{n_i}{N_i} \quad (2.13)$$

In Equation 2.13, N_i is the number of cycles until failure for cyclic loading pattern i . N_p is the number of cyclic loading patterns and, n_i is the number of cycles of loading pattern (i) that are actually applied on the structure, since the displacement range was varied three times during the cyclic bending of each specimen. It was concluded from the study that with the use of both maximum longitudinal strain range and the equivalent strain range, the D_F obtained accurately predicted the fatigue life. Parametric studies were carried out for variable buckle depth, internal pressure, and diameter-to-thickness ratio. It was observed that longitudinal SNCF may not be very sensitive to buckle depth and internal pressure for the range of parameter values considered. However, SNCF was found to be higher in thinner pipes.

Pournara et al. (2015) at the University of Thessaly in Greece continued the research completed by Dama et al. (2007). A study was conducted on the structural capacity of buckled pipes subjected to cyclic bending loads caused by temperature variations and permafrost actions. A total of six 6-inch (152 mm) API 5L X52 pipe specimens with D/t ratio of 35 were tested. The specimens were dented under a rounded wedge indenter (see Figure 2.21). Then a displacement controlled monotonic four-point bending was applied to a post-buckling level. Four of the specimens were further subjected to constant displacement-controlled cyclic bending load range (16, 13, 9 and 8 mm). The displacement was measured through the hydraulic jack stroke, under the same four-point bending set-up (see Figure 2.22). Two of the buckled specimens were subjected to internal pressure cyclic loading range of 1958 psi (218 psi to 2176 psi). A total of 30 cyclic tests were conducted on strip specimens cut from the pipe. Figure 2.23 shows the setup for the cyclic bending of the strip specimens was similar to the one completed by Das et al. (2007b). These specimens were tested at different strain ranges to develop a strain life fatigue curve ($\varepsilon - N$) which is shown in Equation 2.14.

$$\Delta\varepsilon = 0.0102(2N)^{-0.1133} + 0.333(2N)^{-0.4807} \quad (2.14)$$

In the above equation, $\Delta\varepsilon$ is the strain range, and N is the number of cycles to failure.

The SNCF associated with the region of buckling were developed with the aid of ABAQUS, using the expression in Equation 2.10 above. The maximum local strain range in the axial direction at the critical region was represented as $\Delta\varepsilon_{max}$. The nominal strain range due to the applied loading ($\Delta\varepsilon_{nom}$) for displacement-controlled cyclic four-point bending range was expressed as Equation 2.15;

$$\Delta\varepsilon_{nom} = \frac{2\alpha\Delta F}{E\pi D^2 t'} \quad (2.15)$$

and, internal pressure cyclic range was expressed as shown in Equation 2.16.

$$\Delta\varepsilon_{nom} = \frac{D(1 - \nu^2)}{2tE} \Delta p \quad (2.16)$$

In above equations, ΔF is the range of total transverse load applied, α is the distance between the hinge support and point of load application, D is the outside diameter of pipe, t is thickness of the pipe, E is young's modulus, ν is the Poisson's ratio and Δp is the range of imposed internal pressure. The values of $\Delta\varepsilon_{max}$ associated with the buckled region are then substituted into equation 2.10, to estimate the remaining cycle to failure for each specimen. The tool was validated by using the Milner's rule to define a damage factor from the expression in Equation 2.17.

$$D_f = \sum_i \frac{n_i}{N_i} \quad (2.17)$$

In above equation, N_i is the number of cycles corresponding to $\Delta\varepsilon_{max}$, obtained from the strain fatigue curve ($\varepsilon - N$), and n_i is the number of real cycles applied. It was observed that the damage factor for all specimens were close to 1 (unit value), which indicted a good agreement with the experimental results.

2.6.3 Energy Based Approach

Energy is dissipated in fatigue because of plastic deformation of a material that experiences cyclic loading. Most of this energy is converted into heat and is not recoverable as strain energy. The energy per cycle, is measured by the area of the hysteresis loop from the load-deformation plot, and the total energy expended during the life is a summation of all the loop areas (Sandor, 1972). Hysteresis energy is a useful measure for the establishment of failure criteria in fatigue. Das et al. (2007b) proposed a fracture model based on hysteresis loop energy (HLE) after conducting a study on the behavior of wrinkled steel pipelines subjected to cyclic axial loads. Twenty-four 57 mm wide strip specimens cut from X52 grade pipes with D/t of 45 were bent into different internal radius depending on the internal pressure considered as shown in Figure 2.24. These bent pipe strips were subjected to axial cyclic loading until fracture developed at the crest of the strip specimen. It was observed that cyclic loads created a mechanism of strain reversals that led to fracture at tip of the crest after few cycles. The study also found that the pipe still possesses some ductility reserve in wrinkled stage and may still be able to undergo cyclic loading, depending on the severity on the wrinkle. A fracture life assessment model, as shown in Equation 2.18 was proposed for predicting the number of cycles in a wrinkled pipe with D/t of 45. In this equation, N_s is the number of cycles to initiate fracture in strip specimen, U_o is the HLE obtained from the first cycle of the hysteresis loop, and A is a coefficient based on material properties and thicknesses.

$$N_s = A(U_o)^{-2.58} \quad (2.18)$$

When the natural log of Equation 2.18 is taken, and U_o is normalized by the thickness (t), the expression for A is substituted into Equation 2.19, depending on the thicknesses considered, such as 6.0 mm, 6.84 mm and 8.3 mm.

The final equation for the number of cycles required to fracture a strip specimen for a range of material properties and pipe geometry considered in the research was proposed and it is shown in Equation 2.19.

$$\ln(N_s) = -5.3654 - 2.58 \ln(U_o/t) + 0.1642t \quad (2.19)$$

Although, the thicknesses of the field wrinkled pipes can easily be measured, it may not be possible to predict HLE without undertaking a similar test to strip test. Hence, an expression to relate the pipe specimen and strip specimen is given in Equation 2.20.

$$U_o = U_{oc} + 2U_{of} \quad (2.20)$$

In this equation, U_{oc} and U_{of} are HLE absorbed at the crest and foot hinges respectively and represented by Equation 2.21 and 2.22 as follows:

$$U_{oc} = 2M_u(\Delta\theta) \quad (2.21)$$

$$U_{of} = \frac{U_{oc}}{2} \quad (2.22)$$

In above equations, M_u is the ultimate moment capacity, and $\Delta\theta$ is the total angular or rotational change at the crest of the wrinkle in the pipe specimen due to maximum stroke change in a cycle (see Figure 2.25).

Although, Pournara et al. (2015) and Das et al. (2007b) both performed cyclic tests on strip specimens obtained from the pipe material, the results were applied differently to obtain a fatigue life assessment model. Pournara et al. (2015) used the results of the tests to obtain a strain life fatigue curve by using the Coffin-Manson/Basquin fatigue formula. However, Das et al. (2007b) used the results of the tests to obtain a fracture life assessment model based on HLE, where HLE is obtained from cyclic load-deformation plots.

2.7 Current Codes and Standards

2.7.1 CSA Z662-19

The Canadian Standard CSA Z662 was first published by Canadian Standard Association (CSA) in 1994 to help achieve safety and integrity of pipeline transporting oil and gas products throughout its lifecycle. Many researchers believe that the standard may have been too conservative on post-

wrinkling engineering assessment. According to clause 10.10.8.1 of CSA Z662-19 (CSA Z662 2019), wrinkles are formed as a result of load combinations generated from geotechnical movement which result in bending or axial loads combined with operational stress levels, including those imposed by thermal cycles. Wrinkle in this standard is defined as a smooth, sinusoidal-shaped outward and inward deformation of the pipe diameter, over a finite arc of the pipe circumference.

Although this standard provides guidelines for engineering assessment of defects, it does not consider some geotechnical-related loads such as slope movements, fault movements, thaw settlement, frost heave in the design (clause 4.2.4 CSA Z662-19). According to clause 10.3.2 of CSA Z662-19 (CSA Z662 2019), when the operating company detects a wrinkle defect in its pipeline system, it should conduct an engineering assessment to determine the portion susceptible to failure and implement measures to prevent it from happening. CSA Z662 (CSA Z662 2019) states that ripples, wrinkles, and buckles that have been identified as a defect, if not removed or repaired, shall be periodically monitored (clause 10.10.8.2 CSA Z662-19). The wrinkled pipe may either be replaced or be repaired using a steel pressure-containment repair sleeve (Table 10.2 CSA Z662-19). The standard further suggested that the loading conditions that lead to the development of the wrinkle defect should be evaluated for mitigation. The guideline for this clause is presented graphically in Figure 2.26(a) showing maximum allowable wrinkle amplitudes with the maximum allowable operating stresses for liquid and gas pipelines.

Furthermore, with respect to thermal expansion, this standard provides a limit for thermal expansion stress range of both restrained and unrestrained pipelines in clause 4.8.3 and clause 4.8.4 of CSA Z662-19, respectively. In piping, a restrained pipe consists of a soil or support that prevents axial displacement and/or flexural bending of the pipeline. Usually, restrained pipes are buried pipelines and unrestrained pipes are above the ground. A design check for local buckling limit state is not necessary for restrained buried pipelines if the pipeline meets the conditions as specified in Annex C.6.5 of CSA Z662-19. The thermal stress range limit for unrestrained pipelines according to this standard shall be in accordance with Equation 2.23.

$$S_E = (S_b^2 + 4S_t^2)^{1/2} \quad (2.23)$$

Where,

S_E = thermal expansion range, MPa

$S_b = \frac{iM_b \times 10^3}{Z}$ = resultant bending stress, MPa

$S_t = \frac{M_t \times 10^3}{2Z}$ = torsional stress, MPa

i = stress intensification factor

M_b = resultant bending moment, N m

Z = section modulus of pipe, mm³

Thermal expansion stress range limit for unrestrained pipe, shall be in accordance to the following relationship.

$$S_E \leq 0.72S \times T \quad (2.24)$$

Where,

S_E = thermal expansion stress range, MPa

S = specified minimum yield strength, MPa

T = temperature factor.

However, these limits are not valid for pipelines that have already undergone plastic buckling as described in this current study. The limit state design check is exempted for temperature change as high as 65 °C as stated in Annex C.6.5 of CSA Z662-19.

Clause 11.10.7 of CSA Z662-19 (CSA Z662-19 2019), requires offshore pipeline be designed adequately for fatigue life which may be due to stress fluctuations such as wind loads, vortex shedding, wave and current action, but not fatigue on wrinkled onshore and offshore pipeline. However, the scope of this thesis does not include offshore pipelines.

2.7.2 ASME Code for Pressure Piping, B31

The original American code for pressure piping, ASME B31 was first introduced in 1935 as an all-inclusive standard for piping design. It was then divided into various sections to address design of

specific piping systems. The major sections that are related to this study are ASME B31.4 (ASME 2016) and ASME B31.3 (ASME 2014). These two codes address transportation system for liquids and slurries, and process piping for chemical petroleum or related products in buried pipelines, respectively.

Originally, according to Annex 402 of ASME B31.4 (ASME 2016), during design and installation analyses, based on accepted engineering methods, material strengths, and applicable design conditions, pipelines are designed against buckling, fatigue, and fracture. Therefore, allowance was made for wrinkle defect in the code on paragraph 451.6.2.8 of ASME B31.4. This paragraph recommends that no repair is undertaken on wrinkled pipes without cracks, if the ratio of crest-to-trough height (h) to pipe outside diameter (D) is less than 2% for maximum operating hoop stress lesser than 20,000 psi (138 MPa). For operating hoop stress greater than 138 MPa, stricter guidelines are provided in paragraph 451.6.2.8 of ASME B31.4. Wrinkled part of the pipelines can be cut and replaced as a cylinder or repaired with full steel pressure-containing full encirclement sleeve, reinforcing-type full encirclement steel sleeve or mechanical bolt-on clamps but not with composite sleeves (paragraph 451.6.2.9 of ASME B31.4). However, the steel pressure-containing full encirclement sleeve is the only acceptable repair method in CSA Z662 (CSA Z662 2019).

The installation, design and operation of pipelines is carried out specifically to limit the effect of stress fluctuations that may cause fatigue. Paragraph 403.5 ASME B31.4 describes loads that may cause fatigue, and these are the loads induced by internal pressure variations, currents, and vibrations induced by vortex shedding. Nonetheless, stress due to periodic or cyclic loading that may cause yield failure in unrestrained pipelines can be limited, according to paragraph 403.3.2 ASME B31.4 by the following relationship.

$$S_A \leq f[1.25(S_c + S_h) - S_L] \quad (2.25)$$

where,

f = fatigue factor calculated as $f = 6.0N^{-2}$, but cannot exceed 1.2

N = equivalent number of full displacement cycles during the expected service life of the pipeline system

$S_c = 2/3 S_y$ at the lower of the installed or minimum operating temperature

$S_h = 2/3 S_y$ at the higher of the installed or maximum operating temperature

At the initial design of pipeline systems, allowance for thermal expansion and contraction as a result of thermal stresses, which arise from maximum and minimum operating pressure, is established according to paragraph 402.5 of ASME B31.4. The thermal expansion in restrained pipes is calculated as shown in Equation 2.26.

$$S_E = E\alpha(T_1 - T_2) \quad (2.26)$$

where,

E = moduli of elasticity

S_E = thermal expansion stress, psi (MPa)

T_1 = temperature of the pipe at installation or completion of final tie-in, °F (°C)

T_2 = operating temperature, °F (°C)

α = coefficient of thermal expansion, in./in./ °F (mm/mm/°C)

The allowable thermal expansion stress recommended by this code is as follows;

$$S_E \leq 0.9S_y \quad (2.27)$$

where,

S_y = Specified minimum yield strength of pipe material

While thermal expansion in unrestrained pipes can be determined according to the formula;

$$S_E = \sqrt{S_b^2 + 4S_t^2} \quad (2.28)$$

where,

$$S_b = \sqrt{(i_i M_i)^2 + (i_o M_o)^2} / Z = \text{resultant bending stress, psi (MPa)}$$

$$S_t = \frac{M_t}{2Z} = \text{torsional stress, psi (MPa)}$$

i_i = in-plane stress intensification factor

i_o = out-of-plane stress intensification factor

M_i = in-plane bending moment, in.-lb (N.m)

M_o = out-of-plane bending moment, in.-lb (N.m)

M_t = torsional moment, in.-lb (N.m)

Z = section of modulus of the pipe or of the fitting outlet, as applicable, $in.^3$ (cm^3)

And the allowable thermal expansion stress range limit for unrestrained pipes can be calculated using equation (2.27) above, where S_E will replace S_A .

However, consideration for thermal stresses that may arise due to environmental temperature differential that induce cyclic freeze-thaw on the surrounding soils around the pipe walls is neglected. All thermal effects considered are stated in paragraph 301.7 of ASME B31.3.

2.7.3 DNV GL (DNV-OS-F101)

Det Norske Veritas (DNV) was founded as a membership organization in Oslo, Norway in the year 1864. The organization was established to provide a uniform set of rules and procedures, used in assessing the risk of underwriting individual vessels. Three years later, Germanischer Lloyd (GL) was created as an independent classification society, to evaluate the quality of ships and deliver results to stakeholders. Both organizations came together in 2012, to become an international accredited registrar and classification society, providing services in maritime, renewable energy, oil and gas, electrification, food & beverage and healthcare. DNV GL core strength lies in to identify, assess, and advice on risk management. The organization then provided service documents (standards) for the purpose of safeguarding life, property and the environment.

DNV-OS-F101 is a standard on submarine pipeline systems. According to Section 5 D101 of DNV-OS-F101 (DNV-OS-F101 2013), pipelines are checked in the design stage for relevant

failure modes. Limit state criteria was defined for local buckling scenario, to prevent the deformation of pipe wall cross section (Section 5 D301 of DNV-OS-F101). According to Section 5 D600 of DNV-OS-F101 (DNV-OS-F101 2013), pipelines are designed against local buckling, that may arise due to the combination of axial force, bending moment and external or internal pressure. However, different limit states criterion applies to the design against local buckling, depending on the buckling condition. The load-controlled condition and displacement-controlled condition was considered according to the limit state criterion given in Section 5 D605 and D608 of DNV-OS-F101 (DNV-OS-F101 23013) respectively.

According to Section D800 of DNV-OS-F101 (DNV-OS-F101 2013), all submarine pipeline systems must be designed with adequate safety against fatigue failures within the design life. The standard requires that all the stress fluctuations, including large stress magnitudes imposed in the construction phase, be considered when determining the long-term distribution of stress ranges. The fatigue checks include both low-cycle fatigue and high-cycle fatigue. However, special consideration was given to the fatigue assessment of construction details likely to cause stress concentrations, and to the possibility of having low-cycle high strain fatigue (Section 5 D803 of DNV-OS-F101). The design criterion required for this limit state, depends on the method of analysis, which can either be based on fracture mechanics (see Section D804 of DNV-OS-F101) or fatigue tests (see Section D805 of DNV-OS-F101). The scope of this study is limited to fatigue tests, and the following shall be considered when using the calculation methods;

- a) Determination of long-term distribution of stress range
- b) Selection of appropriate S-N curve (characteristic resistance)
- c) Determination of stress concentration factor (SCF) not included in the S-N curve
- d) Determination of accumulated damage.

Although, the standard provided for safety against fatigue failure of pipeline systems with stress concentration. It is important to note that the stress fluctuations in this standard is limited to stresses from

- direct wave action
- vibration of pipeline systems, e.g. due to vortex shedding (current, waves, wind, towing) or fluid flow

- supporting structure movements, e.g. installation vessel
- fluctuations in operating pressure and temperature.

All causes of stress fluctuations above do not include stresses from subsurface geotechnical movement due to temperature variation and cyclic freeze-thaw.

2.8 Summary

The design limits for the effect of temperature variation and cyclic freeze-thaw on the post-buckling stage of pipelines have not been defined in detail in the pipeline operating standards and codes, because of the little research that has gone into it. However, the effect of fatigue that may arise because of other load combinations due to thermal expansion and contraction, currents, vortex shedding, winds etc. are considered when specifying the design criteria in various pipeline standards and codes. A pipeline operating company can subsequently perform an integrity management program, strictly adhering to the guidelines provided in these standards. These guidelines include options that may reduce the likelihood of failure or damage of a pipeline system due to geotechnical incidents such as pipeline settlement, slope movement, and cyclic freeze-thaw. The provisions that are made by pipeline operating companies during system integrity management may now be included in engineering assessment records. These records provide a detailed history of mitigation procedures for future reference.

Different researchers have investigated the behavior of pipelines in the post-wrinkling stage, to make accurate provision for mitigation procedures. Based on engineering observations, it was concluded that pipelines may experience local buckling due to geotechnical movement caused by slope movement and freeze-thaw of surrounding soils (Bidwell et al., 2010; Wilkie and Doblanko 2001). However, local buckling can be intensified by stress and strain concentration in the region of imperfection created in pipelines by construction practices such as; wrinkle bends, girth welds, and UOE pipe forming process (Kashani et al., 2018; Dewanbabee & Das, 2012; Yoosef-Ghodsi, 1995), and operating conditions such as dent, crack, corrosion, and material properties (Nazemi et al., 2009; Corona et al., 2006; Kyriakides and Ju, 1992). The increment of these stresses and localization of strains may lead to the formation of a wrinkle in the pipe wall. As softening begins in the post-buckling region, the load carrying capacity of the pipe reduces, and the wrinkle grows as applied load and/or displacement increases. The wrinkle formation can take different buckling

modes of either a diamond shape or bulging shape depending on the magnitude of the internal pressure (Zhou & Murray, 1995).

Das et al. (2007a) stated that pipes possess some ductility reserve in the post-buckling stage even after formation of a wrinkle defect. However, the effect of fatigue due to temperature variation and cyclic freeze-thaw on the post-buckling stage of a wrinkled pipeline can cause a fracture failure in the region in which stress is concentrated. Therefore, researchers investigated the behavior of wrinkled pipes subjected to cyclic axial and bending loads (Pournara et al., 2015; Zhang, 2010; Das et al., 2007b;) and cyclic internal pressure (Alexander & Kulkarni, 2009). A study similar to the work presented in this thesis was undertaken by Das et al. (2007a). However, Das et al. (2007a) considered only severely wrinkled pipes, which were subjected to load-controlled axial cyclic loads. Additionally, the cyclic load ranges considered by Das et al (2007a) were severe, and therefore did not accurately depict field operating pipeline conditions.

Furthermore, limited studies have gone into the assessment of the remaining life of wrinkled pipelines subjected to combined axial cyclic loads and internal pressure. A prior study by Das et al. (2007b) was completed using energy-based method. This study used innovative and simple strip specimens taken from pipes of same material and geometric properties. The strip specimens were subjected to axial cyclic loads but the effect of biaxial hoop stress due to internal pressure was neglected. Subsequently, the idea of strip specimen was used by Pournara et al. (2015) to estimate the remaining life of wrinkled pipes, subjected to cyclic bending loads, using strain life approach. Alexander et al. (2009) used stress life approach to estimate remaining life of wrinkled pipes subjected to cyclic internal pressure. The stress life approach was also used to estimate the remaining life of pipes with dent defect and further subjected to cyclic internal pressure loading (Durowoju et al., 2016; Cunha et al., 2009). Dama et al. (2007) and Pournara et al. (2015) then considered the strain life approach for LCF to estimate the remaining life of wrinkled steel pipes under cyclic bending loads. The work done so far has actualized the need to assess the remaining life of wrinkled steel pipes subjected to both internal pressure and axial cyclic loads. This assessment will be carried out by using full-scale experiments and finite element analysis tools, considering the relevant imposed stresses as observed in field pipeline operations.

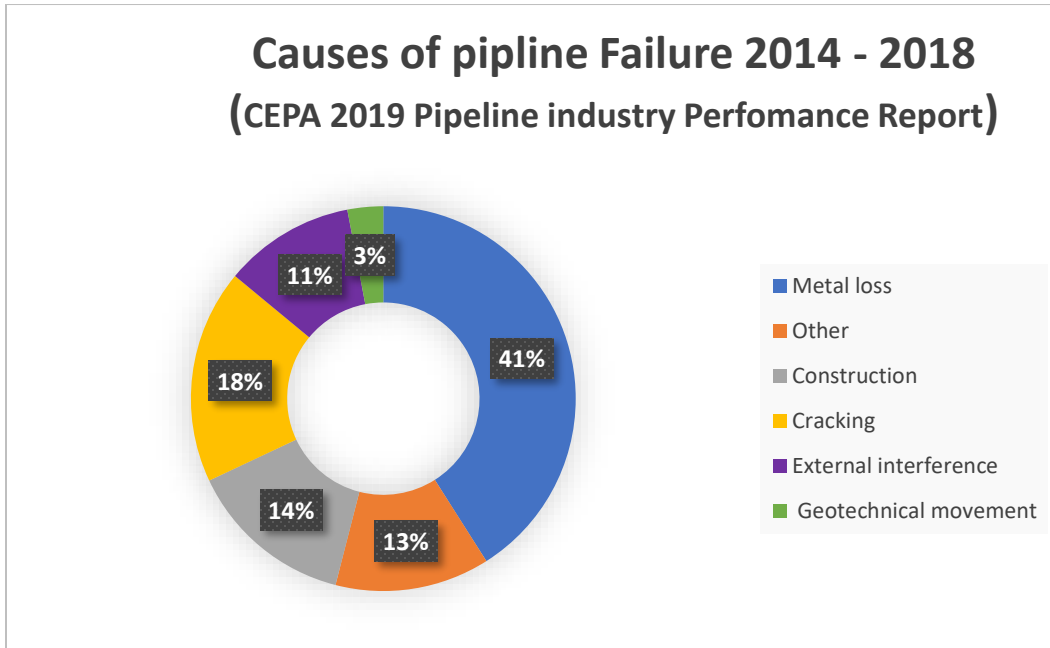


Figure 2.1: Pipeline Industry Performance Report (CEPA 2019)



Figure 2.2: Wrinkle Defect at Slope 92 (Wilkie et al., 2001)

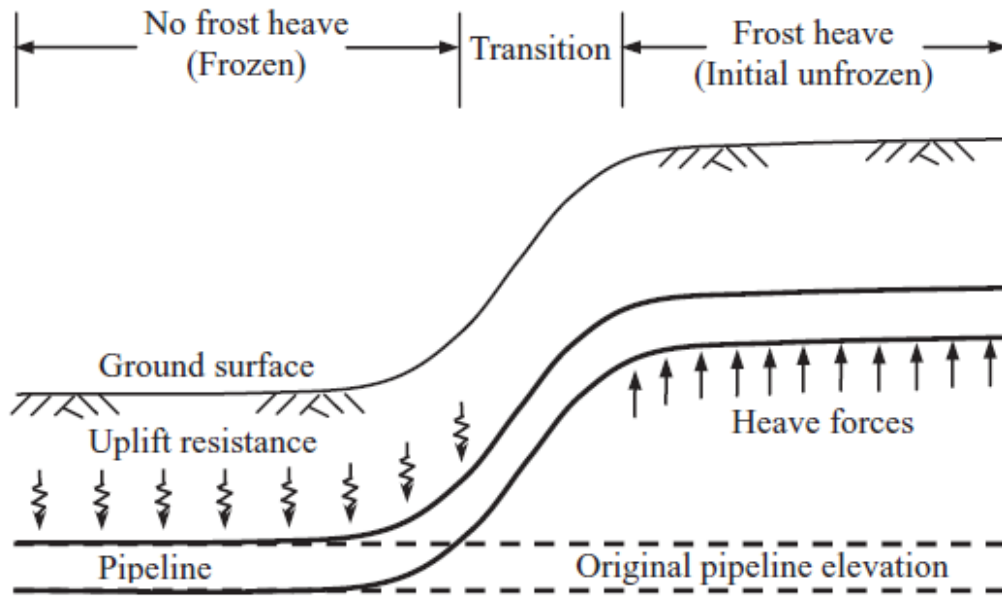


Figure 2.3: Differential Frost Heave of Buried Pipeline (Nixon et al., 2002)

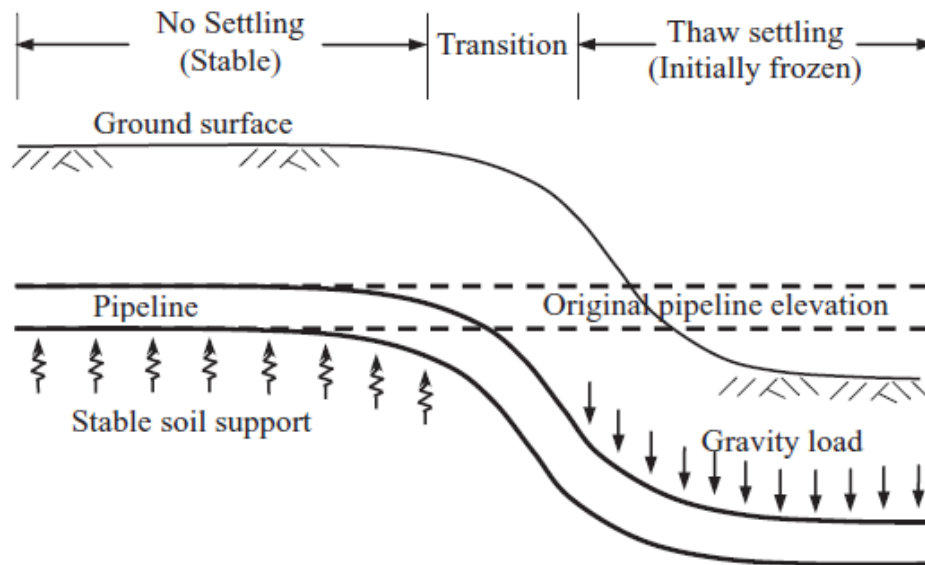


Figure 2.4: Differential Thaw Settlement of Buried Pipeline (Nixon et al., 2002)

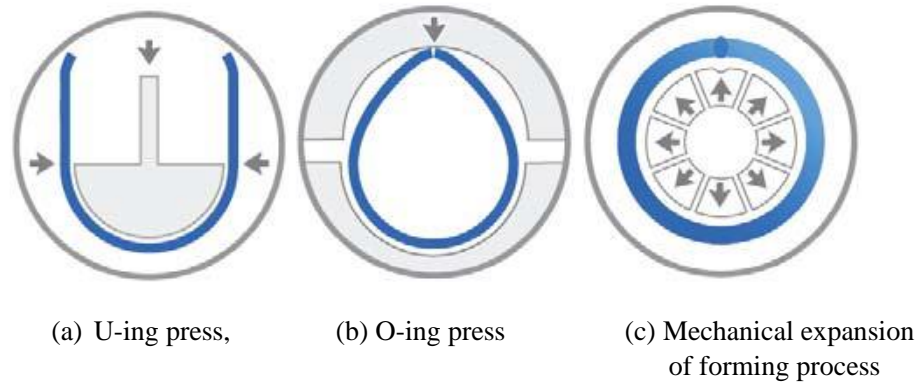


Figure 2.5: UOE Forming Process (Kashani et al., 2018)

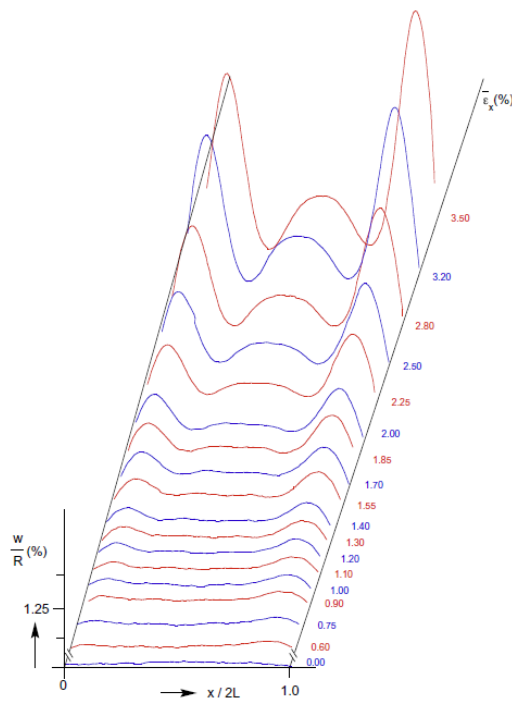


Figure 2.6: Axial Profiles of Radial Tube Displacement Recorded at Different Average strain levels During Monotonic Compression of a Specimen that Shows the Evolution of the Wrinkle (Jiao and Kyriakides, 2011)



Figure 2.7: Collapsed Form of a Defected Specimen Subjected to Cyclic Axial Loads
(Zeinoddini et al., 2015)

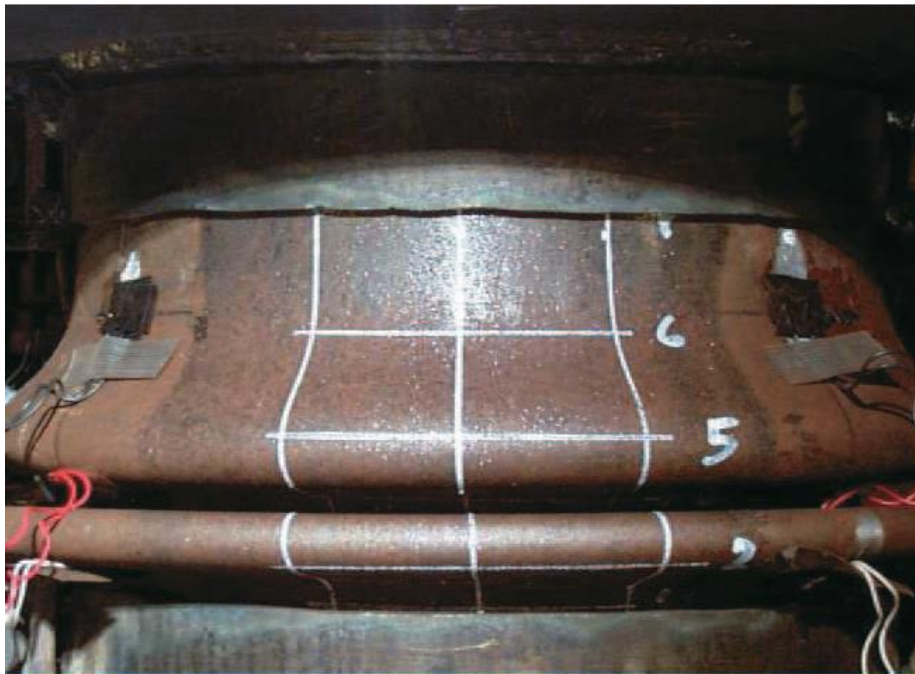


Figure 2.8: Accordion-type Failure of Wrinkled Pipe (Das et al., 2007a)



Figure 2.9: Rupture Failure of Wrinkled Pipe (Nazemi et al., 2009)

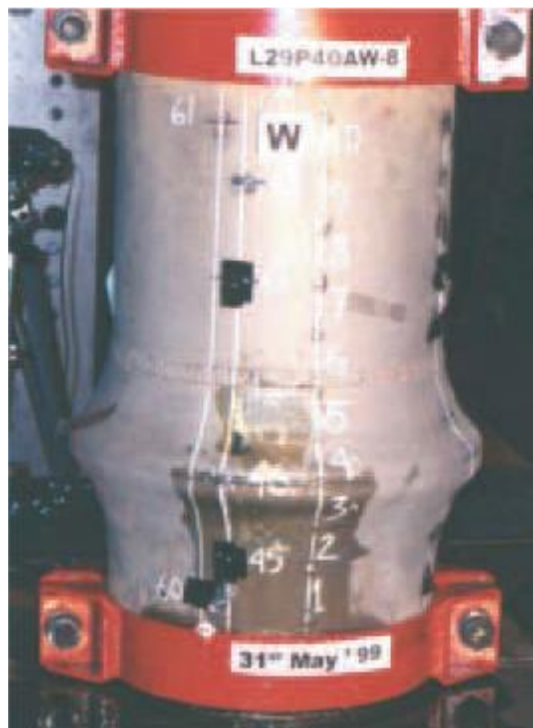


Figure 2.10: Fracture Failure of Wrinkled Pipe (Das et al. 2007a)

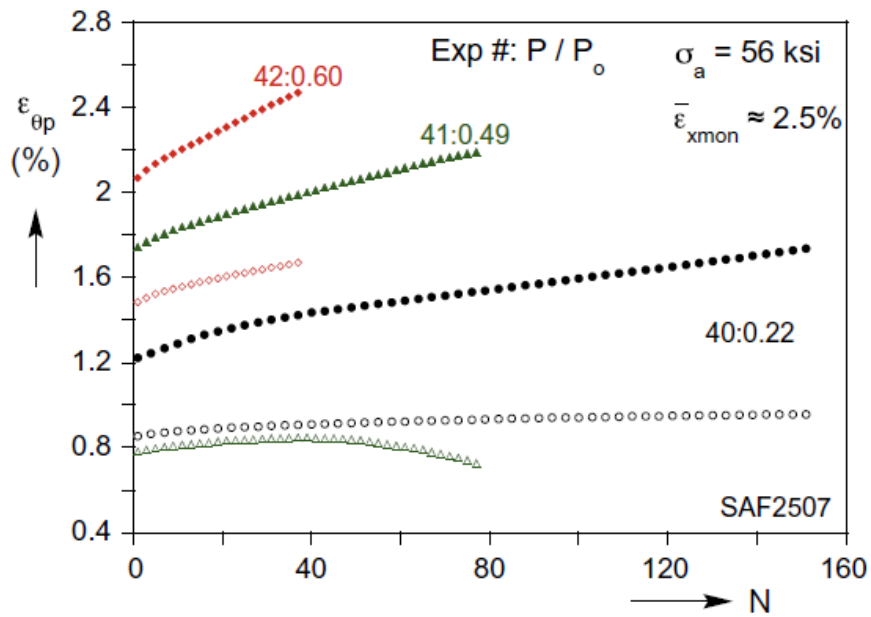


Figure 2.11: Peak Circumferential Strain vs Number of Cycles for Three Different Pressurized tubes (Jiao and Kyriakides 2011)

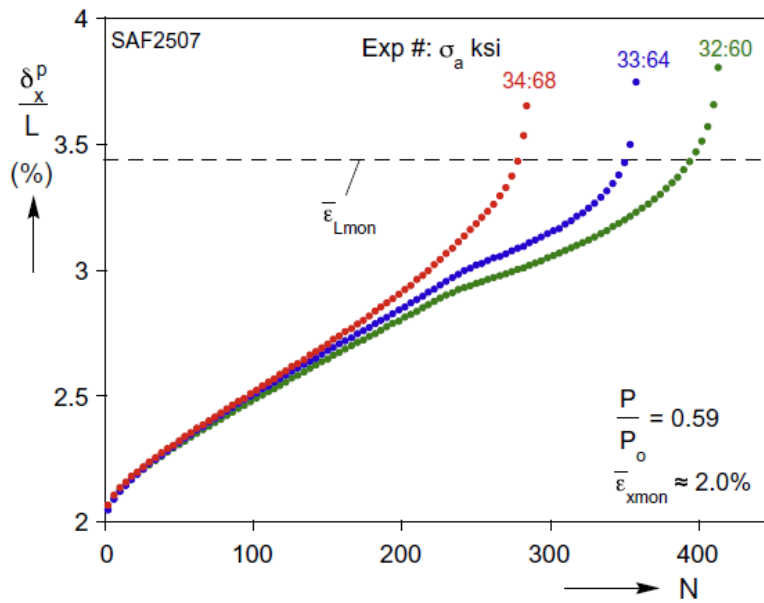


Figure 2.12(a): Peak Axial Strain vs Number of Cycles to Failure for Tested Tubes of Same Pre-strain and Internal Pressure (Jiao and Kyriakides 2011)

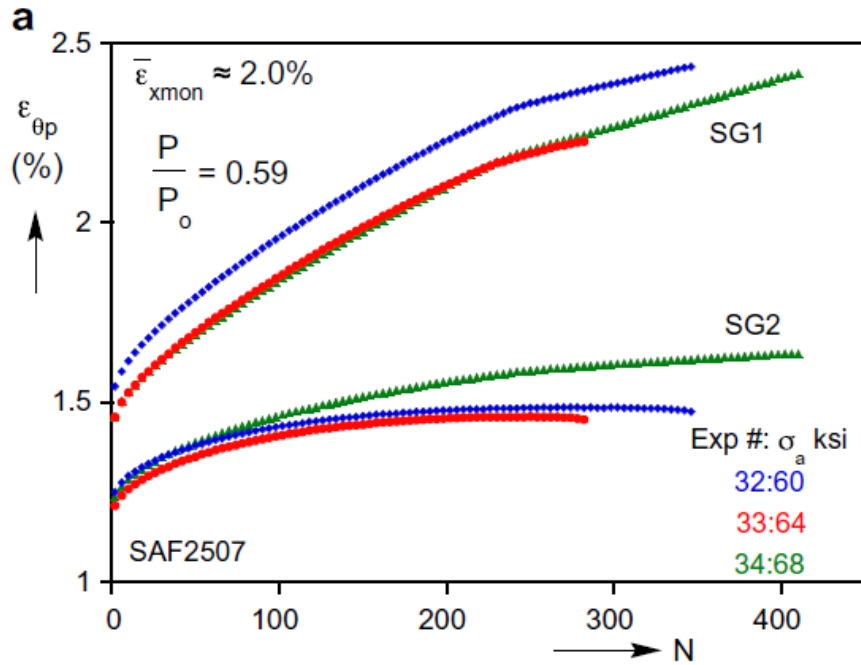


Figure 2.12(b): Peak Circumferential Strain vs Number of Cycles to Failure for Tested Tubes of Same Pre-strain and Internal Pressure (Jiao and Kyriakides 2011)

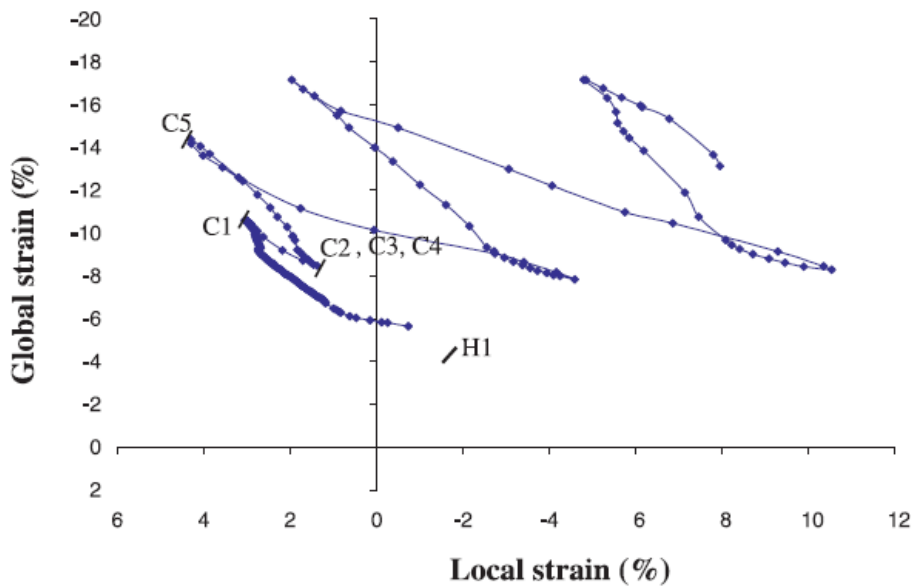


Figure 2.13: Strain at Clip Gauge vs Global Strain (Das et al., 2007a)

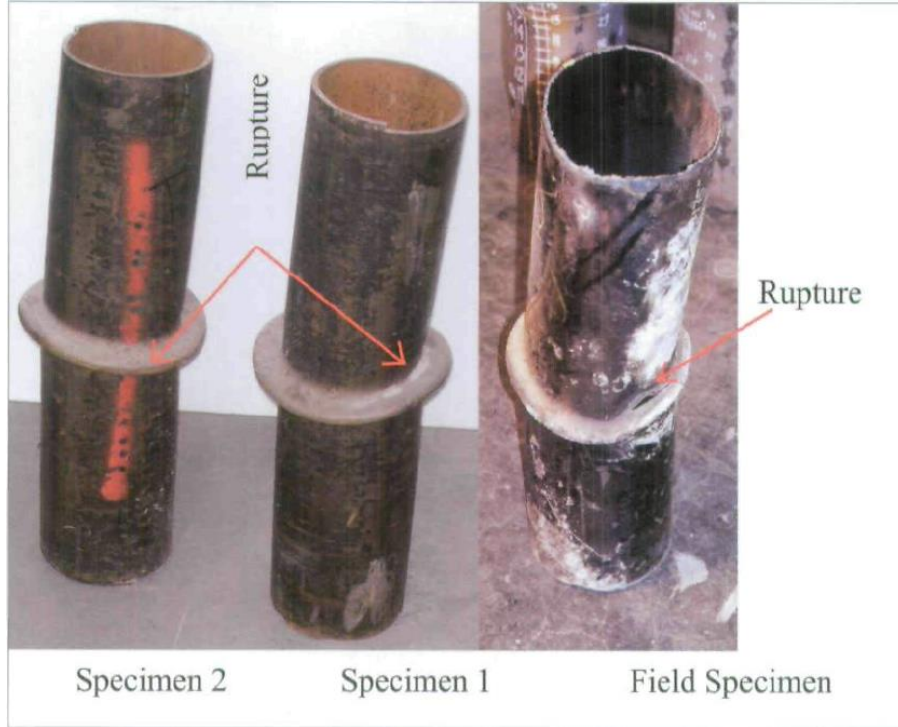


Figure 2.14: Final Deformed Shape of Specimens (Nazemi et al., 2009)



Figure 2.15: Picture of the Specimen Showing Strain Gauges and Repair Location (Alexander and Kulkarni 2009)

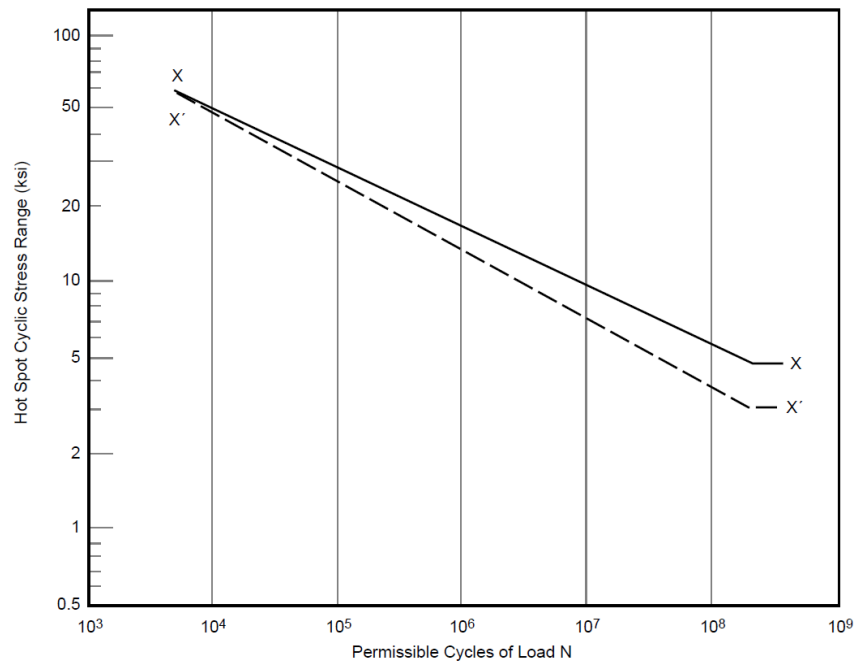


Figure 2.16: S-N Curves for Tubular Connections (API RP2A, 2002)

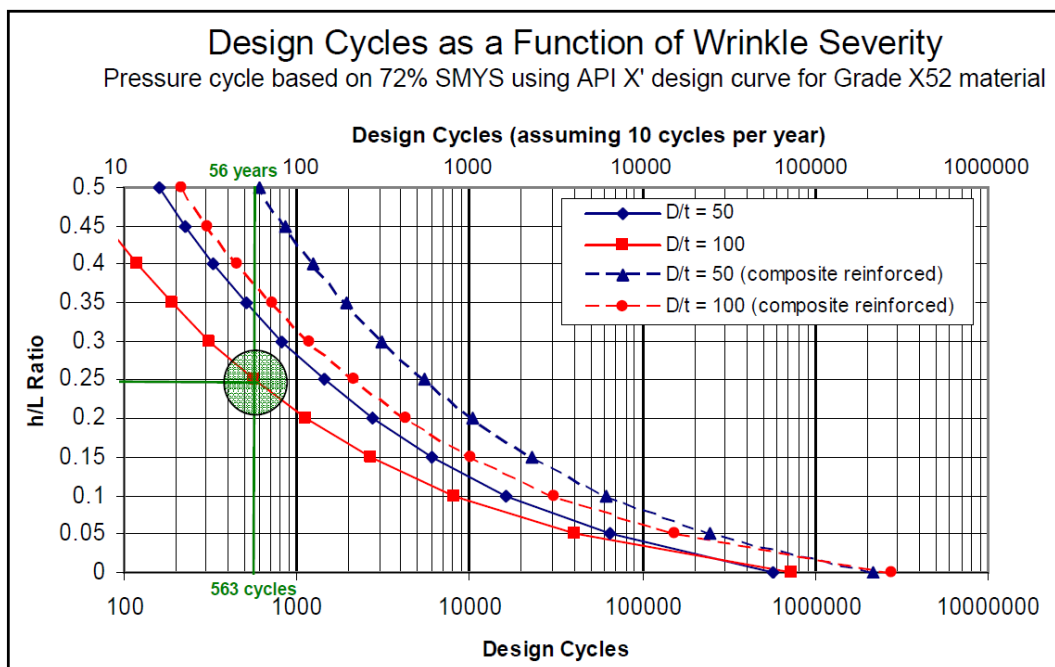


Figure 2.17: Nomograph Relating H/L to Design Life and Years of Service Using Results with and Without Composite Reinforcement (Alexandre et al., 2009)

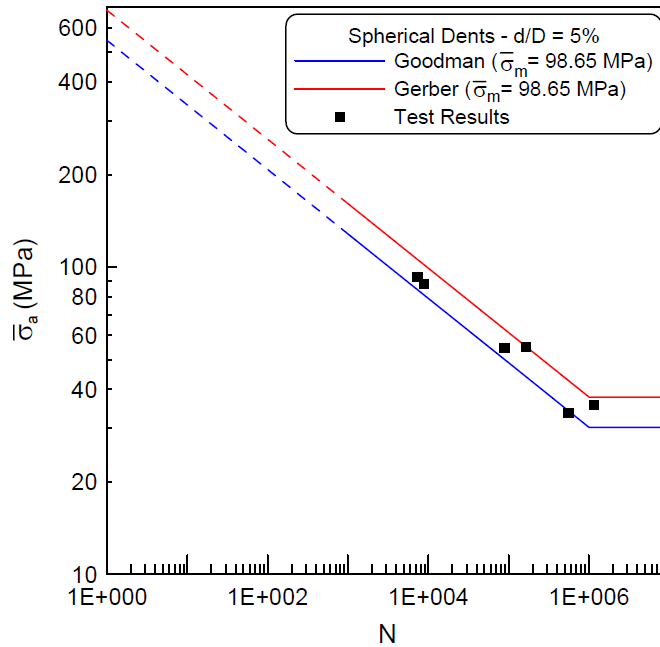


Figure 2.18(a): Fatigue Test Result against Theoretical S-N Curves for 5% Dent Depths (Cunha et al., 2009)

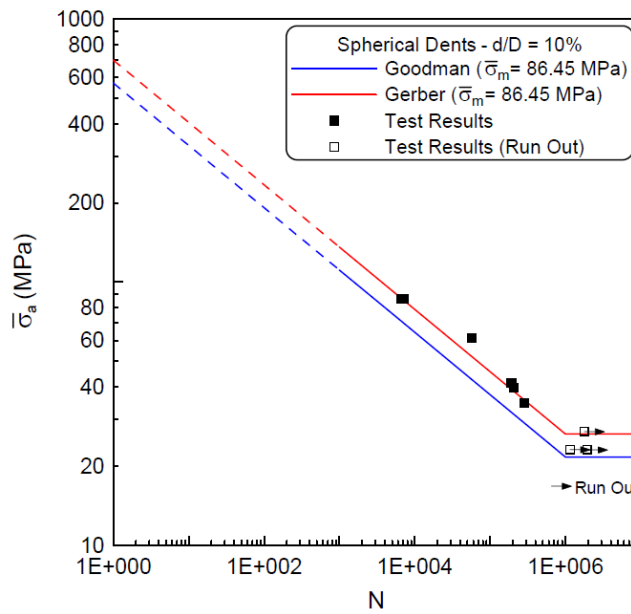


Figure 2.18(b): Fatigue Test Result Against Theoretical S-N Curves for 10% Dent Depths (Cunha et al., 2009)

d/D (%)	d/D (%)	N	$\bar{\sigma}_m$ (MPa)	$\bar{\sigma}_a$ (MPa)		
				Test	Goodman	Gerber
6	Nominal					
	Mean					
	4.6	7,357	98.85	97.81	84.44	105.89
	3.71	8,885	100.19	98.92	81.16	101.78
	6.12	88,761	97.64	51.92	50.07	62.79
	6.01	164,471	99.04	52.34	43.99	55.17
10	6.03	560,229	98.25	31.91	34.02	42.66
	6.24	1,167,172	97.94	33.21	30.12	37.77
	11.81	6,640	86.51	85.27	70.96	86.75
	12.73	7,236	85.49	83.46	69.53	85.00
	13.84	57,572	100.40	54.48	42.55	52.02
	10.29	191,525	86.50	42.94	32.01	39.14
	10.80	208,452	83.99	40.81	31.38	38.36
	10.84	287,671	85.01	35.61	29.07	35.54
	10.82	1,153,504	82.79	23.83	21.65	26.46
	10.45	1,787,213	83.94	28.32	21.65	26.46
10.75	1,931,722	83.43	23.82	21.65	26.46	

Figure 2.18(c): Table Showing the Comparison Between Experimental Results and Theory (Cunha et al., 2009)

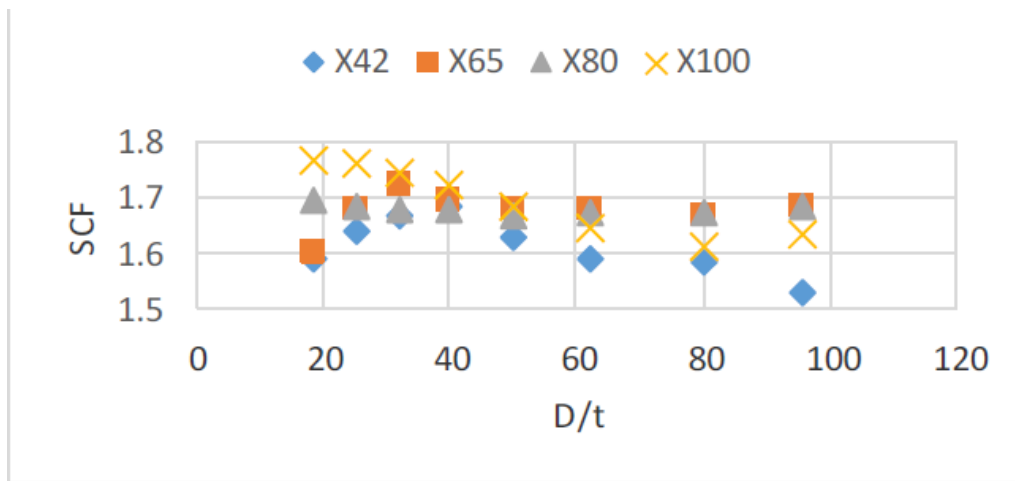


Figure 2.19(a): Effect of Pipe Grade on D/t and SCF (Durowoju et al., 2016)

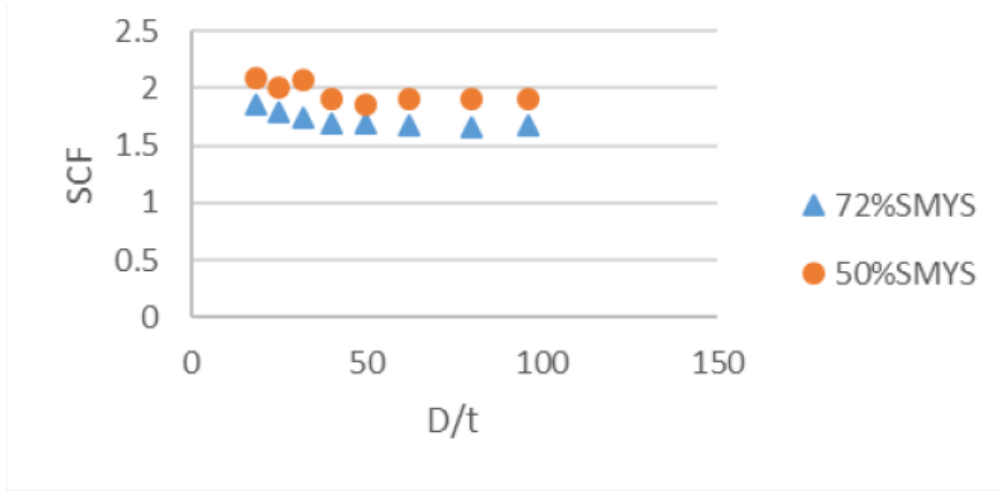


Figure 2.19(b): Effect of Pressure Cyclic Load Range on D/t and SCF (Durowoju et al., 2016)

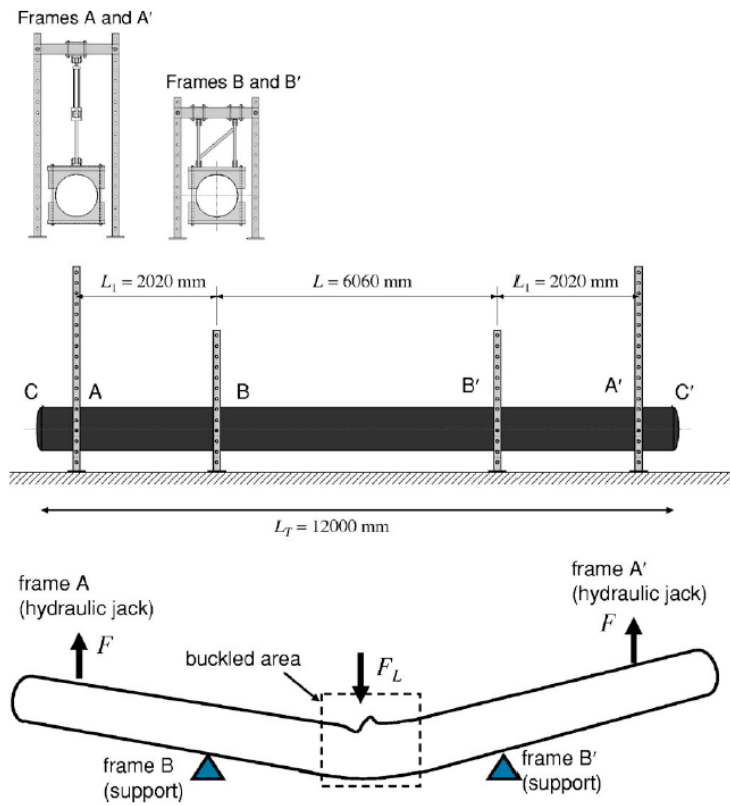


Figure 2.20: Schematics of Four-point Experimental Test Setup (Dama et al., 2007)



Figure 2.21: Denting Setup for Pipe Specimen (Pournara et al., 2015)



Figure 2.22: Monotonic and Cyclic Bending Setup for Dented Pipe Specimen (Pournara et al., 2015)

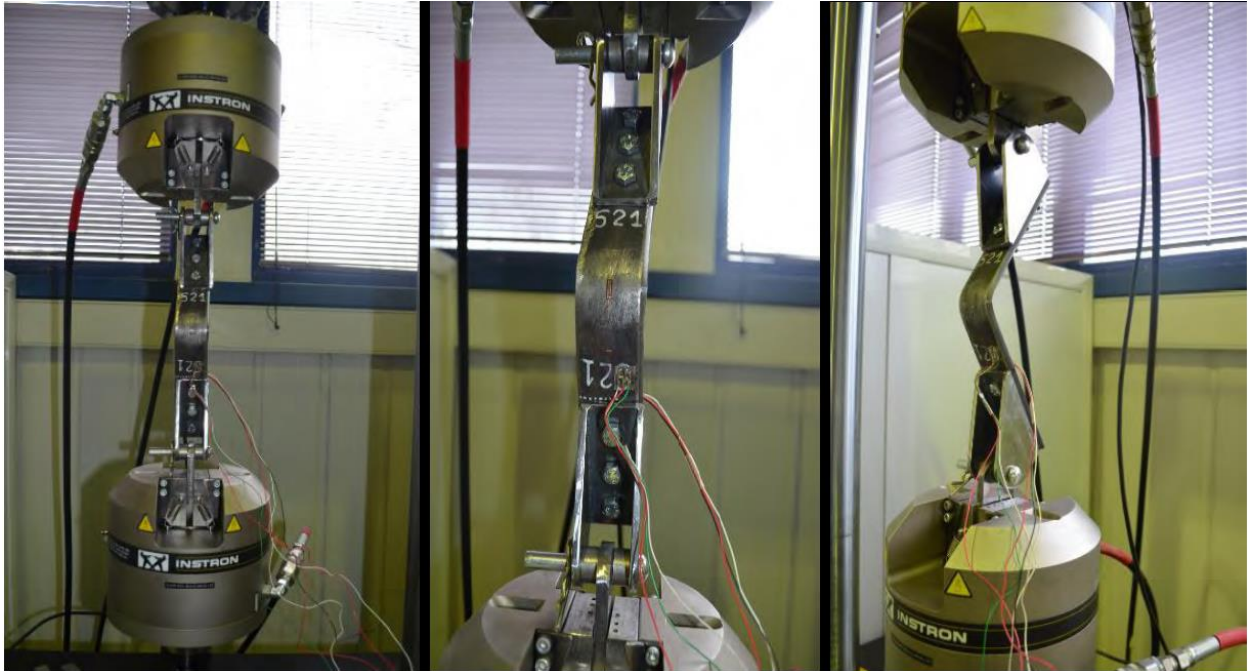


Figure 2.23: Cyclic Bending Setup for Strip Specimen (Pournara et al., 2015)



Figure 2.24: Strip Specimens Cut from Pipes (Das et al., 2007b)

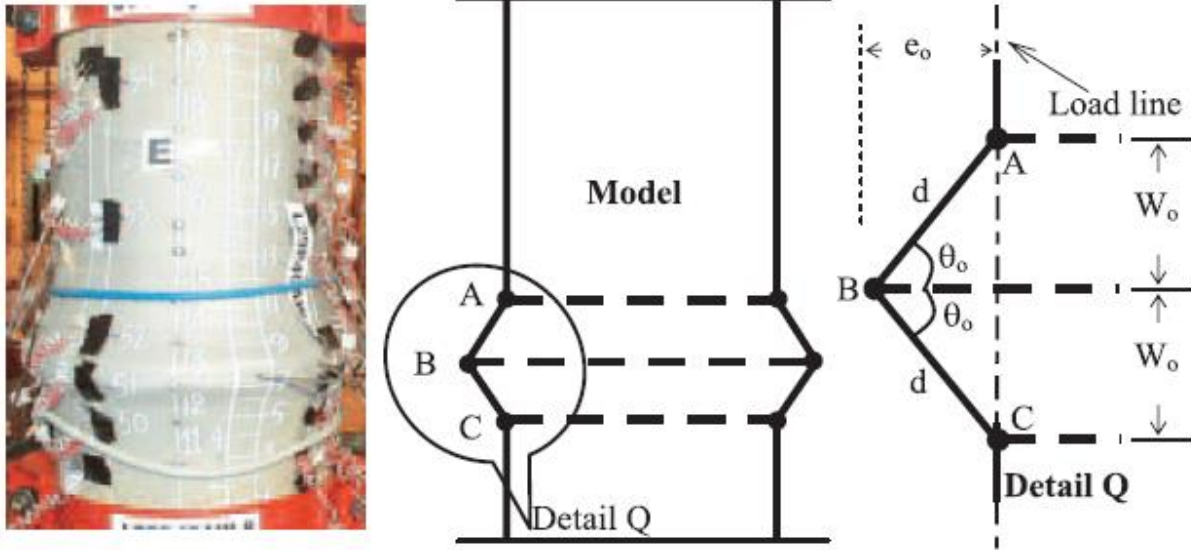


Figure 2.25: Details of Strip Specimens Cut from Pipes (Das et al., 2007b)

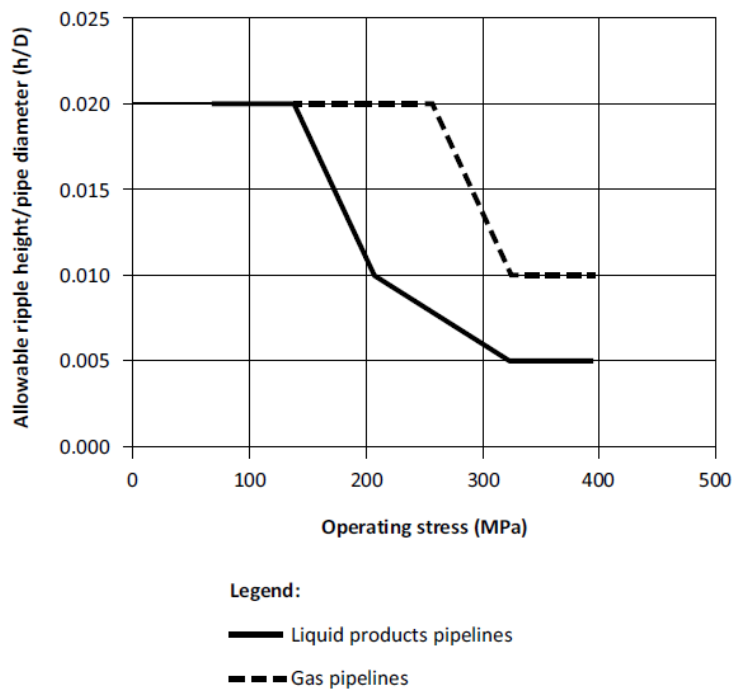


Figure 2.26(a): Recommended Maximum Allowable Ripples, Wrinkles and Buckles for Steel Pipe (CSA Z662, 2019)

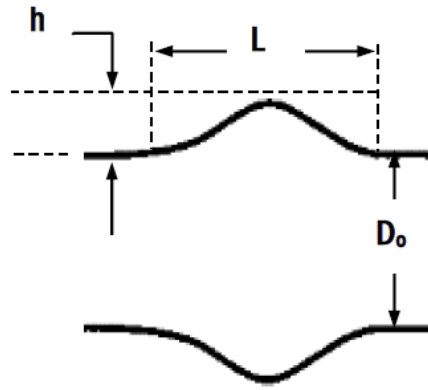


Figure 2.26(b): Geometric Measurement of Wrinkle Profile Parameters

CHAPTER 3

EXPERIMENTAL PROGRAM

3.1 General

The objective of this research is to study the behaviour and assess the fatigue life of buried wrinkled pipelines that are subjected to constant internal pressure and axial load cycles. The axial load cycles were applied such that they simulate the temperature variation of 45°C that a buried pipeline usually experiences in Northern Alberta due to the seasonal variation in the temperature.

According to literature, there have been a previous research on the behaviour of axial load cycles on pressurized pipes undertaken by Das et al. (2007a) at the University of Alberta. Firstly, internal pressure was applied on the wrinkled pipes of grade X52 with D/t of 45. Additionally, a monotonically increasing compressive axial load was applied on pipes with the wrinkle defect while maintaining the internal pressure. The test was concluded by completely unloading the axial load and internal pressure. This process was repeated until a leak or rupture was obtained. Only very few cycles (in the range of 4 to 9 cycles) were required to fail the wrinkled pipe. However, the cyclic load range used in this previous study accumulated excesses, which resulted in severe wrinkle defects and does not adequately depict the behaviour of field pipelines. Das et al. (2007b) then developed a fatigue life assessment model using the innovative concept of strip specimen. Followed by this research, Zhang (2010) at the University of Alberta developed a low cycle fatigue life prediction model for pipelines with wrinkle defect using the strip specimen which was first proposed and developed by Das et al. (2007b). However, strip specimens subjected to cyclic compressive and tensile loads exhibit only a uniaxial stress response. This is because of the neglected effect of combined internal pressure, that registers a biaxial stress in an operating field pipeline. The study by Zhang (2010) was based on strip specimens with wider range of pipe thicknesses (6 mm to 12 mm) as compared to Das et al. (2007b), leaving all other parameters such as; radius of curvature, bend angle and pipe grade similar. The result from the strip tests was then used to predict the fatigue life of wrinkled pipelines, using energy-based method. Similarly, Dama et al. (2007) and Pournara et al. (2015) applied the concept of strip specimen to predict the fatigue life of wrinkled pipelines using the strain life approach. This will be explained further in chapter 6.

Therefore, due to the lack of proper simulation of operational field working conditions from previous researchers, eight full-scale tests were carried out on API 5L (API 5L 2018) pipes of length 660 mm and diameter to thickness ratio (i.e. D/t) of 57 under combined axial tension-compression load cycles with a constant internal pressure (Table 3.1). This experimental study was completed in two different loading phases. In the first phase, the wrinkle was formed by subjecting plain pipe specimens to a constant internal pressure and monotonically increasing axial compressive load similar to Das et al (2007a). However, wrinkle amplitude in the current study was much smaller. The second loading phase involved a displacement controlled axisymmetric tension-compression axial load cycle, with a constant internal pressure. The cyclic axial load was applied using a displacement control method. The test matrix is shown in Table 3.1. As can be found from this table, wrinkle amplitude was varied in the range of 4% and 10.5%, and the internal pressure was 30% and 60% of the yield pressure (p_y).

3.2 Phase 1 – Initiation of Wrinkle Defect

The experimental setup, instrumentation, and procedure exclusive to the wrinkle defect initiation stage are as follows:

3.2.1 Selection of Specimen

The experiment is designed to simulate the operational working conditions of field pipelines, using full-scale tests in order to gather the accurate response of operational pipelines. Therefore, the sizes and grades of the pipes selected are such that they fully represent the type of pipes used in the oil and gas pipeline industry. The D/t of the pipes used is constant throughout and is within acceptable limits of 20 to 80 according to various researchers (Oswell 2011; Wilkie et al. 2001). The API 5L (API 5L, 2018) X42 steel line pipes were 215 mm (8 in) in diameter and 3.76 mm (0.148 in) in thickness to give D/t of 57. The length of the specimens was chosen to avoid lateral instability of the pipes but suitably long enough to allow local buckling or cross-sectional yielding of the pipes in the regions of imperfection. Therefore, they were made 660 mm (26 in) long (see Figure 3.1).

The tension coupon test was performed according to ASTM E8/E8M-13a (ASTM E8, 2013), on coupon strips cut in the longitudinal direction from the tested pipes. These specimens were cut from the area away from the seam weld to avoid any possible effect of residual stress. The coupon tests showed that the mechanical properties of the pipe are in accordance with API 5L X42 standard (API 5L 2018) with a minimum yield strength of 288 MPa (42 ksi) and an ultimate tensile strength

of 384 MPa (56 ksi). These properties may have been higher but affected by the UOE forming process, as described in Section 2.2.2. The longitudinal seams along the pipe length were created using electrical resistance welding (ERW), which is commonly used in oil and gas pipelines with seam welds. This type of welding relies on the electrical resistance of the material and force used to hold the plates together. It does not necessarily require filler metal for welding which may compromise the material properties of the manufactured pipes. However, the effect of the forming process and the longitudinal seam was ignored in this study.

3.2.2 Selection of Wrinkle Defect Profile

As discussed in section 2.7, current codes and standards limit the height of any ripple or wrinkle to a maximum of 2% of the outside pipe diameter, which further reduces depending on the operating stress caused by the gas and liquid (crude or finished products) being transported (see Figure 2.26a). These guidelines, however, have been proven to be extremely conservative by many researchers (Alexander & Kulkarni, 2009; Das et al., 2007a). Therefore, more conspicuous wrinkle geometry profiles were considered in this research.

In the experimental program, the wrinkle geometry profile was measured by the ratio of height, h (*i.e.* height of the wrinkle crest to wrinkle trough) to outside pipe diameter (D_o) (Figure 3.2). The measurement was made using the contour gauge during the tests. The measurement of the wrinkle profile was taken at several intervals during the tests until the targeted wrinkle geometry profile was achieved. As shown in Table 3.1, four wrinkle geometry profiles are considered in this research. This ranges from a slightly greater wrinkle geometry profile (*i.e.* 4%) than as accepted in the codes and standards (which is limited to a maximum value of 2%), to a more severe wrinkle geometry profile (*i.e.* 10.5%). The maximum wrinkle geometry for the pipe geometry ($D/t = 57$) chosen for this research, was taken to be 10.5%. This is associated with the fact that wrinkle defects that are this severe are not left unattended as per current design guidelines. Moreover, Das et al. (2007a) already studied severe wrinkle profiles under axial cyclic loading.

3.2.3 Boundary Conditions

The boundary conditions in the operating field pipelines were simulated in the experimental set-up, such that the interaction between the pipelines and the surrounding soils were relatively defined. This was done to determine the response of field pipelines in operating conditions. Specifically, one end of the pipe which sat on the support was fixed for all six degrees of freedom

to avoid rotation or translation at that end. The top end of the pipe specimen where axial compressive and tensile loads was applied, was free for all six degrees of freedom. However, four steel bars were passed through the bottom and top end plate in order to prevent rotational degree of freedom as cyclic axial loads were applied to the specimen as shown in Figure 3.1. The bars also worked as a guide to maintain a symmetric wrinkle. They also maintain biaxial ratcheting in the longitudinal direction when the pipe is beyond its yield capacity and experiences softening due to plasticity.

3.2.4 Preparation of Specimen

Four API 5L X42 (API 5L, 2018) steel line pipes with D/t of 57 were cut into 660 mm (26 in). The ends of the pipes were machined (bevelled) to 60° to facilitate welding of the pipes to two 50 mm (2 in) thick end plates. The 6401 mm (21 feet) uncut steel pipes were cut roughly into the desired length using a plasma torch. The pipe specimens were then visually inspected to ensure that all the pipes were free of any defects such as corrosion, dents, buckles or ovality. Before the pipes were sent out for welding by an experienced and registered welder, clean cuts into 660 mm (26 in) were made using an industrial-grade metal band saw. This was done to ensure the circular ends of the pipes were smooth enough to sit perpendicularly on the end plates for easy welding. The pipes were marked with lines to identify the corresponding centroids. These lines were used to ensure the centroid of the pipe segment coincided with the centroid of the adjacent endplates, to avoid eccentric loading. Additionally, 1-inch (25 mm) linear graduations were imprinted longitudinally along the entire pipe segment, which allowed for a quick approach to approximate longitudinal strains within the wrinkled region. Figure 3.3 show the details of what is discussed in this paragraph.

The end plates were welded to keep the water confined in the pipe specimen during pressurization and provide inlet and outlet for water in the pipe specimen. Two end plates were welded to each pipe specimen, namely the top and bottom endplates. The top end plates were provided with eight 38 mm (1.5 in) diameter clearance holes at the four vertices. The bottom endplates were provided with four 38 mm (1.5 in) diameter tapped holes with 6 threads per inch, and six 25 mm (1 in) diameter clearance holes. Schematics of the discussion in this paragraph are given in Figure 3.4 (a) and (b).

Four 38 mm (1.5 in) diameter steel solid bars were then passed through each of the holes on the top endplate and then screwed into the bottom endplate. These were to be used as restraints to prevent the rotational degree of freedom of the pipes in the longitudinal axis during ratcheting of the pipe specimen. Seven strain gauges were attached to the specimen in the region of local buckling (wrinkling) where critical strain readings were predicted. The outer surface of the pipes was grinded to remove coating materials, which will hinder the direct contact of the strain gauges to the pipe surface for accurate readings.

3.2.5 Specimen Designation

Each of the pipe specimens tested in this experimental program has a tag that can be used to identify its key features, as shown in Table 3.2. For example, the specimen IP30WA10.5 refers to a pipe specimen that was pressurized internally (*IP*) up to 30% of its yield pressure ($0.3p_y$) in both monotonic and cyclic phases, where the nominal wrinkle defect amplitude (*WA*) was brought to 10.5% of its outer diameter in the monotonic stage.

3.2.6 Test Setup for Monotonic Loading

The experimental testing was performed in the Structural Engineering Laboratory (SEL) at the University of Windsor. Located inside the laboratory, is a rigid reaction frame to which the hydraulic cylinder and load cell with capacity ± 2000 kN were attached as shown in Figure 3.5 and 3.6. Attached on the strong floor below the hydraulic cylinder is a support with a height of 1016 mm (40 in) which was positioned in a way that the center of the support aligned with the center of the hydraulic jack. The strong support is provided with six 25 mm (1 in) diameter clearance holes drilled on the top plate of the support, schematics are shown in Figure 3.7.

The welded pipe assembly was transferred to the support under the hydraulic cylinder, properly aligning the specimen on the support in such a way that there is no allowance for eccentricity during loading. The bottom endplate of the specimen is bolted onto the support using the six clearance holes, maintaining stability in both tension and compression during loading. A swivel head as shown in Figures 3.5 and 3.6 is placed on the specimen top endplate to provide allowance for eccentricity with the hydraulic cylinder during uniaxial loading, without causing damage.

Seven collars 6.7 mm (0.264 in.) thick, and 75 mm (3 in) wide in the longitudinal direction of the pipes were attached to the pipe specimens. Three collars were attached close to the top endplate

and four collars attached towards the bottom endplate, leaving a 125 mm (5 in) allowance in the mid-length of the specimen to facilitate formation of a wrinkle defect away from the end plates.

Two ball valves adjacent to each other were attached to the specimen bottom endplate, where one served as an inlet for water from the hydrostatic pressure pump, and other as a drain when the test has been completed. One ball valve and a pressure transducer adjacent to each other were also attached to the specimen top endplate. The ball valve acted as a drain for excess air stored in the pipe system when pressurizing, and the pressure transducer gave pressure readings in the closed pipe system during pressurization.

The strain gauges attached to the pipe specimen were then connected to strain wires which were used to transmit signals to the Data Acquisition System (DAQ), to take localized strain readings in the region of local buckling (wrinkling). Two Linear Variable Displacement Transducers (LVDTs) were placed on the bottom endplate of the specimen, making sure the tip touches the top endplate of the specimen. This was done in order to capture the global axial displacement of the pipe specimen in the longitudinal direction during axial compression. Detailed photographs and schematics of what is discussed in this subsection are shown in Figures 3.5 and 3.6.

3.2.7 Instruments and Instrumentation for Phase 1

3.2.7.1 Strain Gauges

Seven 5 mm electrical resistance strain gauges were used to measure localized strains in the predicted wrinkle region of each pipe specimen. The strain gauges possessed gauge resistance, gauge length and gauge factor of 119.8 ohms, 5 mm and 2.10, respectively. The strain gauges were placed on the outer surface of the pipe within a range of 65 mm length of the predicted wrinkle region. Schematics of the strain gauge configuration are shown in Figure 3.8.

The surface of the pipe wall was grinded and polished with sandpaper to remove the coatings and paintings, before attaching the strain gauges. The residues on the pipe wall were wiped away with a cleaning solvent. Thereafter, the strain gauges were bonded to the pipe surface using a strong adhesive. Strain wires were then soldered onto the strain gauge silver-clad copper lead wires on one end and attached to the DAQ on the other end, to transmit signals for local strain readings. The signals were captured during the extension and compression of the measuring grid of the strain gauges and produced a simultaneous electric resistance. The limit of these strain gauges rests at approximately 5% strain.

3.2.7.2 LVDT (Linear Variable differential transformer)

A total of two Linear Variable differential transformer (LVDTs) were used during the monotonic tests. The LVDTs were attached to the pipe specimen to measure the axial displacement of the pipe specimen. Figure 3.5 shows the position of the devices.

Generally, LVDTs are miniature transformers that are used to measure linear displacement along one direction in a single axis. LVDTs consist of one primary coil, two secondary coils located at either end of the primary coil, and one armature core that is free to move along its linear axis with an attached arm that touches the monitored component (top endplate of pipe specimen). The primary coil is excited by an Alternating current source which creates a magnetic flux that is coupled to a mobile armature core, which subsequently causes AC voltage to be induced in the secondary coils. The movement of the arm attached to the core, allows the core to move closer to either of the secondary coils and more magnetic flux is generated in the secondary coil closest to the core. The difference between the voltage of both secondary coils is the output given as displacement in the data acquisition system. Because the LVDT relies on coupling magnetic flux, it has an infinite resolution and therefore the smallest movement can be measured, which makes this device reliable for measuring linear displacement.

3.2.7.3 Pressure Pump

An air driven hydraulic pump (see Figure 3.9) was used to pressurize the specimen through the hose attached to the bottom plate. The liquid output pressure of the pump can be adjusted by regulating the incoming air supply at the pressure regulator. The relationship between the area of the air-driven piston and area of the fluid-driven piston is known as the pump ratio. This ultimately decides the fluid pressure output of the pump. This pump, however, discharges 125 psi fluid pressure for every 1 psi operating air pressure. The liquid pressure output supplied to the pipe specimen was recorded in the data acquisition system using the pressure transducer attached to the opening on the top plate of the specimen.

3.2.7.4 Collars

From previous literature, it has been observed that on applying a monotonically increasing compressive load on a pipe specimen, the pipe cross-section yields where the effect of the compressive load is maximum. The maximum effect was at welded joints between the pipe and

the endplates. Since, that is the most recognized weak spot (Alexandre and Kulkarni 2009), that allows wrinkle initiation and growth in this region.

Seven collars were attached to the pipe specimen to create an imperfection that has an effect greater than that of the welded joints, by increasing the thickness of the pipe in the region close to the welded endplates. Each of the collars (Figure 3.10) was made by cutting a 75 mm (3 inches) width of 6.7 mm (0.26 inch) thick 203 mm (8 inches) nominal diameter pipe, to form a ring. Each ring was cut into semi-circular halves, with each end welded to punctured steel angles to make a collar. Each half of the collars were then fastened together with a bolt and screwed through the holes on the steel angles.

3.2.7.5 Pressure Transducer

A 5000 *PSIG* capacity industrial grade pressure transducer with strain gauge-based sensors, were used in this test to transmit pressure signals to the DAQ. The deformation effect on the strain gauges installed in all the welded stainless-steel transducer is caused by the fluid pressure. This leads to subsequent conversion of the pressure to an electrical signal. The electrical signal is transmitted to the DAQ in a response time of less than 3 ms. The pressure transducer that was used has a 4-20 mA output, which is less susceptible to electrical noise and gives accurate data.

3.2.7.6 Hydraulic Cylinder and Load cell

A general purpose 2000 kN capacity, double-acting hydraulic cylinder, equipped with ± 2000 kN load cell, was used to apply tension-compression force on the specimen. The cylinder has a 13-inch (330 mm) pull and push stroke. The cylinder is used to contain a hydraulic fluid and piston which is controlled by using an electric pump to move the piston uniaxially. This generates a compensating tension and compression load effect on the specimen. The working principle of a hydraulic pump is based on pascal's principle, which applies to an incompressible fluid. The resultant force due to the contact between the specimen and the cylinder generates an electrical signal by the load cell which is sent to the DAQ as load readings.

3.2.7.7 Data Acquisition System

A data acquisition system was used to measure electrical signals collected from the pressure transducer, strain gauges, load cell and LVDTs. The DAQ has eight modules equipped with eight channels each, to receive both voltage and strain signals. The data obtained from the voltage and strain-based instruments are processed using the LABVIEW software written by the research

group at the University of Windsor. The software records the data on a spreadsheet at a rate of one reading per second.

3.2.7.8 Contour Gauge

A contour gauge is a tool capable of recording the cross-sectional shape of a surface. Contour gauges consist of a set of plastic or steel pins which are tightly secured in a frame, allowing the pins to move independently in the perpendicular direction. When imposed against an object, the pins move, adapting to the profile of the surface. The gauge can then be used to record the profile of the object.

A 25 mm (10-inch) contour gauge was used to measure the wrinkle defect profile during each test, as shown in Figure 3.11. Specifically, test specimens were incrementally loaded and unloaded while recording the evolution of the wrinkle profile. Multiple wrinkle profiles were inscribed into a logbook during each test (Appendix B). It is important to acknowledge test specimens were never fully unloaded until the completion of the test, to ensure the pipe specimen does not shift while loading and unloading. Hence, the penult loaded wrinkle profile recordings generally showed results with larger wrinkle profiles, in comparison to final unloaded wrinkle profile readings; likely due to elastic spring back.

3.2.8 Monotonic Loading Procedure

This procedure was designed to ensure consistent wrinkle formation and growth; hence, the same loading sequence was developed for all four specimens when applying a monotonically increasing axisymmetric load. The pipe specimen was first filled up with water and pressurized to the desired internal pressure, which was selected as 30% and 60% of the yield pressure ($0.3p_y$, $0.6p_y$) for this research. The internal yield pressure (p_y) is represented in Equation 3.1.

$$p_y = \sigma_y t / R_i \quad (3.1)$$

In this equation, σ_y is the yield strength of the pipe material (288 MPa), t is the thickness of the pipe specimen (3.76 mm) and R_i (211.55 mm) is the internal radius of the pipe. The p_y is then equivalent to 3.1 MPa (450 psi) or 6.2 MPa (897 psi). Allowance was provided for the elongation of the pipe specimen during pressurization, prior to the inception of axial loading, to simulate an unrestrained boundary condition. Then, a monotonically increasing axisymmetric axial compressive load (P_C) was applied to the specimen, as this load was calculated using Equation 3.2.

This load combination represents the normal stress in an operating pipeline for which there have not been any imposed geotechnical displacements (Das et al. 2007a).

$$P_C \equiv C_t + C_v + C_e \quad (3.2)$$

In Equation 3.2, C_t is the thermal expansion/contraction load, C_v is the Poisson's ratio plane strain constraint load, and C_e is the thrust load due to the endplate as shown in the following equations.

$$C_t \equiv A_s E \alpha \Delta T \quad (3.3)$$

$$C_v \equiv -A_s \nu \sigma_h \quad (3.4)$$

$$C_e \equiv \pi R_i^2 p_i \quad (3.5)$$

where, A_s is described as the cross-sectional area of the pipe ($\pi(R_o^2 - R_i^2)$), E is the modulus of elasticity of the pipe material determined from the tensile coupon test (192 GPa). ΔT is the maximum difference between the installation temperature and operating temperature, assumed to be 45°C which is representative to the seasonal temperature variation in Northern Canada, α is the coefficient of thermal expansion for the pipe material ($11.7 \times 10^{-6}/^\circ\text{C}$), ν is the Poisson's ratio of steel (0.3), σ_h is the hoop stress in the pipe wall due to applied internal pressure. The p_i is the applied internal pressure, R_i is the internal radius of pipe specimen (107.66 mm), and R_o is the outer radius of the pipe (109.54 mm).

The net load (P_s) applied on the pipe specimen which excludes the compensated load due to the thrust load acting on the endplate, included in the compressive axial load (P_C) is represented in Equation 3.6.

$$P_s = P_C - C_e \quad (3.6)$$

The axisymmetric axial loading is continued until the target wrinkle amplitude was achieved (as discussed in section 3.2.2). However, the application of loading on the specimen continued well beyond what is shown by Equation 3.2 to achieve the required wrinkle amplitude. This will be discussed in the next chapter.

3.3 Phase 2 – Axial Cyclic Loading

The following subsections discuss the considerations, test setup and loading sequence involved in the axisymmetric axial cyclic loading stage.

3.3.1 Selection of Axial Cyclic Range

A study was conducted by Naeth et al. (1993) at the University of Alberta, to evaluate soil temperature responses to pipeline construction and operation. The conditions of a buried wrinkled pipeline in a region that experiences extreme temperature difference was simulated. Soil temperatures were monitored throughout the year to a depth of 1.1 m, in trenches dug for pipeline construction in the year 1957 and 1981. The observation was that soil temperature becomes less extreme with an increase in depth of the soil. However, at a shallow depth of 0.05 m into the soil, the 1981 and 1957 trenches gave a minimum temperature of -2.6°C and -4.2°C , respectively on January 28, 1983, and a maximum temperature of 32.8°C and 34°C on August 1, 1983. This results in an approximately 40°C difference at extreme seasonal temperatures. The mean monthly soil temperature at 0.3 m depth from October 1982 to September 1983 is shown in Figure 3.12.

However, for the purpose of this research, a more conservative approach was chosen to estimate the extreme seasonal temperature difference as 45°C in Northern Alberta, where most pipelines in Canada are located. Based on the concept of linear thermal expansion, a displacement controlled axial cyclic load was applied on the wrinkled pipe specimen, using the displacement value approximated from Equation 3.7.

$$\Delta L = \alpha \times L_o \times \Delta T \quad (3.7)$$

ΔL is the change in length of the pipe, α is the coefficient of linear expansion for carbon steel ($11.7 \times 10^{-6} \text{ m/m}^{\circ}\text{C}$), L_o is the initial installation length of the pipe assumed to be 40 ft (12 meters) and ΔT is the temperature difference assumed to be 45°C as experienced in Northern Alberta. The change in length of the pipe due to the effect of temperature differential was calculated to be $6.318 \times 10^{-3} \text{ m}$, approximately 6 mm. The axial load cycling of the wrinkled pipe specimen was limited to 3 mm in compression and 3 mm in tension.

3.3.2 Preparation of Specimen

The target wrinkle profile was artificially stimulated in the region of imperfection created by the collars i.e. where the thickness of the pipe specimen is lesser or where there were no collars. Few

alterations were made to the specimen before the commencement of displacement controlled axial cyclic loading stage. Since the loading sequence includes loading in both compression and tension, the specimen was attached to the loading actuator to accommodate the axisymmetric tension-compression load in the longitudinal axis. As shown in Figure 3.4(b), four 38 mm (1.5 in) clearance holes located 3.25 inches (83 mm) away from the four edges of the specimen top plate was used to connect the specimen to the load cell. Furthermore, the specimen was also grinded and polished at the wrinkle region to attach new strain gauges, as the old ones were considered ineffective at this stage.

3.3.3 Test Setup for Axial Cyclic Loading

The experimental testing for this loading phase (phase 1) was also done in the University of Windsor SEL, under the same reaction frame, hydraulic loading actuator and load cell, as used for the monotonic loading. However, a few modifications were made to the setup to be able to apply tensile load (see Figures 3.13 and 3.14).

The swivel head was replaced with a 12-inch (305 mm) long by 12-inch (305 mm) wide by 2-inch (50 mm) thick connecting steel plate. The connecting plate was fabricated to allow a bolted connection with the top plate of the specimen and to the load cell. The plate has four 1-3/8 inches (35 mm) tapped holes at the vertices and one large 100 mm (4 inches) tapped hole at the middle, schematics of the connecting-plate is shown in Figure 3.15(a). Additionally, a 4.5-inch (114 mm) long bar with 100 mm (4 inches) diameter and a 3 mm (0.1168 inch) pitch was fabricated to serve as an adaptor. The adaptor threads into the load cell to provide a 2.5-inch (64 mm) threaded engagement into the load cell and 2-inch (50 mm) threaded engagement into the connecting-plate. Schematics are shown in Figure 3.15(b). The purpose of these fabricated parts was to allow the sequential compressive and tensile loading of the wrinkled specimen.

The wrinkled pipe assembly was then aligned on the support to eliminate eccentricity as previously described in the monotonic setup, properly bolting the specimen on the support top-plate. All collars were removed except for the one close to the welded end plates. This was done to eliminate the possibility of fracture due to stress concentration and residual stresses caused by the welding of the end plates (Figure 3.13). The ball valves attached to the bottom and top plate of the specimen were left intact since the specimen was pressurized internally during this stage. The LVDTs were also placed in the same position as previously described in the monotonic phase.

However, new strain gauges were attached to the wrinkled pipe specimen to generate accurate strain readings, because the previous strain gauges attached were assumed to have reached their strain limits and considered ineffective at this stage. Two strain gauges were attached side by side on the wrinkle crest in the longitudinal direction of the pipe, another two strain gauges were attached on the wrinkle feet in the longitudinal direction of the pipe. The last one was attached to the wrinkle crest in the circumferential direction of the pipe (Figure 3.16a). These strain gauges provided localized strain readings in the wrinkle region during consecutive load cycles.

3.3.4 Instrumentation for Phase 2

3.3.4.1 Strain Gauges

Six new 5 mm electrical resistance strain gauges were used to measure localized cyclic strain behaviour in the wrinkled region of each pipe specimen. Two strain gauges were placed in the longitudinal direction exactly on the wrinkle crest and another one in the circumferential direction (Figure 3.16a and 3.16b). The last two were placed on the wrinkle feet. The former strain gauges were left on the specimen even though it was assumed that they had reached their limit.

3.3.4.2 LVDT

In addition to the two 50 mm, LVDTs that were used to measure the global displacement of the pipe specimen, a 25 mm LVDT was situated such that the local axial cyclic displacement associated with the wrinkle region was measured. The LVDT was attached to a collar fabricated to hold it near the bottom feet of the wrinkle, and the tip of the LVDT was made to touch a small metal plate welded to the collar attached near the top feet of the wrinkle. Figure 3.14 shows this in detail. This 25 mm LVDT was used to control the cyclic displacement range during the axial cyclic test, as it gave a more localized measurement of the wrinkle displacement.

3.3.5 Axial Cyclic Loading Procedure

A displacement controlled axial cyclic load was applied on the wrinkled pipe specimen, limited to a displacement range of 6 mm (± 3 mm), derived from the concept of linear thermal expansion (as discussed in section 3.3.1). This was done to simulate the conditions of a buried wrinkled pipeline in a region that's subjected to an extreme seasonal temperature difference of 45°C (using Northern Alberta as a case study).

Prior to cycling, the applied internal pressure was maintained at 0.3 p_y (450 Psi) or 0.6 p_y (897 Psi) as applied in the monotonic stage. On commencing the loading sequence, a monotonically

increasing axisymmetric compressive load was applied up until the LVDT reading attached at the wrinkle profile gives a 3 mm displacement reading in compression and hence, a displacement control method was used. Furthermore, a subsequent increasing axisymmetric tensile load was applied up to a displacement reading of 3 mm in the opposite direction (in tension). Consequently, a symmetric displacement cycle is achieved in approximately 3-minute (180 seconds) period. Figure 3.17 shows the time-lapse for five complete displacement-controlled cycles, similar to those applied in this experimental program. The axial cyclic loading is continued until a fracture or a leak was found on the pipe wrinkle.

3.4 Determination of Material Properties

The mechanical properties of the pipe specimen were determined before performing full-scale experimental tests. All pipe specimens which were tested were acquired from a single supplier, making sure the pipes are of the same material properties and geometry ratio (D/t of 57).

Six coupon specimens (Figure 3.18) were cut in the longitudinal direction of the steel pipe, away from the seam weld to avoid residual stress effect on the material behaviour according to ASTM E8/E8M-13a. The Uniaxial tensile test was performed on these coupons under a universal testing system, which has a ± 500 kN capacity. A 50 mm gauge extensometer was attached to the coupon during the test. The gauge measures the deformation of the gauge length of the coupon on the application of tensile load by the MTS system (Figure 3.19). The MTS Test Suite TW software was used to record the force, displacement, stress, and strain data generated during testing of the coupon specimens up to rupture.

The data gotten from the tensile test is used to determine the yield strength, tensile strength, Poisson's ratio, as well as engineering stress and strain material behaviour of the pipe specimen, to be used in the full-scale test.

Table 3.1: Wrinkle Defect Profile Measurements

S/N	Internal Pressure (% of p_y)	Wrinkle Amplitude	Exact Wrinkle Amplitude to Diameter Ratio (h/D_o)	Nominal Wrinkle Amplitude to Diameter Ratio ($\approx h/D_o$)
1	30 (Group 1)	22.5	10.45	10.5
2		17.5	8.13	8
3		12.5	5.81	6
4		8.5	3.95	4
5	60 (Group 2)	22.5	10.5	10.5
6		17.5	8.13	8
7		13	6.04	6
8		8.7	4.04	4

Table 3.2: Text Matrix for Experimental Program

S/N	Internal Pressure (% of p_y)	Nominal Wrinkle Amplitude to Diameter Ratio ($\approx h/D_o$)	Specimen Designation
1	30 (Group 1)	10.5	IP30WA10.5
2		8	IP30WA8
3		6	IP30WA6
4		4	IP30WA4
5	60 (Group 2)	10.5	IP60WA10.5
6		8	IP60WA8
7		6	IP60WA6
8		4	IP60WA4



Figure 3.1: Pipe Specimen with Four Straight Bars

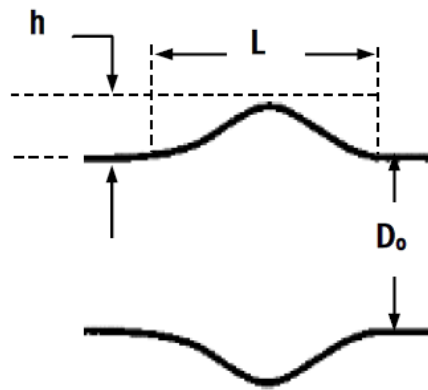


Figure 3.2: Geometric Measurement of Wrinkle Profile Parameters



Figure 3.3: Cut Pipe Specimens with Appropriate Markings and Straight Bars

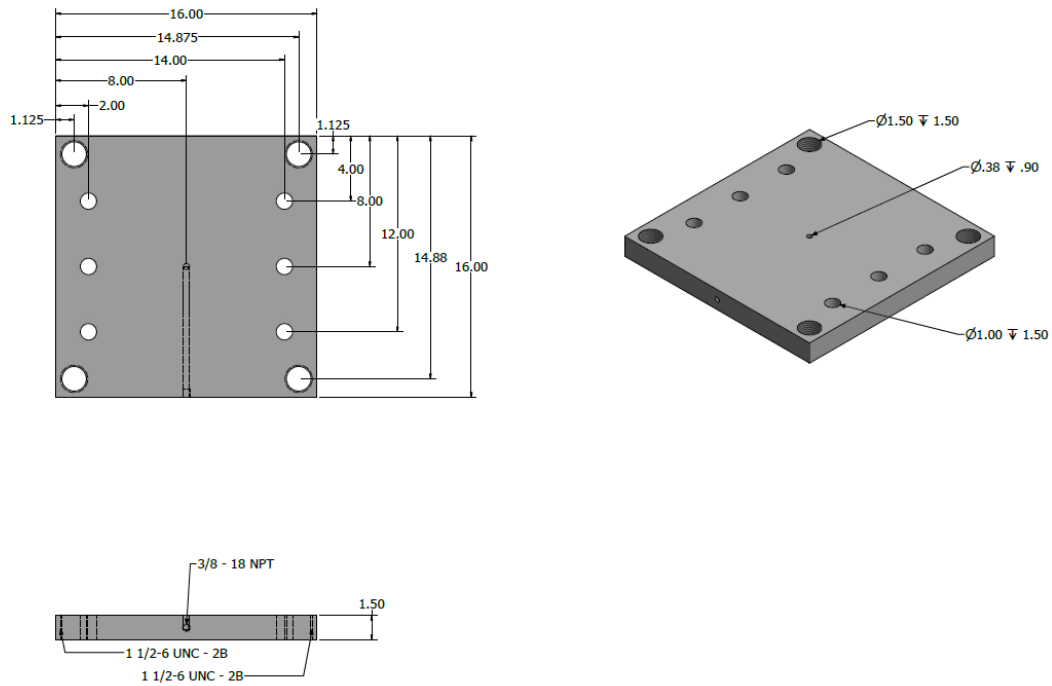


Figure 3.4(a): Schematics of Specimen Bottom Plate

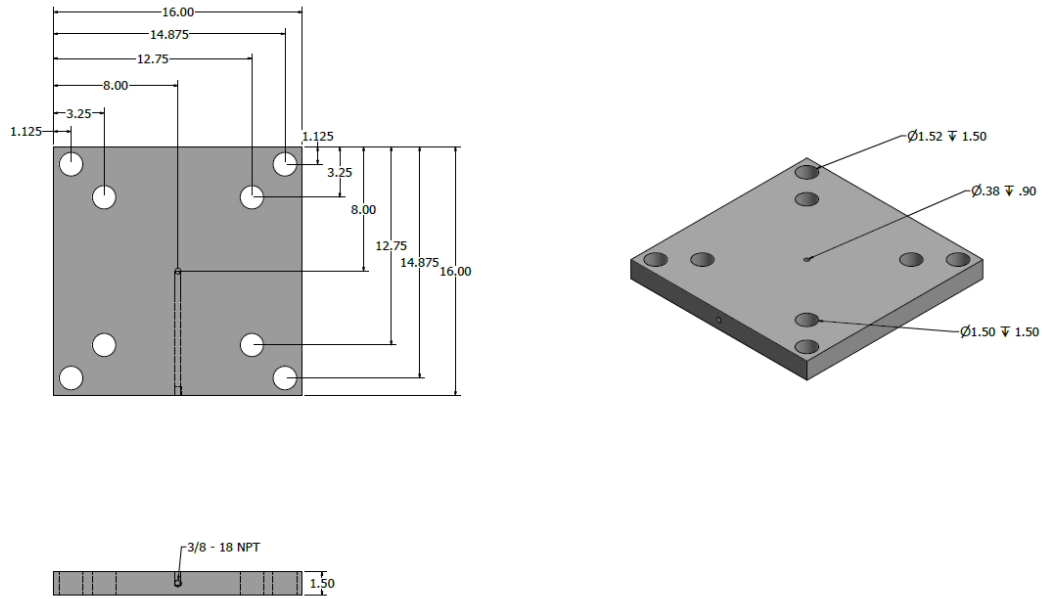


Figure 3.4(b): Schematics of Specimen Top Plate

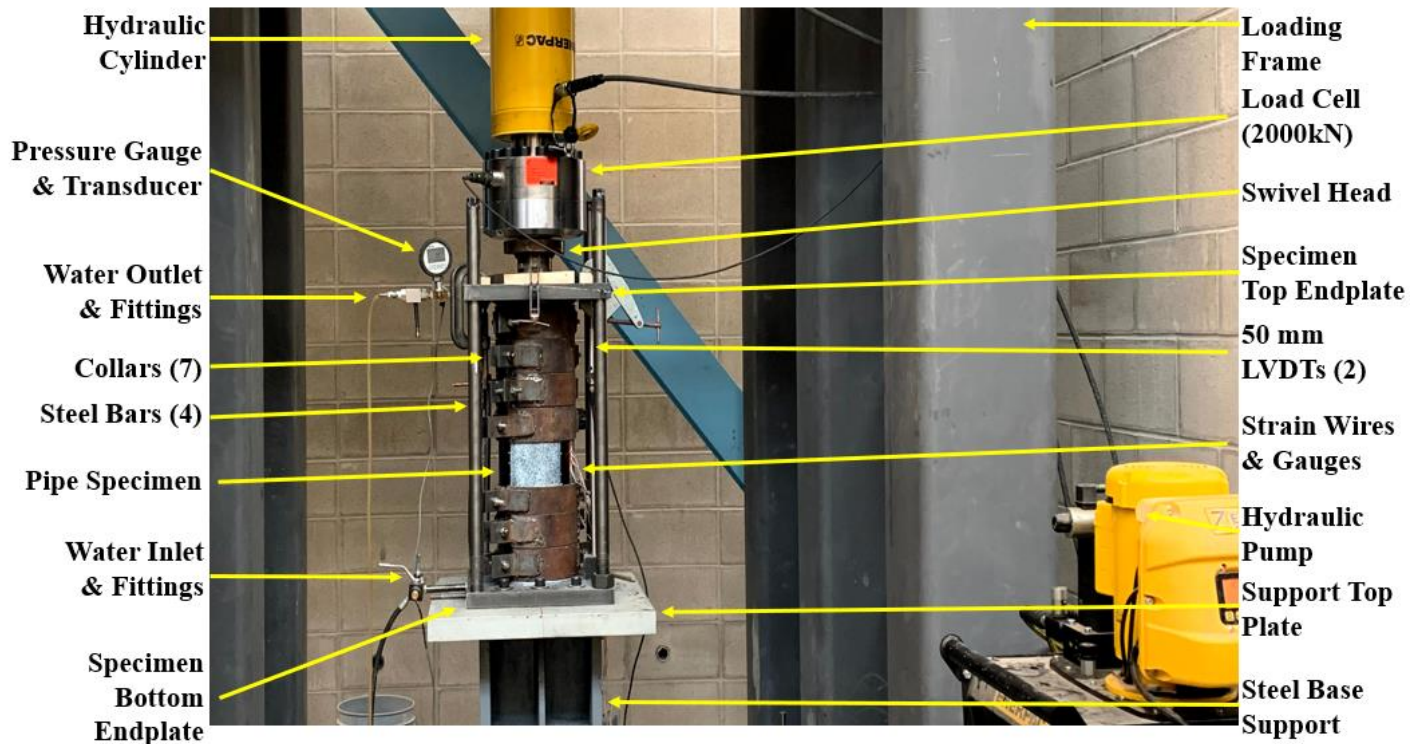


Figure 3.5: Test Setup for Monotonic Loading Stage

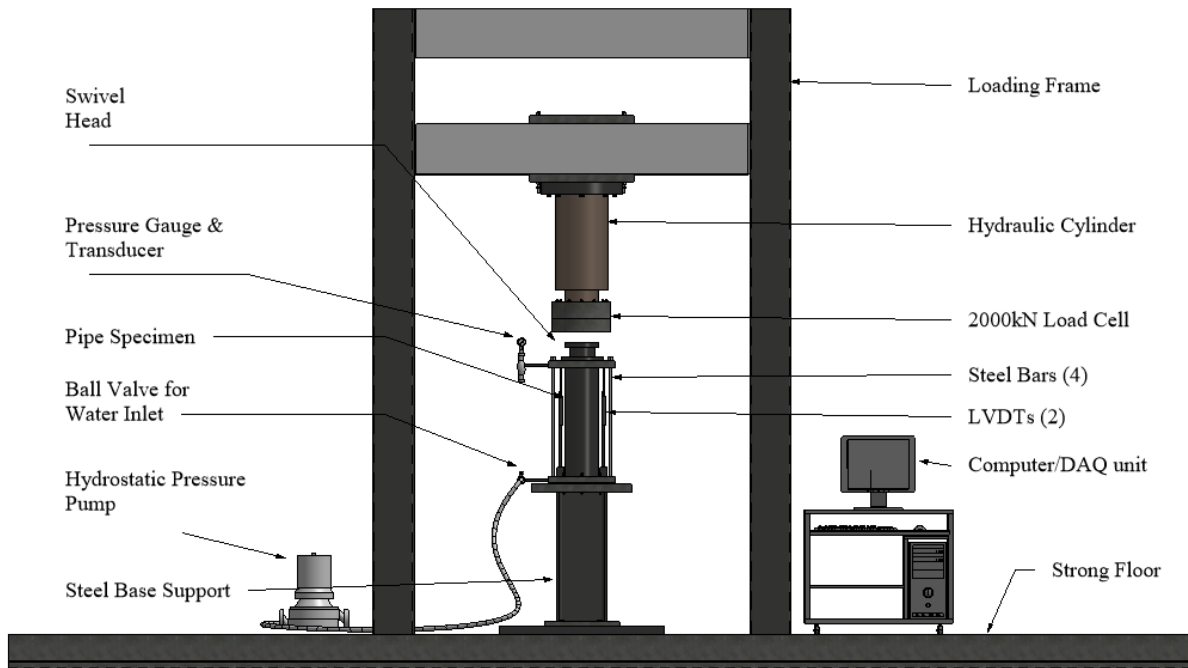


Figure 3.6: Schematics of Test Setup for Monotonic Test

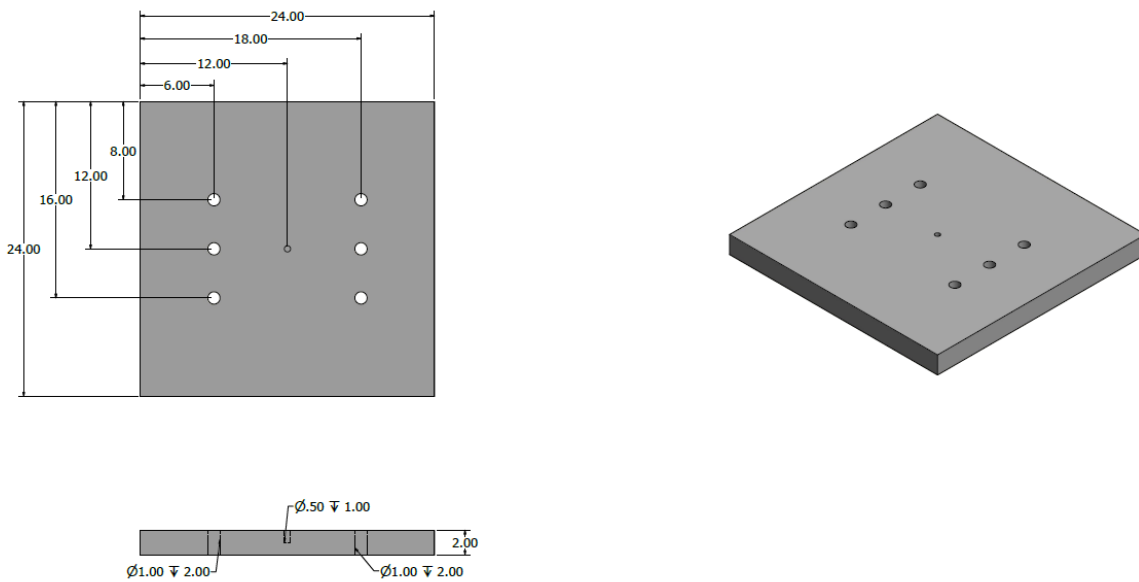


Figure 3.7: Schematics of Support Base Top Plate

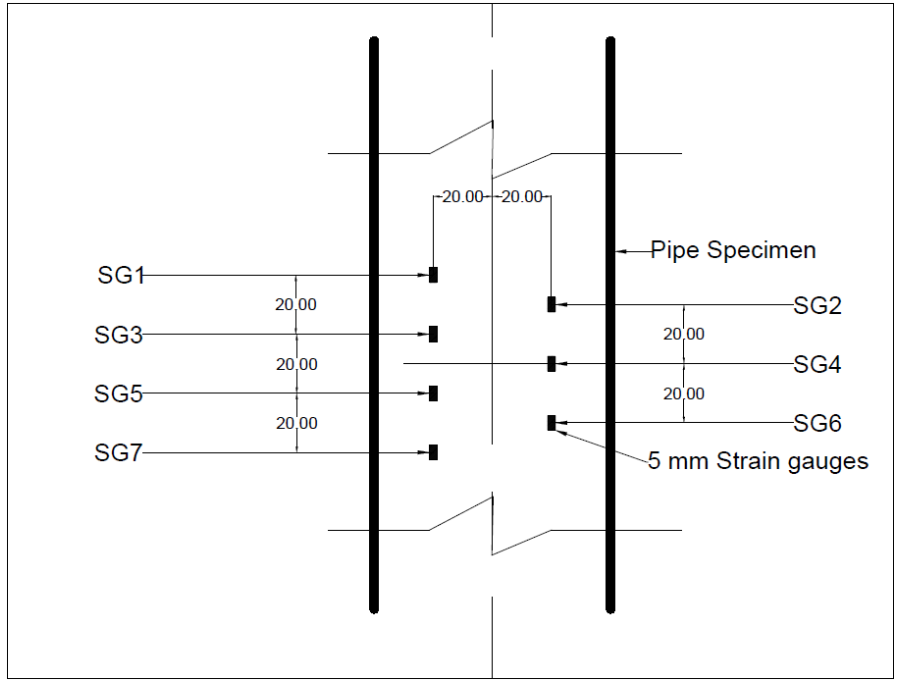


Figure 3.8: Schematics of Strain Gauge Configuration



Figure 3.9: Sprague Air-driven Hydrostatic Pressure Pump



Figure 3.10: Picture of a Steel Collar



Figure 3.11: Wrinkle Profile Measurement using Contour Gauge

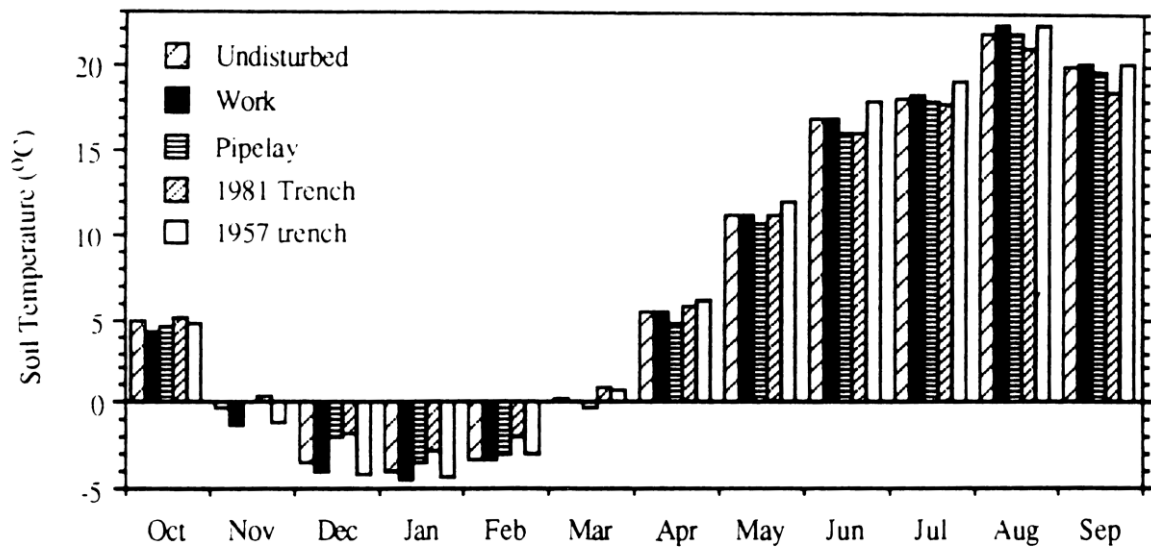


Figure 3.12: Mean Monthly Soil Temperature at 0.3 m Depth at Different Locations Around Pipelines Located in Southern Alberta (Naeth et al., 1993)

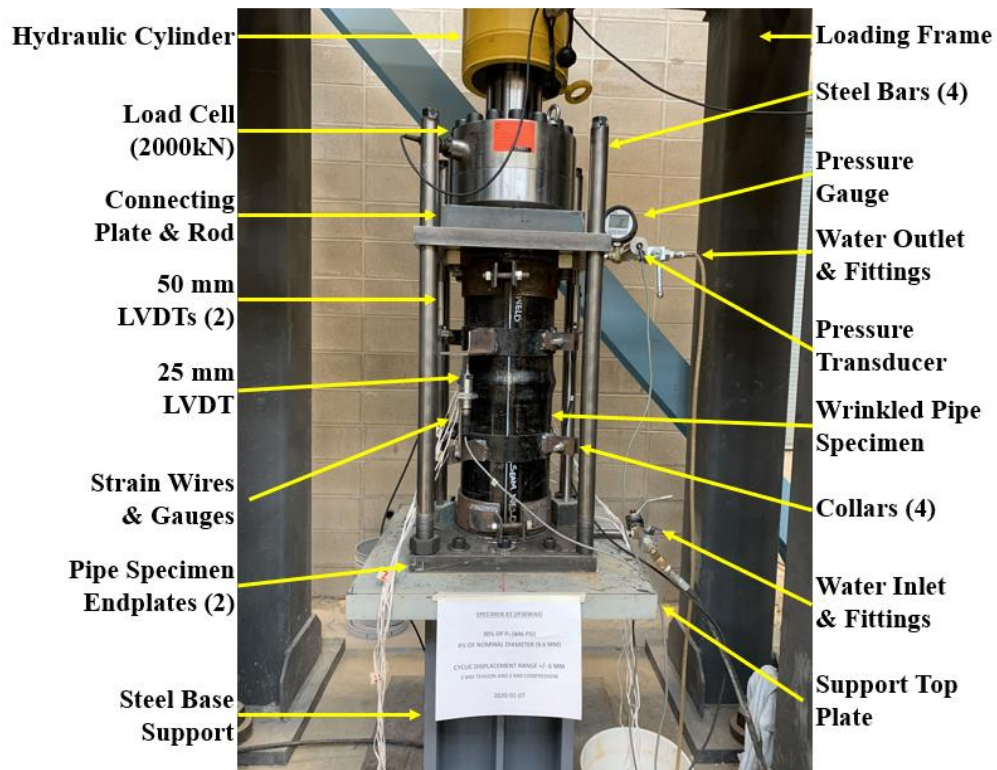


Figure 3.13: Test Setup for Axial Cyclic Loading Stage

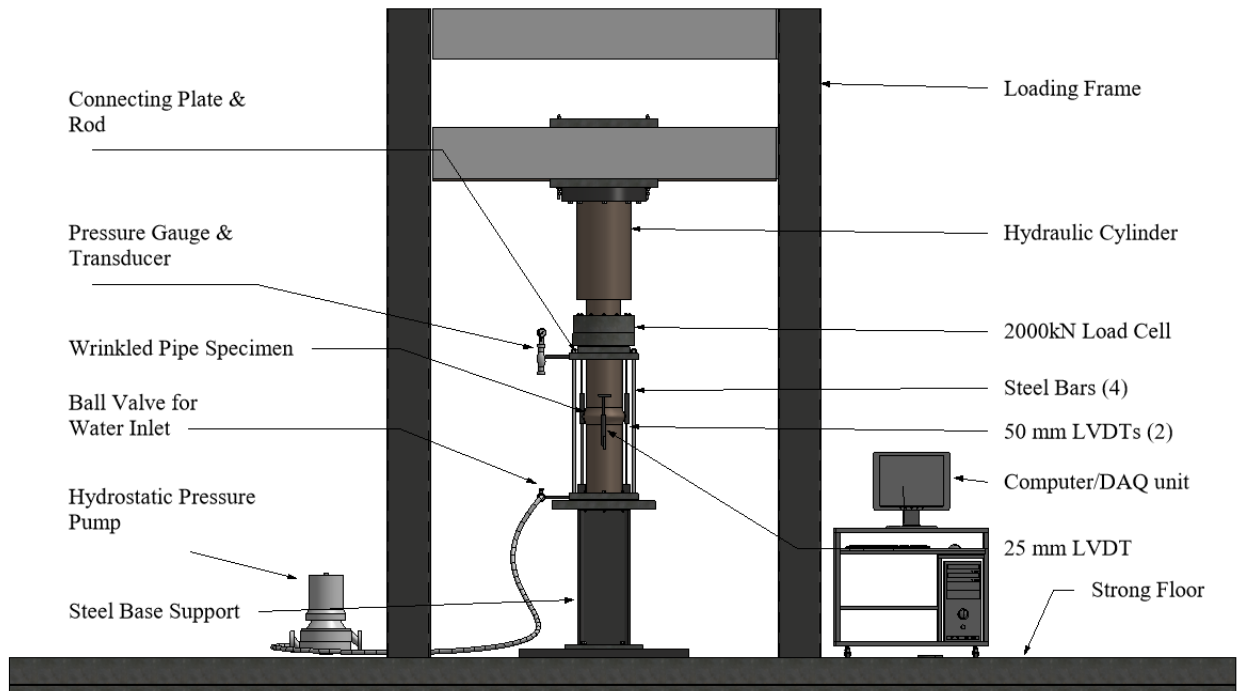


Figure 3.14: Schematics of Test Setup for Axial Cyclic Test

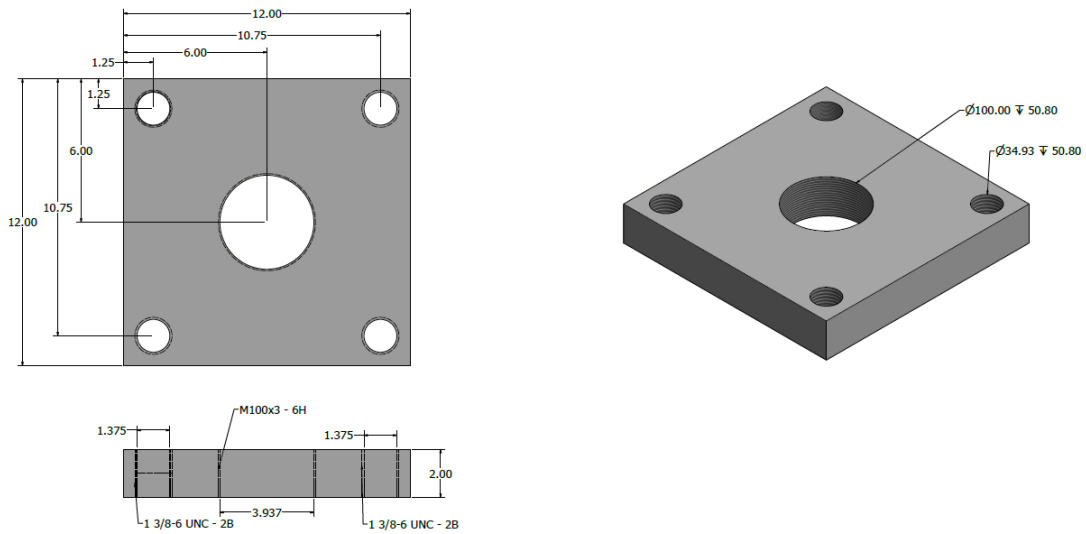


Figure 3.15(a): Load Cell – Pipe Specimen Connecting-Plate

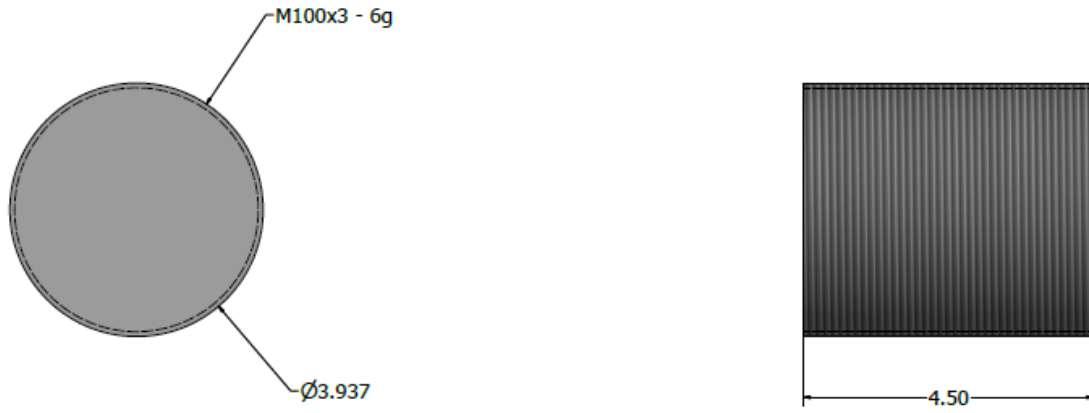


Figure 3.15(b): Load Cell – Connecting Plate Connecting Rod



Figure 3.16a: Strain Gauge Configuration on Wrinkled Pipe.

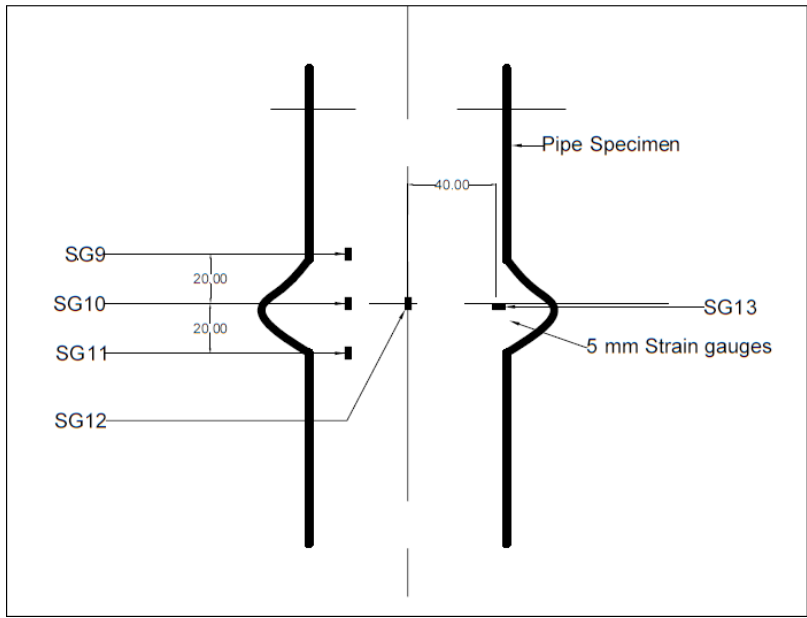


Figure 3.16b: Schematics of Strain Gauge Configuration for Wrinkled Pipe

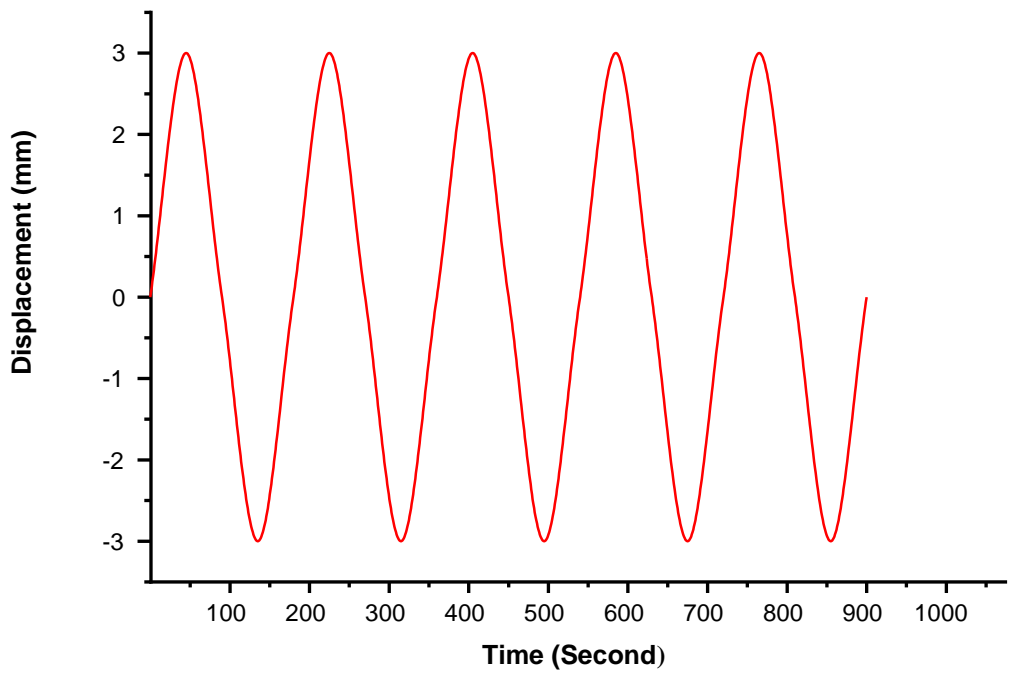


Figure 3.17: Axial Cyclic Test Amplitude Data for Five Cycles



Figure 3.18: Six Pipe Coupon Specimens

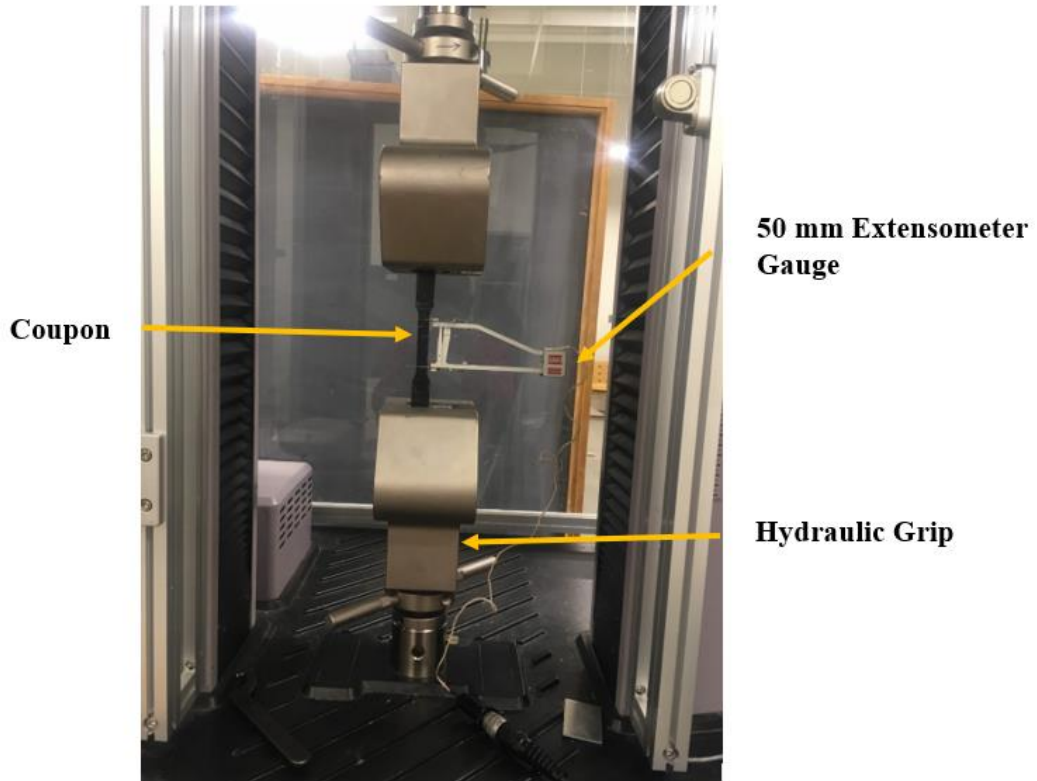


Figure 3.19: Coupon Specimen under MTS Universal Testing Machine

CHAPTER 4

EXPERIMENTAL RESULTS AND DISCUSSION

4.1 General

The purpose of this chapter is to present the results obtained from the experimental program, as discussed in chapter 3. This chapter discusses in detail the global and local deformation behaviour of the pipe specimens tested in phases 1 and 2. Additionally, it describes the material properties obtained from material tests carried out on the coupon specimens. The global observation covers the behaviour of the pipe specimen within the longitudinal range of the specimen top plate and bottom plate. The observation at the wrinkled region (wrinkle feet and crest) is referred to as the local behaviour. The specimens are mentioned according to the designation given in section 3.2.5 (Table 3.2).

4.2 Phase 1 – Initiation of Wrinkle Defect

The results obtained from the loading sequence employed in the initiation of wrinkle defect are presented in a graphical form. Figure 4.1 represent the plot of monotonically increasing applied load against the global deformational behaviour. The global deformational response denoted by (Δ) is defined as the vertical longitudinal displacement of the specimen top plate with respect to the bottom plate, and hence, this is the axial deformation of the entire pipe specimen. This was measured by taking the average of the two LVDTs (Linear Variable Differential Transformers) with a total stroke (displacement range) of 50 mm (see Figure 3.5 where it is shown as 50 mm LVDTs), which was placed between the two end plates of the pipe specimen. The critical points on the load-displacement curve, such as the yield load, ultimate load and maximum displacement are denoted as Y, U and F, respectively. The symbols $F_{10.5}$, F_8 , F_6 , and F_4 etc. refer to maximum displacement of specimens IP30WA10.5, IP30WA8, IP30WA6, and IP30WA4 respectively. The applied load and displacement at the yield (Y) are denoted as P_y and Δ_y , respectively. Similarly, the applied load and displacement at maximum load are denoted as P_u and Δ_u , respectively. It should be noted that the sign convention for the load-displacement behaviour are consistent, where a positive displacement indicates compressive loading and shortening of the specimen. There is also a graphical representation of the local strain behaviour (see Figure 4.2, 4.3, 4.6 and 4.7) of the pipe specimen around the wrinkle region (wrinkle crest and feet), that is used to describe the localization of strain with respect to loading sequence.

4.2.1 Discussion on Behaviour of Group 1 Specimens

4.2.1.1 Load vs. Global Deformation Behaviour

The load vs. global displacement plots corresponding to four of the specimens tested in group 1 (IP30WA10.5, IP30WA8, IP30WA6, and IP30WA4), as measured from the loadcell and 50 mm LVDT are presented in Figure 4.1. The average of the two LVDTs (50mm LVDTs) used to measure the shortening of the pipe specimen as shown in Figure 3.5 is used in the load-deformation plot. It can be observed that the load-deformation behaviour of all the four pipe specimens remained similar throughout the entire loading sequence. This can be due to the fact that there was no change in any test parameter that can affect the wrinkling of the specimens, such as; material properties, geometry ratio, forming process, weld alignment and internal pressure (Cunha et al., 2009; Das et al., 2007; Fatemi and Kenny, 2017; Nazemi et al. 2009) until the target wrinkle defect profile was achieved. All collars were removed as wrinkles became apparent and visible during the tests, except the collars near the welded endplates. For all tested specimens, the collars were removed at a longitudinal displacement of 7 mm to 8 mm after the wrinkle was clearly visible. This was done to remove the effect of stress concentration caused by nearby collars in the post-wrinkling region.

The onset of longitudinal yielding is indicated as Y in Figure 4.1, where the yield load was recorded as 629 kN, 630 kN, 630kN, and 632 kN for pipe specimens IP30WA10.5, IP30WA8, IP30WA6, and IP30WA4, respectively (see Table 4.1). The yield load was obtained using the offset method. A parallel line to the linear elastic portion of the load-deformation curve is drawn and offset 0.2% away from the origin. The values for the ultimate load capacity (U) for each of the pipe specimens are given in Table 4.1. This is the load at which pipe specimen can no longer resist the applied axial load if a load-controlled method is used, strain reversal at the crest of the wrinkle begins to occur, and wrinkle becomes visible. Pipe Specimen IP30WA6 included in the graph, has a graphical representation that slightly mismatches the remaining three curves for other three specimens. This was because of the experimental mismanagement that arose during pressurization. Due to mechanical fault, the hydraulic pump was not maintaining pressure in the specimen at targeted magnitude during the test, and as such targeted pressure magnitude was maintained by operating the pump manually. Furthermore, the increasing displacement controlled monotonic loading is continued until the longitudinal displacement (F). Point F refers to the loading stage required for the target wrinkle profile (see Table 4.1).

4.2.1.2 Load vs. Local Strain Behaviour

As measured from the electrical resistance strain gauges (5 mm gauge length) placed in the longitudinal direction of the pipe as shown in Figure 3.8 is discussed next. Figure 4.2 shows the longitudinal local strain behaviour in the outside face of the wrinkle region (near the wrinkle crest and feet) for specimen IP30WA10.5. It is observed that when an increasing axi-symmetric axial compressive load was applied on the specimen, compressive longitudinal strains were generated in the critical area. The compressive longitudinal strains are plotted in the positive axis of the plot. The wrinkle starts to form at maximum compressive longitudinal strain of 1.87% at the wrinkle crest. The axial compressive loading was continued in both strain gauges (SG4 and SG5 in Figure 3.8) until the target wrinkle was achieved. However, a strain reversal initiated near the wrinkle crest (SG4) and thus, the strain value moved in the opposite direction and finally the strain value became tensile. However, compressive strain increased near the wrinkle feet (SG5 in Figure 3.8) until the target wrinkle was achieved and loading process in phase 1 stopped. The mechanism of strain reversal near the wrinkle crest and increasing compressive strain near the wrinkle foot is similar for all pipe specimens tested.

Figure 4.3 shows the relationship between the load and local longitudinal strain behaviour for specimens IP30WA10.5, IP30WA8, IP30WA6, and IP30WA4 near the crest of the wrinkle. The maximum compressive strain values captured for all Group 1 pipe specimens tested are highlighted in Table 4.2. However, the several strain gauges stopped working when the test was being continued and hence, the critical strain values shown in the table may not be absolute maximum values. Additionally, strain gauge for each specimen was not located in the foot. The graphical plots to show the comparison between local strain behaviour near the crest and foot of the wrinkle for all specimens is given in Appendix A.

4.2.1.3 Discussion on Wrinkle Defect

The specimens were tested according to the defined test matrix (see Table 3.2). Each specimen was pressurized at $0.3p_y$ before applying monotonically increasing axial compressive load using a displacement control method up until the target wrinkle was achieved. It can be observed from Figure 4.4 that the wrinkle formed around six-thirteenths ($6/13$ or 305 mm) of the total pipe length (660 mm), this was due to the position of the collars initiating an imperfection around this region. The distinguishing characteristic amongst these specimens is the wrinkle amplitude (h), which

ranges from severe wrinkle for specimen IP30WA10.5 with wrinkle amplitude 22.5 mm, to large wrinkle for specimen IP30WA8 with wrinkle amplitude 17.5 mm, followed by a moderate wrinkle for specimen IP30WA6 with wrinkle amplitude 12.5 mm, and the smallest wrinkle for specimen IP30WA4 with wrinkle amplitude 8.5 mm. Details of the wrinkle defect profile measurement log is shown in Appendix B.

4.2.2 Discussion on Behaviour of Group 2 Specimens

4.2.2.1 Load vs. Global Deformation Behaviour

Similarly, the load vs. global displacement plots corresponding to four of the Group 2 specimens tested (IP60WA10.5, IP60WA8, IP60WA6, and IP60WA4), as measured from the load cell and LVDTs, are presented in Figure 4.5. The average of the two LVDTs (50 mm LVDTs) was used to measure the shortening of the pipe specimen in Figure 3.5 is used in the load-deformation plot. It can be observed that the load-deformation behaviours of the pipe specimens remained similar throughout the loading sequence. This is due to the fact that there was no change in the test parameters that may affect the wrinkling of the specimens, such as; material properties, geometry ratio, forming process, weld alignment and internal pressure (Cunha et al., 2009; Das et al., 2007; Fatemi and Kenny, 2017; Nazemi et al. 2009) until the target wrinkle profile was achieved. All collars were removed as wrinkles became apparent during the tests, except the collars near the welded end plates. For all tested specimens, the collars were removed at a longitudinal displacement of 7 mm to 8 mm when the wrinkle was visible. This was done, to avoid the effect of the stress concentration on the wrinkling behaviour.

The onset of longitudinal yielding is indicated as Y in Figure 4.5, where the yield load is 687 kN, 712 kN, 677 kN, and 685 kN for pipe specimens IP60WA10.5, IP60WA8, IP60WA6, and IP60WA4, respectively (see Table 4.3). The yield load was obtained using the offset method. A parallel line to the linear elastic portion of the load-deformation curve is drawn and offset 0.2% away from the origin. The values for the ultimate load capacity (U) for each pipe specimens are also presented in Table 4.3. This is the load at which pipe specimen can no longer resist load-controlled increasing axial load, strain reversal at the crest of the wrinkle begins to occur, and wrinkle becomes visible. Furthermore, the increasing displacement-controlled monotonic loading was continued until the longitudinal displacement (F) which represents the displacement when the target wrinkle profile was achieved (see Table 4.3).

4.2.1.2 Load vs. Local Strain Behaviour

As measured from the electrical resistance strain gauges placed in the longitudinal direction (see Figure 3.8) of the pipe, Figure 4.6 shows the longitudinal local strain behaviour in the wrinkle region (near the wrinkle crest, SG5 and feet SG3) for specimen IP60WA8. It was observed that when an increasing axi-symmetric axial compressive load was applied on the specimen, compressive longitudinal strains were generated in the critical area. The compressive longitudinal strains are plotted in the positive axis of the graph. The wrinkle starts to form at maximum compressive longitudinal strain of 2.36% at the wrinkle crest. The axial compressive loading was continued until the target wrinkle is achieved. A strain reversal initiated near the wrinkle crest in the opposite direction, to produce a longitudinal tensile strain for the specimen. The extent of the tensile strain is not depicted in its entirety in Figure 4.6, because strain gauges stopped working during the test. However, compressive strain increased near the wrinkle feet until the target wrinkle was achieved. The mechanism of strain reversal near the wrinkle crest and increasing compressive strain near the wrinkle foot is similar for all pipe specimens tested.

Figure 4.7 shows the relationship between the load and local longitudinal strain behaviour for specimens IP60WA10.5, IP60WA8, IP60WA6, and IP60WA4 near the crest of the wrinkle. The maximum compressive strain values captured for all Group 2 pipe specimens tested are highlighted in Table 4.4. However, the strain gauges may have stopped working and critical strain values may have not been captured in some cases.

4.2.2.3 Discussion on Wrinkle Defect

The specimens were tested according to the defined test matrix (see Table 3.2). Each specimen was pressurized to an internal pressure of $0.6p_y$ before applying monotonically increasing axial compressive load up until the target wrinkle was achieved. It can be observed from Figure 4.8 that the wrinkle was similarly located around six-thirteenths ($6/13$ or 305 mm) of the total pipe length (660 mm), this was due to the position of the collars initiating an imperfection around this region. The distinguishing characteristic amongst these specimens is the wrinkle amplitude (h), which ranges from severe wrinkle for specimen IP60WA10.5 with wrinkle amplitude 22.5 mm (10.5%), to large wrinkle for specimen IP60WA8 with wrinkle amplitude 17.5 mm (8%), followed by a moderate wrinkle for specimen IP60WA6 with wrinkle amplitude 13 mm (6%), and the smallest

wrinkle for specimen IP60WA4 with wrinkle amplitude 8.7 mm (4%). Details of the wrinkle defect profile measurement log is shown in Appendix B.

4.3 Phase 2 – Axial Cyclic Loading

The results obtained from the loading sequence involved a displacement-controlled axial cyclic loading of a pressurised wrinkled pipe, are discussed in this section. Specifically, this section will discuss the number of cycles applied to each wrinkled pipe specimen to cause failure. Failure in this study refers to the occurrence of leak or rupture in the pipe specimen wall leading to the loss of containment. Furthermore, this section will discuss the effect of load-displacement hysteresis on the behaviour of the wrinkled specimen. The effect of the local strain hysteresis will also be highlighted with relevant figures, to adequately represent the behaviour of the wrinkled region.

4.3.1 Discussion on Behaviour of Group 1 Specimens

4.3.1.1 Cycles to Failure

This subsection discusses loading procedure involved in the axial cyclic loading of the wrinkled pipe specimen. A displacement controlled axial cyclic load was applied on the wrinkled pipe specimen. The total displacement applied to each wrinkled pipe specimen was 6 mm (displacement range of ± 3 mm) as explained in Section 3.3.5. The wrinkled pipe specimens and their corresponding number of cycles to leak or rupture is given in Table 4.5.

The relationship between the number of cycles (N_f) to failure and the wrinkle amplitude ratio (h/D_o) is presented in Figure 4.9. This figure reveals that the relationship between the wrinkle amplitude ratio and number of cycles that lead to failure is proportional and the relationship is linear as shown in Equation 4.1.

$$h/D_o = 1.7179(N_f) + 20.812 \quad (4.1)$$

In this equation, h is the height of the wrinkle amplitude in mm, D_o is the outer diameter of the pipe specimen, and N_f is the number of cycles that causes the failure. This relationship indicates that it will take larger number of displacement cycles for a specimen with a larger wrinkle amplitude to fail by fracture or leak. A linear fitted curve is generated for the relationship between wrinkle amplitude ratio and cycles to failure. The explained variance in the relationship between the data and fitted regression line, usually referred to as coefficient of determination (R^2) is found to be 0.9664. Although R^2 is usually within the range of 0 to 1. A R^2 value that is closer to 1

generally indicate good fit. Hence, R^2 values obtained from this analysis suggests a dependency of wrinkle amplitude ratio on displacement controlled axial cycles applied on the wrinkled pipes. Based on this relationship, the number of cycles to failure for a corresponding wrinkle amplitude ratio observed can be generated, for ranges of parameters considered in this study. For example, at wrinkle amplitude ratio of 7%, the number of cycles to cause leak or rupture is predicted as 33 cycles.

A research was undertaken in the University of Windsor laboratory by Singh (2019). In this study, full-scale tests were carried out on API 5L X42 grade pipes with D/t 50, to study the effect of pressure cycle induced fatigue on wrinkled pipes. It was observed that the increase in the wrinkle amplitude led to a reduction in the fatigue life, hence, an inversely proportional relationship was found. This previous study shows that the behaviour of wrinkled pipelines to fatigue life, is highly dependent on the type of imposed cyclic loads, that is a load-controlled cycle as Singh used, or a displacement-controlled cycle which was used in the current study.

4.3.1.2 Load vs. Deformation Behaviour

The wrinkled pipe specimens were subjected to several strain reversals under constant displacement limits (± 3 mm) which has resulted in a load-displacement hysteresis curves for specimen IP30WA4 as shown in Figure 4.10. The load was measured through the loadcell attached to the loading actuator. The displacement data was acquired through the 25 mm LVDT as shown in Figures 3.13 and 3.14. Figure 4.10 shows only six load-displacement cycles for clarity. It can be observed that there exists a cycle-dependent softening with increasing number of cycles. This is as a result of the gradual decrease in the resistance of the wrinkled pipe specimen to plastic deformation, thereby reducing the load-carrying capacity of the wrinkled pipe. Therefore, the load required to enforce the displacement limits reduced with an increasing number of cycles. At the initial load-displacement cycle applied on the test, a maximum compressive and tensile axial force of 549 kN and 576 kN, respectively were required, which later reduced to 408kN and 356 kN respectively, in the last cycle that initiated failure. The maximum axial compressive and tensile force obtained from the tested specimens is shown in Table 4.6. This cyclic softening phenomenon, however, is identical for all cycled Group 1 specimens (see Appendix A).

4.3.1.3 Hysteresis Loop Energy

Subsequent loading and unloading of a wrinkled pipe specimen, will lead to rapid absorption of energy at the wrinkle crest. The area enclosed by the load-displacement hysteresis curve is known as the hysteresis loop energy (HLE). This is the concept that was introduced by Das et al (2007b) and subsequently used by others (Zhang 2010; Pournara et al. 2015). The HLE provides an indication of work done, or energy absorbed, per cycle.

Figure 4.11 shows the relationship between HLE and the number of cycles for all specimens in Group 1. It was observed that for specimen IP30WA4, there was a reduction in the HLE with the increase in the number of cycles. This insinuates that the wrinkled pipe specimen loses its energy-absorption capacity with increasing cycles and loses all of it when the wrinkled specimen is fractured. The rate of cyclic softening was rapid with the increasing number of cycles until it approached a stabilized hysteresis loop near half of the remaining life. Beyond the stabilized hysteresis loop, the wrinkled pipe specimen initiates apparent failure due to plastic straining at the tip of the wrinkle crest. This failure is apparent considering the slight slope observed towards the last few cycles, as compared with the steep slope in the first few cycles. This observation is identical for all specimens tested.

The sum of the HLE in all cycles that causes the failure for a wrinkled specimen, indicates the total HLE it took for a specimen to fracture. Figure 4.12 shows the graphical relationship between wrinkle amplitude ratio (h/D_o) and the total HLE for each wrinkled pipe specimen. The total HLE for each wrinkled pipe specimen is computed by cycle to cycle addition of the area enclosed by the load-displacement hysteresis curve. This figure reveals that the relationship between the wrinkle amplitude ratio (h/D_o) and the total HLE for each wrinkled pipe specimen is inversely proportional and the relationship is linear as shown in Equation 4.2.

$$S_{30} = -7340.3(h/D_o) + 118685 \quad (4.2)$$

In this equation, S_{30} is the total HLE required to fail Group 1 wrinkled pipe specimen. It was observed from the relationship that the total HLE for each specimen reduced with increase in the severity of the wrinkle profile. A linear fitted curve is generated, as done in subsection 4.3.1.1 above. The coefficient of determination (R^2) is equivalent to 0.914, which generally shows a good fit. This observation is in good agreement with other literature, that a very severe wrinkle has a lesser energy-absorption capability left in its post-wrinkling stage (Das et al. 2007b; Zhang 2010).

In these previous studies, displacement-controlled axial cyclic loads were applied on strip specimens cut from the pipe specimens, which neglected the effect of internal pressure. However, according to the current research at the University of Windsor, full-scale pipe specimens were tested under displacement-controlled loading, while maintaining internal pressure unchanged. This study shows that the displacement-controlled axial cyclic load will slower the rate of energy-absorption in a severe wrinkle, which increases the number of cycles to failure. Based on this relationship, the energy-absorption capacity for a corresponding wrinkle amplitude ratio observed, can be generated. For example, at wrinkle amplitude ratio of 7%, the total HLE is given as 67200 J.

4.3.1.4 Load vs. Local Strain Behaviour

Electrical resistance strain gauges were attached to the wrinkle crest and feet to determine the local strain response in the wrinkle region. Two strain gauges were attached on the wrinkle crest in the longitudinal direction (SG10 and SG12 in Figure 3.16b), another one was placed in the circumferential direction to measure hoop strain (SG13). Two more strain gauges were placed on the wrinkle feet (SG9 and SG11). As shown in Figure 4.13, a compressive axi-symmetric load applied to the wrinkled pipe specimen creates a corresponding tensile strain at the wrinkle crest in the longitudinal and hoop directions, while creating a compressive strain at the wrinkle feet. However, a tensile axi-symmetric load will create a corresponding compressive strain at the wrinkle crest in the longitudinal and hoop direction, while creating a tensile strain at the wrinkle feet.

Figures 4.14 (a) and (b) are the graphical representation of the local longitudinal strain behaviour at the wrinkle crest (obtained from SG10 in Figure 3.16) in the first few cycles for specimens IP30WA4 and IP30WA6, respectively. It can be observed that each loop in the hysteresis, moves in the tensile strain direction as cyclic deformation occur. This phenomenon is described as structural ratcheting, and in this study is usually accompanied by a reduction in the cyclic plastic strain (ratcheting strain) from cycle to cycle. Ratcheting is due to the asymmetric stress cycling that a structural component may experience, until the deterioration of performance or failure of the component occur. Basically, a structure under load reversals accumulates cyclic plastic strain progressively from cycle to cycle. Moreover, in this study, the hysteresis loops tended to a stable behaviour such that they approached symmetry about the mean strain, rather than the zero-strain

axis. Figure 4.15(a) is the graphical representation of the local longitudinal strain behaviour at wrinkle crest in the first few cycles for specimen IP30WA8. Figure 4.15(b) represents the local longitudinal strain behaviour at the wrinkle crest from cycle 12 to 16 for specimen IP30WA10.5. Ratcheting was also observed at the wrinkle crest in both these specimens in the compressive strain direction as cyclic deformation occur. The deformation was accompanied by reduction in the ratcheting strain. However, the local hoop strain behaviour at the wrinkle crest for specimen IP30WA4 (Figure 4.16) experiences ratcheting in the tensile strain direction as cyclic deformation occurs. A cyclic plastic strain reduction is experienced from cycle to cycle. This behaviour is similar for measurement observed at the circumferential strain for all Group 1 specimens tested (see Appendix A).

Figure 4.17 shows the graphical representation of the local longitudinal strain behaviour at the wrinkle feet in the first few cycles for specimen IP30WA4. It is also observed here that each loop in the hysteresis moves in the tensile strain direction as cyclic deformation occur. The ratcheting is as well accompanied by a reduction in the cyclic plastic strain from cycle to cycle. This phenomenon was observed for all longitudinal strain measurement at the wrinkle feet of all Group 1 specimens (Appendix A).

4.3.1.5 Failure Patterns and Visual Observations

During the tests and on completion of the tests, visual observations were made in relation to the structural behaviour of the wrinkled pipe specimens. Some of these observations were as a result of the boundary conditions created for the test or loading sequence undertaken during the test. Some structural observations that was gathered from wrinkled field pipelines can be explained using the data collected from this study.

It was observed from longitudinal strain data collected from the wrinkle crest of specimens IP30WA4 and IP30WA6 (Figures 4.14 (a) and (b)), that each loop in the hysteresis moves in the tensile strain direction as structural ratcheting occur. However, for more severe wrinkle defects as can be found in specimens IP30WA8 and IP30WA10.5 (Figure 4.15 (a) and (b)), each loop in the hysteresis moves in the compressive strain direction as ratcheting occur. This implies that for small wrinkles pressurized at low internal pressure ($0.3p_y$), the wrinkle crest-cross section bent towards the extrados (external face) of the pipe during unidirectional progressive accumulation of ratcheting strain. However, the wrinkle crest-cross section shrunk towards the intrados (interior

face) of the pipe when the severely wrinkled pipes underwent structural ratcheting. The latter observed phenomenon, may lead to a visible crease or folding at the exterior face of the wrinkle crest when a severely wrinkled pipeline is subjected to load reversals, as observed in this test in Figure 4.18. To corroborate this statement, similar observation was made by Das et al. 2007a (Figure 4.18b) for laboratory tests conducted using extreme load-controlled cyclic loads.

Figure 4.19 shows the photograph of circumferential fracture as observed in Specimen IP30WA8. This failure mode is the typical fracture mode in this study, which is prevalent for all tested specimens of Group 1. See Appendix C for the failure mode of Group 1 Specimens. The presence of a circumferentially oriented fracture suggests dominance of localized longitudinal stress concentration. This can be supported with the theory in fatigue analysis that fracture surfaces are flat and perpendicular to the predominant maximum principal stress axis. However, due to the absence of any physical indications of damage on the exterior face (extrados) of the wrinkled pipe wall during the test, it can be inferred that the fatigue crack initiated from the inside surface (intrados) of the wrinkle defects and propagated outwards till complete failure.

Precisely, the mechanism of fatigue failure occurs in three stages; stage 1 is the initiation or nucleation of crack, stage 2 is the propagation of the cracks and stage 3 is the fracture. It is presumed that the stress risers develop as result of dislocation of metallic crystals at the region of stress concentration to form several micro-cracks, in this case was in the intrados of the wrinkle crest. In the second stage, the micro-cracks get bigger or overlap to form macro-cracks. These macro-cracks then propagate in a plane normal to the maximum principal stress axis. The maximum principal stresses in this case, are inferred to occur at the longitudinal axis of the wrinkle crest. Eventually, due to continuous cyclic load reversals, the macro-cracks dominate the material and the cross-section of the pipe wall is reduced. The reduction of the cross-section of the pipe wall led to a corresponding decrease in the load carrying capacity of the wrinkled pipe specimen, which to led to apparent brittle fracture at the tip of the wrinkle crest.

4.3.2 Discussion on Behaviour of Group 2 Specimens

4.3.2.1 Cycles to Failure

Similar to the observation made for Group 1 specimens, the relationship between the wrinkle amplitude ratio (h/D_o) and number of cycles that lead to failure (N_f) of Group 2 specimens is

proportional (see Figure 4.20). The test data can be fitted linear relationship which is represented by Equation 4.3.

$$h/D_o = 3.0448(N_f) + 7.1473 \quad (4.3)$$

This relationship indicates that it will take larger number of displacement cycles for a specimen with a larger wrinkle amplitude to fail by a fracture or a leak at the wrinkle crest. The coefficient of determination (R^2) for linear relationship is found to be equivalent to 0.9999. Hence, R^2 values obtained from this analysis also suggests a dependency of wrinkle amplitude ratio on the displacement controlled axial cycles applied on the wrinkled pipes. Based on this relationship, the number of cycles to failure for a corresponding wrinkle amplitude ratio observed can be generated, for ranges of parameters considered for Group 2 specimens. For example, at wrinkle amplitude ratio of 8%, the number of cycles to cause leak or rupture is given as 31 cycles.

The relationship between wrinkle amplitude (h/D_o) ratio and number of cycles to failure (N_f) for both Group 1 and Group 2 is plotted in Figure 4.21. This relationship establishes that wrinkle defects that are developed under lower internal pressure takes longer displacement-controlled load cycles before a leak or a fracture occurs, hence, less vulnerable to failure. However, the study carried out by Navjot (2019), suggested that wrinkle defects that are developed under lower internal pressure, when subjected to pressure cyclic induced fatigue, are more vulnerable to fracture or leak. This shows the dependency of the fatigue life of buried pipelines on field operating pressure and type of cyclic loading, that is load-controlled cyclic load and displacement-controlled cyclic load.

4.3.2.2 Load vs. Deformation Behaviour

Figure 4.22 is a graphical representation of the cycle by cycle load-deformation relationship, taken at 5-cycle intervals for specimen IP60WA4. It can be observed that there exists a cycle-dependent softening with increasing number of cycles. This is as a result of the gradual decrease in the resistance of the wrinkled pipe specimen to plastic deformation, thereby reducing the load-carrying capacity of the wrinkled pipe. Therefore, the load range (i.e. maximum to minimum load) required to enforce the displacement limits reduce with an increasing number of cycles. At the very first load-displacement hysteresis curve, a maximum compressive and tensile axial force of 701 kN and 702 kN respectively were imposed, which later reduced to 585 kN and 476 kN respectively, in the

last cycle that caused the failure. The maximum axial compressive and tensile force obtained from the tested specimens is shown in Table 4.6.

4.3.2.3 Hysteresis Loop Energy

Figure 4.23 shows the graphical relationship between HLE and the number of cycles for all Group 2 specimens. It was observed that for specimen IP60WA4, there is a reduction in HLE with an increase in the number of cycles. Similarly, this insinuates that the wrinkled pipe specimen loses its energy-absorption capacity with increasing cycles and loses all of it when the wrinkled specimen is fractured. This failure is apparent considering the slight slope observed towards the last few cycles, as compared with the steep slope in the first few cycles. However, this observation is specific to only specimen IP60WA4, IP60WA6 and IP60WA8. Specimen IP60WA10.5 exhibits a rather different behaviour, as there is a slight increase in HLE with the increase in the number of cycles, after the steep decrease noticed in the first five cycles. This is contrary to the behaviour of all Group 1 specimens and Group 2 specimens with small wrinkle defect, but apparent for highly pressurised pipes with severe wrinkle defect.

The sum of the HLE in all cycles that initiates failure for a wrinkled specimen, indicates the total HLE it took for a specimen to fracture. Figure 4.24 shows the graphical relationship between wrinkle amplitude ratio (h/D_o) and the total HLE for each wrinkled pipe specimen. This figure reveals that the relationship between the wrinkle amplitude ratio and the total HLE for each wrinkled pipe specimen is inversely proportional. A linear fitted relationship can be represented by Equation 4.4.

$$S_{60} = -2101.4(h/D_o) + 97733 \quad (4.4)$$

In this equation, S_{60} is the total HLE required to fail a Group 2 wrinkled pipe specimen. It was observed from the relationship that the total HLE for each specimen reduced with increase in the severity of the wrinkle profile. The coefficient of determination (R^2) of linear curve is 0.955, which generally shows a good fit. It was observed that the total HLE for each specimen reduced with increase in the severity of the wrinkle profile. This observation is in good agreement with other literature, that a very severe wrinkle has a lesser energy-absorption capability left in its post-wrinkling stage (Das et al. 2007b; Zhang 2010). However, this study shows that the displacement-controlled axial cyclic load will slower the rate of energy-absorption in a severe wrinkle, which increases the number of cycles to failure. Based on this relationship, the energy-absorption

capacity for a corresponding wrinkle amplitude ratio observed, can be generated. For example, at wrinkle amplitude ratio of 7%, the total HLE is given as 83200 J.

4.3.2.4 Load vs. Local Strain Behaviour

Similar to Group 1 specimens, electrical resistance strain gauges were attached to the wrinkle defect of specimen of Group 2. A displacement-controlled compressive axi-symmetric load creates a corresponding tensile strain on the extrados of the wrinkle crest in the longitudinal and hoop direction, while creating a compressive strain at the wrinkle feet. However, a tensile axi-symmetric load applied to the wrinkled pipe specimen creates a corresponding compressive strain at the wrinkle crest both in the longitudinal and hoop direction, while creating a tensile strain at the wrinkle feet (see Figure 4.13).

Figure 4.25 is the graphical representation of the local longitudinal strain behaviour at the wrinkle crest (obtained from SG12 in Figure 3.16b) in the first few cycles for specimen IP60WA4. It was observed that each loop in the hysteresis, moves in the tensile strain direction as cyclic deformation occur. This phenomenon is described as structural ratcheting, and in this study is usually accompanied by a reduction in the cyclic plastic strain from cycle to cycle. Figure 4.26(a), (b) and (c) is the graphical representation of the local longitudinal strain behaviour at wrinkle crest in the first few cycles for specimens IP60WA6, IP60WA8 and IP60WA10.5 respectively. Ratcheting was also observed at the wrinkle crest in these specimens in the compressive strain direction as cyclic deformation occur. The deformation was accompanied by reduction in the ratcheting strain. However, the local hoop strain behaviour at the wrinkle crest for specimen IP60WA4 (Figure 4.27) experiences ratcheting in the tensile strain direction as cyclic deformation occurs. A ratcheting strain reduction is experienced from cycle to cycle. This behaviour is similar for measurements observed at the circumferential strain for all Group 2 wrinkled pipe specimens (see Appendix A).

Figure 4.28 shows the graphical representation of the local longitudinal strain behaviour at the wrinkle feet in the first few cycles for specimen IP60WA4. It was also observed here that each loop in the hysteresis moves in the tensile strain direction as cyclic deformation occur. The structural ratcheting is as well accompanied by a reduction in the cyclic plastic strain from cycle to cycle. This phenomenon was observed for all longitudinal strain measurement at the wrinkle feet of all Group 2 wrinkled pipe specimens tested (see Appendix A).

4.3.2.5 Failure Patterns and Visual Observations

Completing the cyclic loading on Group 2 specimens, has shown that each loop in the hysteresis moves in the tensile strain direction as structural ratcheting occur, when longitudinal strain data are collected from the wrinkle crest of specimen IP60WA4 (Figures 4.25). However, for moderate to severe wrinkle defects, each loop in the hysteresis moves in the compressive strain direction as ratcheting occur (see Figure 4.26 (a), (b) and (c)). This implies that for very small wrinkle defects pressurized at a high internal pressure ($0.6p_y$), the wrinkle crest-cross section bent towards the extrados of the pipe during unidirectional progressive accumulation of ratcheting strain. However, the wrinkle crest-cross section shrunk towards the intrados (interior part) of the pipe when the severely wrinkled pipes underwent structural ratcheting. This may lead to a flat appearance as a result of folding, at the exterior face of the wrinkle crest when a severely wrinkled pipeline is subjected to several load reversals, as observed in this test in Figure 4.29.

Figure 4.30 shows the photograph of longitudinal fracture along the pipe seam weld, as it was observed for group 2 specimens IP60WA4, IP60WA6 and IP60WA8, after axial cyclic loading. However, specimen IP60WA10.5 fractured circumferentially along the pipe seam weld (see Appendix C).

4.4 Material Tests

Six tensile coupon tests were conducted according to ASTM E8/E8M-13a (as mentioned in section 3.4), to determine the mechanical properties of pipe materials used for the experimental program in this study. The data from the tensile coupon tests were analyzed to produce “engineering or nominal stress-strain” curves. These engineering stress-strain relationships assume that the cross-sectional area at the gauge length of the coupon, remained unchanged during the deformation of the coupon. The results obtained from the tension coupon test are generally expressed in the form of engineering stress-strain curves, as they provide a straight-forward approach to obtaining material properties: including but not limited to the Young’s Modulus (E), yield strength (σ_y), ultimate tensile strength (σ_{uts}), maximum elongation and reduction in cross-sectional area. Figure 4.31 shows the engineering stress-strain curve for all 6 coupons tested. It was observed that the results from the coupon tests agree with each other and hence, coupon 6 was selected as the subject of the subsequent analysis. The yield strength is defined as the stress at which the material begins to deform plastically. The yield strength was obtained using the offset method. A parallel line to

the linear elastic portion of the stress-strain curve is drawn and offset 0.2% (in this study) away from the origin. The stress at the point where the parallel line intersects the stress-strain curve is taken as the yield strength, which is 288 MPa. The young's modulus is described as the elastic stiffness of a solid material. Young's modulus is calculated by determining the slope of the initial linear elastic portion of the engineering stress-strain curve, which is given as 192 GPa. The ultimate tensile strength is defined as the maximum stress the material can withstand. This property is derived by normalising the maximum force applied to the specimen by the unchanged cross-sectional area of the coupon specimen gauge length. The fracture strength and strain are taken at the stress and strain the material fractures. The summary of the material properties obtained from the tension coupon test for coupon 6 is given in Table 4.7.

4.5 Summary

In summary, the following observations and conclusions can be made from the experimental results obtained from the experimental program:

1. There exists a strain reversal during the initiation of the wrinkle at the wrinkle crest, on applying monotonically increasing compressive displacement to the pipe specimen. However, the strain at the feet of the wrinkle increased monotonically as the compressive load increased monotonically.
2. Wrinkle defects developed while subjected to high internal pressure (Group 2 specimens) undergo a lower number of cycles, in comparison to wrinkle defects developed with a low internal pressure (Group 1 specimens). This suggests that buried pipelines with wrinkle defects that are operating at high pressure are more vulnerable to fatigue failure.
3. There exists a strong direct correlation between the wrinkle amplitude and the number of cycles to failure and this correlation was found both in Group 1 and 2 specimens. This indicates that an increase in the wrinkle defect amplitude leads to a longer fatigue life, if load cycles are applied using a displacement-controlled load cycle. However, in an earlier study performed by Singh (2019) on wrinkled pipes subjected to pressure cyclic loads, there was an increase in the fatigue life with decrease in the wrinkle defect amplitude.
4. The HLE reduced with increasing axial cyclic loading. This suggests that the wrinkled pipe specimen loses its energy-absorption capability with increasing cycles to failure. It was also observed that the total HLE for each wrinkled pipe specimen reduced with increase in

the severity of the wrinkle profile. This observation suggests that the most severe wrinkle defect has the least energy-absorption capability left in its post-wrinkling stage.

5. Results obtained from the longitudinal strain axis near the wrinkle crest for specimens tested at low internal pressure ($0.3p_y$), indicate that local strain hysteresis loop moves in the tensile strain direction for small wrinkle defects, as cyclic deformation occurs. However, the local strain hysteresis loop moves in the compressive strain direction for severe wrinkle defects. For specimens tested at higher internal pressure ($0.6p_y$), results obtained from the longitudinal strain axis near the wrinkle crest indicate that local strain hysteresis loop moves in the tensile strain direction for very small wrinkle defect. However, the local strain hysteresis loop moves in the compressive strain direction for moderate to severe wrinkle defects. The movement of the hysteresis in the compressive strain direction gives rise to the apparent folding or flat appearance at the wrinkle crest of a wrinkled pipe that has experienced cyclic loading as a result of temperature differential in the region of permafrost.
6. The localized longitudinal stress concentrations gave rise to the circumferentially oriented fatigue cracks in specimens tested at lower internal pressure ($0.3p_y$). However, the cracks apparent in specimens tested at higher internal pressure ($0.6p_y$), are longitudinally oriented because of hoop stress concentrations. Since there were no indications of physical damage on the exterior surface of the wrinkle defect, it was concluded that fracture failure occurs as a result of fatigue damage initiating from the interior surface of the wrinkle.
7. There is a movement of the load vs local strain hysteresis in the compressive strain direction for wrinkled pipe specimens that fail at higher number of cycles. This shows that wrinkled field pipelines that have an apparent crease or flat appearance at the wrinkle crest exterior, experienced high number of cycles before leak or rupture.

Table 4.1: Critical Loads and Displacements During Wrinkle Initiation Phase for Group 1 ($0.3p_y$) Specimens

Specimen ID	At Yield Load (Point Y)		At Ultimate Load (Point U)		At Maximum Displacement (Point F)	
	Δ_Y (mm)	P_Y (kN)	Δ_U (mm)	P_U (kN)	Δ_F (mm)	P_F (kN)
IP30WA10.5	1.1	629	3.5	762	31	322
IP30WA8	1.1	630	3.4	764	19	364
IP30WA6	1.1	630	4.2	766	13.1	460
IP30WA4	1.1	632	3.2	765	8.1	531

Table 4.2: Maximum Local Compressive Strain Values for Group 1 ($0.3p_y$) Specimens Under Monotonic Loading

Specimen ID	Load at Maximum Reversed Strain (kN)	Maximum Local Strain (%)	
		Compressive Strain at Crest (%)	Compressive Strain at Foot (%)
IP30WA10.5	757	1.87	4.58
IP30WA8	693	2.27	5.80 *
IP30WA6	737	2.48	4.54 *
IP30WA4	698	2.26	4.59

* critical strain values not captured till end of the test, because strain gauge stopped working. Strain values displayed are the last data from the working strain gauge

Table 4.3: Critical Loads and Displacements During Wrinkle Initiation Phase for Group 2 ($0.6p_y$) Specimens

Specimen ID	At Yield Load (Point Y)		At Ultimate Load (Point U)		At Maximum Displacement (Point F)	
	Δ_Y (mm)	P_Y (kN)	Δ_U (mm)	P_U (kN)	Δ_F (mm)	P_F (kN)
IP60WA10.5	1.3	687	4.9	822	30.8	471
IP60WA8	1.3	712	4.2	820	17.5	531
IP60WA6	1.3	677	4.7	825	12.2	588
IP60WA4	1.3	685	4.7	825	8.1	661

Table 4.4: Maximum Local Compressive Strain Values for Group 2 ($0.6p_y$) Specimens Under Monotonic Loading

Specimen ID	Load at Maximum Reversed Strain (kN)	Maximum Local Strain (%)	
		Compressive Strain at Crest (%)	Compressive Strain at Foot (%)
IP30WA10.5	774	1.33 *	7.4
IP30WA8	812	2.36	5.26
IP30WA6	789	0.62 *	3.3 *
IP30WA4	773	2.31	3.9

* critical strain values not captured till end of the test, because strain gauge stopped working. Strain values displayed are the last data from the working strain gauge

Table 4.5: Cyclic Test Results (Phase 2)

Specimen ID		Exact Wrinkle Amplitude to Diameter Ratio h/D_o (%)	Total Hysteresis Loop Energy (J)	No. of Cycles to Failure
Group 1	IP30WA10.5	10.45	43040	39
	IP30WA8	8.13	53063	34
	IP30WA6	5.81	84487	32
	IP30WA4	3.95	85832	27
Group 2	IP60WA10.5	10.5	76447	39
	IP60WA8	8.13	79037	32
	IP60WA6	6.04	86428	25
	IP60WA4	4.04	89381	19

Table 4.6: Maximum Compressive and Tensile Load at Initial and Final Cycle for All Specimens

Specimen ID		Cycle Count	Maximum Load (kN)	
			Maximum Compressive Load (kN)	Maximum Tensile Load (kN)
Group 1	IP30WA10.5	Initial Cycle	327	64
		Final Cycle	286	18
	IP30WA8	Initial Cycle	348	178
		Final Cycle	307	148
	IP30WA6	Initial Cycle	457	375
		Final Cycle	381	309
	IP30WA4	Initial Cycle	549	576
		Final Cycle	408	356
Group 2	IP60WA10.5	Initial Cycle	483	79
		Final Cycle	501	199
	IP60WA8	Initial Cycle	517	185
		Final Cycle	517	213
	IP60WA6	Initial Cycle	591	382
		Final Cycle	563	418
	IP60WA4	Initial Cycle	701	702
		Final Cycle	585	476

Table 4.7: Material Properties from Tension Test on Coupon 6

Property	Value
Modulus of Elasticity (E)	192 GPa
Yield Strength (offset = 0.2%, σ_y)	288 MPa
Ultimate Tensile strength (σ_{uts})	384 MPa
Strain @ Ultimate Tensile Strength (ϵ_{utsy})	20.6%
Fracture Stress (σ_f)	275MPa
Fracture Strain (ϵ_f)	37.1%
% of Elongation	26%

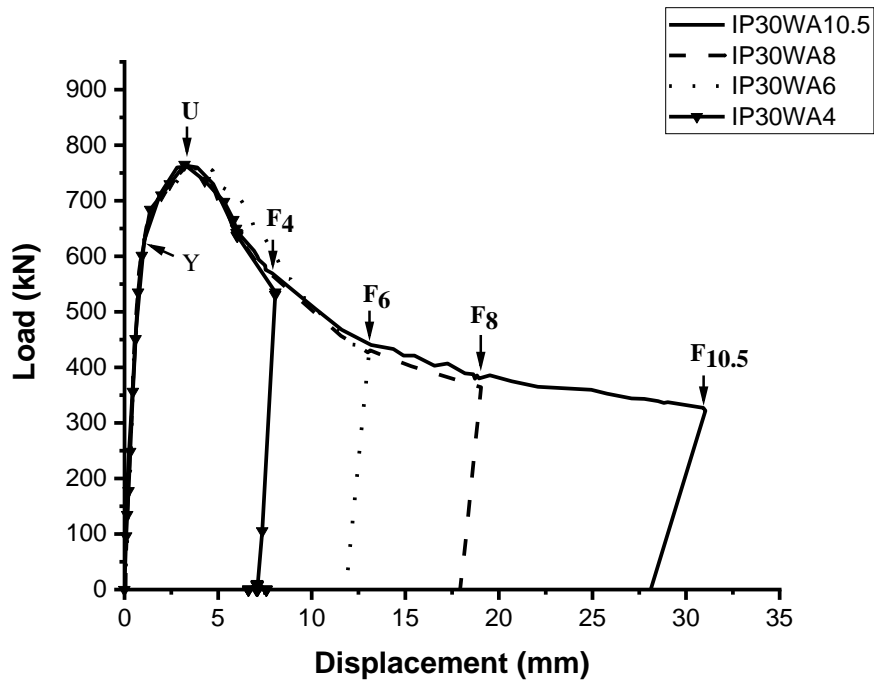


Figure 4.1: Load vs. Global Displacement Behaviour for Group 1 Specimens

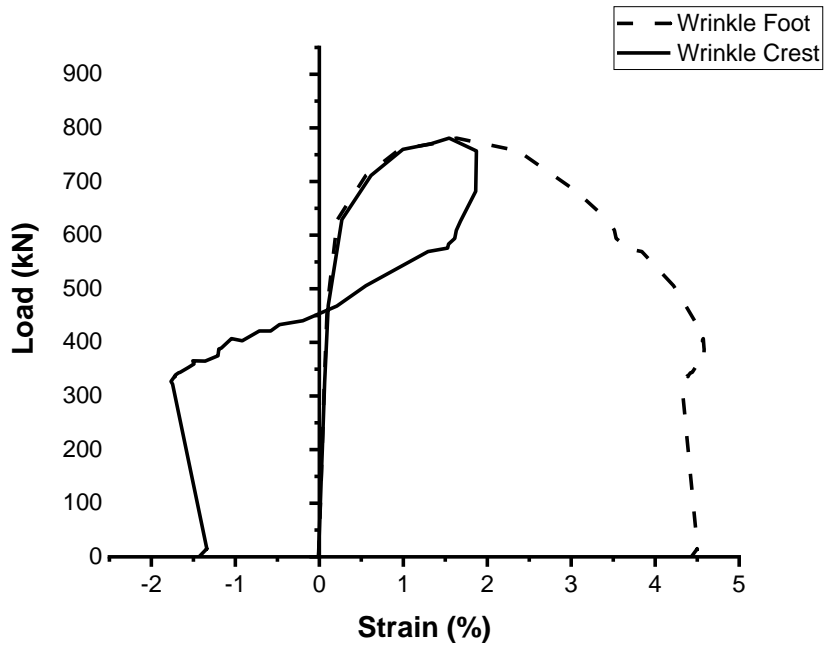


Figure 4.2: Load vs. Local Strain Behaviour for Specimen IP30WA10.5

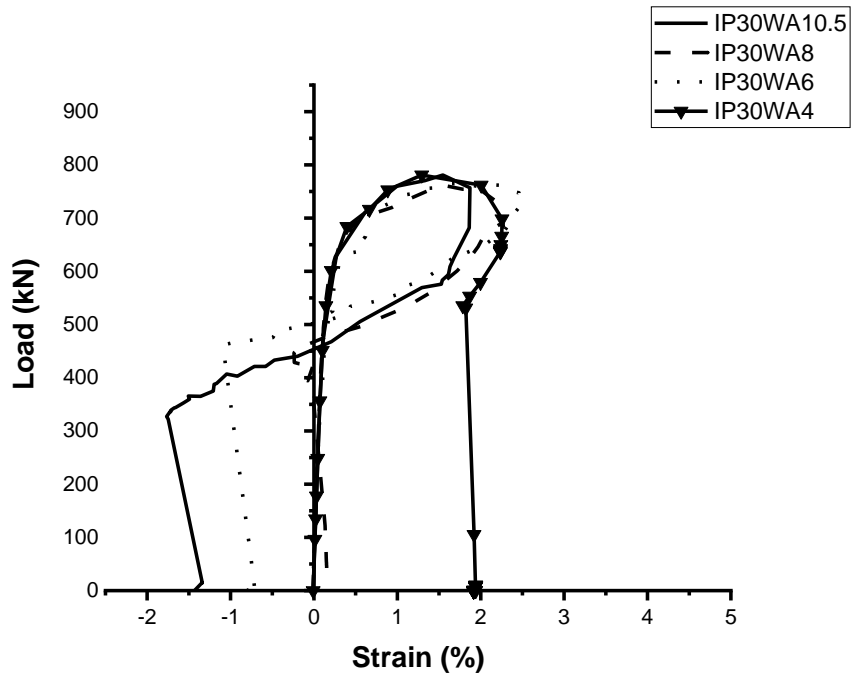


Figure 4.3: Load vs. Local Strain Behaviour for All Group 1 Specimens Near the Wrinkle Crest



Figure 4.4: Deformed Shape of Group 1 ($0.3p_y$) Specimens

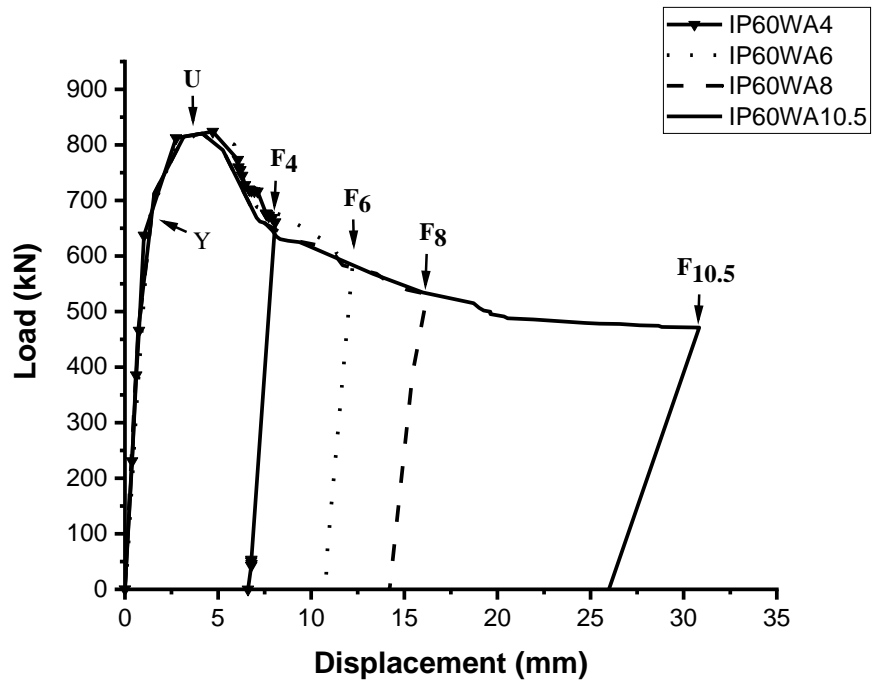


Figure 4.5: Load vs. Global Displacement Behaviour for Group 2 Specimens

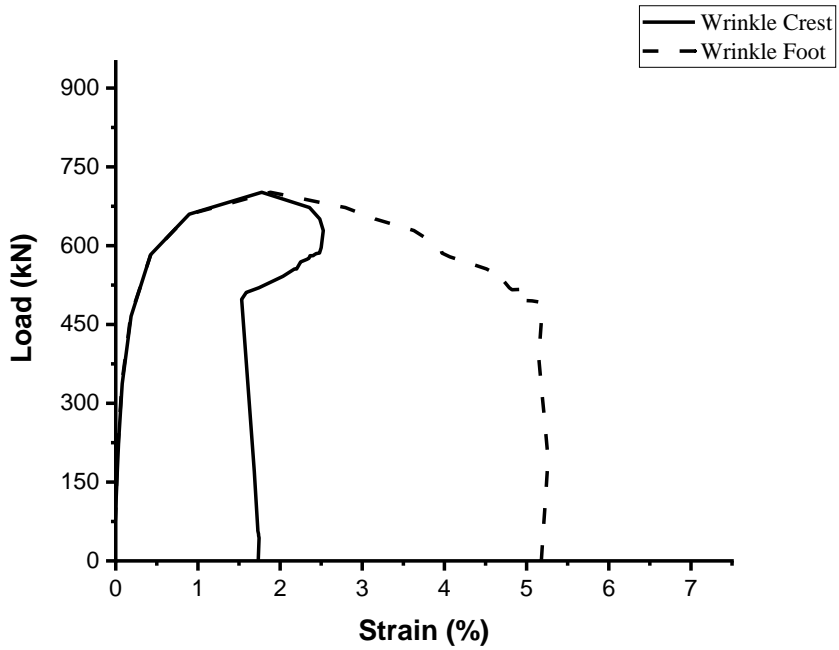


Figure 4.6: Load vs. Local Strain Behaviour for Specimen IP60WA8

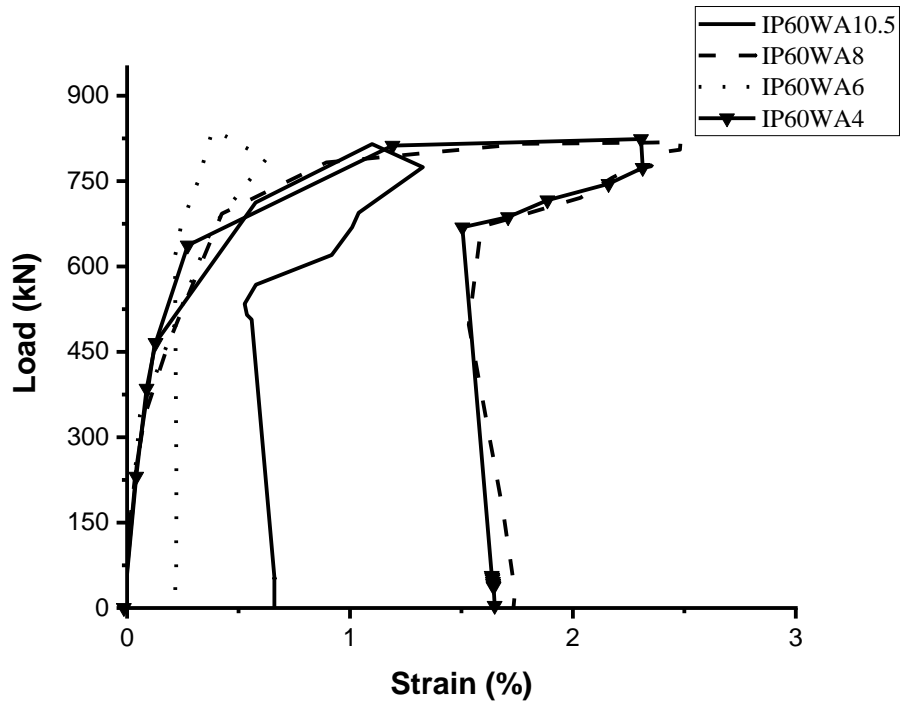


Figure 4.7: Load vs. Local Strain Behaviour for All Group 2 Specimens Near the Wrinkle Crest



Figure 4.8: Deformed Shape of Group 2 ($0.6p_y$) Specimens

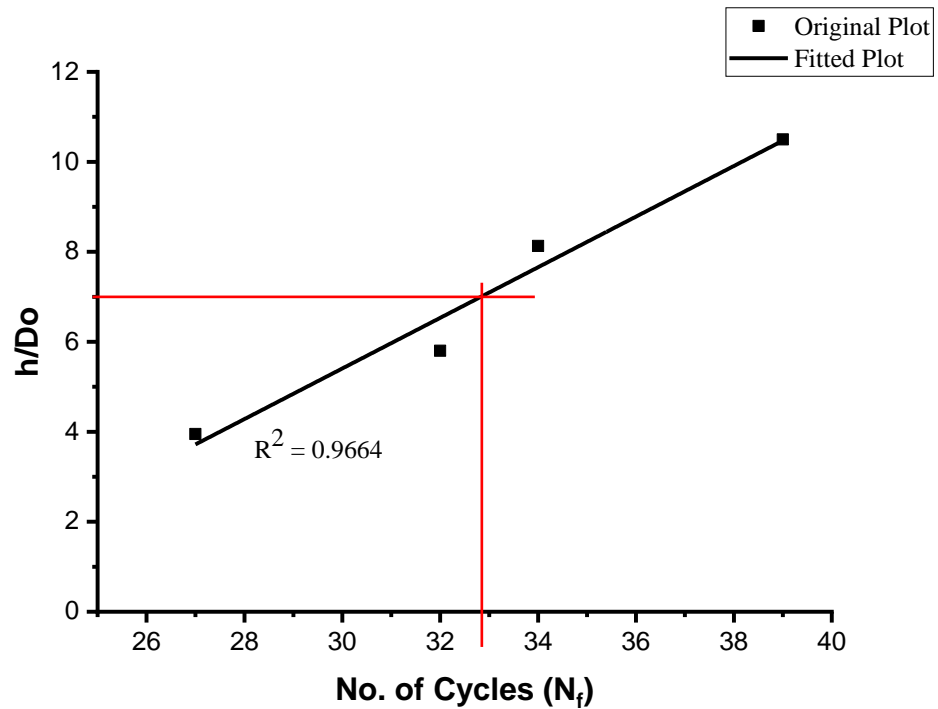


Figure 4.9: Relationship Between Wrinkle Amplitude Ratio and No. of Cycles to Failure for Group 1 ($0.3p_y$) Specimens

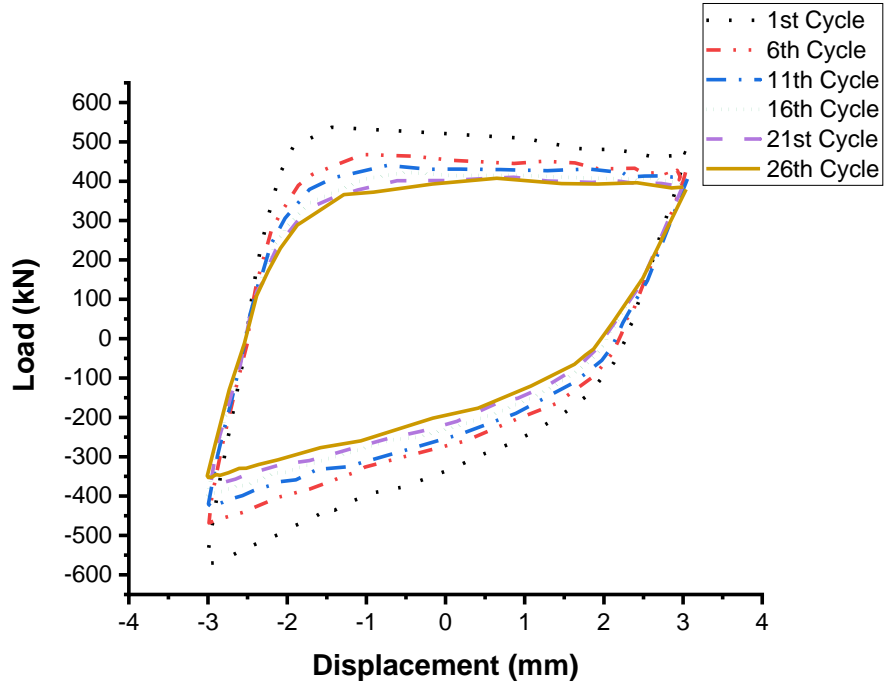


Figure 4.10: Load vs. Displacement Hysteresis curve for IP30WA4

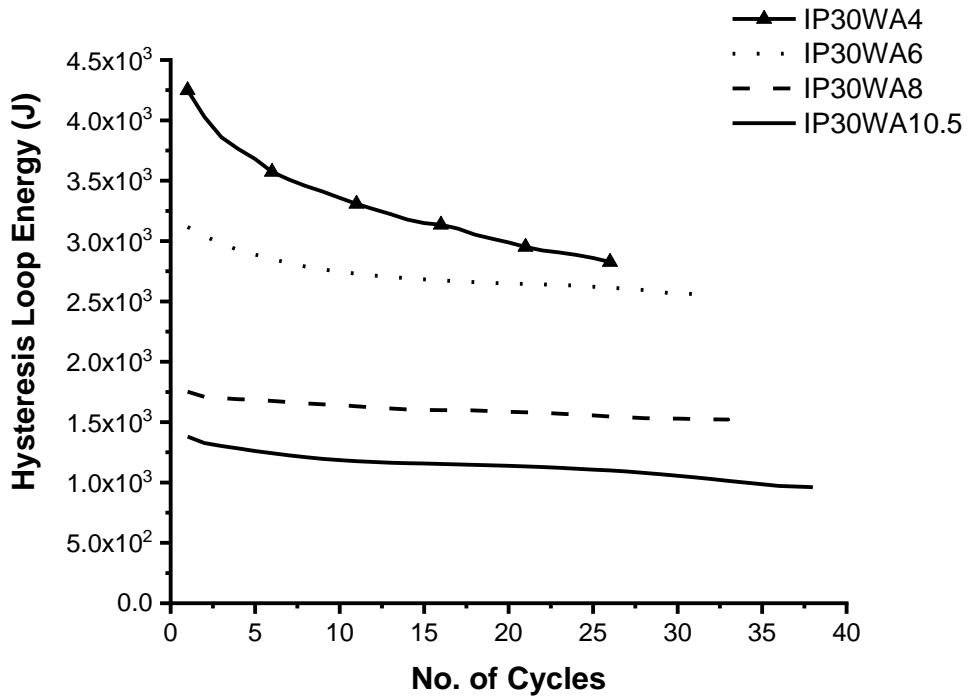


Figure 4.11: Relationship Between HLE and Number of Cycles for Group 1 ($0.3p_y$) Specimens

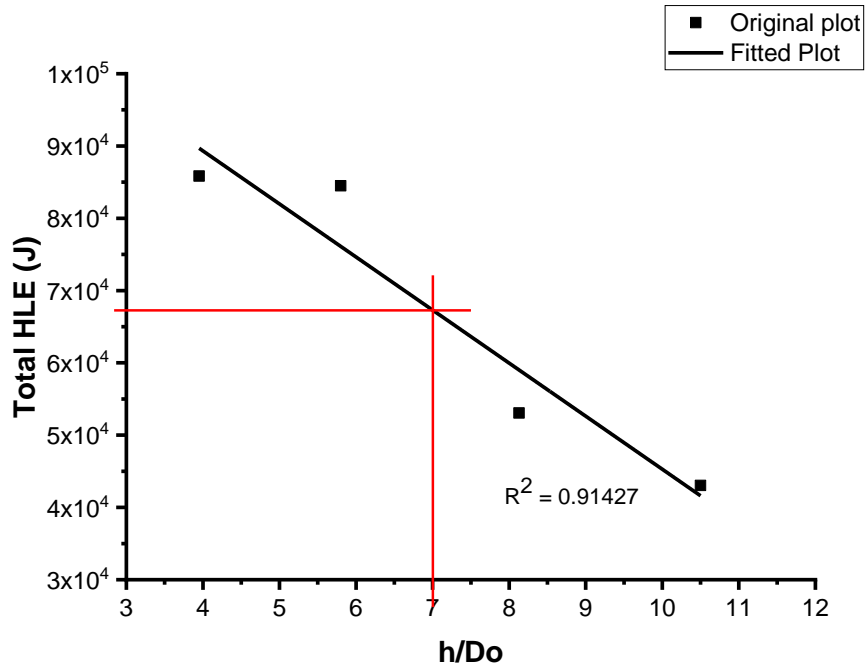


Figure 4.12: Relationship Between Total Hysteresis Loop Energy and Wrinkle Amplitude Ratio for Group 1 ($0.3p_y$) Specimens

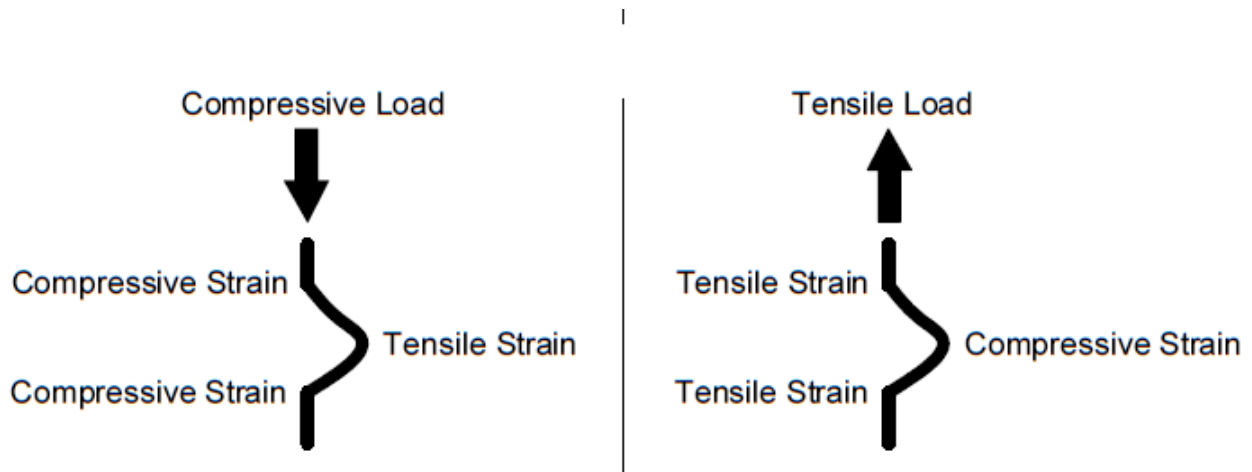


Figure 4.13: Strain Movement Around the Wrinkle Region During Axial Cyclic Loading

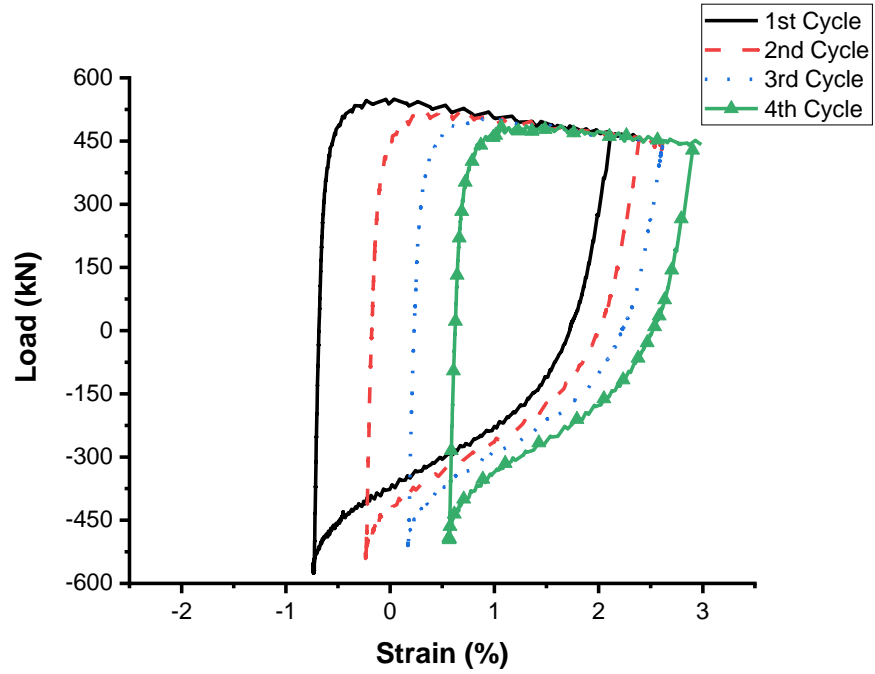


Figure 4.14(a): Relationship Between Local Longitudinal Strain and Applied Load at Wrinkle Crest for Specimen IP30WA4

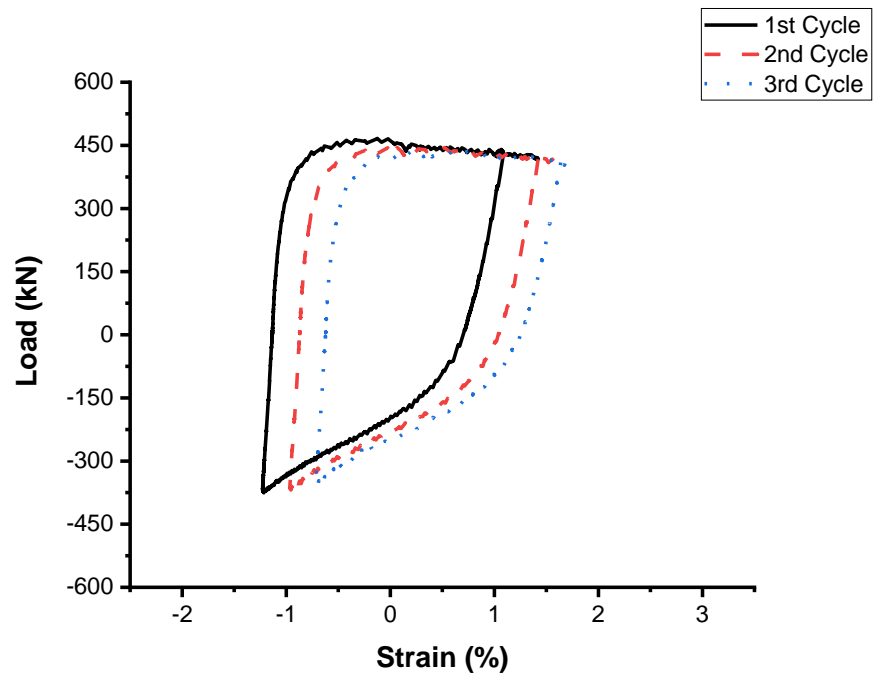


Figure 4.14(b): Relationship Between Local Longitudinal Strain and Applied Load at Wrinkle Crest for Specimen IP30WA6

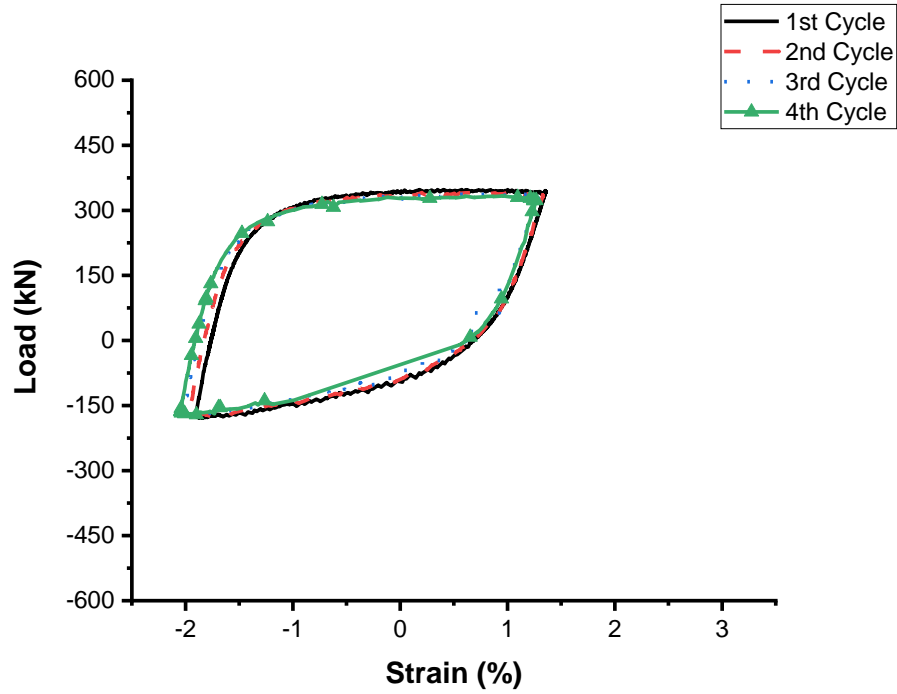


Figure 4.15(a): Relationship Between Local Longitudinal Strain and Applied Load at Wrinkle Crest for Specimen IP30WA8

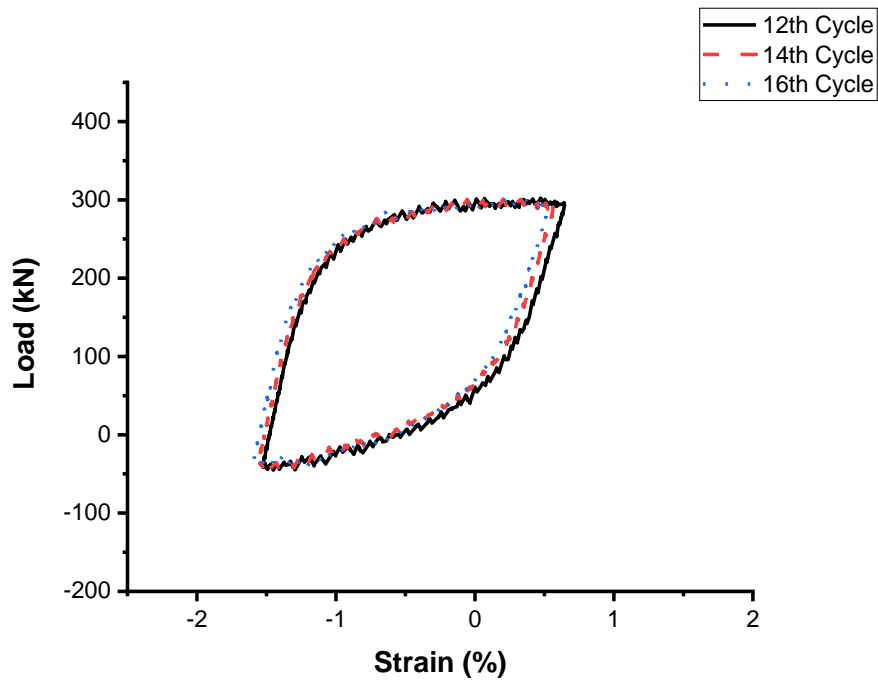


Figure 4.15(b): Relationship Between Local Longitudinal Strain and Applied Load at Wrinkle Crest for Specimen IP30WA10.5

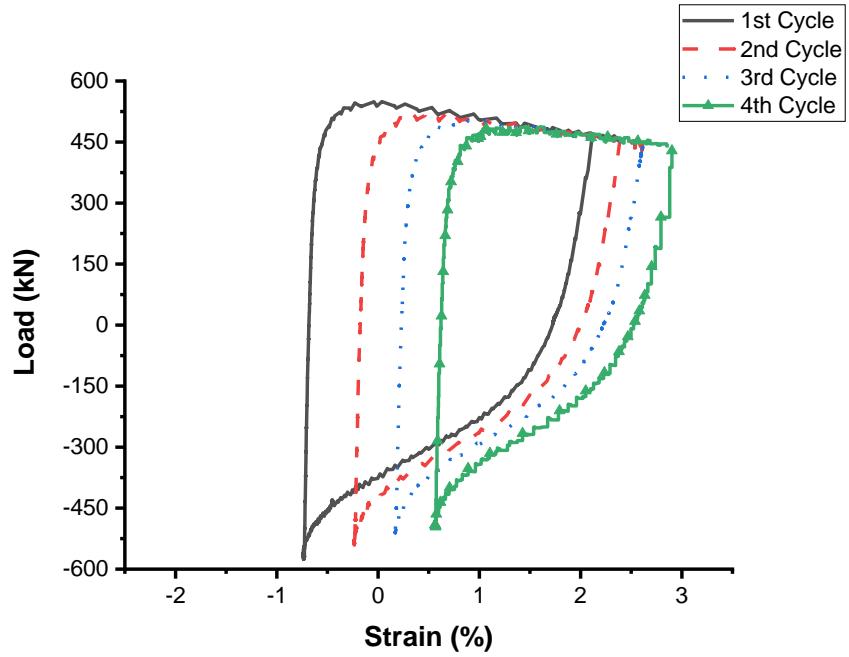


Figure 4.16: Relationship Between Local Hoop Strain and Applied Load at Wrinkle Crest for Specimen IP30WA4

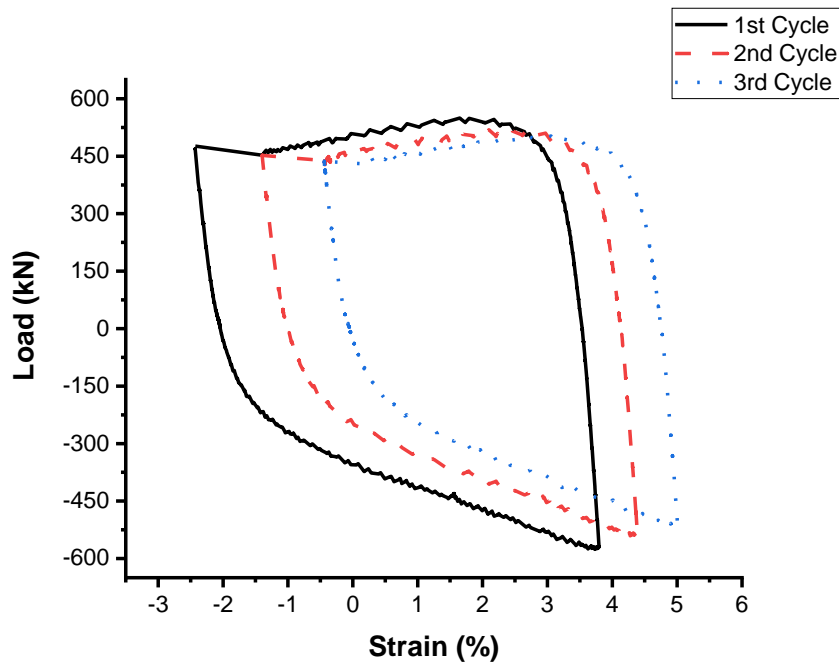


Figure 4.17: Relationship Between Local Longitudinal Strain at Wrinkle Feet and Applied Load for Specimen IP30WA4



Figure 4.19: Visible Circumferential Fracture at Wrinkle Crest for Specimen IP30WA8

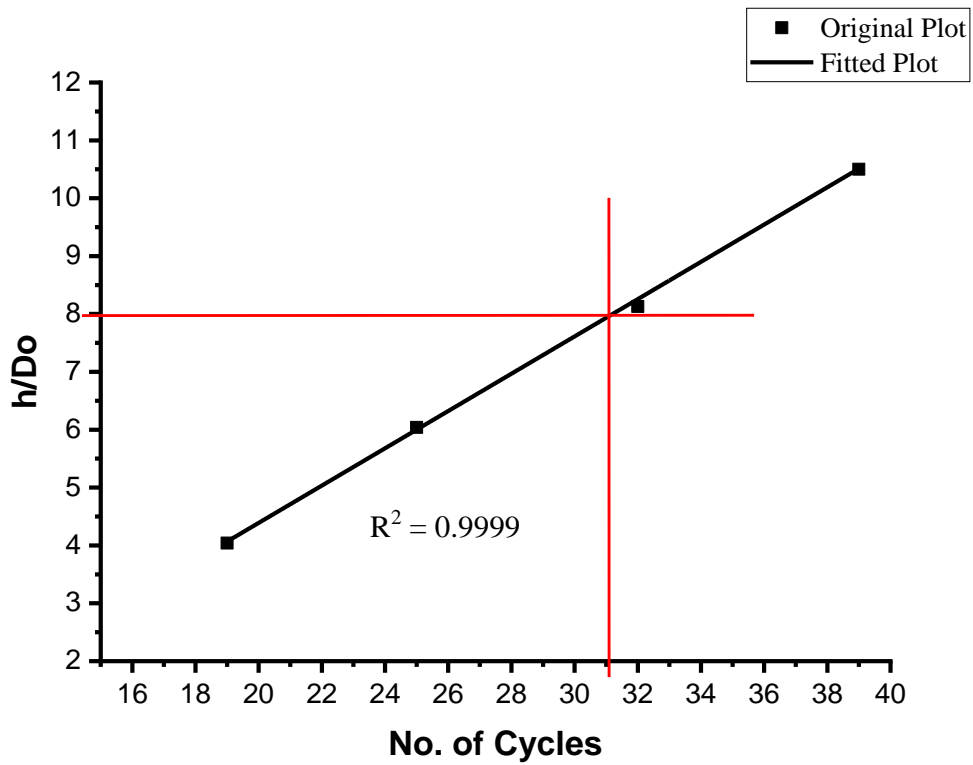


Figure 4.20: Relationship Between Wrinkle Amplitude Ratio and No. of Cycles to Failure for Group 2 ($0.6p_y$) Specimens

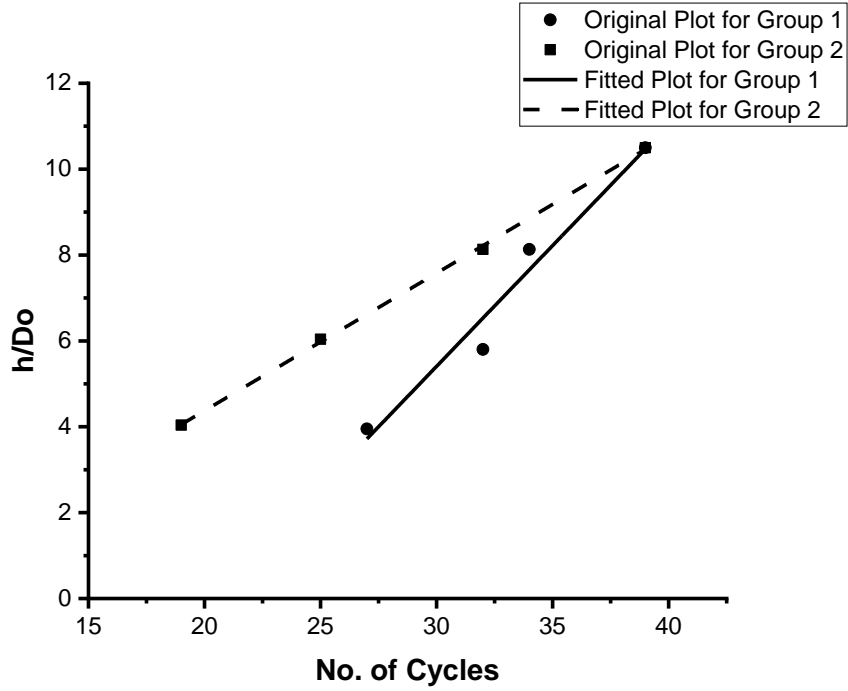


Figure 4.21: Relationship Between Wrinkle Amplitude Ratio and No. of Cycles to Failure for All Specimens

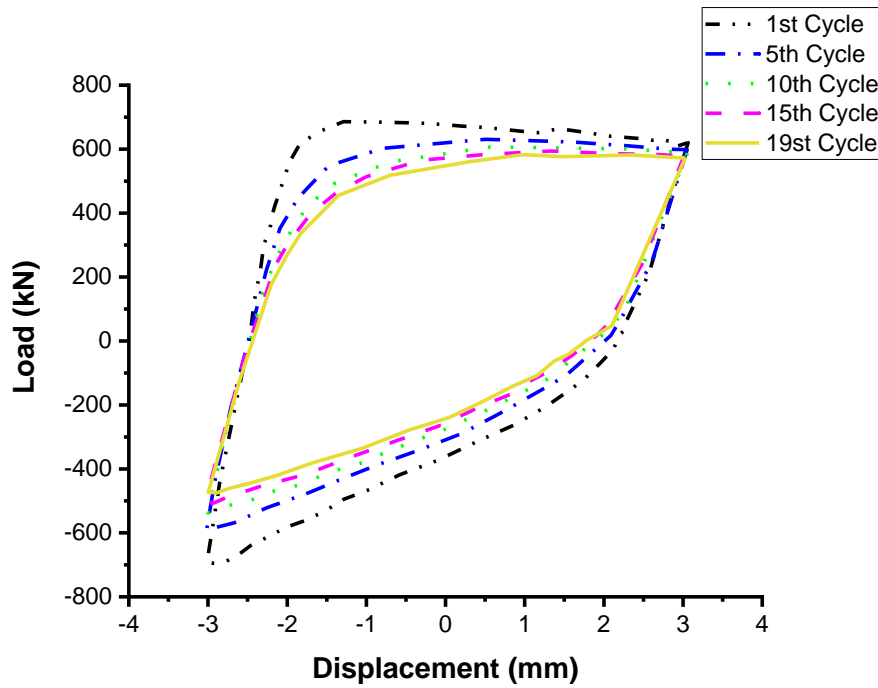


Figure 4.22: Load vs. Displacement Hysteresis curve for IP60WA4

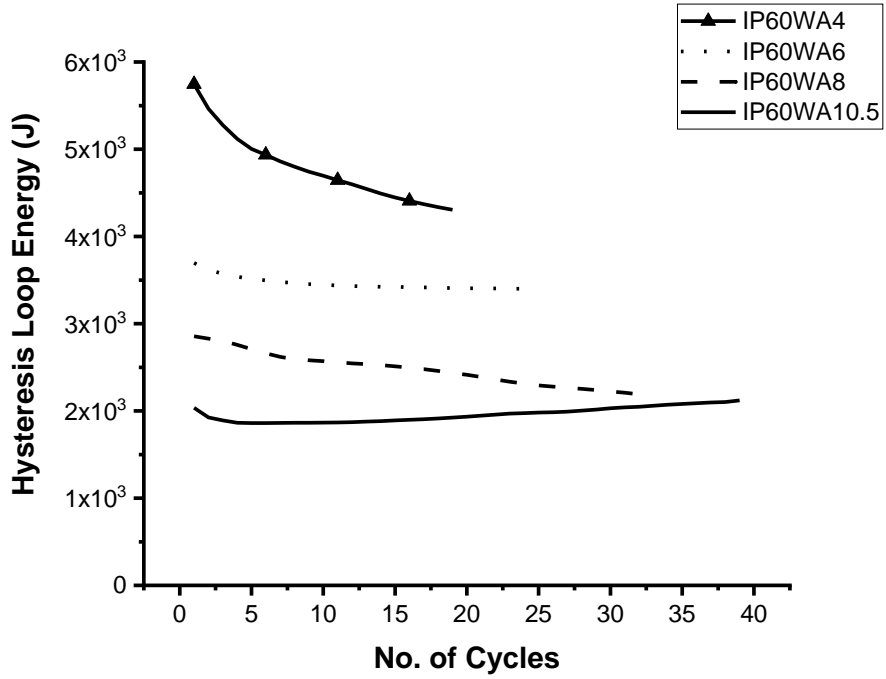


Figure 4.23: Relationship Between HLE and Number of Cycles for Group 2 ($0.6p_y$) Specimens

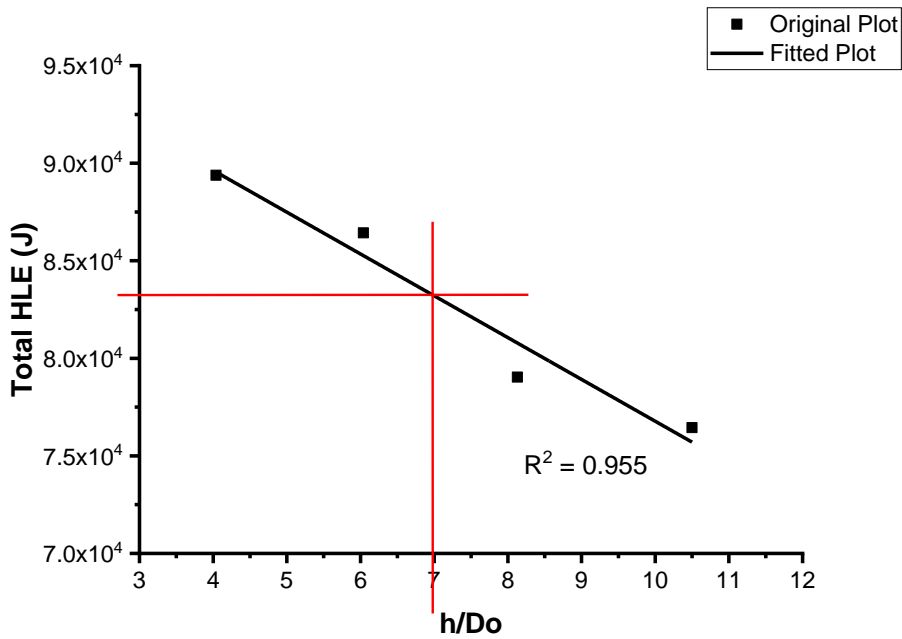


Figure 4.24: Relationship Between Total Hysteresis Loop Energy and Wrinkle Amplitude Ratio for Group 2 ($0.6p_y$) Specimens

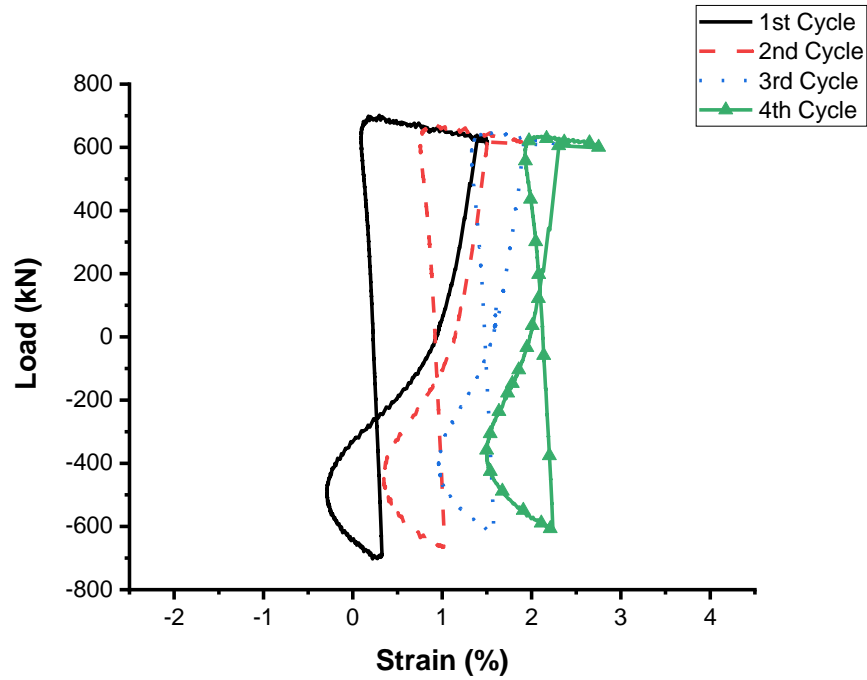


Figure 4.25: Relationship Between Local Longitudinal Strain and Applied Load at Wrinkle Crest for Specimen IP60WA4

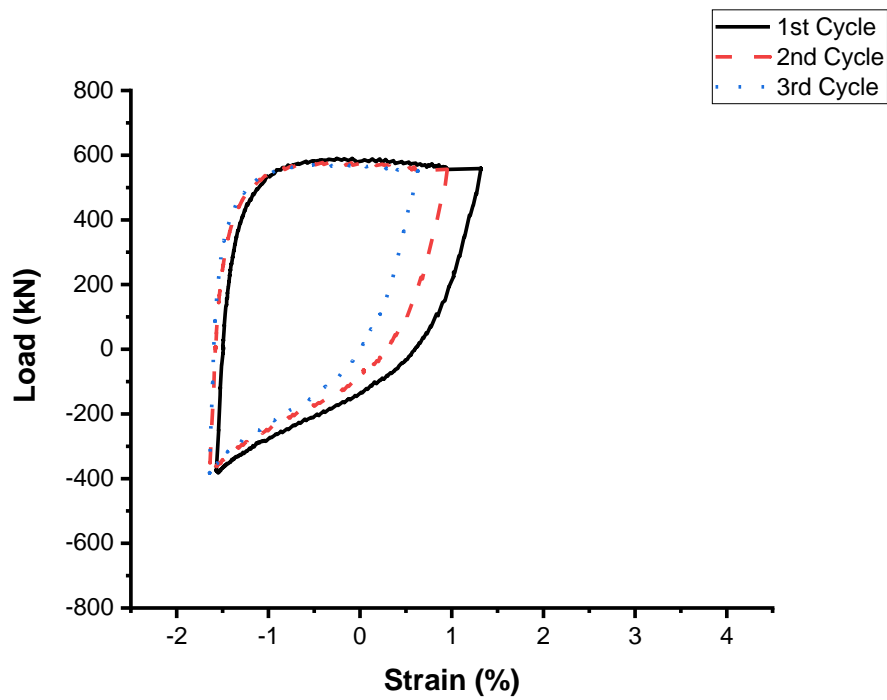


Figure 4.26(a): Relationship Between Local Longitudinal Strain and Applied Load at Wrinkle Crest for Specimen IP60WA6

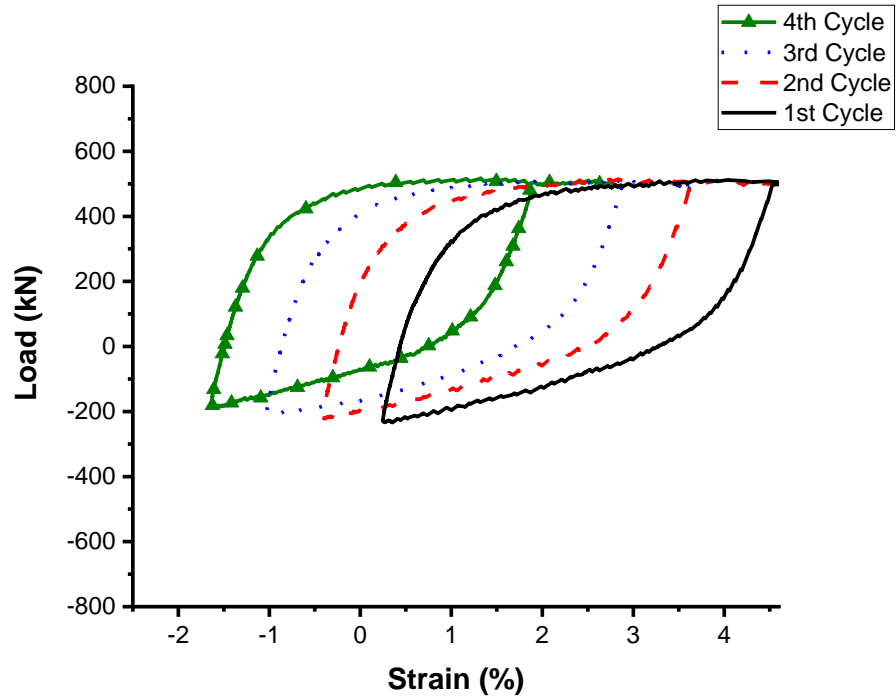


Figure 4.26(b): Relationship Between Local Longitudinal Strain and Applied Load at Wrinkle Crest for Specimen IP60WA8

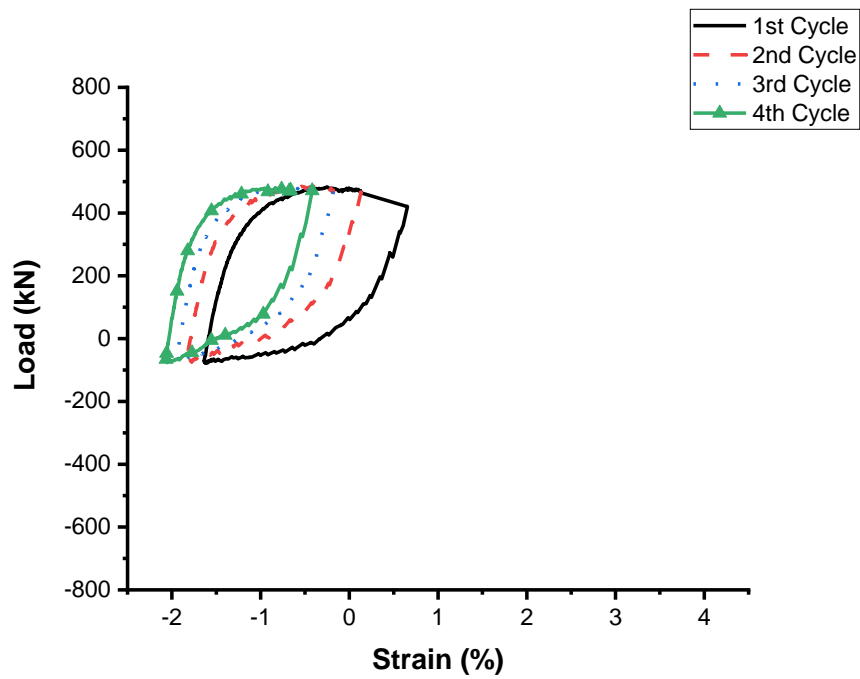


Figure 4.26(c): Relationship Between Local Longitudinal Strain and Applied Load at Wrinkle Crest for Specimen IP60WA10.5

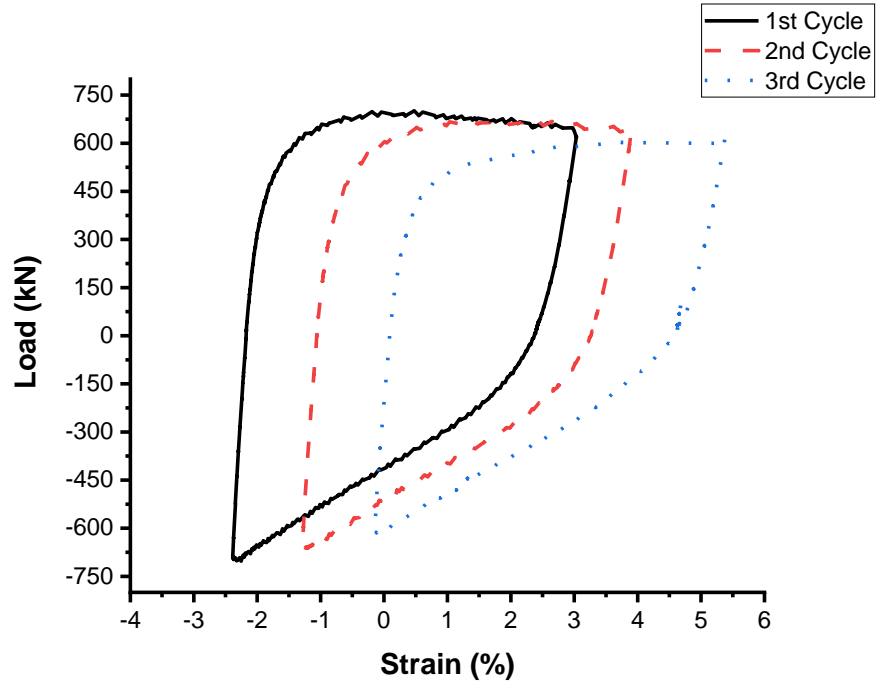


Figure 4.27: Relationship Between Local Hoop Strain and Applied Load at Wrinkle Crest for Specimen IP60WA4

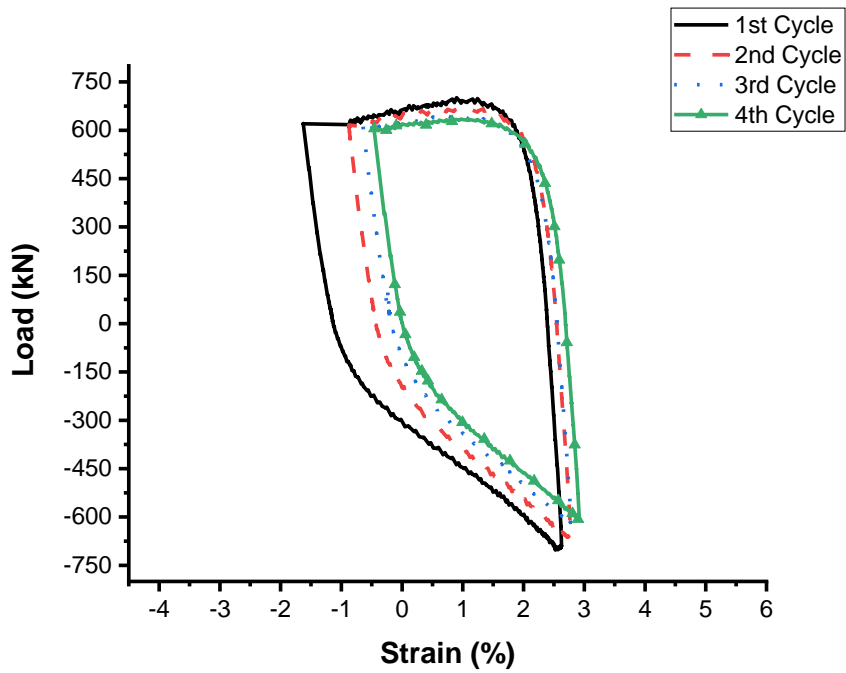


Figure 4.28: Relationship Between Local Longitudinal Strain and Applied Load at Wrinkle Feet for Specimen IP60WA4



Figure 4.29: Visible Flat Appearance at Wrinkle Crest for Specimen IP60WA10.5



Figure 4.30: Visible Longitudinal Fracture at Wrinkle Crest for Specimen IP60WA6

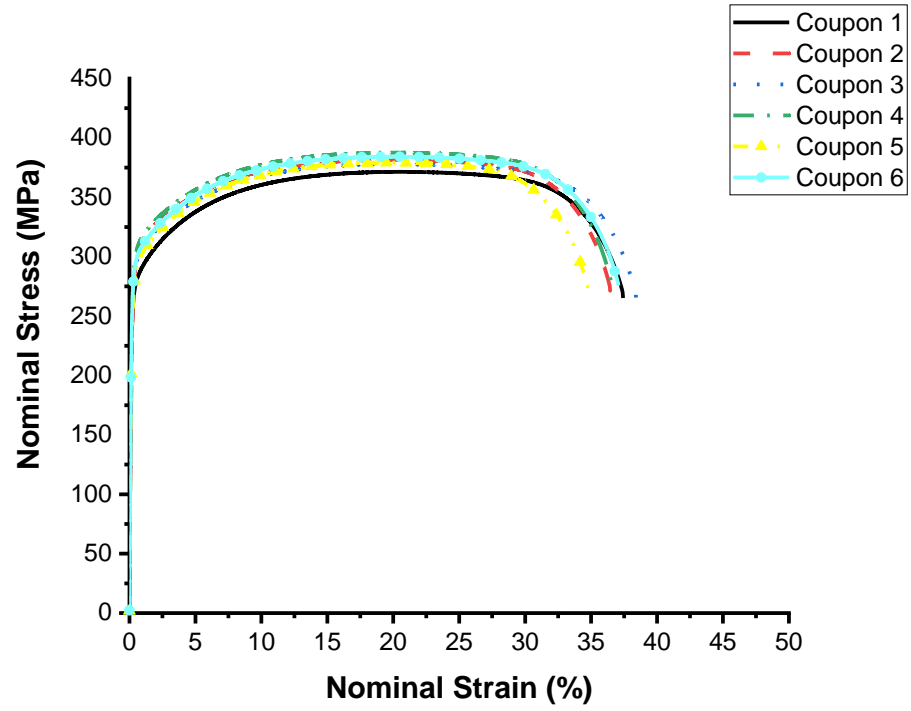


Figure 4.31: Nominal Stress and Strain Behaviour of API 5L X42 Pipe Material

CHAPTER 5

FINITE ELEMENT MODELLING (FEM)

5.1 General

Full-scale experimental testing has been the traditional and most reliable way of determining the structural behaviour of wrinkled pipelines subjected to operational and external loadings. However, the process of experimental testing for every variable parameter in this study such as operational pressure, wrinkle geometry, and axial load case is labour intensive and uneconomical. This problem is prominent across all engineering fields, which is why engineers have been motivated to develop a numerical procedure for analyzing structures using finite element analysis (FEA) methods. A commercially available software Abaqus/CAE version 6.14 (licensed by Dassault Systèmes Simulia Corp., 2014) was used to develop these Finite element (FE) models which were validate using experimental results discussed in chapter 4.

The Abaqus/CAE software has been used by researchers in the past to simulate the behavior of wrinkled pipelines under the effect of combined loadings (Alexander and Kulkarni, 2009; Cunha et al., 2009; Das et al., 2007b; Pournara et al., 2015). The software gives an almost similar behavior as that of tested specimens because it can solve non-linear geometry, material, boundary and contact problems. The concept of FEA is basically the discretization of a structure into finite elements to form individual stiffness matrices, which are assembled together at the nodes to form a linear and non-linear equilibrium equation. These equilibrium equations are solved by Abaqus software, using the Newton-Raphson method to solve these non-linear equilibrium problems iteratively at each loading increment. The solution strategy that can be employed when simulating the initiation of a wrinkle in a pipe segment can be force-control for behavior of the pipe in the elastic range. The displacement-control is employed in the elastic-plastic range after the ultimate load, so as to achieve a more stable equilibrium. The Abaqus software uses the implicit method to solve static non-linear problems but uses the explicit method for dynamic non-linear problems. Since the load application process is quasi-static, the problem in this study was solved implicitly.

The objective of finite element analysis (FEA) is to develop FE models for the test specimens and validate the behavior of the FE models using test data. Numerical (FE) models were developed in the Abaqus/CAE, simulating the boundary condition and load application procedure as it was in the experiment. The data obtained from the global and local load-deformation behavior from the

numerical and experimental analysis will be compared for consistency. Depending on the consistency, the numerical model will predict specimen behaviour with variable parameters.

5.2 Finite Element Model

The Finite element modelling of the pipe specimen is divided into two phases just as in the experimental program; the wrinkle initiation phase and axial cyclic loading phase.

5.2.1 Phase 1: Initiation of Wrinkle Defect

5.2.1.1 Assembly

A total of three-part instances was modelled individually and then assembled together to model the specimen setup in the experimental procedure. The three instances created are; the two end plates and the cylindrical pipe. The two end plates, each of them adjacent to the top and bottom of the pipe were modelled using a deformable part type with shell base feature, because of the symmetry of the geometry. They were assigned the appropriate thickness of 38.1 mm, width and length of 406.4 mm x 406.4 mm, respectively as it is in the experimental specimen. The pipe instance also made of a deformable part type with shell base feature, was divided into two sections, one of which represents the geometry of the pipe itself and the other represents the geometry of the pipe section attached to the collars. The section which represents the pipe with collars was modelled such that the thickness of the cylindrical section simulates the total thickness of 10.46 mm which includes both the collars and pipe. This section property was assigned to the segment of the pipe at either ends of the pipe model near the end plates, separated from the original pipe thickness of 3.76 mm using datum partitioning. The sectioning of the pipe segment is shown in Figure 5.1, which represents the general pipe assembly.

All three-part instances were assembled together through coincident points that are located on the centerline that passes through the whole specimen. These position constraints allow proper arrangement of the pipe specimen model, bringing together all three parts as an assembly. The whole assembly model is shown in Figure 5.1.

5.2.1.2 Interaction

During the fabrication and load application process in the experimental procedure, several interactions existed amongst different parts of the specimen which were simulated in Abaqus. The tie constraint which is used to bond surfaces together permanently just like the welding phenomenon, was used to tie the circumferential ends of the pipe to the end plates by using the surface to surface discretization method. The surface of the end plates was chosen as the master surface and the pipe nodes was chosen as slave surface. This is because the master nodes can penetrate slave surfaces, but slave nodes cannot penetrate the master surface. This way, there will be no movement between the pipe and endplates, hence, the slave nodes cannot slide or separate from the master surface. The tie constraint therefore practically allows the tying of all degree-of-freedom (DOFs) of both surfaces together.

As discussed in subsection 3.2.7.4, collars were attached to the pipe specimen to create an imperfection that has an effect greater than that of the welded joints. However, as discussed in subsection 4.2.1, collars were removed as wrinkles became apparent and visible during the tests, except the collars near the welded endplates. A contact non-linearity was used to simulate the collars by defining a surface-to-surface contact between adjacent surfaces to the wrinkled region and the collars. The adjacent surfaces on either side of the wrinkled region where the contact non-linearity was simulated is approximately 88.3 mm in length. The modelled contact interaction was rendered inactive during the axi-symmetric loading step, to simulate collars removal. Furthermore, the geometry of the collars in this region were also deleted as a part, using the model change type of interaction. The step is apparent in the visualization module during the post-processing of the finite element model.

A coupling constraint which provided a constraint between a reference node *RP-1* or *RP-2* (located at the centre of the end plates) and the nodes on the surface of the end plates, was used to uniformly distribute load on the top end plate and define the boundary condition on the bottom end plate (see Figure 5.1). The continuum distributing type of coupling constraint was used at the top end plate because it uniformly distributes load over the surface of the endplate. Compared to other coupling constraints (structural and kinematic coupling), other weighting methods monotonically decrease loading magnitude with increase in radial distance from the reference node.

5.2.1.3 Loads and Boundary Conditions

The loads and boundary conditions were defined in steps, simulating the experimental procedure employed during testing. Initially, the bottom end plate of the pipe specimen was clamped to the support, to constrain translational and rotational degree of freedoms (DOFs). Abaqus offers the Encastre option which fixed all rotational and translational DOFs of node *RP-2* (*RP-2* is coupled to all the slave surface nodes on the bottom end plate). Next, the pipe specimen was internally pressurized to the desired pressure range ($0.3p_y$ or $0.6p_y$). Abaqus allows the uniform distribution of pressure on the internal region of the modelled pipe part and also endplates in the load module. Thereafter, a monotonic displacement-controlled axisymmetric load was applied on the specimen until deformation occurs. Abaqus allows application of displacement on reference node *RP-1* (*RP-1* is coupled to the slave surface nodes on the top end plate) in the vertical direction (U_3). In the last monotonic step, the specimen is unloaded to zero load by applying a concentrated force of negligible magnitude on *RP-1*.

5.2.1.4 Material Properties

A uniaxial tensile test was performed on six pipe coupons according to ASTM E8/E8M – 13a (ASTM 2013), to obtain the elastoplastic stress-strain behavior of the pipe material. Figure 5.2 shows the graphical representation of a typical nominal or engineering stress-strain behavior which was obtained from coupon 6. It is observed from the figure that material first exhibits a linear elastic behavior, followed by a gradual hardening and softening characterized by plastic flow and hardening rules. Hence, for the purpose of material definition in this model, the elastic material properties highlighted in Table 4.7 are considered, where modulus of elasticity (E) is 192 GPa, Poisson ratio (ν) is 0.3 and yield strength (σ_y) is given as 288 MPa.

Generally, the behavior of ductile materials (such as steel) is assumed to be identical in initial linear elastic portion of the stress-strain curve in both tension and compression. Complications due to instability and buckling may arise during compression test on coupons, and as such was avoided. Since no material tests were performed to measure the stress-strain relationship of the pipe material in compression, the compressive behavior is assumed to be identical to tensile behavior. The coupon specimens tested, were taken in the longitudinal direction of the pipe, and no attempts were made to determine the pipe material properties in the circumferential direction. Therefore, for the scope of this work the mechanical properties in the longitudinal direction were assumed to be

identical to the mechanical properties in the circumferential direction. These assumptions however, are typical for modelling pipeline structures, and have been corroborated by previous researchers (Das et al., 2007; Dewanabee & Das, 2012; Nazemi et al., 2009).

As discussed in the experimental results, the pipe specimens undergo plastic deformation depending on the wrinkle amplitude. The elastic-plastic response of the pipe specimen can be predicted with Abaqus by properly defining von-Mises yield criterion as well as associated plastic flow rule and hardening rule. The von-Mises yield criterion was used to predict the yield stress of an isotropic and ductile material (in this case pipe material) subjected to complex loading. The von-Mises yield surface is represented by an ellipse in a two-dimensional stress state and a cylindrical shape in a three-dimensional stress state. The associated flow rule is used to determine the direction of the plastic straining, which is in the direction normal to the yield surface. Isotropic hardening was used in this model. The yield surfaces increase uniformly in all directions when isotropic hardening occurs, such that the yield stress is always greater than the previous one as plastic straining occurs. Isotropic hardening, however, ignores the Bauschinger effect, and is appropriate for this model since there is no reverse in loading direction in the first phase.

The classical metal plasticity model in Abaqus is used to define the post-yield behavior for most metals. Abaqus connects the given stress-strain data pairs with a series of straight-line segments to form a continuous, piecewise-linear plasticity curve, which is used to approximate the actual material behavior. The given stress-strain data pairs can be derived from the uniaxial tensile coupon test, which is given in terms of nominal stress and strain. However, in Abaqus material model, true stress (Cauchy stress) and logarithmic (true) strain plastic strain is required. This basically takes into consideration the instantaneous deformed state of the material and not the initial undeformed state. The nominal stress and strain data can be converted to true stress and plastic strain using Equation 5.1 and Equation 5.2.

$$\sigma_{true} = \sigma_{nom}(1 + \varepsilon_{nom}) \quad (5.1)$$

$$\varepsilon_{true}^{pl} = \ln(1 + \varepsilon_{nom}) - \frac{\sigma_{true}}{E} \quad (5.2)$$

Where σ_{true} is the true stress, ε_{true}^{pl} is the logarithmic or true plastic strain, σ_{nom} is the nominal or engineering stress, ε_{nom} is the nominal or engineering strain and E is the Young's modulus. However, these analytical equations may be valid only up to the ultimate strength, the onset of necking that follows, prohibits the use of these equations (Ling, 2004; Shengwen et al., 2019). Several studies have been conducted to establish the true stress and strain behavior of a ductile material beyond the ultimate strength, after the onset of necking. Ling (2004) proposed a method for estimating uniaxial true stress and strain after necking using the weight-average method. A linear strain hardening model was adopted as the upper bound, and a power-law fit which represented the strain hardening region beyond yielding was used as a lower bound. The weight factor was determined iteratively by comparing the experimental and simulated result from FEM of the coupon specimen (see Section 5.2.3), until a satisfactory agreement was achieved. For the purpose of defining the material model for the pipe part of the assembly, the true stress beyond necking (σ_{true}^*) was established as a function of the true strain beyond necking (ε_{true}^*). This was possible using the weighted-average method, as shown in Equation 5.3.

$$\sigma_{true}^* = \sigma_{true}^{ut} \left[w \cdot \left(\frac{\varepsilon_{true}^*}{\varepsilon_{true}^{ut}} \right)^n + (1 - w) \cdot (1 + \varepsilon_{true}^* - \varepsilon_{true}^{ut}) \right] \quad (5.3)$$

Where σ_{true}^{ut} is the true stress corresponding to ultimate strength, ε_{true}^{ut} is the true strain corresponding to the ultimate strength, n is the power-law material constant and w is the weight constant. Figure 5.3 shows the graphical relationship between the true stress and logarithmic strain of the pipe material before and after necking, considering the instantaneous deformed state. The figure shows the ultimate strength (U) after which necking begins, and the fracture point (F) where the specimen is completely damaged. The true stress and logarithmic strain data imported into the Abaqus material model is also given in Table 5.1. The table shows values corresponding to post-yielding behaviour, where the initial plastic strain is zero, because there will be no plastic straining just before yielding occurs. The pipe collars and end plates were modelled as elastic materials, since they experienced no plastic deformation.

5.2.1.5 Element Selection

The shell element is believed to be most effective for finite element analysis of pipelines with material or geometry nonlinearity problems under complex loading, that experiences bending or

buckling. This has been corroborated by previous researchers (Das et al., 2007b; Nazemi, 2009; Souza & Murray, 1996). The choice of the element is generally dependent on the geometry to be analysed, which in this case is a thin walled structure. The S4R shell type element from the Abaqus/Standard library was used to model the discrete elements in the whole pipe assembly including the end plates. The S4R is a general purpose (thick and thin) 4-node, linear, doubly curved shell element with reduced integration. The element has four nodes and does not suffer from transverse shear locking, nor does it have any unconstrained hourglass modes. Each of the four nodes has six DOFs namely; the translational DOFs (u_1 , u_2 and u_3) and rotational DOFs (θ_1 , θ_2 and θ_3), where axis 1,2 and 3 are sequentially perpendicular to each other like X, Y and Z as shown in Figure 5.1.

A number of five integration points through the thickness of the shell element was chosen for this model, which is the default number provided by Abaqus. However, it is possible to change the number of integration points as suited. By default, Simpson's rule was chosen for numerical integration. The top surface of the conventional shell element is the surface in the positive normal direction, while the surface in the negative normal direction is referred to as the bottom surface. Therefore, the section points through the thickness of the shell are numbered consecutively in the positive normal direction, starting from the bottom surface. The S4R element allows the definition of pressure load application on the surfaces, and as such a positive pressure load applied on the element produces a load that acts in the direction positive to the normal surface. Generally, reduced integration elements use fewer number of integration points compared to full integration elements, and as such most likely yield a less accurate solution. Despite the fact, the reduced integration elements are generally preferred as they are less computationally costly.

5.2.1.6 Mesh Convergence Study

A mesh convergence study was undertaken to determine the optimum mesh density that provides a balance between the accuracy of the solution and computational resources. Generally, in most finite element modelling applications, finer mesh densities typically yield more accurate results, in comparison to coarse mesh densities. However, the discretization of the structure into smaller elements establishes large number of equations depending on fineness of the elements, which usually requires more time for the model to establish a solution.

The pipe part of the model was chosen as the focus of this mesh study, since that is the area deformation is predicted to occur. The meshes of the other parts (end plates and collars) were adjusted accordingly to satisfy the contact and constraint requirements of the program. Abaqus allows the use of mesh seeds to serve as markers along the edges of a region to specify the target mesh density in that region. These seeds can be applied globally on the entire part or can be applied locally along the edge or boundary of a region. Abaqus CAE preprocessor then generates different meshes, depending on the local seeds assigned. The mesh density of the pipe part was varied as shown in Table 5.2.

The relationship between load applied on the pipe structure and the global displacement response, depending on the mesh densities for the simulated specimen IP30WA4, is shown in Figure 5.4. It can be observed that the maximum load at the final displacement increases as mesh becomes finer, as shown in Figure 5.5. Therefore, it is apparent that the post-buckling behavior of the pipe model is highly sensitive to varying mesh densities. Furthermore, this can also be corroborated as shown in Figure 5.6, where the maximum von Mises stress at the wrinkle crest reduced with finer element sizes at the midsection around the wrinkle region (where collars are omitted).

As shown in Figures 5.4, 5.5, and 5.6, the model converges with elements smaller than size 6 mm. The 4 mm element mesh size was originally be considered appropriate for this model since it is the most accurate. However, since there exists a significantly high increase in run-time for this mesh size, the 5 mm mesh size was chosen. Furthermore, the percentage error for the maximum load at the final displacement, and the von Mises stress at the wrinkle region between 5 mm element and 4 mm element is negligible. These observations further corroborate the decision to choose 5 mm as optimum mesh density.

In terms of computational cost, it can be observed that the run-time for elements smaller than 6 mm is relatively longer in comparison to larger elements, due to the number of discretized elemental equations. Hence, the element size of the region outside the wrinkle region was refined by increasing the element size to 10 mm. Figure 5.7(a) and (b) shows the schematics of the refined mesh in the pipe and endplate assembly in the model. Table 5.3 shows the configuration of the workstation system.

5.2.1.7 Load Histories

The loading history was divided into several steps. The loading history was applied in the numerical (FE) model to simulate the experimental loading history as described in Section 3.2.8 for the monotonic loading phase. However, it should be noted that the displacement-controlled method was used in the FE model rather than the load-controlled method, to overcome the problem of instability (singularity in the stiffness matrix) at the limit load point. The loading steps in the FE models are described in detail as follows:

Step 1: Internal Pressurization of Pipe

Prior to this step, there exist a default initial step where the bottom plate of the modelled pipe assembly is fixed for all degrees of freedom ($U_1 = U_2 = U_3 = \theta_1 = \theta_2 = \theta_3 = 0$), and symmetry is maintained in such a way that displacement is allowed only in one direction U_3 ($U_1 = U_2 = \theta_1 = \theta_2 = \theta_3 = 0$). This boundary conditions remain active all through the analysis.

In this first step, pressure was applied uniformly as a distributed load on the elements located on the internal surface of the pipe and endplates model. The magnitude of the internal pressure applied was $0.3p_y$ or $0.6p_y$, just as in the experiment, to give an internal pressure value of 450 psi (3.1 MPa) or 897 psi (6.2 MPa). Since the magnitude is defined with a positive sign, this indicates that the pressure was applied in the direction of the outward normal of the element.

Step 2: First Axisymmetric Loading

In this loading step, an increasing displacement controlled axisymmetric compressive load applied on the specimen is simulated in the FE model by defining a displacement boundary condition. The displacement boundary condition is applied on the reference node *RP-1* (used to couple the slave surface of the top endplate) in the U_3 direction, while keeping other DOFs at zero. The displacement is applied until a magnitude that satisfies the longitudinal displacement value (usually within the range of 7 mm to 8 mm) where the collars were removed in the experiment.

Step 3: Continued Axial Compressive Load

The surface-to-surface contact simulated between the pipe wall and collars was deactivated in this step, and the geometry of the collars were removed. Thereafter, the axial compressive load in U_3 direction was continued on the same reference node *RP-1*, up until the target wrinkle profile was

achieved. All these interactions and boundary conditions were defined while keeping the internal pressure activated, symmetry maintained in the longitudinal direction, and bottom endplate fixed.

Step 4: Unload Pipe

In the conclusion of the monotonic loading phase, the internal pressure and axial load applied in the preceding steps were removed to completely unload the pipe. The defined load and displacement boundary conditions were deactivated this step, and the FE model was unloaded to zero or a negligible load magnitude. This step was included to account for elastic spring back action which the specimen encounters when test is completed in the experiment.

5.2.2 Phase 2: Axial Cyclic Loading

The following subsections discuss the modelling of the axial cyclic load phase in addition to the modelled wrinkle initiation phase. This section is necessary to validate the load vs. global deformation behavior, and the load vs. local strain behaviour, as observed in the discussed experimental results in Sections 4.3.1 and 4.3.2. These observations will validate the numerical quantification of the localized maximum strain range associated with the most critical part of the wrinkled region. Therefore, it leads to the estimation of the remaining fatigue life of the wrinkled pipes.

5.2.2.1 Element and Mesh Selection

The collection of nodes, elements, surfaces, and sets generated from each FE model belonging to the deformed geometry of the wrinkle initiation stage (phase 1) were imported as a new part instance for FE models of phase 2. Figure 5.8 is a representation of the part instance of specimen IP30WA4 which was obtained from the phase 1 output database in form of an orphan mesh. An orphan mesh part contains no feature information, that is no associated geometric features can be added; however, a geometry can be created from the orphan mesh using the Abaqus plug-ins option. New top and bottom endplates part instances were created in the new FE model and assembled to the imported deformed pipe geometry. All nodes along the circumferential edge of the orphan mesh pertaining to the deformed pipe, and the top and bottom endplates were coupled using surface-to-surface tie constraints. Similar to phase 1, all the elements belonging to the endplates were modelled using the S4R shell element. However, the elements belonging to the deformed pipe were modelled using S3 triangular general-purpose shell element.

5.2.2.2 Loads and Boundary Conditions

The boundary conditions defined in the initial default step in phase 1 are repeated here, where the bottom plate was fixed for all DOFs and symmetry is maintained in one direction (U_3). As discussed in the previous phase, the internal pressure applied on the internal surface of the pipe wall and endplates were deactivated during the unloading of the specimen. However, to simulate the resumption of internal pressurization in the second phase of the test, pressure was distributed on the internal surface of the pipe and endplates at a magnitude of $0.3p_y$ or $0.6p_y$ (similar to the previous modelling phase). In another loading step, a symmetric displacement controlled axial cyclic load was simulated in the model. This was done by applying a displacement boundary condition on reference node *RP-1*.

5.2.2.3 Material Properties

In order to adequately simulate the post-wrinkling behavior of the pipe specimen subjected to axisymmetric axial cyclic loads, a combined hardening rule was defined for the pipe material model. A combined hardening rule model was needed for the pipe material definition to consider the Bauschinger effect and adequately depict the subsequent dampening of HLE (hysteresis loop energy) with consecutive load cycles. Chapter 6 discusses in the detail the purpose for this approach and results obtained from this method.

5.2.2.4 Load Histories

The load histories in this phase are applied to the edited geometric features of the orphan mesh imported from phase 1. The loading steps required to model the axial cyclic loading phase are divided into two steps, as discussed below:

Step 1: Resumption of Internal Pressure

In order to simulate the continuous pressurization of the wrinkled pipe in the field, pressure was applied uniformly as a distributed load on the internal surface of the pipe and endplates. Similar to the first phase, the magnitude of the internal pressure was simulated to be $0.3p_y$ or $0.6p_y$ just as in the experiment, to give an internal pressure value of 450 psi (3.1 MPa) or 897 psi (6.2 MPa). Since the magnitude is defined with a positive sign, this indicates that the pressure was applied in the direction of the outward normal of the element.

Step 2: Applied Axial Cyclic Loading

A displacement-controlled axisymmetric axial cyclic load was simulated in the final loading step by applying a displacement boundary condition on reference node *RP-1*. The magnitude of the displacement was such that they depict the symmetric displacement limits used in the tests. The magnitudes were defined by using the tabular type amplitude provided in Abaqus. Figure 3.16 shows the graphical representation of the amplitude data for five cycles applied to the FE model. However, this displacement amplitude data was defined for each pipe specimen FE model for first two loading cycles only, as the maximum local strain range is expected to be from the first cycle. These maximum strain values were then be computed into a strain life model to predict the fatigue life of wrinkled pipes.

5.2.2.5 Solution Strategies

Abaqus/Standard generally uses Newton-Raphson's (Newton's) method as a numerical technique for solving nonlinear equilibrium equations. The motivation for this option is the convergence rate achieved by Newton's method in comparison to the convergence rates exhibited by other methods (modified Newton or Quasi-Newton methods) is higher. The Newton's method shows a quadratic convergence when the initial estimate is close to the solution, while other methods are between one and two. However, Newton's method has the highest computational costs because it calculates the Jacobian matrix at every iteration.

In structural finite element analysis, the unknown variables are usually nodal displacements. In the Abaqus iterative algorithms, the displacement increments are calculated at each iteration and the total displacements are updated using the increments until they converge. Therefore, calculating the incremental displacements is the most important step in the solution process. Abaqus/Standard has the capability of adaptively adjusting the size of the time steps by monitoring the number of convergence iterations using the default automatic incrementation scheme, which was adopted in this model. Generally, time steps that are too small can help convergence, but this increases the computational cost to finish solving an entire load increment. On the other hand, if the time step is too large, the numerical method may not converge, and the iteration stops when it reaches the maximum allowed iterations. This necessitates the use of automatic time stepping in this model.

The purpose of nonlinear finite element analysis is to satisfy the equilibrium equation (Eq. 5.4), which is equivalent to making the residual force (R^i) in Equation 5.5 vanish.

$$K_T^i \Delta d^i = F - P(d^i) \quad (5.4)$$

$$R^i = F - P(d^i) \quad (5.5)$$

Where $K_T^i \Delta d^i$ is the tangent stiffness and R^i is the residual force. The iteration stops when the magnitude of the residual force is less than a specific tolerance value. In that case, the iteration converges, and the solution is the current displacement. However, in some cases, the iteration may not converge no matter the number of iterations conducted. In order to prevent an infinite loop of the convergence iteration, the Abaqus program usually stops when the iteration counter reaches a specified maximum allowed number of iterations.

5.2.3 Material Property Verification

A numerical model was developed to simulate the uniaxial tension test conducted on coupon specimen 6 (as described in section 3.4), to verify the elastic-plastic response of the pipe material when wrinkle is initiated. The numerical (FE) model was developed using the same commercially available finite element analysis code Abaqus/CAE version 6.14, as used to simulate the behaviour of wrinkled pipe.

The elastic-plastic material property data for the model was extracted from the results of the experimental coupon test on coupon 6, where the modulus of elasticity (E) is 192 GPa and Poisson ratio (ν) is 0.3. The plastic material behaviour defined in the model was limited to the true stress and true strain data obtained prior to the onset of necking in the experimental test. Since no attempts were made to determine the pipe material properties in the circumferential direction, the material behavior was assumed to be the same in all direction, and as such isotropic.

The S4R shell type element from the Abaqus/Standard library was used to model the discrete elements in the coupon model, which was also used in the pipe for phase 1. The S4R is a general purpose 4-node, linear, doubly curved shell element with reduced integration. The element has four nodes and does not suffer from transverse shear locking, nor does it have any unconstrained hourglass modes. Each of the four nodes has six DOFs namely; the translational DOFs (U_1 , U_2 and U_3) and rotational DOFs (θ_1 , θ_2 and θ_3), where axis 1,2 and 3 are sequentially perpendicular to each other. Upon selecting an appropriate element, the coupon specimen was discretized using Abaqus CAE preprocessor with approximately 3.5 mm global seeding (see Figure 5.9).

The boundary conditions were defined in one step. The coupon model was partitioned to include both the grip segment and the 50 mm gauge length of the coupon. Initially, one end of the coupon which was attached to the hydraulic grip in the test was simulated by fixing the surface of the partitioned grip segment for all translational and rotational DOFs ($U_1 = U_2 = U_3 = \theta_1 = \theta_2 = \theta_3 = 0$). The encastre option in the Abaqus load module was used to simulate this boundary condition. Also, symmetry was maintained in the model by allowing movement only in the longitudinal direction of the coupon (U_2). This was achieved by fixing the surface nodes of the other partitioned grip segment for all DOFs except U_2 (see Figure 5.10). Furthermore, a monotonic displacement-controlled axisymmetric load was simulated in the coupon model until rupture in one step. This was achieved by applying a displacement on reference node *RP-1* (*RP-1* is coupled to the slave surface nodes on the cross section of the grip segment) in the longitudinal direction of the coupon (U_2).

The results obtained from the FE analysis are represented graphically in terms of engineering stress-strain behaviour in Figure 5.11, and the results from the coupon test are superimposed in the same plot. It can be observed that both the experimental test results and simulated coupon FEA results show good agreement with each other prior to the rupture point, where the curve starts to soften. Beyond the necking point, the FEA overestimates the material resistance to applied load, and does not accurately depict the physical behaviour observed from the coupon test. It should be noted that this discrepancy that initiates well beyond the onset of necking, giving rise to excessively large strains were not observed in the wrinkle initiation stage of the experimental program. Hence, it was concluded that the defined elastic-plastic material behaviour is suitable for accurately predicting the material response of the wrinkled pipe specimens.

Table 5.1: Plastic Material Properties Used for The Pipe Model

True Stress (MPa)	True Plastic Strain
202.5	0
319.7	0.012
355.3	0.035
382.1	0.059
403.4	0.083
421.1	0.107
436.3	0.132
449.9	0.157
462.0	0.182
477.8	0.216
499.1	0.259
526.9	0.313
563.3	0.380
608.1	0.456

Table 5.2: Effect of Mesh Density on the Accuracy and Duration of Analysis

Global Element Size (mm)	No. of Elements	No. Of Elements in Wrinkled Region	Von-Mises (Mpa)	% Error	Max Load (Before Unloading) (kN)	% Error	Run-time (Seconds)	Increase in Run-time (Seconds)	No. of Equations
4	12455	4225	410.5	0	576.5	0	254	123	116638
5	10862	2700	413.3	6.7	574.3	0.4	200	69	89188
6	10039	1921	416.0	13.3	573.4	0.5	180	49	75166
8	9167	1105	428.3	43.3	560.4	2.8	150	19	60478
10	8708	680	447.1	88.9	553.3	4.0	131	0	52828

Table 5.3: Workstation System Configuration Details

Item	Value
Operating System Name	Microsoft Windows 10 Home
System Type	x64-based PC
Processor	Intel® Core™ i7-6700 CPU @ 3.40 GHz, 4 Cores, 8 Logical Processors
Installed Physical Memory (RAM)	16.0 GB
Total Available Memory (RAM)	15.9 GB

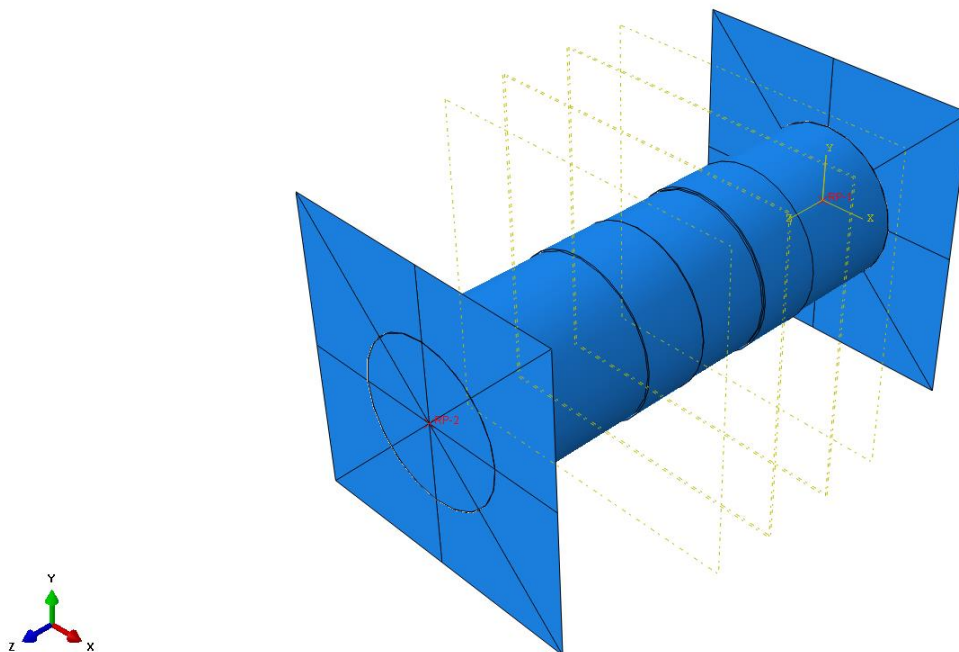


Figure 5.1: General Pipe Assembly

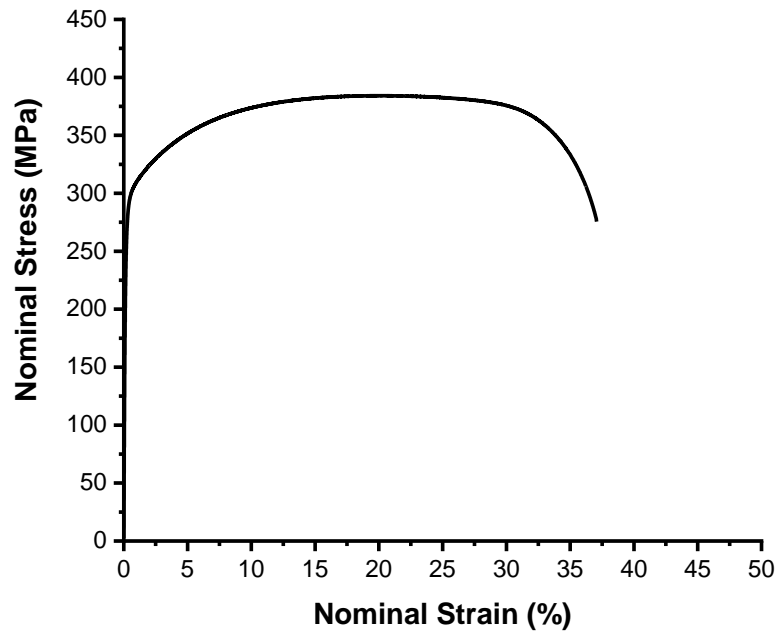


Figure 5.2: Nominal Stress and Strain Behaviour of API 5L X42 Pipe Material from Coupon 6

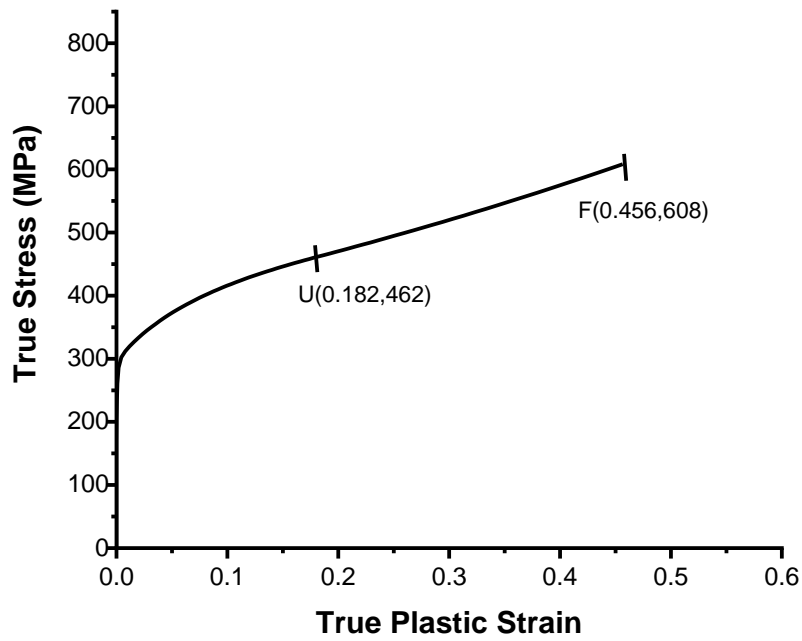


Figure 5.3: True Stress and True Plastic Strain Behaviour till Fracture

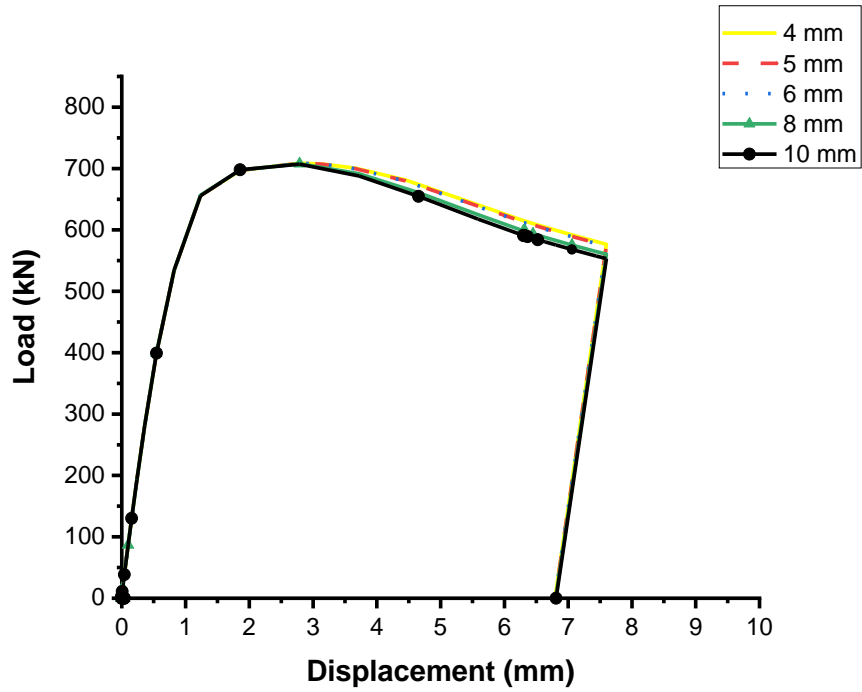


Figure 5.4: Load vs. Global Displacement Behaviour for Specimen IP30WA4 with Varying Mesh Densities

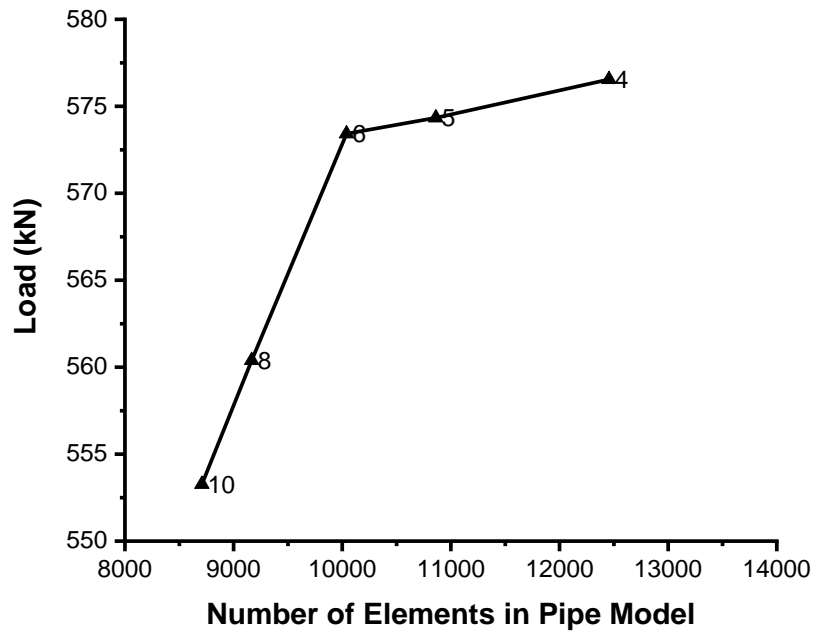


Figure 5.5: Load at Maximum Displacement vs. Varying Mesh Density for Specimen IP30WA4

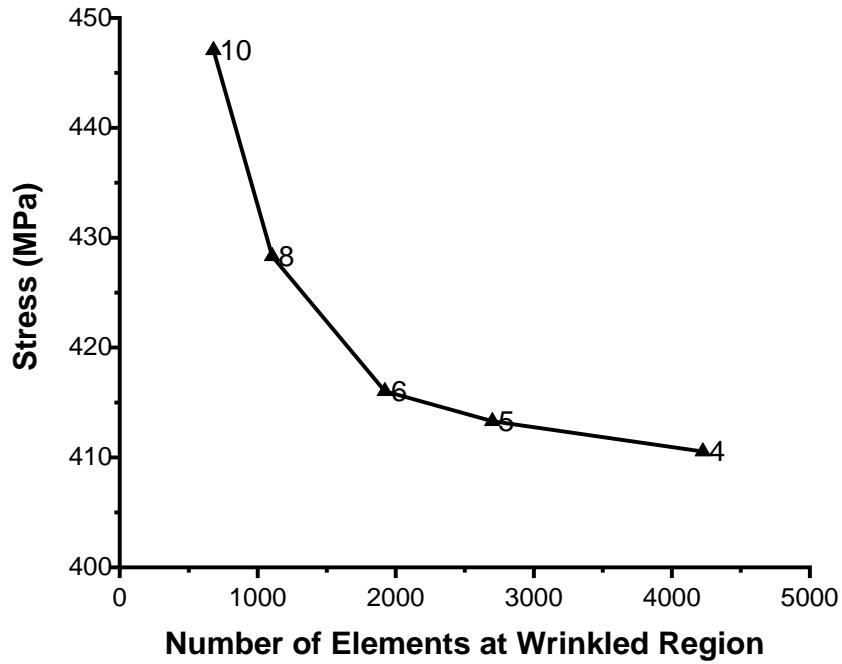


Figure 5.6: von Mises Stress at Wrinkle Crest vs. Mesh Density for Specimen IP30WA4

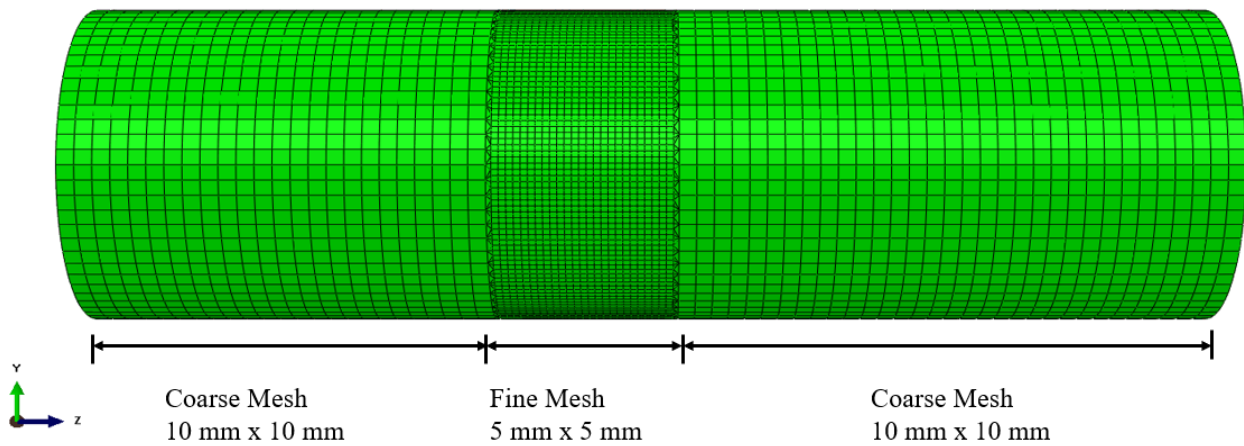


Figure 5.7(a): Typical Pipe Mesh

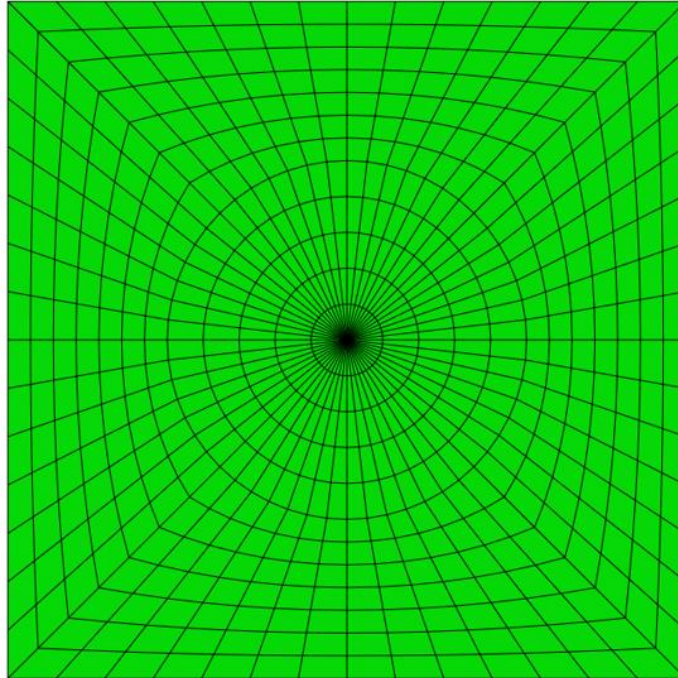


Figure 5.7(b): Typical Endplate Mesh

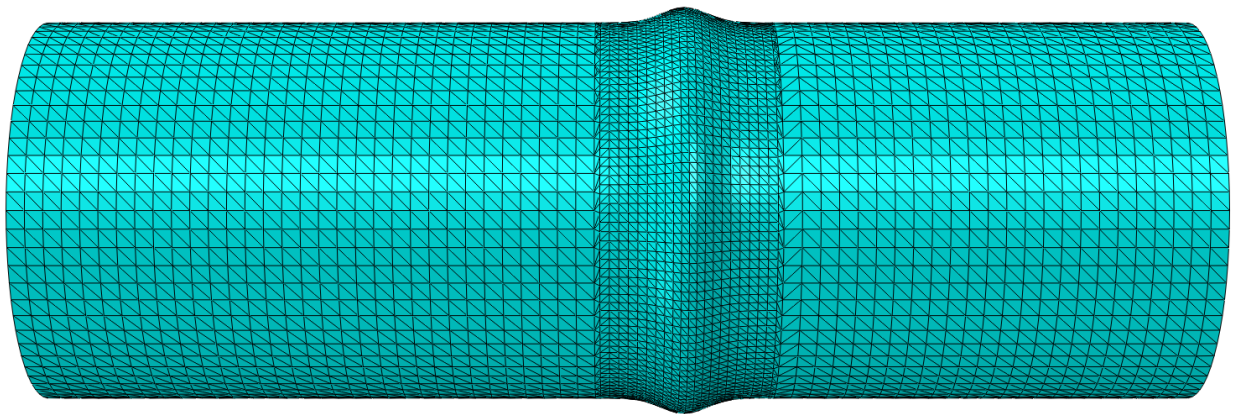


Figure 5.8: Meshing of Imported Deformed Pipe Geometry

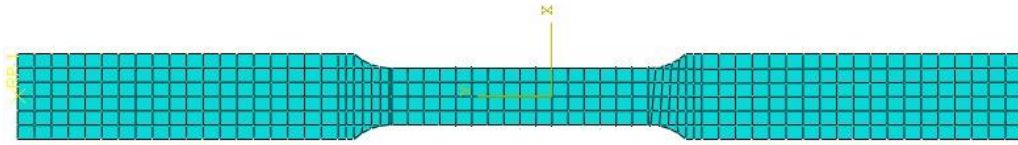


Figure 5.9: Element Selection and Meshing for Coupon 6 FE Model

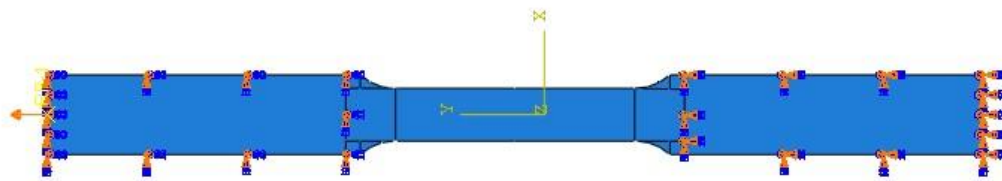


Figure 5.10: Schematics of Boundary Conditions Associated with Coupon 6 FE Model

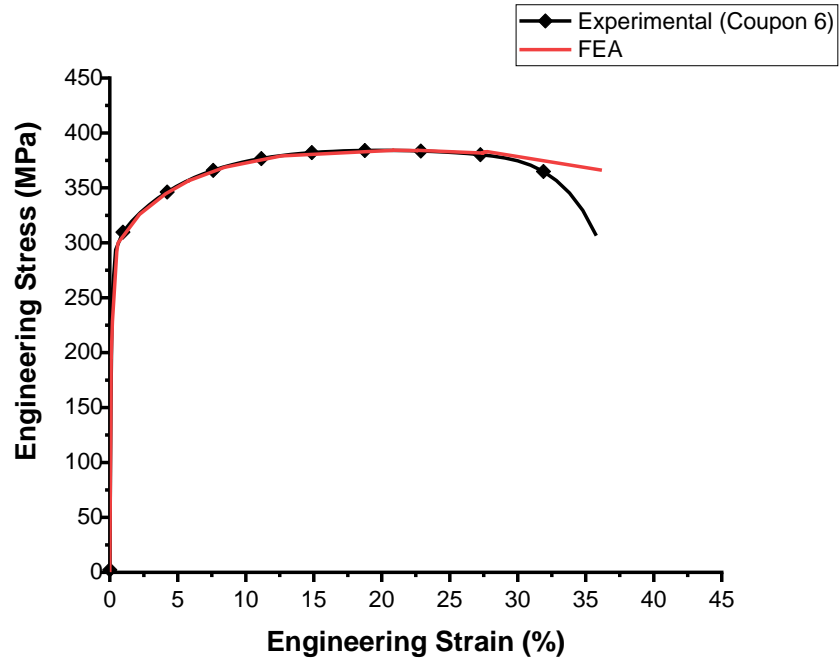


Figure 5.11: API 5L X42 Elastic-plastic Material Verification

CHAPTER 6

VALIDATION OF FINITE ELEMENT MODEL

6.1 General

Finite element analysis (FEA) is a powerful tool which can be used to evaluate complex structural engineering problems. However, results obtained from finite element analyses need to be validated using experimental test data. A good agreement justifies the application of the numerical tool for the prediction of the complex structural behavior.

The primary objective of the numerical analysis is to develop a numerical tool that can simulate the complicated structural behaviour that was observed from the axial cyclic loading on the specimens. As a result, calibration of the numerical models was done based on global and local behaviour. A good correlation between the FEA and test models is obtained for the wrinkle defect initiation and axial cyclic loading phase.

Therefore, the purpose of this chapter is to discuss the procedure of validating the developed finite element (FE) model, against the physical test data presented in Chapter 4.

6.2 Phase 1 – Initiation of Wrinkle Defect

The experimental test data belonging to the wrinkle initiation phase (see Section 4.2) was used to validate the results obtained from the wrinkle formation in the FE model. Specifically, the load vs. global and local deformation behaviours (obtained from loadcell and LVDT data) of each pipe specimen was compared with the global deformation behaviour obtained from the FEA results. This is graphically represented in Figures 6.1 through 6.8. Additionally, the wrinkle profiles measured with the contour gauge from the experimental tests was used to validate the wrinkle amplitude obtained from the FEA data (Table 6.1).

A summary of the experimental and FEA results for both groups obtained from the wrinkle formation phase (phase 1) are provided in Table 6.1 and Table 6.2. The key information provided in these tables are obtained from the global load-deformation behaviour and wrinkle amplitude. Critical points in terms of load-displacement behaviour (yield, ultimate and maximum displacement) were compared. The % *Error* between the experimental results and FEA results were then calculated. It is to be noted that % *Error* in this context is defined as the difference between the predicted result using FEA ($FEA_{predicted}$), and the results obtained through

experimental methods ($Experimental_{result}$), normalized by the experimental results ($Experimental_{result}$); as shown in Equation 6.1.

$$\% Error = \frac{FEA_{predicted} - Experimental_{result}}{Experimental_{result}} \times 100 \quad (6.1)$$

6.2.1 Discussion on Group 1 Specimens

6.2.1.1 Comparison for Load-Displacement Behaviour

Figures 6.1, 6.2, 6.3, and 6.4 show the comparison in the load vs. global displacement behaviours of specimens in Group 1 obtained from the tests and FEA results for Specimens IP30WA10.5, IP30WA8, IP30WA6, and IP30WA4, respectively. It can be observed that linear-elastic portion (stiffness) of the graphs are in good agreement, and most of the hardening and softening portion are almost similar. Except for the minor discrepancy observed in specimen IP30WA6, which was due to the mismanagement of the internal pressure during the experimental procedure. Due to mechanical fault, the hydraulic pump was not maintaining pressure in the specimen at targeted magnitude during the test, and as such targeted pressure magnitude was maintained by operating the pump manually. Furthermore, as observed from evaluated errors in Table 6.1, aside from the displacement at the ultimate load, the FEA results are within the accepted tolerance (<10%) of the experimental results. Therefore, it was concluded that the developed model is capable of predicting the load vs global displacement behaviour of the tested specimens.

6.2.2 Discussion on Group 2 Specimens

6.2.2.1 Comparison for Load-Displacement Behaviour

Figures 6.5, 6.6, 6.7, and 6.8 show the graphical representation of the Group 2 specimens for load vs. global displacement behaviour obtained from the experimental work and FEA for specimens IP60WA10.5, IP60WA8, IP60WA6, and IP60WA4, respectively. It can be observed that the linear-elastic portion (stiffness) of the graphs are in good agreement, and most of the hardening and softening portion are in a good agreement. As observed from evaluated errors in Table 6.2, the FEA results are within the accepted tolerance (<10%) of the experimental results. Therefore, it was concluded that the developed model is capable of predicting the load vs. global displacement behaviour of the tested specimens.

6.2.3 Comparison of Wrinkled Shape

Figures 6.9 through 6.12 show the comparison between the wrinkle profile obtained from the tests and FEA of Group 1 Specimens. It can be observed that the severity of the wrinkle increases with increase in the wrinkle amplitude, since the internal pressure is similar for all Group 1 specimens. Similarly, from Table 6.1, it can be observed that height of the wrinkle amplitude for each FEA deformed shape is within acceptable tolerance of the experimental deformed configuration.

6.3 Phase 2 – Axial Cyclic Loading

The experimental results obtained from the axial cyclic loading of the wrinkled pipe specimen (phase 1), was used to validate the axial cyclic response of the finite element model. Specifically, the localized load-strain hysteresis loop obtained from the test specimen was compared with the same data obtained from the FE model at the wrinkle crest. The strain response at the wrinkle crest could not be captured for the entirety of the cyclic load history due to the curvature gradient created by the wrinkle defect. This limitation is similar for all pipe specimens tested. However, in order to estimate the remaining fatigue life of the tested wrinkled pipes using the strain life fatigue approach ($\Delta\varepsilon-N$), the cycle for which the localized strain range is maximum is considered. According to the experimental results from subsection 4.3.4, the observed phenomenon of ratcheting which is accompanied by the reduction of the cyclic plastic strain (ratcheting strain) with increasing number of cycles, agrees well with the results obtained from FEA.

6.3.1 Comparison of Cyclic Load vs. Local Strain Behaviour

Similar to the observations made from the results of the experimental testing as discussed in section 4.5, the wrinkled pipe specimens lose the energy-absorption capacity with increasing cycles. This statement can be verified with Figure 6.13a, which shows the graphical representation of the localized cyclic load-strain response at the crest of the wrinkled pipe IP30WA4 at various cycles. As observed in the simulated FEA results, each loop in the hysteresis experiences ratcheting with increasing number of cycles. A similar behaviour was also observed from the test specimen IP30WA4 (see Figure 4.13a and this figure is also presented in this chapter as Figure 6.13b).

Figures 6.14 to 6.17 show the first cyclic load-strain response for all specimens of Group 1 obtained from the FE analysis and tests. These plots validate the summary of observations from section 4.5, that the most severe wrinkle defect profile has the least energy-absorption capability left in its post-wrinkling stage. Furthermore, the comparison shows that difference in the cyclic

load-strain response for each specimen is proximate. The differences are small, and it can be identified with the fact that the J_2 flow plasticity model with combined hardening for material inelastic behaviour was not sufficiently defined. The defined stabilized data type for the combined hardening model was extracted from the monotonic tensile tests performed on the coupon strip specimens. Ideally, the data should be extracted from a strain-controlled fatigue test done on coupon strip specimens of X42 pipe material cut from pipes used for the full-scale test. The comparison for cyclic load vs. local strain behaviour for Group 2 specimens is not discussed in this study due to the restrictions placed on the University of Windsor structural laboratory during COVID-19 pandemic. Hence, material properties could not be obtained from tension testing on coupon strip specimens.

6.4 Strain-Life Fatigue Assessment

The strain-based approach was developed in the late 1950s and early 1960s by both L.F. Coffin and S.S. Manson, in response to the need to analyze problems involving short fatigue lives. This approach to fatigue considers the plastic deformation that may occur in the localized regions where fatigue cracks begin, and stresses and strains are concentrated. This procedure allows a more detailed analysis of local yielding, therefore, gives an improved remaining life estimate of ductile materials with short fatigue lives.

In order to employ the strain life approach ($\Delta\varepsilon$ - N), the values of the maximum local strain range ($\Delta\varepsilon_{max}$) computed numerically are used as input into an appropriate fatigue curve of the pipe material to predict the remaining number of cycles to failure. The appropriate fatigue curve of the pipe material is obtained from the Coffin-Manson-Basquin fatigue formula, given in Equation 6.1.

$$\frac{\Delta\varepsilon_{max}}{2} = \frac{\sigma'_f}{E} (2N_f)^b + \varepsilon'_f (2N_f)^c \quad (6.1)$$

In this equation, σ'_f is a fatigue strength coefficient, ε'_f is the fatigue ductility coefficient, b is the fatigue strength exponent, c is the fatigue ductility exponent, and N_f is the number of cycles to failure. Usually, the strain-life curves are obtained from material fatigue tests, where a material is loaded under different strain amplitudes for completely reversed ($R = -1$) cyclic loading between constant strain limits. From the stabilized hysteresis loop of each material cyclically loaded at different strain amplitudes, the plot of the elastic strain amplitude and plastic strain amplitudes against number of reversals to failure are obtained (see Figure 6.18a). If the data from different

tests are plotted, the elastic strains (ε_e) often give a straight line of shallow slope on a log-log plot (b), equivalent to Equation 6.2. The plastic strains (ε_p) give a straight line of steeper slope (c) on the same plot, equivalent to Equation 6.3.

$$\varepsilon_e = \frac{\sigma_f'}{E} (2N_f)^b \quad (6.2)$$

$$\varepsilon_p = \varepsilon_f' (2N_f)^c \quad (6.3)$$

The Coffin-Manson-Basquin fatigue life equation (Equation 6.1) is a combination of Equations 6.2 and 6.3. Therefore, it becomes apparent that at short lives, the plastic strains are large compared to the elastic strains, which makes the curve tend to approach the plastic strain line (Figure 6.18a), and the hysteresis loops fat. Inversely, at long lives, the elastic strains are dominant, which makes the curve tend to elastic strain line, and hysteresis loops thin.

Ideally, longitudinal strips should be cut from the X42 8-inch (211.58 mm) diameter pipe specimens and tested under cyclic loading through a special set-up until fatigue crack failure occurs. Local strain values should then be extracted from the most critical region of the strip specimens and correlated with local strain values obtained from finite element analysis for validation. The material fatigue data and curve obtained from this process was used to estimate the remaining life of the buckled pipes by Dama et al. (2007) and Pournara et al. (2015) at the University of Thessaly in Greece. However, in the current study, due to time limitation, strain-controlled fatigue tests could not be performed on the material, and the cyclic material properties could not be generated experimentally for the X42 pipe material. Therefore, the cyclic material properties for material pipe grade X42 were obtained from ASM handbook paper on fatigue resistance of steels (Boardman, 1990). The material properties for constants σ_f' , ε_f' , b and c are given as 902 MPa, 0.17, -0.12 and -0.42 respectively.

It is widely accepted that fatigue strength of a material is greatly influenced by the mean stress; where mean stress (σ_m) is defined by the average of the maximum (σ_{max}) and minimum (σ_{min}) stresses, as shown in Equation 6.4.

$$\sigma_m = \frac{\sigma_{max} + \sigma_{min}}{2} \quad (6.4)$$

For a strain-controlled cyclic test conducted with a non-zero mean strain, full or partial cycle dependent relaxation of the mean stress is achieved with continued cycling. If the cyclic plastic strain from the cycle dependent softening is large enough, the resulting mean stress shifts towards zero, this behaviour is observed in the current study and it is referred to as mean stress relaxation (see Figure 6.18b). In order to correct the effect of mean stress, Morrow subtracted the mean stress from the fatigue strength in the elastic part of the original Basquin equation, as given in Equation 6.5; presuming that mean stress effect is insignificant in the part which is dominated by plastic strains.

$$\frac{\Delta\varepsilon_{max}}{2} = \frac{\sigma'_f - \sigma_m}{E} (2N_f)^b + \varepsilon'_f (2N_f)^c \quad (6.5)$$

However, Manson and Halford modified both the elastic and plastic terms of the strain-life equation to maintain the independence of the elastic-plastic strain ratio from mean stress. The Manson-Halford equation is given in Equation 6.6.

$$\frac{\Delta\varepsilon_{max}}{2} = \frac{\sigma'_f - \sigma_m}{E} (2N_f)^b + \varepsilon'_f \left(\frac{\sigma'_f - \sigma_m}{\sigma'_f} \right)^{c/b} (2N_f)^c \quad (6.6)$$

The fatigue life of the wrinkled pipes is now estimated by correlating the reversals to failure obtained from the mean stress effect correction models discussed above.

6.5 Numerical Quantification of Strain Values

In order to quantify the maximum local strain values at the most critical region of the wrinkle, maximum principal strain values were extracted from the finite element analysis. The maximum principal strain values were obtained from the internal surface (intrados) of the pipe model (see Figure 6.19). The failure initiated from the internal surface of the wrinkle of the pipe, hence, integration node number one (section point at bottom) will generate the most critical strain values. The maximum principal strain values were extracted from the intrados of the pipe model, because of the failure mode observed from the experimental test. The fracture failure in the tests initiated from the inside surface and propagated towards the external surface of the pipe specimen. Figure 6.20 shows the plot of the maximum principal strain on the inside surface of the pipe, considering

approximately 5-inch (120 mm) distance across the wrinkle profile for Group 1 specimens. This figure shows that the specimen with the smallest wrinkle amplitude after deformation (IP30WA4) accumulates the most plastic strain when subjected to axial cyclic loads. This observation agrees with the experimental results, which further confirms the concept that an increase in wrinkle amplitude leads to an increase in the fatigue life of pipelines subjected to displacement controlled axial cyclic loading. The maximum local strain range was then computed as the difference between the maximum and minimum principal strain in the first loading cycle, located at the wrinkle crest. Table 6.3 shows the computed maximum local longitudinal strain range for Group 1 specimens.

The strain-based approach carried out by Pournara et al. (2015) to estimate the remaining life of buckled pipes gave similar observation as the current study. Although, buckled pipes subjected to cyclic bending loads failed at LCF range (200 to 920) significantly higher than in the current study (19 to 39). The buckled pipe specimen that required the most load reversals, accumulated the least plastic strain during the four-point bending. Therefore, buckled pipes that failed at 920 cycles, had a maximum local strain range of 1.42%. Whereas, buckled pipes that failed at 550 and 200 cycles, had a maximum local strain range of 1.78% and 2.71%, respectively.

6.6 Correlation of Number of Cycles to Failure

The maximum local strain range values extracted from the FE analyses, are substituted into the strain life models to estimate the number of cycles to failure. The values of the mean stress that are used to correct the strain life model are highlighted in Table 6.3. These mean stress values are then used in the strain life model to generate different equations, depending on wrinkle amplitude. The results computed for the number of cycles to failure (N_f) using Basquin and Morrow model, are fairly similar with minor disparity. The pattern from these fatigue life models agree with the argument that an increase in wrinkle amplitude leads to an increase in the fatigue life (Figure 6.21). However, when N_f gotten from these two models are compared with the N_f obtained from the test results, the differences in the number of cycles to failure are significant. These discrepancies can be associated with the fact that the material fatigue data used for this analysis, do not represent the cyclic material behaviour of the pipe specimens tested in this study in their entirety. Although, the Mason-Halford model gives a more conservative approximation for N_f , the pattern does not align with the former argument that an increase in wrinkle amplitude leads to an increase in the fatigue life. The Morrow model, however, is recommended in this study as the suitable fatigue analysis

model to estimate the number of cycles to failure of a wrinkled pipe subjected to axial cyclic loading.

6.7 Summary

This chapter validates the numerical analysis conducted on Group 1 and Group 2 specimens, by comparing the results of the finite element analysis with results obtained from experimental program. The generated finite element model adequately depicts the elastic-plastic behaviour of the pipe specimen in the wrinkle initiation stage, and as such can be inducted for further parametric study. The multi-stage finite element (FE) model developed, also validates the local longitudinal strain behaviour of Group 1 specimens at the most critical region (wrinkle crest), depending on the wrinkle amplitude. The fatigue life of the wrinkled pipe specimens was estimated using different strain life models, depending on the quantified maximum local strain range from the FE model. The Morrow strain life model was then recommended as the suitable strain life model, for the range of parameters considered in this study.

Table 6.1: Summary of Experimental and FEA Results for Group 1 Specimens

Critical Points			Specimen ID			
			IP30WA10.5	IP30WA8	IP30WA6	IP30WA4
At Yield Point	Δ_Y (mm)	Experimental	1.1	1.1	1.5	1.1
		FEA	1.1	1.1	1.1	1.1
		% Error	0	0	27.63	0
	P_Y (kN)	Experimental	629	630	607	632
		FEA	640	640	640	640
		% Error	1.75	1.59	5.44	1.27
At Ultimate Point	Δ_U (mm)	Experimental	3.5	3.4	5.1	3.2
		FEA	2.8	2.8	2.8	3.01
		% Error	20	17.65	45.10	5.94
	P_U (kN)	Experimental	762	764	771	765
		FEA	710	710	721	723
		% Error	6.82	7.07	6.49	5.49
At Maximum Displacement	Δ_F (mm)	Experimental	31	19	13.1	8.1
		FEA	31.2	19	13	8
		% Error	0.65	0	0.76	1.23
	P_F (kN)	Experimental	322	364	460	541
		FEA	325	391	461	587
		% Error	0.93	7.42	0.22	8.5
Wrinkle Amplitude	h (mm)	Experimental	22.5	17.5	12.5	8.5
		FEA	21.58	17.08	13.32	9
		% Error	4.09	2.4	6.56	5.88

Table 6.2: Summary of Experimental and FEA Results for Group 2 Specimens

Critical Points			Specimen ID			
			IP60WA10.5	IP60WA8	IP60WA6	IP60WA4
At Yield Point	Δ_Y (mm)	Experimental	1.3	1.3	1.3	1.3
		FEA	1.2	1.2	1.2	1.2
		% Error	0.08	0.08	7.70	0.08
	P_Y (kN)	Experimental	687	712	677	685
		FEA	643	643	643	643
		% Error	6.40	9.69	5.02	6.13
At Ultimate Point	Δ_U (mm)	Experimental	4.7	4.2	4.7	4.7
		FEA	4.3	4.3	4.3	4.3
		% Error	8.51	2.38	8.51	8.51
	P_U (kN)	Experimental	822	820	825	825
		FEA	790	790	790	790
		% Error	3.89	3.66	4.24	4.24
At Maximum Displacement	Δ_F (mm)	Experimental	30.8	17.5	12.2	8.1
		FEA	30.6	18.1	12	8
		% Error	0.65	3.43	1.64	1.23
	P_F (kN)	Experimental	471	531	588	661
		FEA	458	531	580	610
		% Error	2.76	0	1.36	7.72
Wrinkle Amplitude	h (mm)	Experimental	22	17.5	13	8.7
		FEA	21.9	18.1	12.2	9
		% Error	0.45	3.43	6.15	3.44

Table 6.3: Summary of Comparison of Results from Strain Life Fatigue Models for Group 1 Specimens

Specimen ID	P_{max} (kN)	P_{min} (kN)	σ_{max} (MPa)	σ_{min} (MPa)	Mean Stress Values (MPa)	Max strain Range (FEA)	Original Cycle to failure (N_f)	N_f Basquin	N_f Morrow	N_f Mason - Halford
IP30WA10.5	305	-75	242	-59	92	0.0313	39	190	183	66
IP30WA8	343	-166	272	-132	70	0.048	34	63	62	29
IP30WA6	414	-327	328	-259	35	0.052	32	52	51	34
IP30WA4	497	-572	394	-454	-30	0.07	27	25	25	38

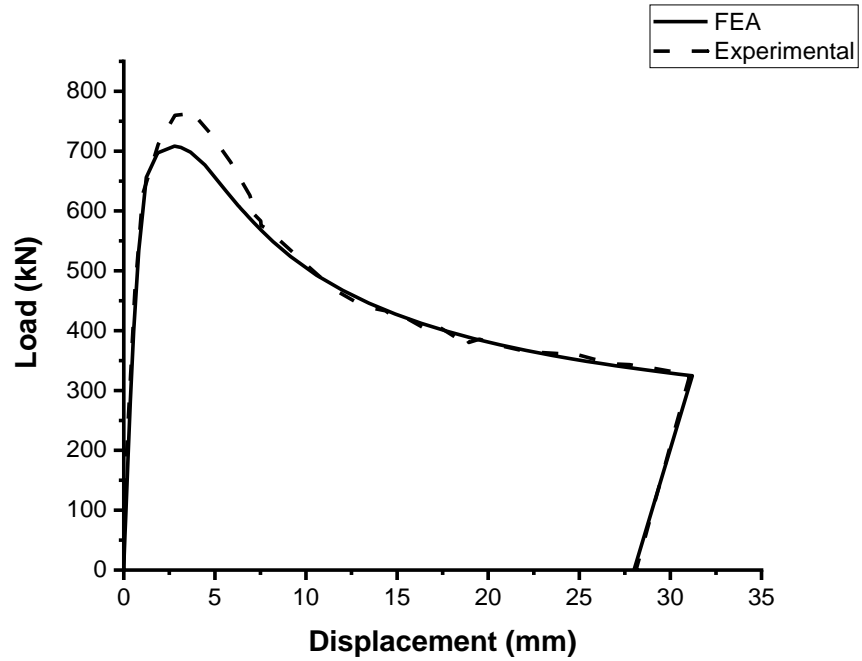


Figure 6.1: Comparison for Load vs Displacement Plot Between Experimental and FEA Results for Specimen IP30WA10.5

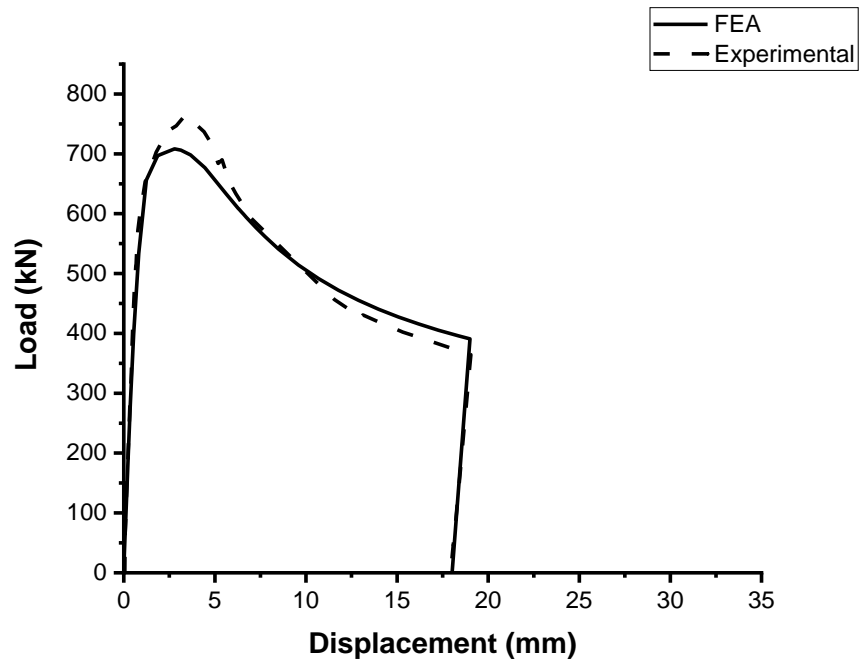


Figure 6.2: Comparison for Load vs Displacement Plot Between Experimental and FEA Results for Specimen IP30WA8

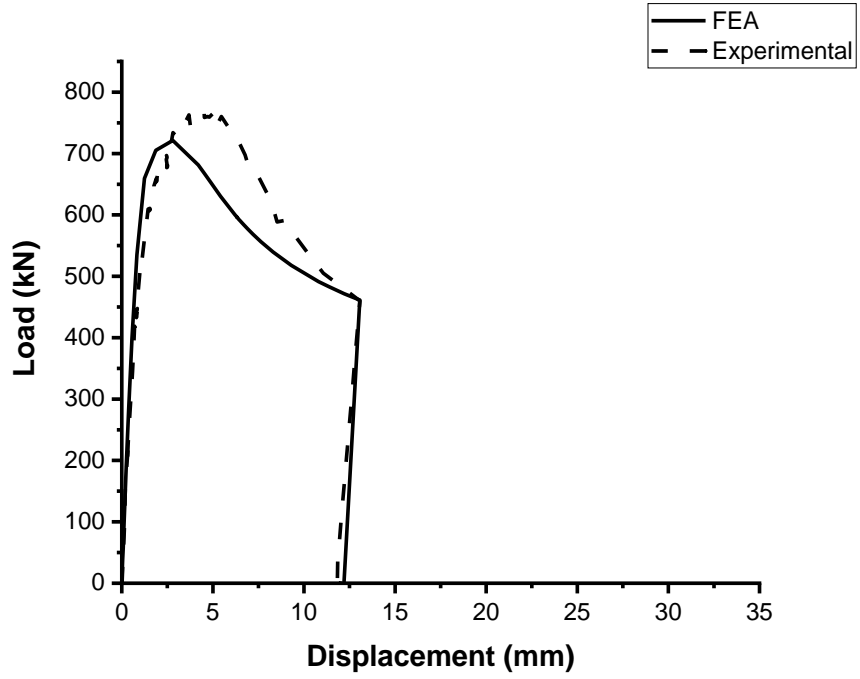


Figure 6.3: Comparison for Load vs Displacement Plot Between Experimental and FEA Results for Specimen IP30WA6

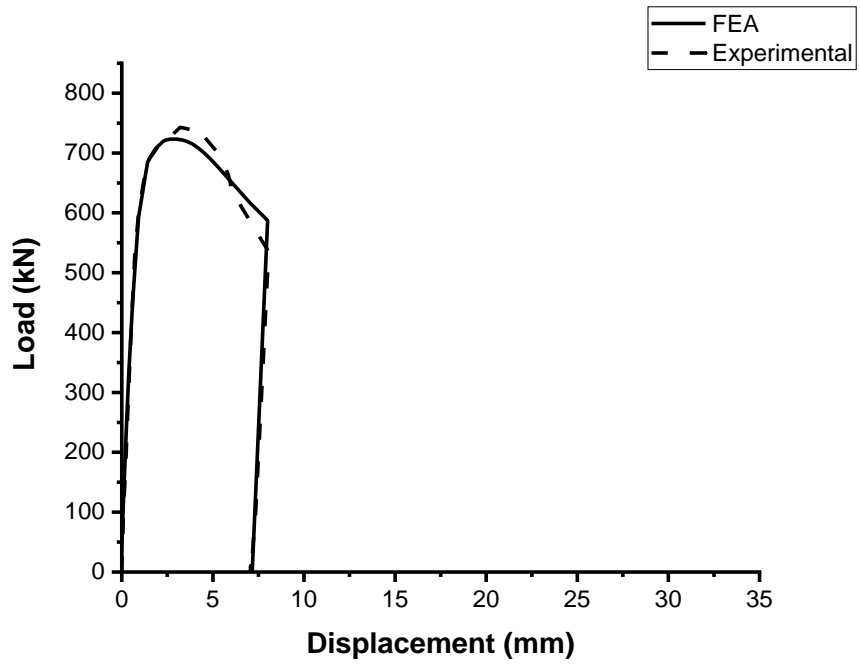


Figure 6.4: Comparison for Load vs Displacement Plot Between Experimental and FEA Results for Specimen IP30WA4

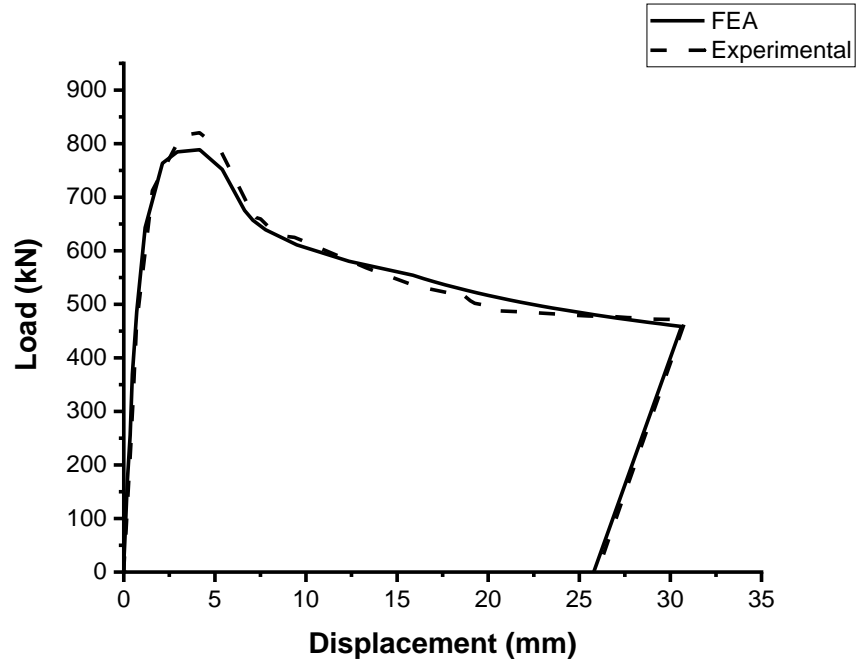


Figure 6.5: Comparison for Load vs Displacement Plot Between Experimental and FEA Results for Specimen IP60WA10.5

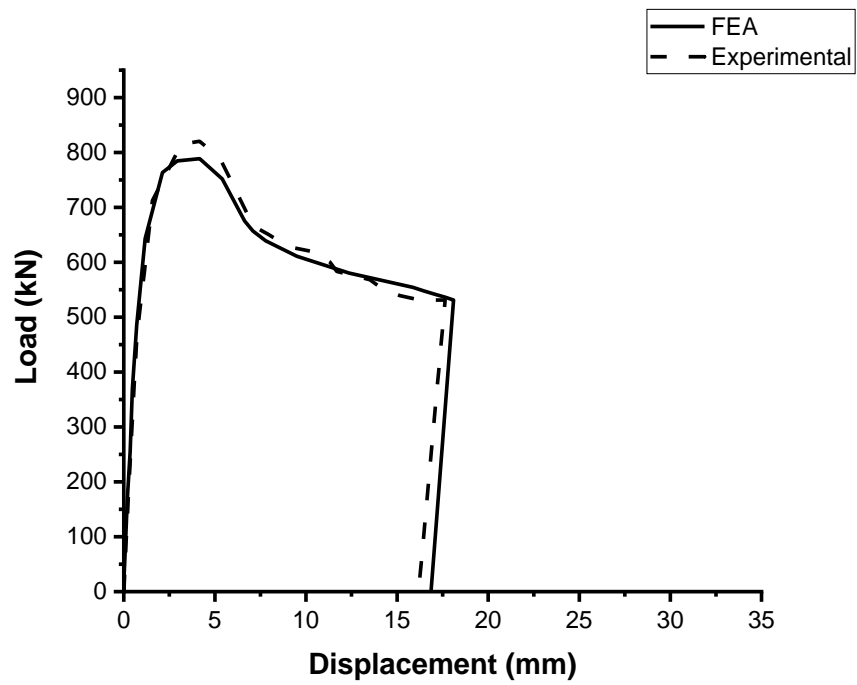


Figure 6.6: Comparison for Load vs Displacement Plot Between Experimental and FEA Results for Specimen IP60WA8

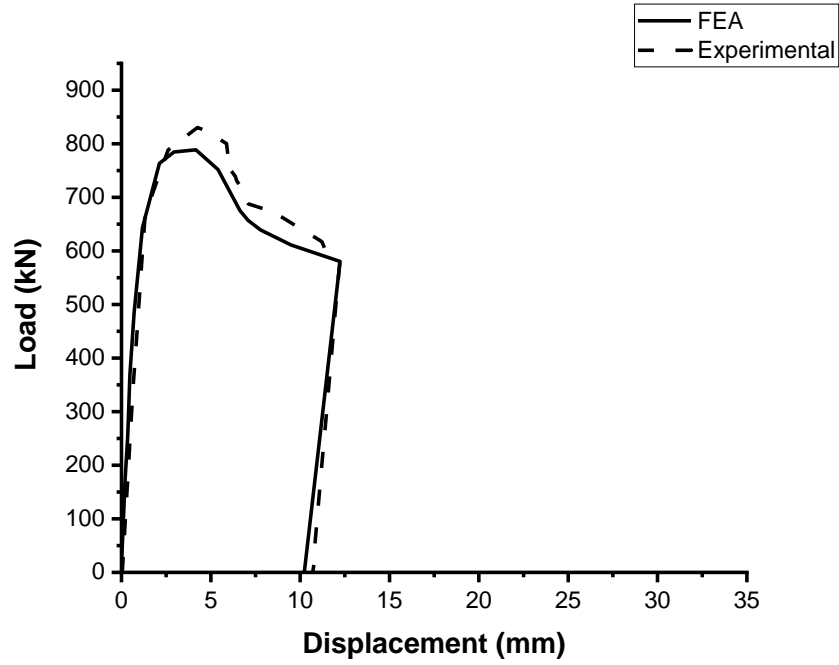


Figure 6.7: Comparison for Load vs Displacement Plot Between Experimental and FEA Results for Specimen IP60WA6

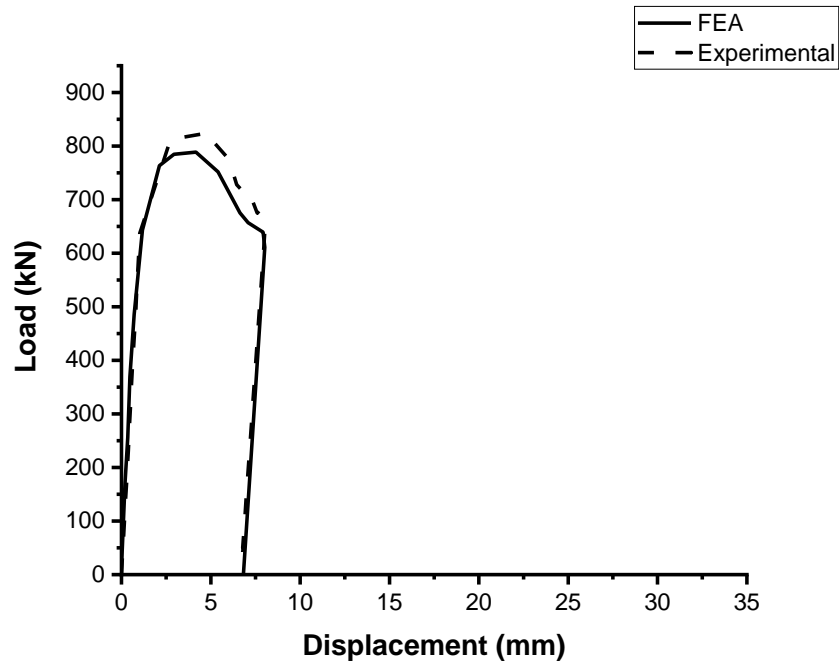
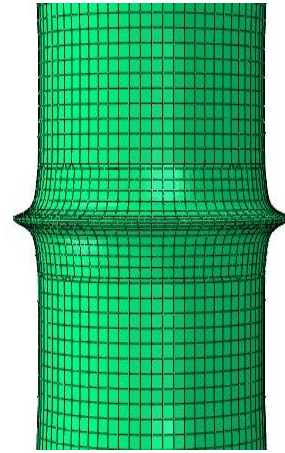


Figure 6.8: Comparison for Load vs Displacement Plot Between Experimental and FEA Results for Specimen IP60WA4



Experiment



FEA

Figure 6.9: Comparison of Deformed Shape for Specimen IP30WA10.5



Experiment



FEA

Figure 6.10: Comparison of Deformed Shape for Specimen IP30WA8



Experiment



FEA

Figure 6.11: Comparison of Deformed Shape for Specimen IP30WA6



Experiment



FEA

Figure 6.12: Comparison of Deformed Shape for Specimen IP30WA4

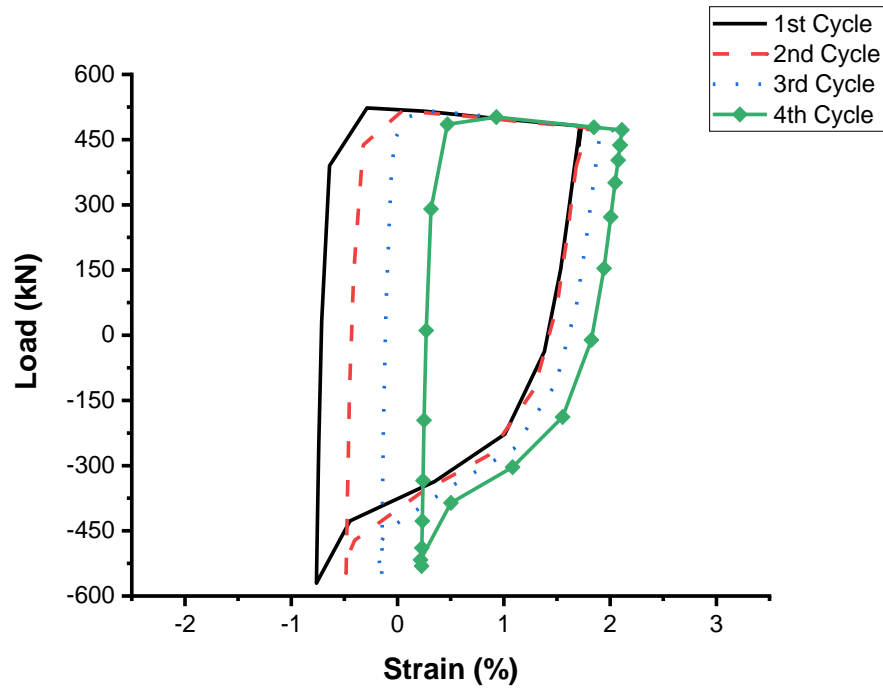


Figure 6.13a: Relationship Between Local Longitudinal Strain and Applied Load at Wrinkle Crest Obtained from FEA for Specimen IP30WA4

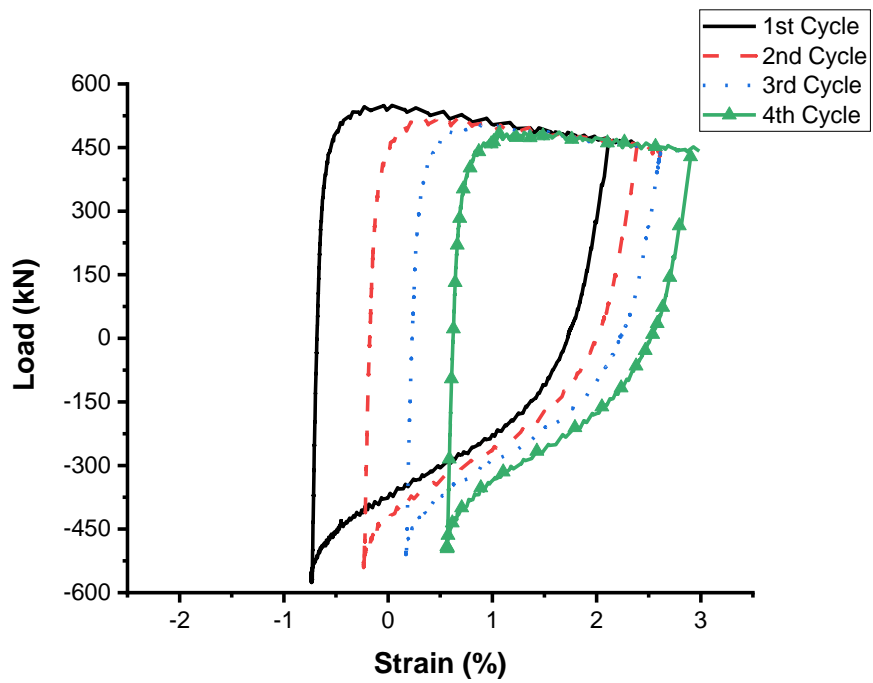


Figure 6.13b: Relationship Between Local Longitudinal Strain and Applied Load at Wrinkle Crest Obtained from Experiment for Specimen IP30WA4

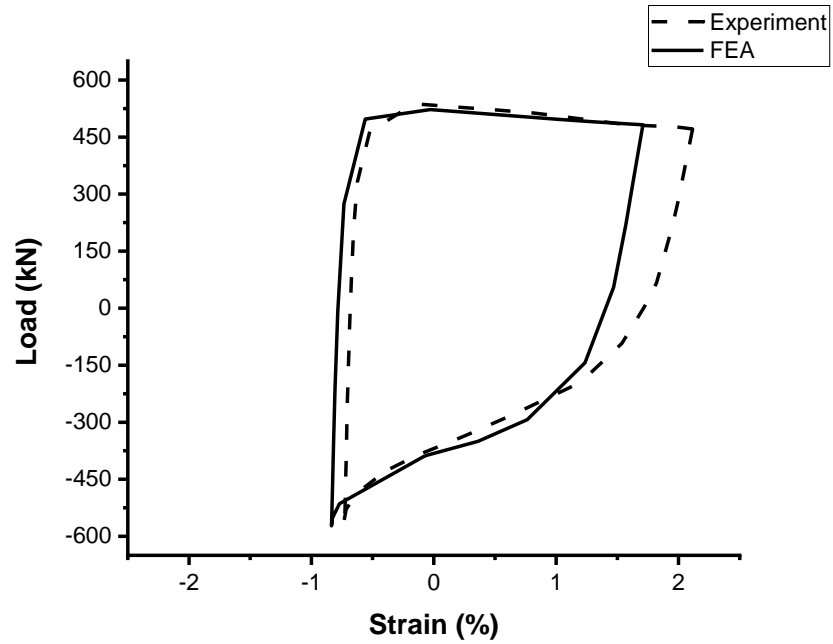


Figure 6.14: First Cycle Comparison for the Relationship Between Local Longitudinal Strain and Applied Load at Wrinkle Crest for Specimen IP30WA4

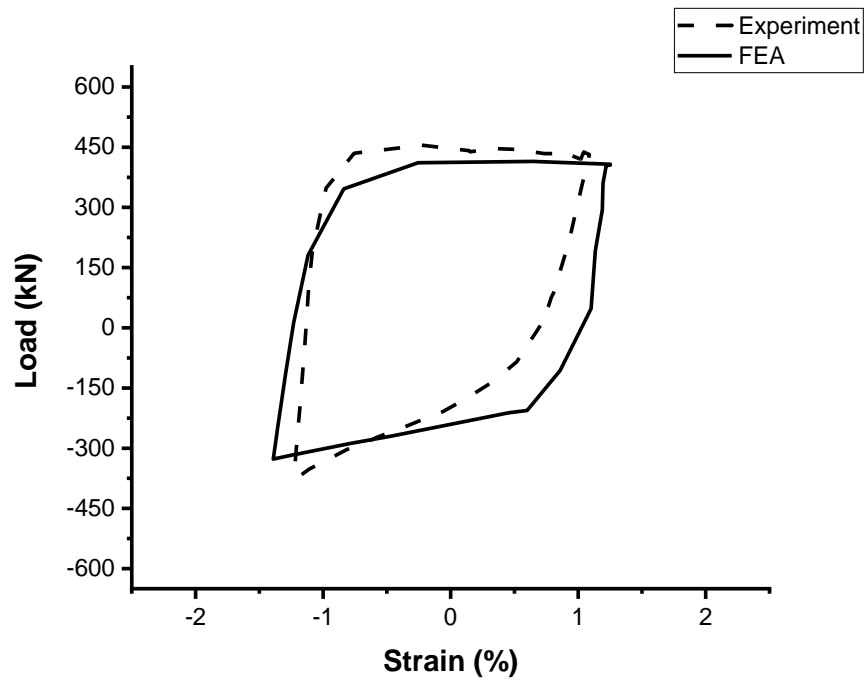


Figure 6.15: First Cycle Comparison for the Relationship Between Local Longitudinal Strain and Applied Load at Wrinkle Crest for Specimen IP30WA6

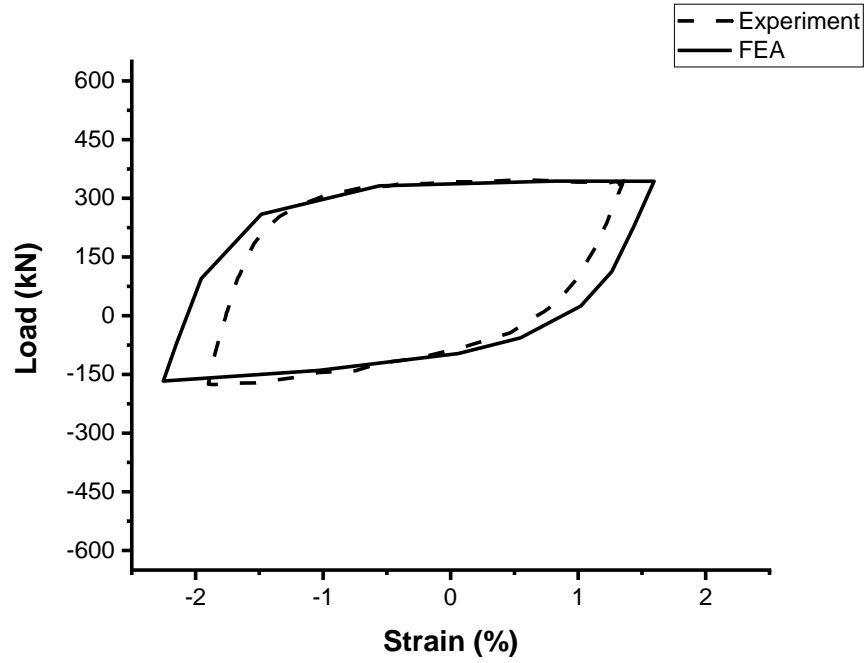


Figure 6.16: First Cycle Comparison for the Relationship Between Local Longitudinal Strain and Applied Load at Wrinkle Crest for Specimen IP30WA8

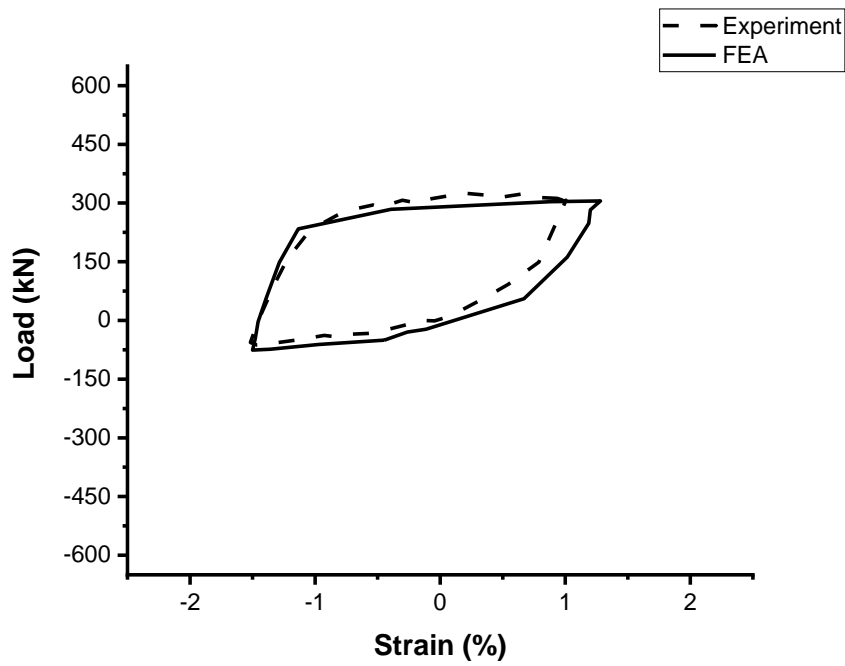


Figure 6.17: First Cycle Comparison for the Relationship Between Local Longitudinal Strain and Applied Load at Wrinkle Crest for Specimen IP30WA10.5

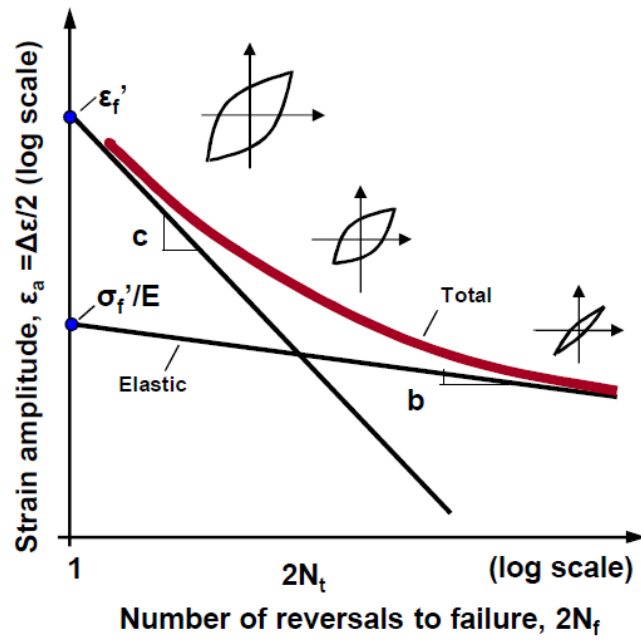


Figure 6.18a: Fatigue Strain-Life Curve (Dowling, 2013)

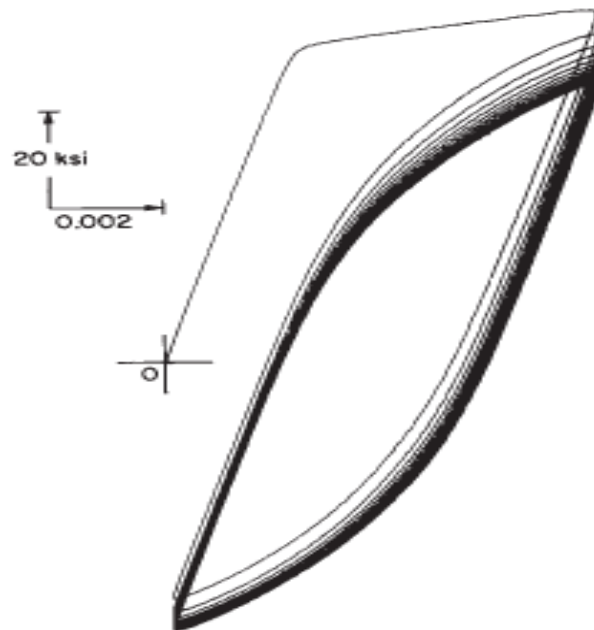
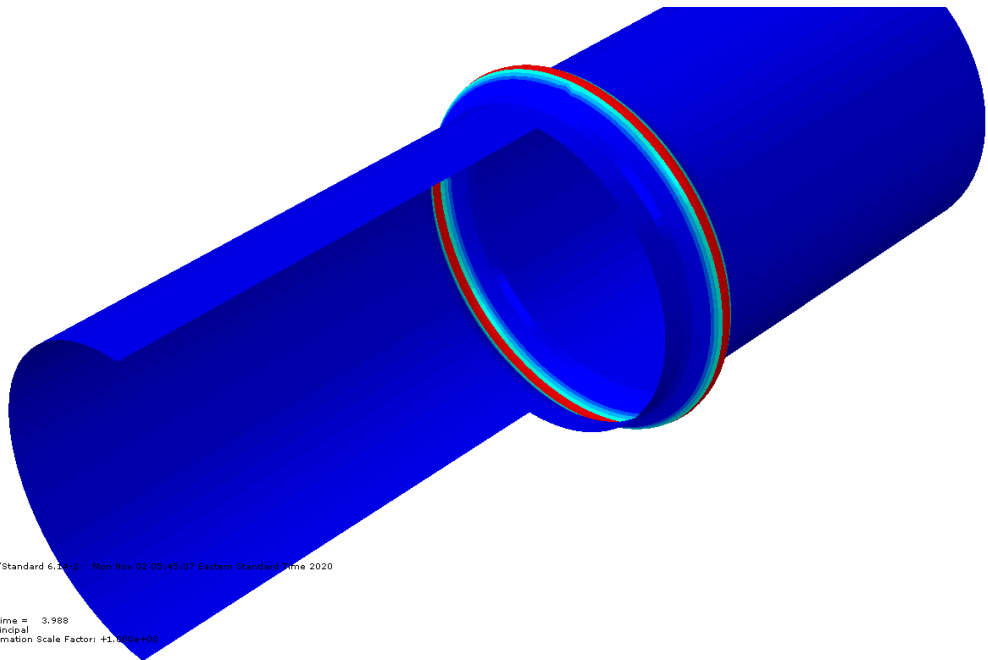
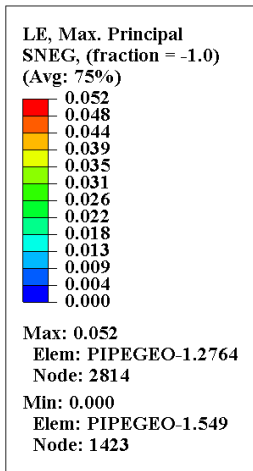


Figure 6.18b: Cycle-Dependent Relaxation of Mean Stress for an AISI 1045 Steel (Dowling, 2013)



ODB: 0%.odb Abaqus/Standard 6.24.0 Mon Nov 02 05:45:07 Eastern Standard Time 2020

Step: Axialloading
Increment: 25; Step Time = 3.988
Primary Vari: LE, Max. Principal
Deformed Vari: U; Deformation Scale Factor: +1.000e+000

Figure 6.19: FEA Results for Maximum Principal Strain After One Cycle for Specimen IP30WA8

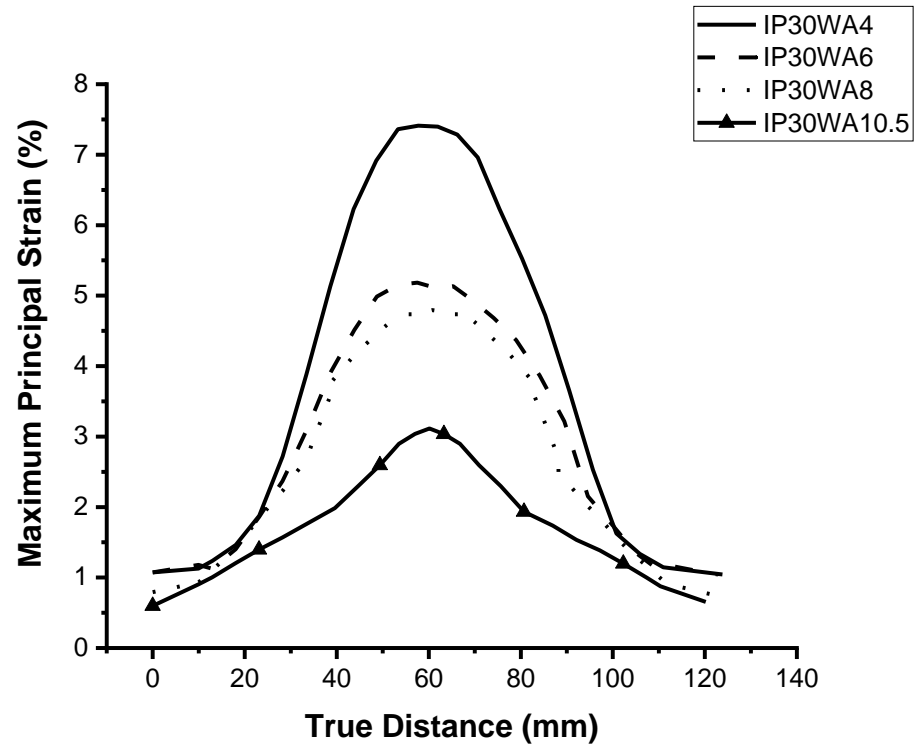


Figure 6.20: Maximum Principal Strain Along Wrinkled Region Obtained from FEA Analysis

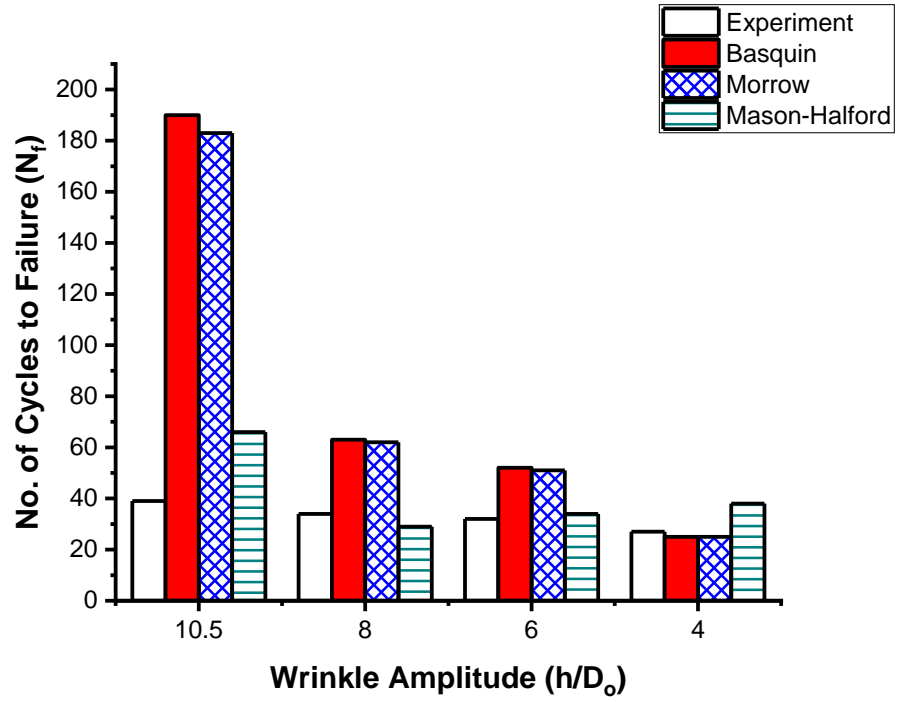


Figure 6.21: Comparison of Cycles to Failure Obtained from Strain Model and Experiment

CHAPTER 7

SUMMARY, CONCLUSIONS AND RECOMMENDATIONS

7.1 Summary

Previous field observations have established that oil and gas pipelines installed in vicious environment undergo large geotechnical movements, which can cause the growth of wrinkle defect on the pipe wall. However, the continuous operation of this wrinkled pipelines does not pose an immediate threat to the safety and integrity of pipeline segment when the pipeline is subjected to a monotonically increasing deformation. The effect of temperature variation and cyclic freeze-thaw over time, however, lead to stress reversal in the most critical region of the pipeline segment; and thereby lead to a fatigue induced rupture failure (Das et al., 2007a). The literature review and the evaluation of current codes and standards have actualized the need to develop a numerical tool for assessment of the remaining life of wrinkled steel pipelines subjected to combined internal pressure and axial cyclic loading. Hence, this study was initiated with the intention to assess the failure condition and failure mode of wrinkled pipelines when subjected to axial cyclic loads, and to quantify the magnitude of the local strain ranges within the critical regions, based on wide ranges of wrinkle geometries.

For proper understanding of the failure mode experienced by wrinkled pipes when subjected to axial cyclic loads, a two-phase experimental program was carried out on API 5L (API 5L 2018) X42 steel pipes, with D/t of 45. In the first phase, a monotonically increasing compressive axial load was applied on pipes at a maintained internal pressure (either $0.3p_y$ or $0.6p_y$) up to a target wrinkle defect profile. The targeted wrinkle defect profile ranges from 4% to 10.5% of the pipe's outer diameter. These wrinkles simulated severity of wrinkle defect ranging from small to severe. The second loading phase involved a displacement-controlled axisymmetric tension-compression axial cyclic loading until a fracture was observed at the crest of the wrinkle defect. This second loading phase replicates the temperature variation that reads 45°C that a buried field pipeline experiences in Northern Alberta due to the seasonal variation in the temperature.

The experimental program was completed, and the two phases were simulated using a nonlinear finite element analysis numerical modeling technique, with the aid of ABAQUS. The results obtained from the numerical modeling, were used to validate the test data obtained from testing the six pipe specimens. It was observed that there exists a good agreement between the FEA and

experimental results, and as such, the FE model is capable of simulating the elastoplastic behaviour of the pipe specimens. Following this observation, the magnitude of plastic strains associated with the most critical region of the wrinkled pipe model that causes failure were extracted. These quantified strains values were then incorporated into different strain life models, to predict the LCF life of wrinkled pipelines with the parameters (material and geometry) considered in this study. It was concluded that the methodology provided in this study is sufficient for developing a numerical tool for predicting the fatigue life of wrinkled field pipelines. However, further strain-controlled cyclic tests on strips specimens need to be carried out on the material to generate cyclic material properties necessary for LCF analysis.

7.2 Conclusions

The data collected from the full-scale experimental program, and numerical modeling of buried pipes with wrinkled defects were analyzed in this study. The following conclusions were made from the analysis:

1. An increase in the wrinkle defect amplitude of a pressurized pipe subjected to a displacement-controlled axial load reversal, leads to increase in the fatigue life. However, this is contrary to previous study conducted by Singh (2019) on wrinkled pipes when subjected to pressure cyclic loads which is a load-controlled cyclic load.
2. Pressurized pipes with the most severe wrinkle defect are made up of the least total HLE, therefore they have the least energy-absorption capability left in their post-wrinkling stage.
3. The direction of the progressive accumulation of ratcheting strain on the strain axis, determines the establishment of folding or crease on the wrinkle crest. This explains the visible folding found pipelines buried pipelines in regions of permafrost.
4. For pressurized pipes that possess longer fatigue lives when subjected to load reversals, ratcheting strain is accumulated in the compressive strain direction. Therefore, pipes with visible crease or folding are favourable in terms of fatigue life.
5. Buried pipelines with wrinkle defects that are operating at high pressure are more vulnerable to fatigue failure when subjected to axial cyclic loads. However, high operating pressure is favorable in terms of fatigue life, when wrinkled pipelines experience pressure cyclic loads (Singh 2019).

6. The Morrow strain life model was considered suitable for predicting fatigue life for the range of parameters considered in this study.
7. Local longitudinal stress concentration gives rise to circumferential cracks for pipelines pressurized at low internal pressure. However, local hoop stress concentration gives rise to longitudinal cracks for pipelines operating at high pressure subjected to load reversals.

7.3 Recommendations

This research has provided several significant contributions toward the objectives of this project. To the best of the author's knowledge, this research is amongst the only few of its kind, and only a few similar studies have been documented in recent times. In order to achieve confidence in understanding the behaviour of wrinkled energy pipelines that are subjected to axial cyclic loads, the following recommendations should be taken into consideration;

1. Further full-scale experimental program and FE analyses should be carried out, to examine the effect of different pipe properties including but not limited to:
 - Pipe Material Properties (API 5L Grades; A, B, X42, X46, X52, X56, X60, X65, X70, X80)
 - Seamless Pipes
 - Wrinkle Geometry Ratio (h/D_o)
 - Pipe Geometry Ratio (D_o/t)
 - Monotonic and Axial Cyclic Load Histories
2. With the advancement of technology, innovative ways to extract the local strain behaviour of wrinkled pipes when subjected to load reversals should be adopted. For example, 3-dimensional Digital Image Correlation (3D DIC). This becomes necessary as strain readings were not fully captured during cyclic loading in this research, because of the delicate nature of the strain gauges.
3. An enhanced material model considering the effect of cyclic hardening should be developed for the cyclic phase. The material model defined in the FE model may include but not limited to kinematic hardening or combined isotropic-kinematic hardening models. Improving the material definition in the cyclic stage may give more accuracy to model results.

4. Strain-controlled fatigue test should be undertaken on coupon strip specimens of X42 pipe material cut from pipes used for full-scale tests. This is necessary to obtain the appropriate material fatigue curve associated with the tested pipe specimen, hence, increase the accuracy of the proposed strain life approach in this research.

REFERENCES

- ANSYS 2016. “Ansys Suite of Engineering Simulation Software” Canonsburg, Pennsylvania, USA.
- API 2012, “API RP 2A: Recommended Practice for Planning, Designing and Constructing Fixed Offshore Platforms.” American Petroleum Institute, Washington D.C, USA.
- API 5L 2018, “API 5L: Specification for Line pipes.” American Petroleum Institute, Washington D.C, USA.
- ASME 2014, “ASME B31.3: Process Piping. A Supplement to ASME B31 Code for Pressure Piping” American Society of Mechanical Engineers. New York, NY, USA.
- ASME 2016, “ASME B31.4: Pipeline Transportation Systems for Liquids and Slurries. A Supplement to ASME B31 Code for Pressure Piping” American Society of Mechanical Engineers. New York, NY, USA.
- ASME 2018, “ASME B31.8: Gas Transmission and Distribution Piping Systems. A Supplement to ASME B31 Code for Pressure Piping” American Society of Mechanical Engineers. New York, NY, USA.
- ASTM 2006, “ASTM A479/A479M: Standard Specification for Stainless Steel Bars and Shapes for Use in Boilers and Other Pressure Vessels” American Society for Testing and Materials, 2006, West Conshohocken, PA, USA.
- ASTM 2015, “ASTM A29/A29M: Standard Specification for General Requirements for Steel Bars, Carbon and Alloy, Hot-Wrought” American Society for Testing and Materials, 2015, West Conshohocken, PA, USA.
- ASTM 2013, “ASTM E8/E8M: Standard Test Methods for Tension Testing of Metallic Materials” American Society for Testing and Materials, 2013, West Conshohocken, PA, USA.
- Alexander, C., and Kulkarni, S., 2009. “Evaluating the Effects of Wrinkle Bends on Pipeline Integrity.” Proceedings of IPC2008 7th Int. Pipeline Conference Sept 29 – Oct. 3, 2008, Calgary, Alberta, Canada, pp. 61-74, 2008 <https://doi.org/10.1115/ipc2008-64039>
- Bidwell, A., Sen, M., Yoosef-Ghodsi, N., and Pederson, I., 2010. ”Geotechnical Characterization and Finite Element Pipe / Soil Interaction Modeling of a Pipeline Installed in an Actively

- Moving , Permafrost Slope.” 63rd Canadian Geotechnical Conference and 6th Canadian Permafrost Conference, Calgary, Alberta, Canada, 2010 pp. 562–569.
- Boardman, B., 1990. “Fatigue Resistance of Steels” ASM Handbbok, Properties and Selection: Iron, Steels, and High-Performance Alloys, Vol 1, pp. 673-688. <https://doi.org/10.31399/asm.hb.v01.9781627081610>
- CEPA: Canadian Energy Pipeline Association, 2019. “Report: Committed to Safety Committed to Canadians.” [online] Cepa.com. Available at: <https://www.cepa.com/wp-content/uploads/2015/11/15-CEPA-0027_Report_EN_FINAL_one-up_Oct13-2015.pdf>., viewed on 2020/03/03
- Corona, E., Lee, L. H., and Kyriakides, S., 2006. “Yield Anisotropy Effects On Buckling Of Circular Tubes Under Bending.” International Journal Of Solids And Structures, Vol 43 (22–23), pp. 7099–7118. <https://doi.org/10.1016/j.ijsolstr.2006.03.005>
- CSA. (2015). CAN/CSA-Z662:19., 2019. “Oil and Gas Pipeline Systems.” Canadian Standard Association. Mississauga, Ontario, Canada.
- Cunha, S. B., Pinheiro, B. C., and Pasqualino, I. P., 2009. “High Cycle Fatigue of Pipelines With Plain Dents: Simulations, Experiments and Assessment.” Proceedings of OMAE2007, 26th Int. Conference on Offshore Mechanics and Arctic Engineering June 10-15, 2007, San Diego, California, USA. pp. 123–132. <https://doi.org/10.1115/omae2007-29130>
- Dama, E., Karamanos, S. A., and Gresnigt, A. M., 2007. “Failure Of Locally Buckled Pipelines.” Journal Of Pressure Vessel Technology, Transactions of the ASME, 129(2), pp. 272–279. <https://doi.org/10.1115/1.2716431>
- Das, S., Cheng, J. R., and Murray, D. W., 2007a. “Behavior Of Wrinkled Steel Pipelines Subjected To Cyclic Axial Loadings.” Canadian Journal of Civil Engineering, vol 34(5), pp. 598–607. <https://doi.org/10.1139/106-165>
- Das, S., Cheng, J. J. R., and Murray, D. W., 2007b. “Prediction Of The Fracture Life Of A Wrinkled Steel Pipe Subject To Low Cycle Fatigue Load”. Canadian Journal of Civil Engineering, vol. 34(9), pp. 1131–1139. <https://doi.org/10.1139/107-032>
- de Carvalho Pinheiro, B., Pasqualino, I. P., and da Cunha, S. B., 2009. “Fatigue Life Analysis of

- Steel Pipelines With Plain Dents Under Cyclic Internal Pressure.” Proceedings of IPC2008, 7th International Pipeline Conference, Sept. 29 to Oct. 3, 2008, Calgary, Alberta, Canada. pp. 629–638. <https://doi.org/10.1115/ipc2008-64690>
- Dassault Systemes (2007), “ABAQUS/CAE Version 6.7” Dassault Systemes Simulia Corp. Waltham, MA, USA.
- Dewanbabee, H., and Das, S., 2012. “Structural Behavior of Corroded Steel Pipes Subject to Axial Compression and Internal Pressure: Experimental Study.” *Journal of Structural Engineering*, Vol 139(1), pp. 57–65. [https://doi.org/10.1061/\(asce\)st.1943-541x.0000596](https://doi.org/10.1061/(asce)st.1943-541x.0000596)
- Dowling N. E., 2013 “Mechanical Behaviour of Materials: Engineering Methods for Deformation, Fracture, and Fatigue.” Upper Saddle River, New Jersey, Prentice Hall.
- Durowoju, M., Pu, Y., Benson, S., and Race, J., 2016. “Fatigue Assessment of Pipeline with Plain Dents Under Cyclic Pressure Loading Using Finite Element Method.” ASME 2016 35th International Conference on Ocean, Offshore and Arctic Engineering. June 19-24, 2016, Busan, South Korea. V005T04A042. <https://doi.org/10.1115/OMAE2016-54863>
- DNV. 2013 DNV-OS-F101. “Submarine Pipeline Systems” Det Norske Veritas AS. Oslo, Norway.
- Fatemi, A., and Kenny, S., 2017. “Parameters Affecting the Local Buckling Response of High Strength Linepipe.” *Journal of Offshore Mechanics and Arctic Engineering*, Vol 139(3), pp. 031702/1 - 15. <https://doi.org/10.1115/1.4035995>
- Ghaednia, H., Das, S., Wang, R., and Kania, R., 2017. “Dependence Of Burst Strength On Crack Length Of A Pipe With A Dent-Crack Defect.” *Journal of Pipeline Systems Engineering and Practice*, Vol 8(2), pp. 1–10. [https://doi.org/10.1061/\(ASCE\)PS.1949-1204.0000259](https://doi.org/10.1061/(ASCE)PS.1949-1204.0000259)
- Jiao, R., and Kyriakides, S., 2011. “Ratcheting And Wrinkling Of Tubes Due To Axial Cycling Under Internal Pressure: Part I Experiments.” *International Journal of Solids and Structures*, Vol 48(20), pp. 2814–2826. <https://doi.org/10.1016/j.ijsolstr.2011.05.027>
- Kashani, M. T., Mohareb, M., Asadi, M., and Smith, M., 2018. “Effect of UOE Forming Process on the Buckling Strains of Steel Pipes.” Proceedings of IPC2018, 12th International Pipeline Conference, Sept. 24-28, Calgary, Alberta, Canada. V002T06A003

<https://doi.org/10.1115/ipc2018-78131>.

- Kyriakides, S., and Ju, G.T., 1992. "Bifurcation And Localization Instabilities In Cylindrical Shells Under Bending-I. Experiments." *International Journal of Solids and Structures*. Vol 19. pp. 1117-1142. [https://doi.org/10.1016/0020-7683\(92\)90139-K](https://doi.org/10.1016/0020-7683(92)90139-K)
- Li, H., Lai, Y., Wang, L., Yang, X., Jiang, N., Li, L., Wang, C., and Yang, B., 2018. "Review Of The State Of The Art: Interactions Between A Buried Pipeline And Frozen Soil." *Cold Regions Science and Technology*, October 2018, Vol 157, pp. 171–186
- Ling Y., 2004. "Uniaxial True Stress-Strain after Necking," *AMP J. Technol.*, vol. 5, no. 1, pp. 37–48.
- Murray, D. W., 1997. "Local Buckling, Strain Localization, Wrinkling And Postbuckling Response Of Line Pipe." *Engineering Structures*, Vol. 19, No. 5, pp. 360-371, 1997. [https://doi.org/10.1016/S0141-0296\(96\)00096-X](https://doi.org/10.1016/S0141-0296(96)00096-X).
- Naeth, M. A., Chanasyk, D. S., McGill, W. B., and Bailey, A. W. 1993, "Soil temperature regime in mixed prairie rangeland after pipeline construction and operation.", *Canadian Agricultural Engineering*, Vol 35(2), pp. 89–95.
- Natural Resources Canada 2019. "Energy and the Economy" <https://www.nrcan.gc.ca/science-data/data-analysis/energy-data-analysis/energy-facts/energy-and-economy/20062>
- Navjot, S., 2019. "Thesis: Pressure Cycle Induced Fatigue Failure of Wrinkled Energy Pipelines." University Windsor Available at "https://ca01.primo.exlibrisgroup.com/permalink/01UTON_UW/1k10brt/cdi_proquest_journals_2312608903" viewed on 2020/27/02.
- Nazemi, N., Sara, K., and Das. S., 2009. "Behaviour of Wrinkled Linepipe Subjected to Internal Pressure and Eccentric Axial Compression Load". *Journal of Pipeline Engineering*, Vol. 8 issue 3, Sept. 2009. pp. 183 - 187
- Nixon, J. F., Sortland, K. A., and James, D. A., 2002. "Geotechnical Aspects Of Northern Gas Pipeline Design." *Proceeding of the 5th Canadian Permafrost Conference*, Calgary, Alberta, Canada. pp. 299–307.

- Oswell, J. M., 2011. "Pipelines In Permafrost: Geotechnical Issues And Lessons." *Canadian Geotechnical Journal*, Vol 48(9), pp. 1412–1431. <https://doi.org/10.1139/t11-045>
- Paquette, J. A., and Kyriakides, S., 2006. "Plastic Buckling Of Tubes Under Axial Compression And Internal Pressure." *International Journal of Mechanical Sciences*, Vol 48(8), pp. 855–867. <https://doi.org/10.1016/j.ijmecsci.2006.03.003>.
- Paul, S. K. (2019). "A critical review of experimental aspects in ratcheting fatigue: Microstructure to specimen to component." *Journal of Materials Research and Technology*, Vol 8(5), pp. 4894–4914. <https://doi.org/10.1016/j.jmrt.2019.06.014>.
- Pournara, A. E., C., P., Kamanos, Sy. A., and Perdikaris., 2015. "Structural Integrity of Buckled Steel Pipes." *Proceedings of ASME 2015 34th International Conference on Ocean, Offshore and Arctic Engineering*. May 31 – June 5, St. John's, Newfoundland, Canada. OMAE2015-41386. pp. 1–12.
- Sandor, B.I., 1972. "Textbook: Fundamentals Of Cyclic Stress And Strain." University of Winsconsin Press, Madison.
- Shengwen T., Xiaobo R., Jianying H., and Zhiliang Z., 2019. "Stress-strain Curves of Metallic Materials and Post Necking Strain Hardening Characterization: A Review." *Fatigue and Fracture of Engineering Materials and Structures*. Vol 43, pp. 3-19 <https://doi.org/10.1111/ffe.13134>.
- Wilkie S.A., Doblanko R.M., and Fladager. S. J., 2001. "Northern Canadian Pipeline Deals With Effects Of Soil Movement." *Oil and Gas Journal*. Vol 99, No. 20. pp. 62-66. <https://doi.org/10.1115/ipc2018-78131>.
- Yoosef-Ghodsi, N., Kulak, G.L., and Murray, D.W. 1995. "Some Test Results for Wrinkling of Girth-Welded Line Pipe" *Proceedings of 14th International Conference on Offshore Mechanics and Arctic Engineering*, 18th to 22nd of June 1995, Copenhagen, Denmark. Volume 5. ISBN 0-7918-1311-8.
- Zeinoddini, M., Ezzati, M., and Fakheri, J., 2014. "Uniaxial Strain Ratcheting Behavior Of Dented Steel Tubular: An Experimental Study." *Engineering Failure Analysis*, vol 44, pp. 202–216. <https://doi.org/10.1016/j.engfailanal.2014.05.016>

- Zeinoddini, M., Ezzati, M., and Parke, G. A. R., 2015. "Plastic Buckling, Wrinkling And Collapse Behaviour Of Dented X80 Steel Line Pipes Under Axial Compression." *Journal of Loss Prevention in the Process Industries*, vol. 38, pp. 67–78. <https://doi.org/10.1016/j.jlp.2015.09.002>
- Zhang, J., 2010. "Thesis: Development of LCF Life Prediction Model for Wrinkled Steel Pipes." University of Alberta. Available at "<https://era.library.ualberta.ca/items/1edd918c-7745-4283-8a99-8f98b5d7a84a>." viewed on 2019/27/03
- Zhou, Z., and Murray, D. W. 1995. "Analysis Of Postbuckling Behavior Of Line Pipe Subjected To Combined Loads." *International Journal of Solids and Structures*, Vol 32(20), pp. 3015–3036. [https://doi.org/10.1016/0020-7683\(94\)00261-T](https://doi.org/10.1016/0020-7683(94)00261-T)

APPENDIX A – Relationship Between Load, Strain and Displacement for All Tested Specimens

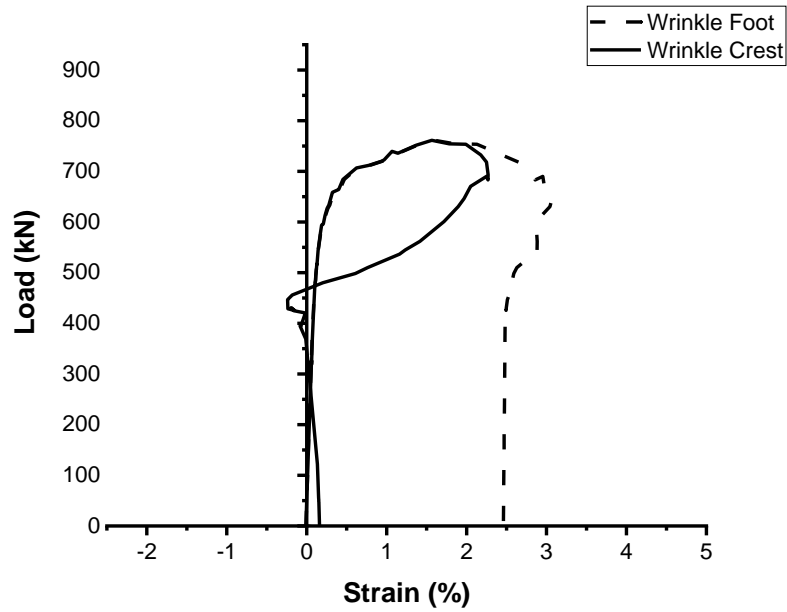


Figure A.1: Load vs. Local Strain Behaviour for Specimen IP30WA8

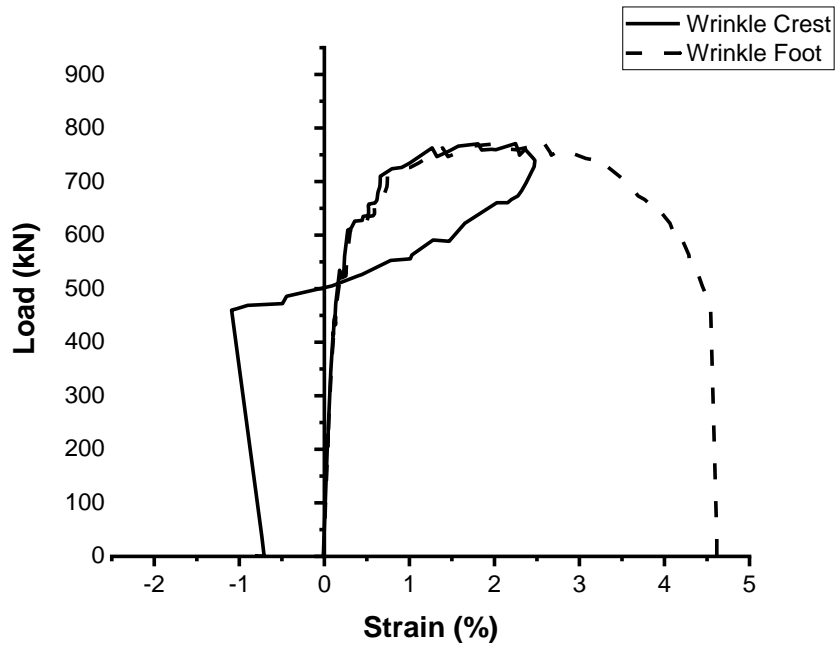


Figure A.2: Load vs. Local Strain Behaviour for Specimen IP30WA6

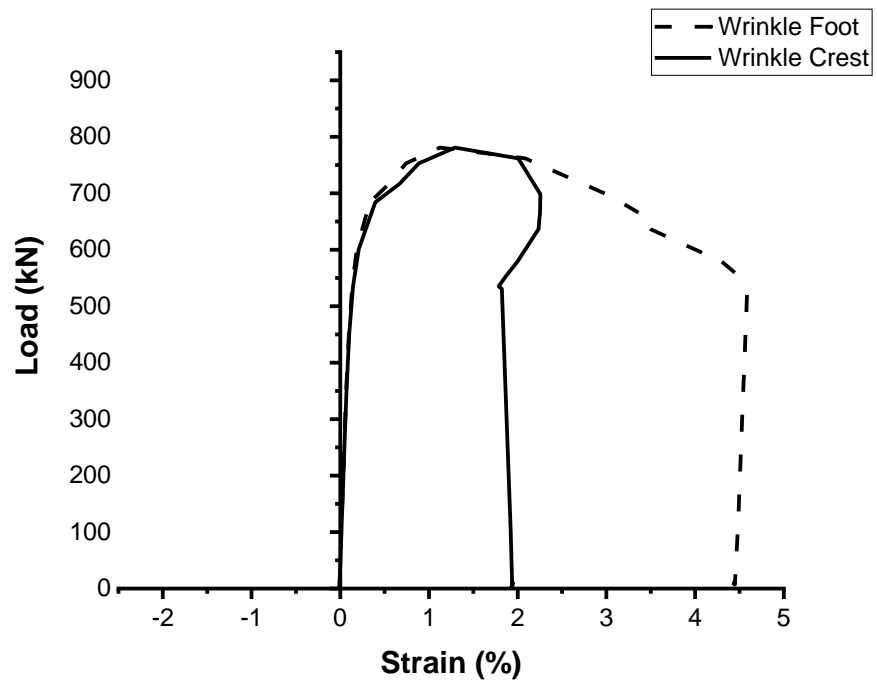


Figure A.3: Load vs. Local Strain Behaviour for Specimen IP30WA4

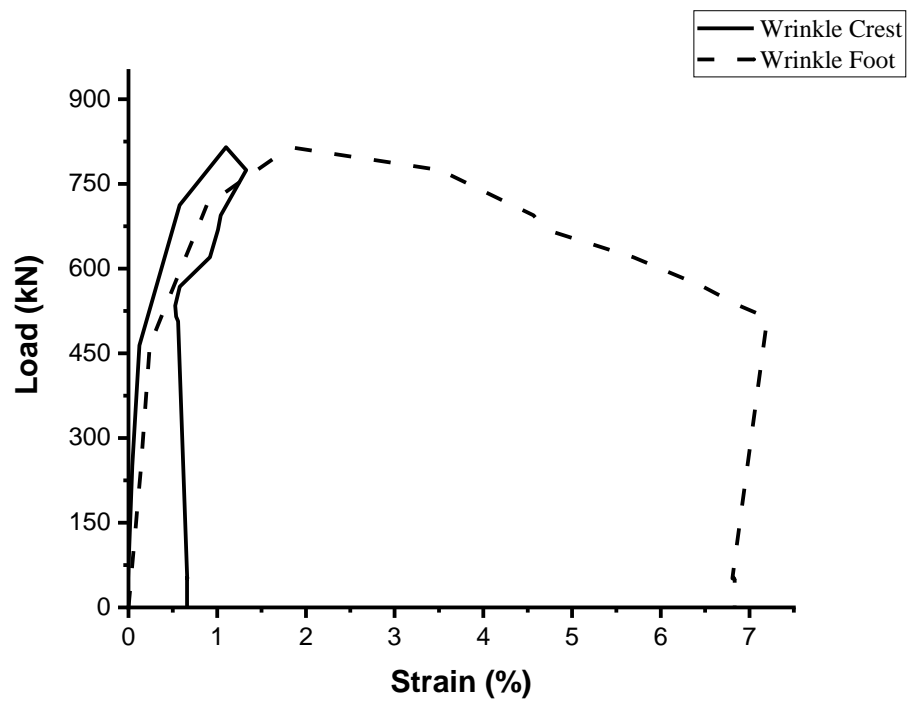


Figure A.4: Load vs. Local Strain Behaviour for Specimen IP60WA10.5

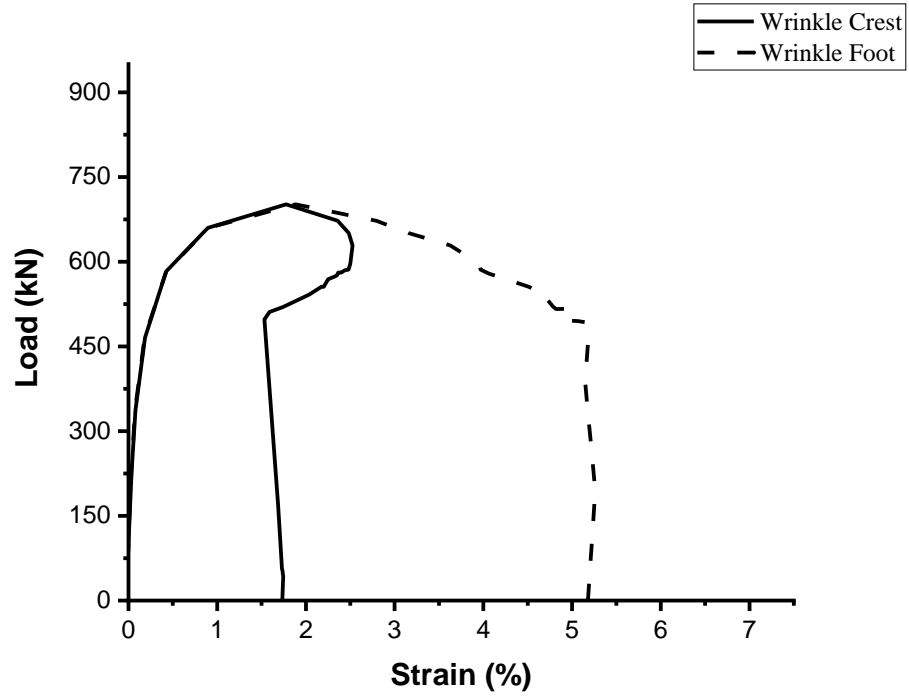


Figure A.5: Load vs. Local Strain Behaviour for Specimen IP60WA8

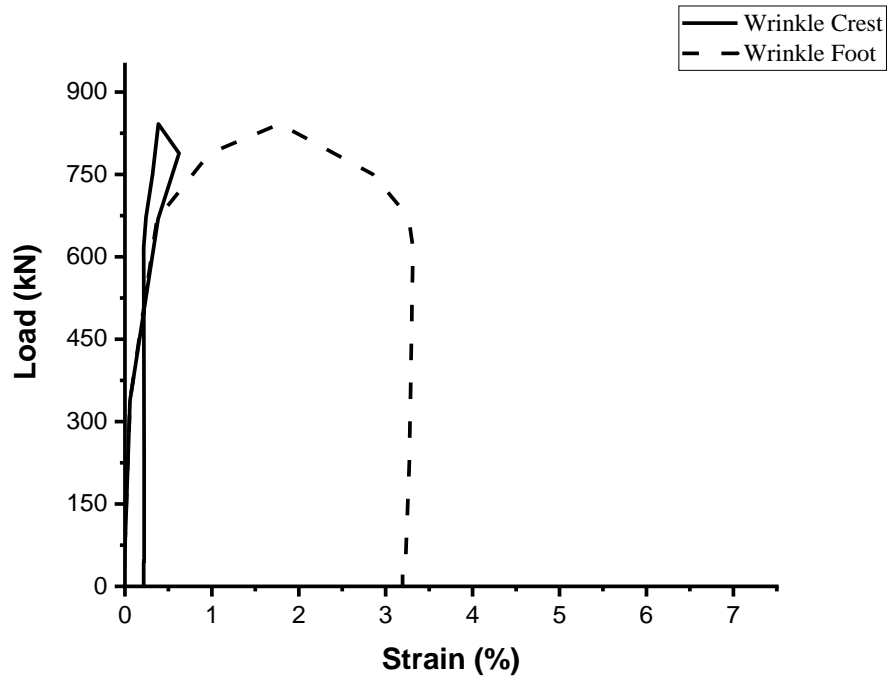


Figure A.6: Load vs. Local Strain Behaviour for Specimen IP60WA6

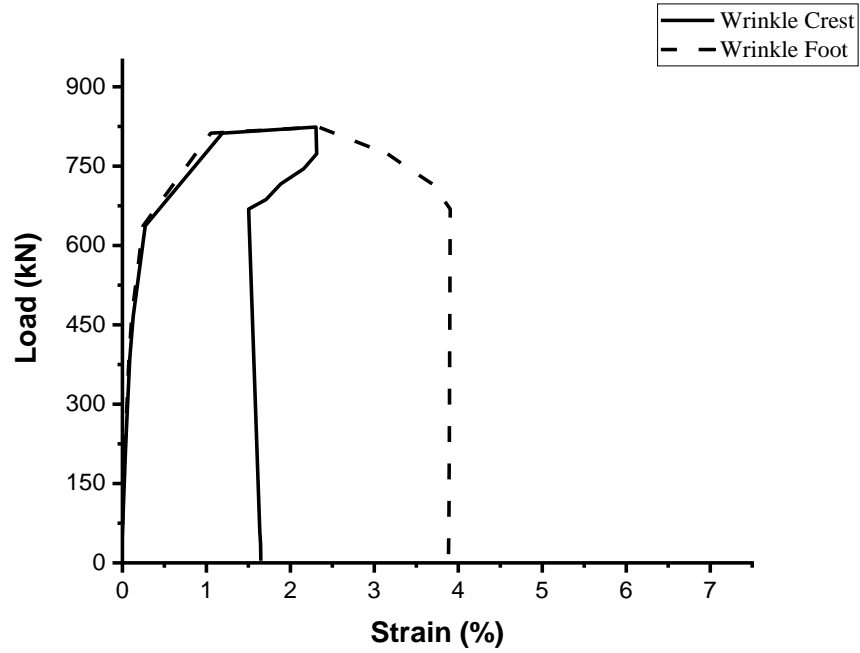


Figure A.7: Load vs. Local Strain Behaviour for Specimen IP60WA4

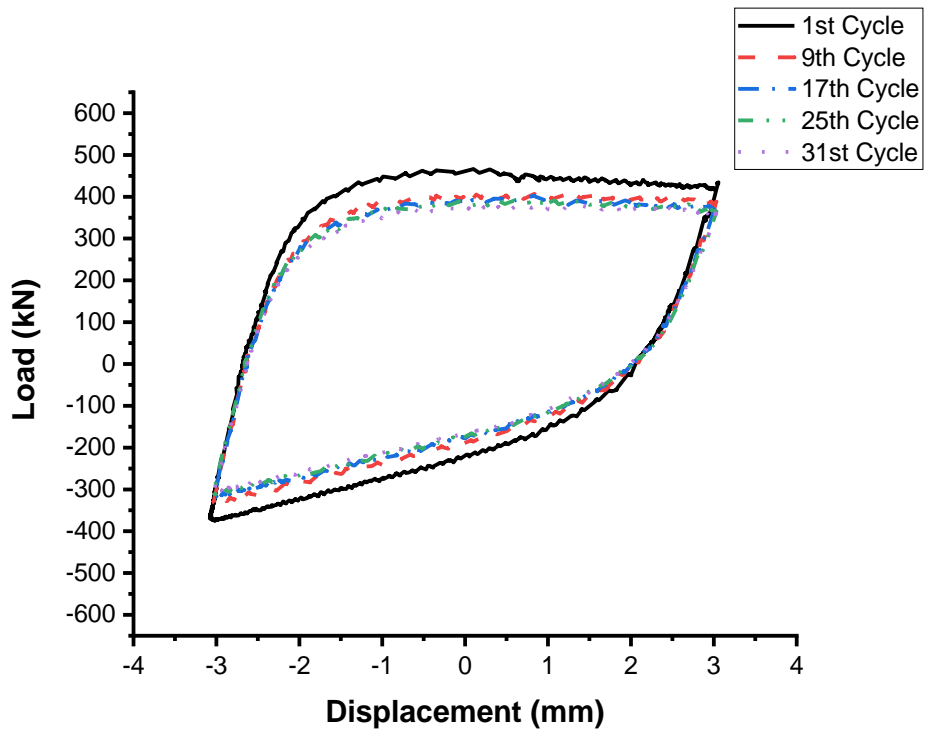


Figure A.8: Load vs. Displacement Hysteresis curve for IP30WA6

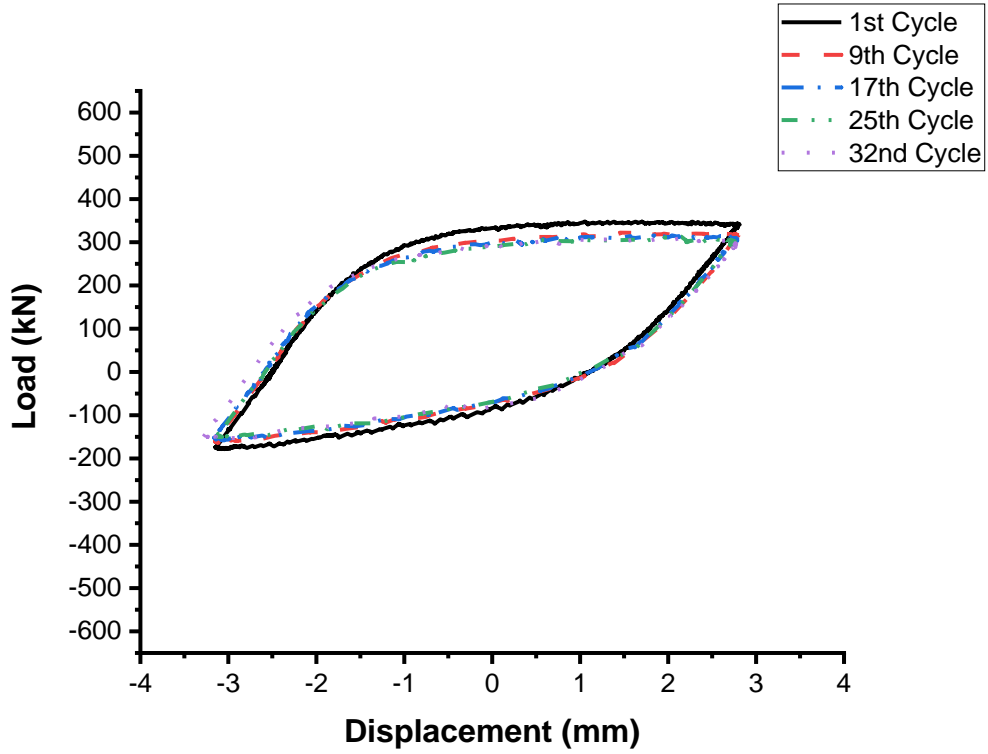


Figure A.9: Load vs. Displacement Hysteresis curve for IP30WA8

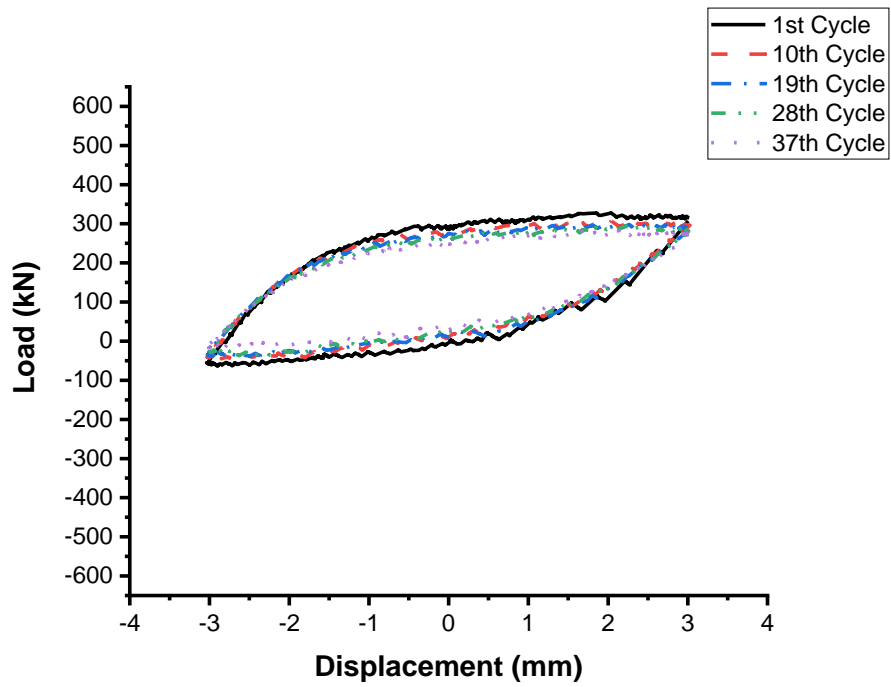


Figure A.10: Load vs. Displacement Hysteresis curve for IP30WA10.5

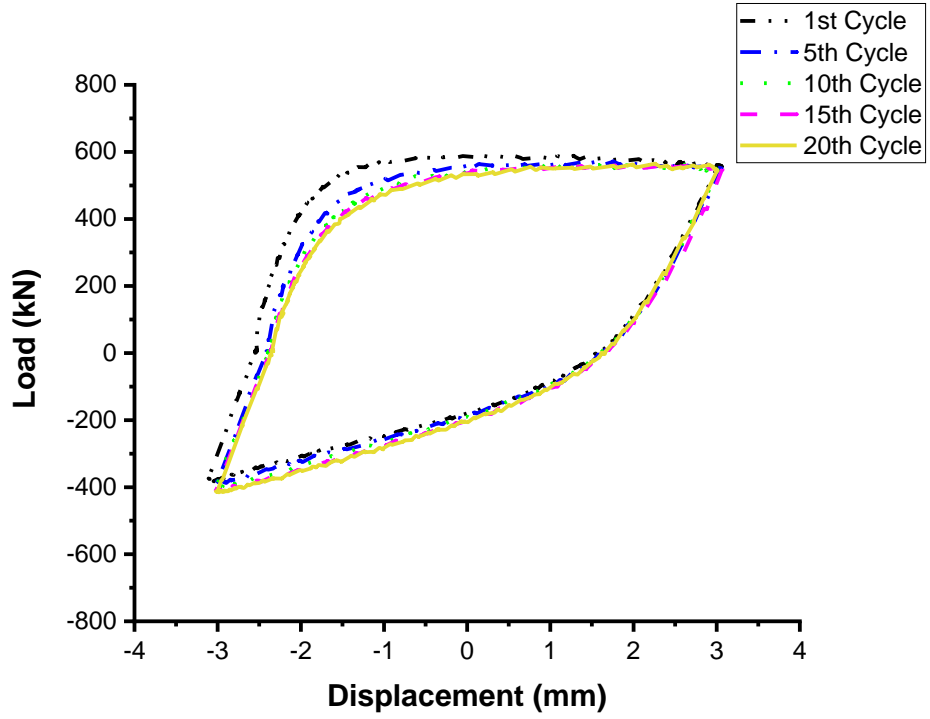


Figure A.11: Load vs. Displacement Hysteresis curve for IP60WA6

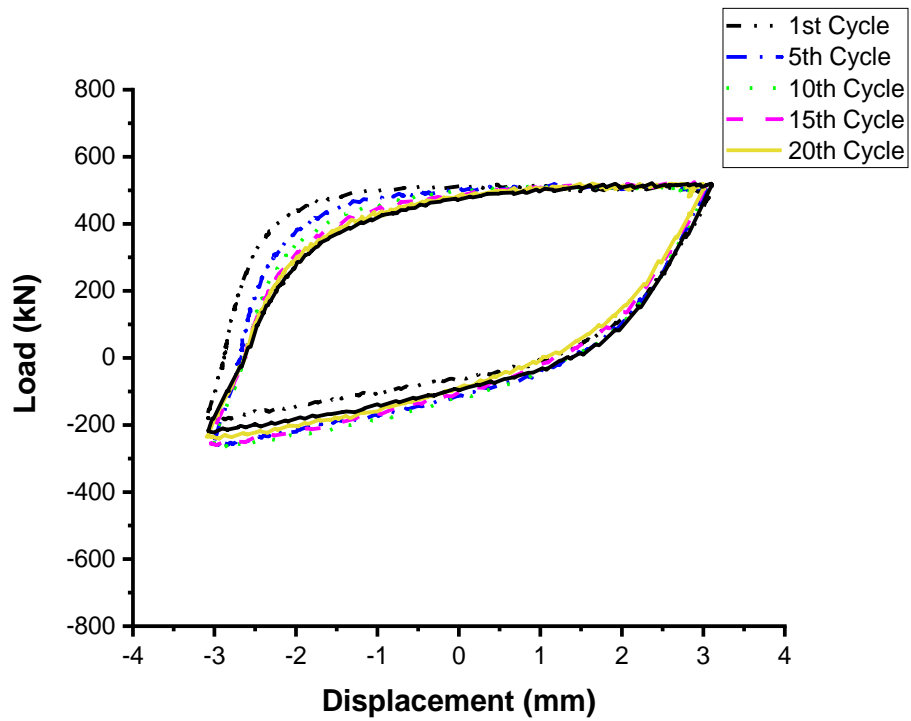


Figure A.12: Load vs. Displacement Hysteresis curve for IP60WA8

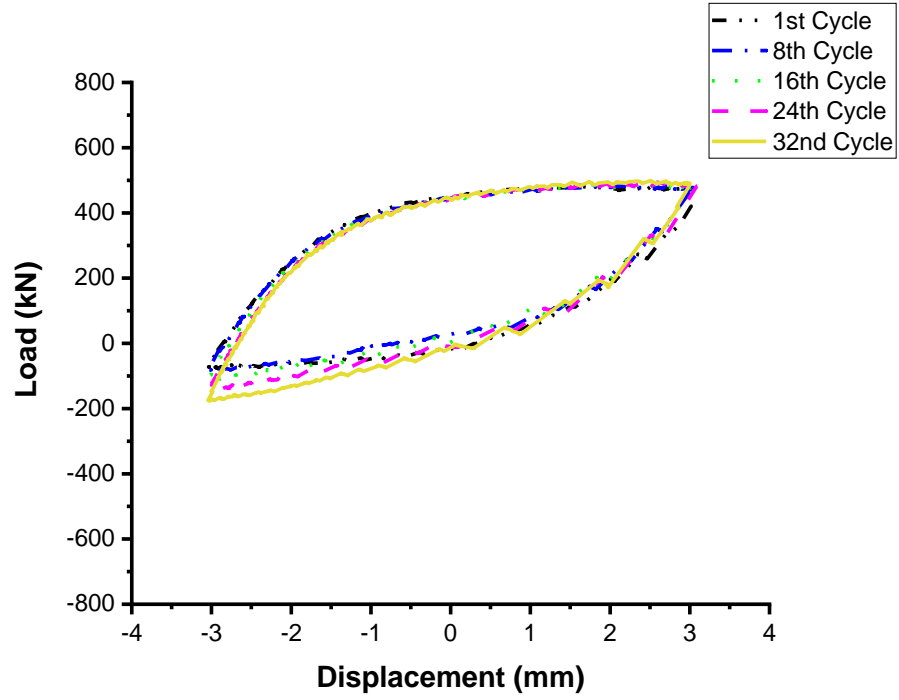


Figure A.13: Load vs. Displacement Hysteresis curve for IP60WA10.5

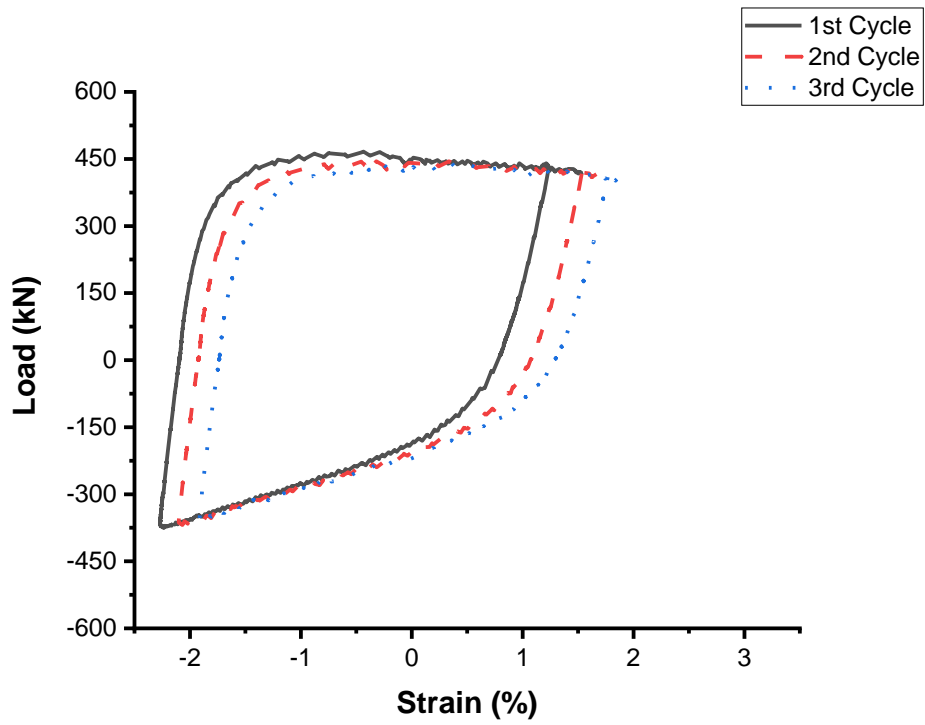


Figure A.14: Relationship Between Local Hoop Strain and Applied Load at Wrinkle Crest for Specimen IP30WA6

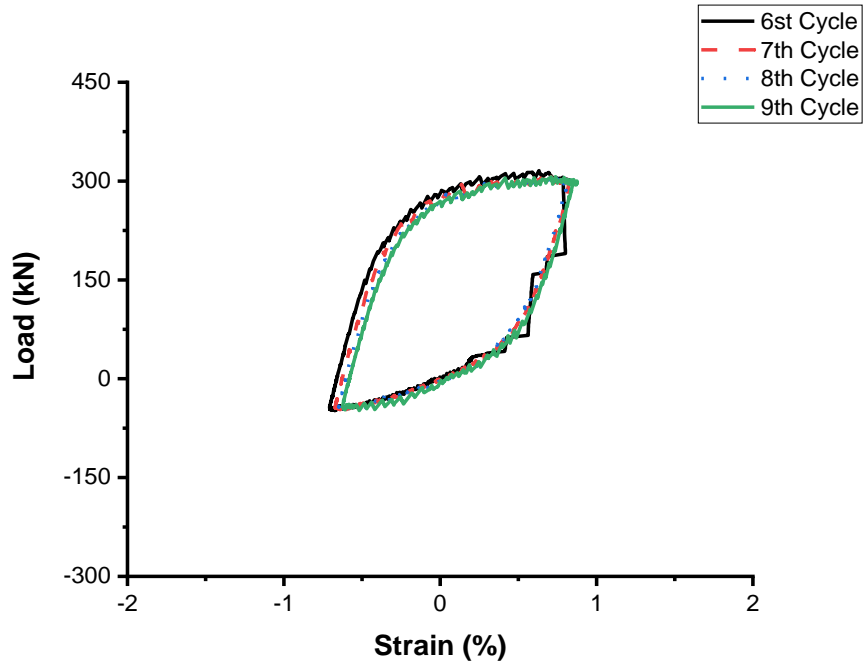


Figure A.15: Relationship Between Local Hoop Strain and Applied Load at Wrinkle Crest for Specimen IP30WA10.5

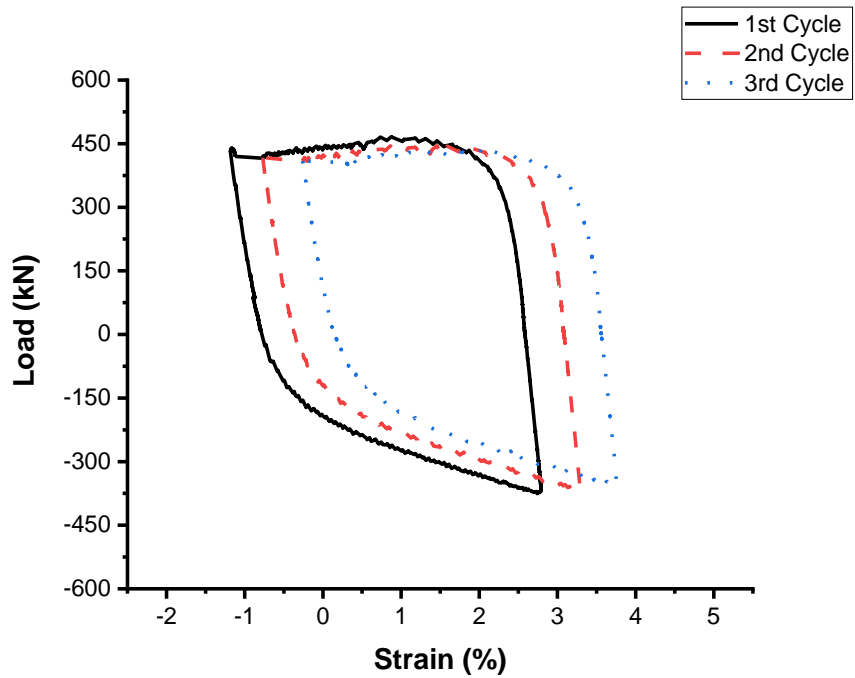


Figure A.16: Relationship Between Local Longitudinal Strain at Wrinkle Feet and Applied Load for Specimen IP30WA6

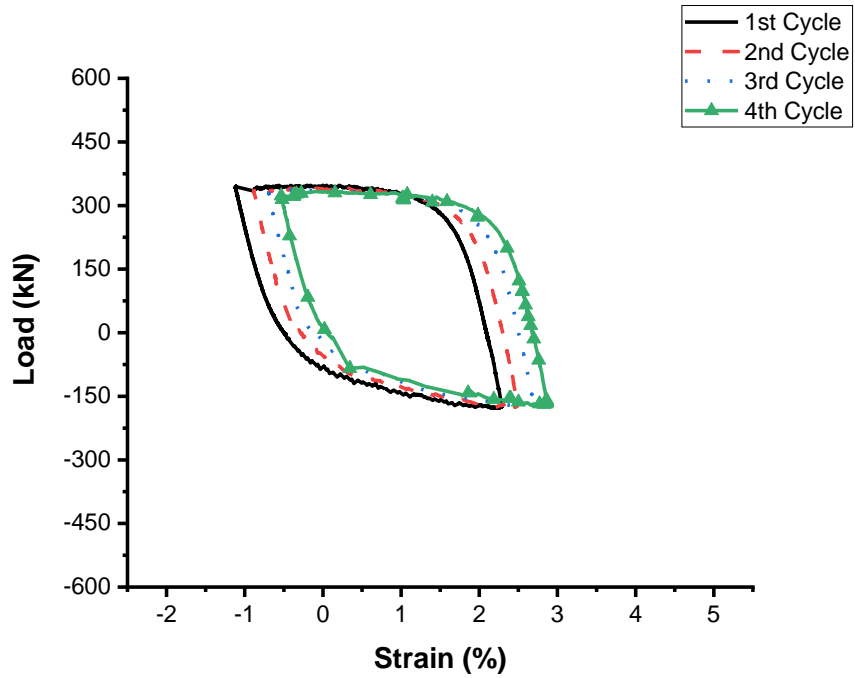


Figure A.17: Relationship Between Local Longitudinal Strain at Wrinkle Feet and Applied Load for Specimen IP30WA8

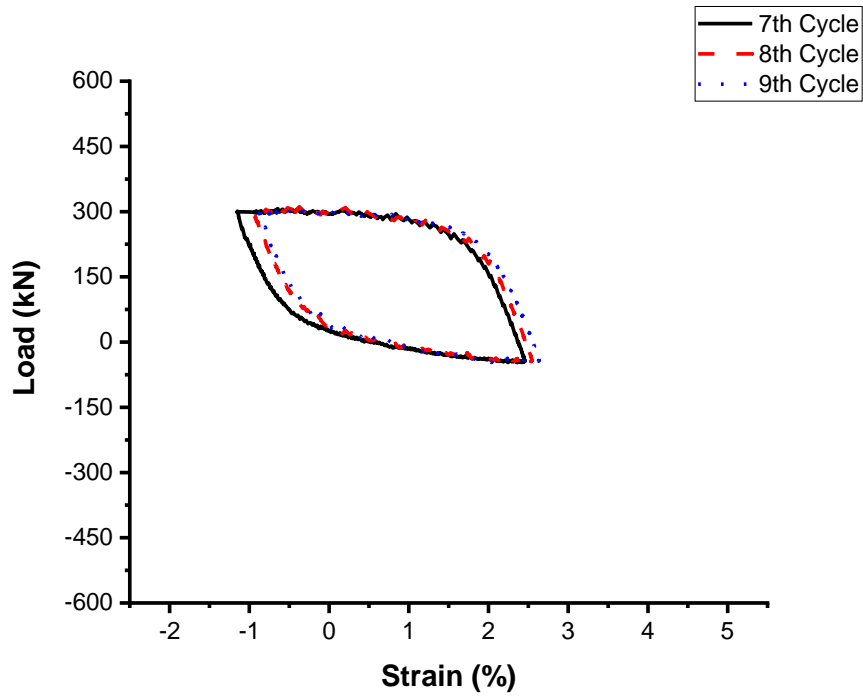


Figure A.18: Relationship Between Local Longitudinal Strain at Wrinkle Feet and Applied Load for Specimen IP30WA10.5

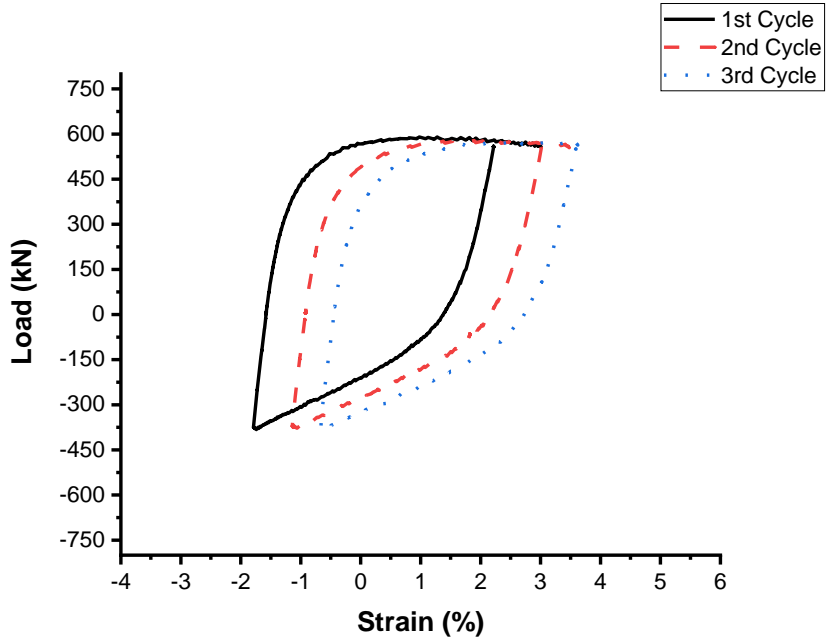


Figure A.19: Relationship Between Local Hoop Strain and Applied Load at Wrinkle Crest for Specimen IP60WA6

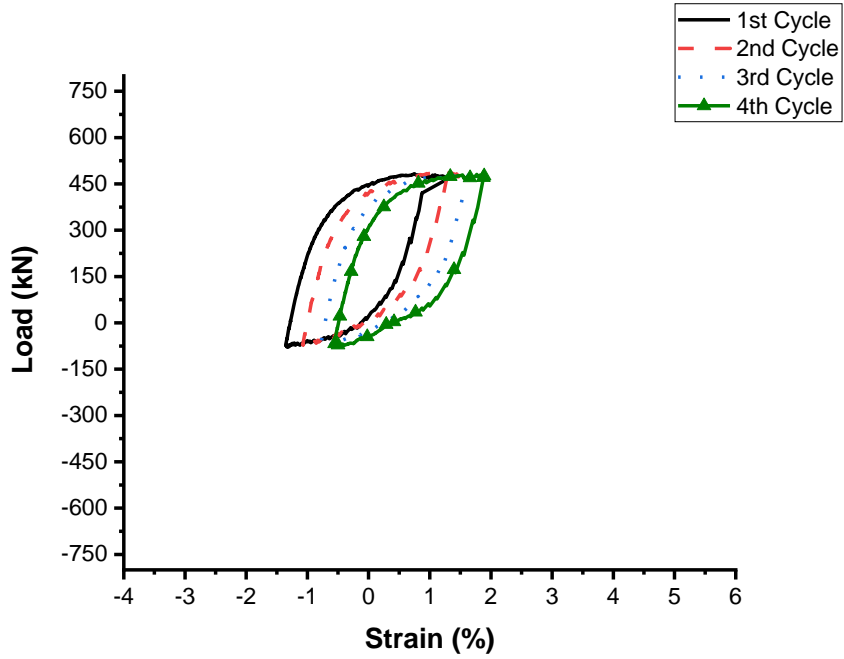


Figure A.20: Relationship Between Local Hoop Strain and Applied Load at Wrinkle Crest for Specimen IP60WA10.5

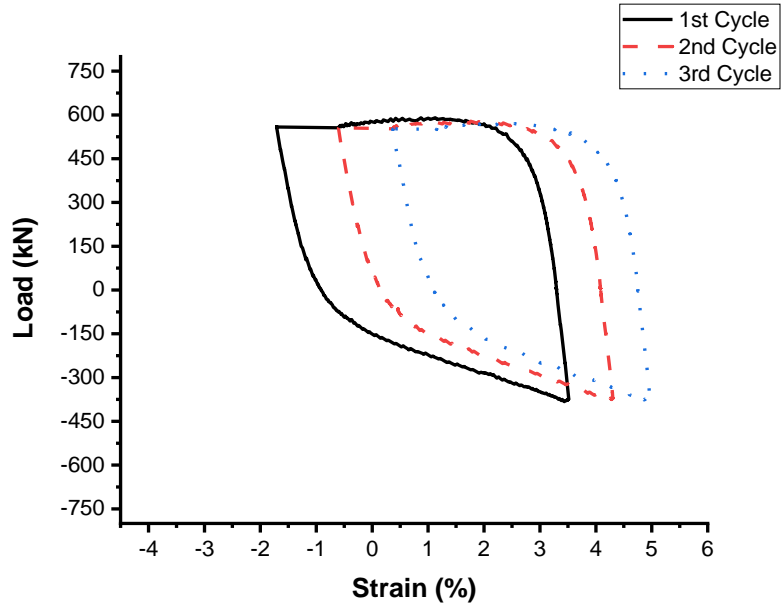


Figure A.21: Relationship Between Local Longitudinal Strain and Applied Load at Wrinkle Feet for Specimen IP60WA6

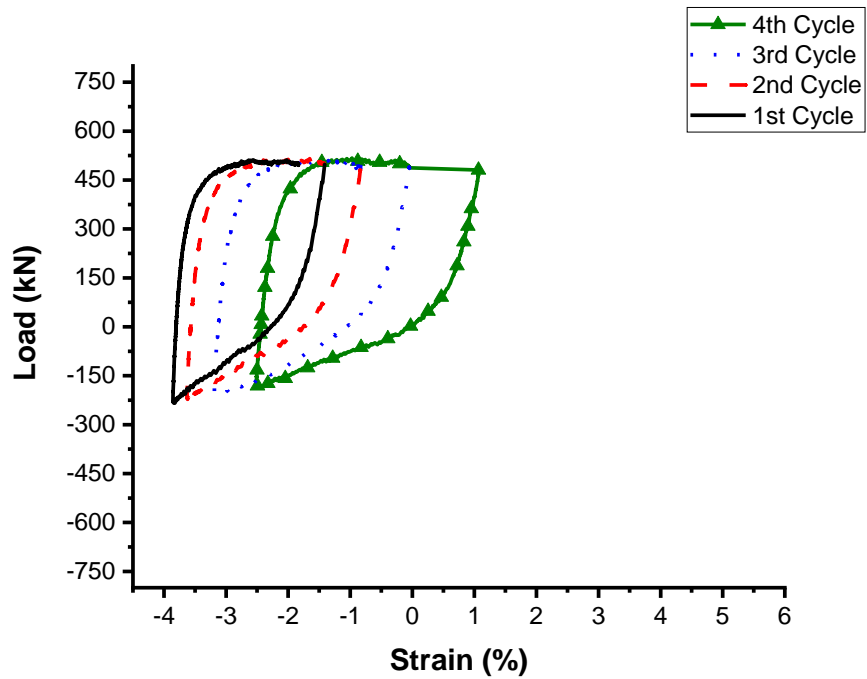
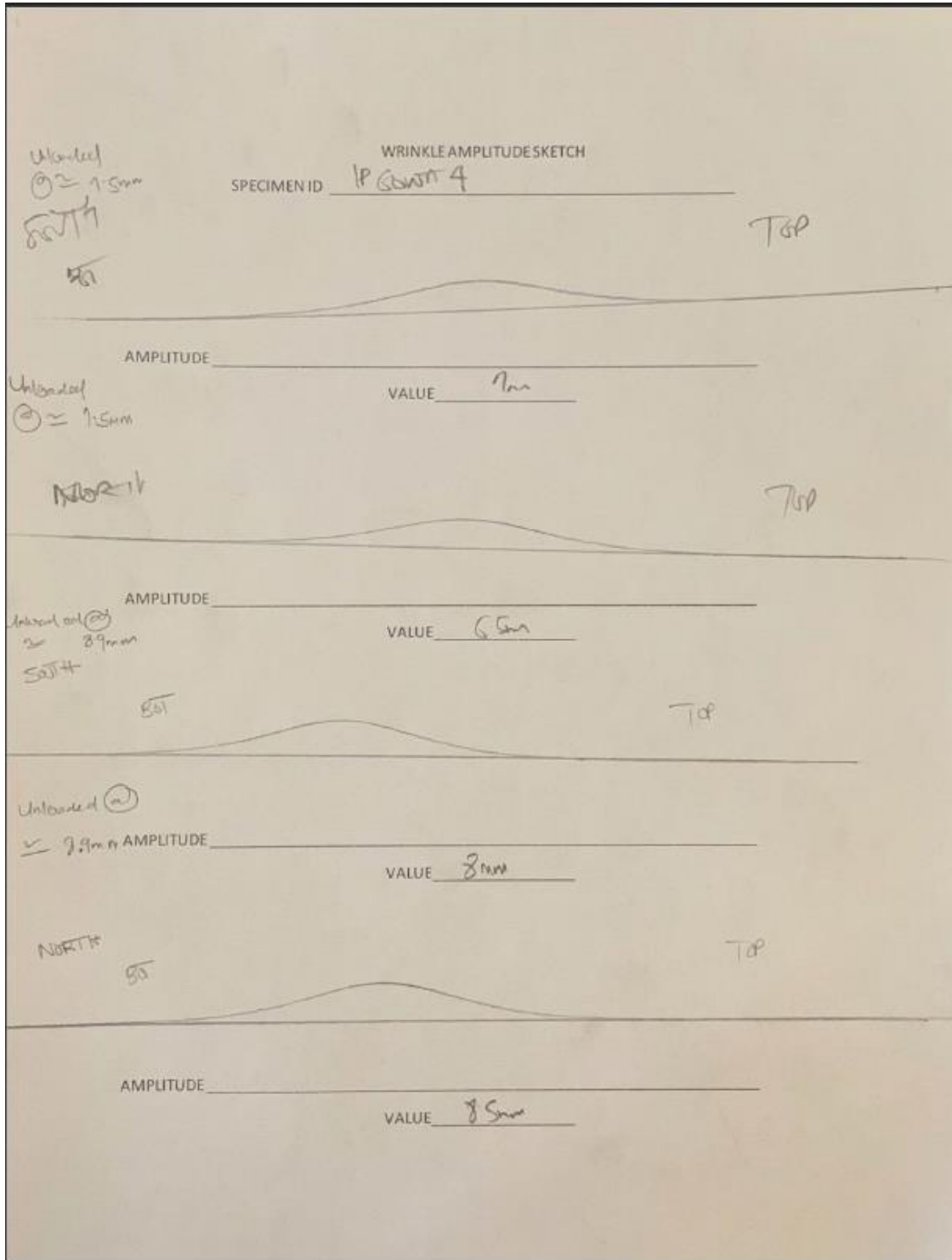
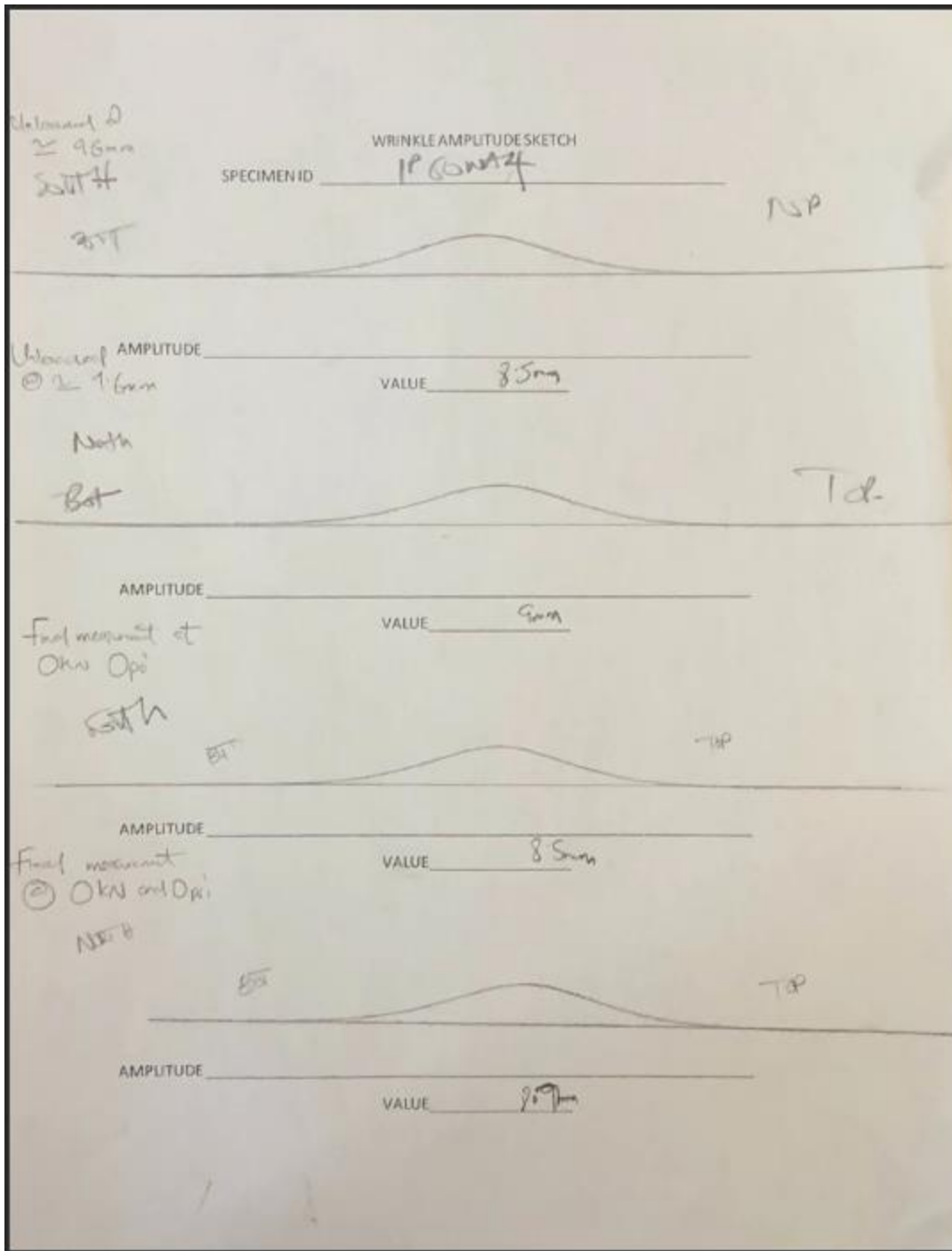


Figure A.22: Relationship Between Local Longitudinal Strain and Applied Load at Wrinkle Feet for Specimen IP60WA8

APPENDIX B – Wrinkle Profile Measurement Log





(b) Page 2 of 2

Figure B.1: Wrinkle Profile Measurement Log for Specimen IP60WA4

APPENDIX C – Pictures of Tested Specimens



(a) IP30WA4



(b) IP30WA6



(a) IP30WA8



(d) IP30WA10.5

Figure C.1: Entire View of Each Group 1 Specimen Tested



(a) IP60WA4



(b) IP60WA6



(a) IP60WA8



(b) IP60WA10.5

Figure C.2: Entire View of Each Group 2 Specimen Tested



(b) IP30WA4



(b) IP30WA6



(b) IP30WA8



(d) IP30WA10.5

Figure C.3: Close View of the Location of Crack in Each Group 1 Specimen



(a) IP60WA4



(b) IP60WA6



(a) IP60WA8



(d) IP60WA10.5

Figure C.4: Close View of the Location of Crack in Each Group 2 Specimen

APPENDIX D – Copyright Clearances

ELSEVIER LICENSE TERMS AND CONDITIONS

Nov 30, 2020

This Agreement between Mr. Habib Sobanke ("You") and Elsevier ("Elsevier") consists of your license details and the terms and conditions provided by Elsevier and Copyright Clearance Center.

License Number 4958960982721

License date Nov 30, 2020

Licensed Content Publisher Elsevier

Licensed Content Publication International Journal of Solids and Structures

Licensed Content Title Ratcheting and wrinkling of tubes due to axial cycling under internal pressure: Part I experiments

Licensed Content Author Rong Jiao,Stelios Kyriakides

Licensed Content Date Oct 1, 2011

Licensed Content Volume 48

Licensed Content Issue 20

Licensed Content Pages 13

Start Page 2814

End Page 2826
Type of Use reuse in a thesis/dissertation

Portion figures/tables/illustrations

Number of figures/tables/illustrations 4

Format electronic

Are you the author of this Elsevier article? No

Will you be translating? No

Title Behaviour of Wrinkled Energy Pipes Subjected to Axial Cyclic Induced Fatigue Failure

Institution name University of Windsor

Expected presentation date Dec 2020

Portions fig 10a, fig 12, fig 13a, fig 21

Mr. Habeeb Sobanke
1662 University avenue west

Requestor Location Windsor, ON N9B 1C2
Canada
Attn: Mr. Habeeb Sobanke

Publisher Tax ID GB 494 6272 12

Total 0.00 CAD

Terms and Conditions

INTRODUCTION

1. The publisher for this copyrighted material is Elsevier. By clicking "accept" in connection with completing this licensing transaction, you agree that the following terms and conditions apply to this transaction (along with the Billing and Payment terms and conditions established by Copyright Clearance Center, Inc. ("CCC"), at the time that you opened your Rightslink account and that are available at any time at <http://myaccount.copyright.com>).

GENERAL TERMS

2. Elsevier hereby grants you permission to reproduce the aforementioned material subject to the terms and conditions indicated.

3. Acknowledgement: If any part of the material to be used (for example, figures) has appeared in our publication with credit or acknowledgement to another source, permission must also be sought from that source. If such permission is not obtained then that material may not be included in your publication/copies. Suitable acknowledgement to the source must be made, either as a footnote or in a reference list at the end of your publication, as follows:

"Reprinted from Publication title, Vol /edition number, Author(s), Title of article / title of chapter, Pages No., Copyright (Year), with permission from Elsevier [OR APPLICABLE SOCIETY COPYRIGHT OWNER]." Also Lancet special credit - "Reprinted from The Lancet, Vol. number, Author(s), Title of article, Pages No., Copyright (Year), with permission from Elsevier."

4. Reproduction of this material is confined to the purpose and/or media for which permission is hereby given.

5. Altering/Modifying Material: Not Permitted. However figures and illustrations may be altered/adapted minimally to serve your work. Any other abbreviations, additions, deletions and/or any other alterations shall be made only with prior written authorization of Elsevier Ltd. (Please contact Elsevier's permissions helpdesk here). No modifications can be made to any Lancet figures/tables and they must be reproduced in full.

6. If the permission fee for the requested use of our material is waived in this instance, please be advised that your future requests for Elsevier materials may attract a fee.

7. Reservation of Rights: Publisher reserves all rights not specifically granted in the combination of (i) the license details provided by you and accepted in the course of this licensing transaction, (ii) these terms and conditions and (iii) CCC's Billing and Payment terms and conditions.

8. License Contingent Upon Payment: While you may exercise the rights licensed immediately upon issuance of the license at the end of the licensing process for the

transaction, provided that you have disclosed complete and accurate details of your proposed use, no license is finally effective unless and until full payment is received from you (either by publisher or by CCC) as provided in CCC's Billing and Payment terms and conditions. If full payment is not received on a timely basis, then any license preliminarily granted shall be deemed automatically revoked and shall be void as if never granted. Further, in the event that you breach any of these terms and conditions or any of CCC's Billing and Payment terms and conditions, the license is automatically revoked and shall be void as if never granted. Use of materials as described in a revoked license, as well as any use of the materials beyond the scope of an unrevoked license, may constitute copyright infringement and publisher reserves the right to take any and all action to protect its copyright in the materials.

9. **Warranties:** Publisher makes no representations or warranties with respect to the licensed material.

10. **Indemnity:** You hereby indemnify and agree to hold harmless publisher and CCC, and their respective officers, directors, employees and agents, from and against any and all claims arising out of your use of the licensed material other than as specifically authorized pursuant to this license.

11. **No Transfer of License:** This license is personal to you and may not be sublicensed, assigned, or transferred by you to any other person without publisher's written permission.

12. **No Amendment Except in Writing:** This license may not be amended except in a writing signed by both parties (or, in the case of publisher, by CCC on publisher's behalf).

13. **Objection to Contrary Terms:** Publisher hereby objects to any terms contained in any purchase order, acknowledgment, check endorsement or other writing prepared by you, which terms are inconsistent with these terms and conditions or CCC's Billing and Payment terms and conditions. These terms and conditions, together with CCC's Billing and Payment terms and conditions (which are incorporated herein), comprise the entire agreement between you and publisher (and CCC) concerning this licensing transaction. In the event of any conflict between your obligations established by these terms and conditions and those established by CCC's Billing and Payment terms and conditions, these terms and conditions shall control.

14. **Revocation:** Elsevier or Copyright Clearance Center may deny the permissions described in this License at their sole discretion, for any reason or no reason, with a full refund payable to you. Notice of such denial will be made using the contact information provided by you. Failure to receive such notice will not alter or invalidate the denial. In no event will Elsevier or Copyright Clearance Center be responsible or liable for any costs, expenses or damage incurred by you as a result of a denial of your permission request, other than a refund of the amount(s) paid by you to Elsevier and/or Copyright Clearance Center for denied permissions.

LIMITED LICENSE

The following terms and conditions apply only to specific license types:

15. **Translation:** This permission is granted for non-exclusive world **English** rights only unless your license was granted for translation rights. If you licensed translation rights you may only translate this content into the languages you requested. A professional translator must

perform all translations and reproduce the content word for word preserving the integrity of the article.

16. Posting licensed content on any Website: The following terms and conditions apply as follows: Licensing material from an Elsevier journal: All content posted to the web site must maintain the copyright information line on the bottom of each image; A hyper-text must be included to the Homepage of the journal from which you are licensing at <http://www.sciencedirect.com/science/journal/xxxxx> or the Elsevier homepage for books at <http://www.elsevier.com>; Central Storage: This license does not include permission for a scanned version of the material to be stored in a central repository such as that provided by Heron/XanEdu.

Licensing material from an Elsevier book: A hyper-text link must be included to the Elsevier homepage at <http://www.elsevier.com> . All content posted to the web site must maintain the copyright information line on the bottom of each image.

Posting licensed content on Electronic reserve: In addition to the above the following clauses are applicable: The web site must be password-protected and made available only to bona fide students registered on a relevant course. This permission is granted for 1 year only. You may obtain a new license for future website posting.

17. For journal authors: the following clauses are applicable in addition to the above:

Preprints:

A preprint is an author's own write-up of research results and analysis, it has not been peer reviewed, nor has it had any other value added to it by a publisher (such as formatting, copyright, technical enhancement etc.).

Authors can share their preprints anywhere at any time. Preprints should not be added to or enhanced in any way in order to appear more like, or to substitute for, the final versions of articles however authors can update their preprints on arXiv or RePEc with their Accepted Author Manuscript (see below).

If accepted for publication, we encourage authors to link from the preprint to their formal publication via its DOI. Millions of researchers have access to the formal publications on ScienceDirect, and so links will help users to find, access, cite and use the best available version. Please note that Cell Press, The Lancet and some society-owned have different preprint policies. Information on these policies is available on the journal homepage.

Accepted Author Manuscripts: An accepted author manuscript is the manuscript of an article that has been accepted for publication and which typically includes author incorporated changes suggested during submission, peer review and editor-author communications.

Authors can share their accepted author manuscript:

- immediately via their non-commercial person homepage or blog by updating a
 - preprint in arXiv or RePEc with the accepted manuscript via their research
 - institute or institutional repository for internal institutional uses or as part of an
 - invitation-only research collaboration work-group directly by providing copies
 - to their students or to research collaborators for their personal use
 - for private scholarly sharing as part of an invitation-only work group on
 - commercial sites with which Elsevier has an agreement
- After the embargo period via non-commercial hosting platforms such as their
 - institutional repository via commercial sites with which Elsevier has an
 - agreement

In all cases accepted manuscripts should:

- link to the formal publication via its DOI bear a CC-BY-NC-ND license - this is easy to
- do if aggregated with other manuscripts, for example in a repository or other site, be
- shared in alignment with our hosting policy not be added to or enhanced in any way to appear more like, or to substitute for, the published journal article.

Published journal article (JPA): A published journal article (PJA) is the definitive final record of published research that appears or will appear in the journal and embodies all value-adding publishing activities including peer review co-ordination, copy-editing, formatting, (if relevant) pagination and online enrichment.

Policies for sharing publishing journal articles differ for subscription and gold open access articles:

Subscription Articles: If you are an author, please share a link to your article rather than the full-text. Millions of researchers have access to the formal publications on ScienceDirect, and so links will help your users to find, access, cite, and use the best available version.

Theses and dissertations which contain embedded PJAs as part of the formal submission can be posted publicly by the awarding institution with DOI links back to the formal publications on ScienceDirect.

If you are affiliated with a library that subscribes to ScienceDirect you have additional private sharing rights for others' research accessed under that agreement. This includes use for classroom teaching and internal training at the institution (including use in course packs and courseware programs), and inclusion of the article for grant funding purposes.

Gold Open Access Articles: May be shared according to the author-selected end-user license and should contain a CrossMark logo, the end user license, and a DOI link to the formal publication on ScienceDirect.

Please refer to Elsevier's posting policy for further information.

18. **For book authors** the following clauses are applicable in addition to the above: Authors are permitted to place a brief summary of their work online only. You are not allowed to download and post the published electronic version of your chapter, nor may you scan the

printed edition to create an electronic version. **Posting to a repository:** Authors are permitted to post a summary of their chapter only in their institution's repository.

19. **Thesis/Dissertation:** If your license is for use in a thesis/dissertation your thesis may be submitted to your institution in either print or electronic form. Should your thesis be published commercially, please reapply for permission. These requirements include permission for the Library and Archives of Canada to supply single copies, on demand, of the complete thesis and include permission for Proquest/UMI to supply single copies, on demand, of the complete thesis. Should your thesis be published commercially, please reapply for permission. Theses and dissertations which contain embedded PJAs as part of the formal submission can be posted publicly by the awarding institution with DOI links back to the formal publications on ScienceDirect.

Elsevier Open Access Terms and Conditions

You can publish open access with Elsevier in hundreds of open access journals or in nearly 2000 established subscription journals that support open access publishing. Permitted third party reuse of these open access articles is defined by the author's choice of Creative Commons user license. See our open access license policy for more information.

Terms & Conditions applicable to all Open Access articles published with Elsevier:

Any reuse of the article must not represent the author as endorsing the adaptation of the article nor should the article be modified in such a way as to damage the author's honour or reputation. If any changes have been made, such changes must be clearly indicated.

The author(s) must be appropriately credited and we ask that you include the end user license and a DOI link to the formal publication on ScienceDirect.

If any part of the material to be used (for example, figures) has appeared in our publication with credit or acknowledgement to another source it is the responsibility of the user to ensure their reuse complies with the terms and conditions determined by the rights holder.

Additional Terms & Conditions applicable to each Creative Commons user license:

CC BY: The CC-BY license allows users to copy, to create extracts, abstracts and new works from the Article, to alter and revise the Article and to make commercial use of the Article (including reuse and/or resale of the Article by commercial entities), provided the user gives appropriate credit (with a link to the formal publication through the relevant DOI), provides a link to the license, indicates if changes were made and the licensor is not represented as endorsing the use made of the work. The full details of the license are available at <http://creativecommons.org/licenses/by/4.0>.

CC BY NC SA: The CC BY-NC-SA license allows users to copy, to create extracts, abstracts and new works from the Article, to alter and revise the Article, provided this is not done for commercial purposes, and that the user gives appropriate credit (with a link to the formal publication through the relevant DOI), provides a link to the license, indicates if changes were

made and the licensor is not represented as endorsing the use made of the work. Further, any new works must be made available on the same conditions. The full details of the license are available at <http://creativecommons.org/licenses/by-nc-sa/4.0>.

CC BY NC ND: The CC BY-NC-ND license allows users to copy and distribute the Article, provided this is not done for commercial purposes and further does not permit distribution of the Article if it is changed or edited in any way, and provided the user gives appropriate credit (with a link to the formal publication through the relevant DOI), provides a link to the license, and that the licensor is not represented as endorsing the use made of the work. The full details of the license are available at <http://creativecommons.org/licenses/by-nc-nd/4.0>. Any commercial reuse of Open Access articles published with a CC BY NC SA or CC BY NC ND license requires permission from Elsevier and will be subject to a fee.

Commercial reuse includes:

- Associating advertising with the full text of the Article
- Charging fees for document delivery or access
- Article aggregation
- Systematic distribution via e-mail lists or share buttons

Posting or linking by commercial companies for use by customers of those companies.

20. Other Conditions:

v1.10

Questions? customercare@copyright.com or +1-855-239-3415 (toll free in the US) or +1-978-646-2777.

ELSEVIER LICENSE
TERMS AND CONDITIONS

Nov 30, 2020

This Agreement between Mr. Habib Sobanke ("You") and Elsevier ("Elsevier") consists of your license details and the terms and conditions provided by Elsevier and Copyright Clearance Center.

License Number 4958961259344

License date Nov 30, 2020

Licensed Content
Publisher Elsevier

Licensed Content
Publication Journal of Constructional Steel Research

Licensed Content Title Strain ratcheting of steel tubulars with a rectangular defect under axial cycling: A numerical modeling

Licensed Content Author M. Zeinoddini,M. Peykanu

Licensed Content Date Dec 1, 2011

Licensed Content Volume 67

Licensed Content Issue 12

Licensed Content Pages 12

Start Page 1872
End Page 1883
Type of Use reuse in a thesis/dissertation
Portion figures/tables/illustrations

Number of
figures/tables/illustrations 1

Format both print and electronic

Are you the author of this
Elsevier article? No

Will you be translating? No

Title Behaviour of Wrinkled Energy Pipes Subjected to Axial Cyclic
Induced Fatigue Failure

Institution name University of Windsor

Expected presentation date Dec 2020

Portions figure 13

Mr. Habeeb Sobanke
1662 University avenue west

Requestor Location

Windsor, ON N9B 1C2
Canada
Attn: Mr. Habeeb Sobanke

Publisher Tax ID GB 494 6272 12

Total 0.00 CAD

Terms and Conditions

INTRODUCTION

1. The publisher for this copyrighted material is Elsevier. By clicking "accept" in connection with completing this licensing transaction, you agree that the following terms and conditions apply to this transaction (along with the Billing and Payment terms and conditions established by Copyright Clearance Center, Inc. ("CCC"), at the time that you opened your Rightslink account and that are available at any time at <http://myaccount.copyright.com>).

GENERAL TERMS

2. Elsevier hereby grants you permission to reproduce the aforementioned material subject to the terms and conditions indicated.

3. Acknowledgement: If any part of the material to be used (for example, figures) has appeared in our publication with credit or acknowledgement to another source, permission must also be sought from that source. If such permission is not obtained then that material may not be included in your publication/copies. Suitable acknowledgement to the source must be made, either as a footnote or in a reference list at the end of your publication, as follows:

"Reprinted from Publication title, Vol /edition number, Author(s), Title of article / title of chapter, Pages No., Copyright (Year), with permission from Elsevier [OR APPLICABLE SOCIETY COPYRIGHT OWNER]." Also Lancet special credit - "Reprinted from The Lancet, Vol. number, Author(s), Title of article, Pages No., Copyright (Year), with permission from Elsevier."

4. Reproduction of this material is confined to the purpose and/or media for which permission is hereby given.

5. Altering/Modifying Material: Not Permitted. However figures and illustrations may be altered/adapted minimally to serve your work. Any other abbreviations, additions, deletions and/or any other alterations shall be made only with prior written authorization of Elsevier Ltd.

(Please contact Elsevier's permissions helpdesk [here](#)). No modifications can be made to any Lancet figures/tables and they must be reproduced in full.

6. If the permission fee for the requested use of our material is waived in this instance, please be advised that your future requests for Elsevier materials may attract a fee.
7. **Reservation of Rights:** Publisher reserves all rights not specifically granted in the combination of (i) the license details provided by you and accepted in the course of this licensing transaction, (ii) these terms and conditions and (iii) CCC's Billing and Payment terms and conditions.
8. **License Contingent Upon Payment:** While you may exercise the rights license immediately upon issuance of the license at the end of the licensing process for the transaction, provided that you have disclosed complete and accurate details of your proposed use, no license is finally effective unless and until full payment is received from you (either by publisher or by CCC) as provided in CCC's Billing and Payment terms and conditions. If full payment is not received on a timely basis, then any license preliminarily granted shall be deemed automatically revoked and shall be void as if never granted. Further, in the event that you breach any of these terms and conditions or any of CCC's Billing and Payment terms and conditions, the license is automatically revoked and shall be void as if never granted. Use of materials as described in a revoked license, as well as any use of the materials beyond the scope of an unrevoked license, may constitute copyright infringement and publisher reserves the right to take any and all action to protect its copyright in the materials.
9. **Warranties:** Publisher makes no representations or warranties with respect to the licensed material.
10. **Indemnity:** You hereby indemnify and agree to hold harmless publisher and CCC, and their respective officers, directors, employees and agents, from and against any and all claims arising out of your use of the licensed material other than as specifically authorized pursuant to this license.
11. **No Transfer of License:** This license is personal to you and may not be sublicensed, assigned, or transferred by you to any other person without publisher's written permission.
12. **No Amendment Except in Writing:** This license may not be amended except in a writing signed by both parties (or, in the case of publisher, by CCC on publisher's behalf).
13. **Objection to Contrary Terms:** Publisher hereby objects to any terms contained in any purchase order, acknowledgment, check endorsement or other writing prepared by you, which terms are inconsistent with these terms and conditions or CCC's Billing and Payment terms and conditions. These terms and conditions, together with CCC's Billing and Payment terms and conditions (which are incorporated herein), comprise the entire agreement between you and publisher (and CCC) concerning this licensing transaction. In the event of any conflict between your obligations established by these terms and conditions and those established by CCC's Billing and Payment terms and conditions, these terms and conditions shall control.
14. **Revocation:** Elsevier or Copyright Clearance Center may deny the permissions described in this License at their sole discretion, for any reason or no reason, with a full refund payable to

you. Notice of such denial will be made using the contact information provided by you. Failure to receive such notice will not alter or invalidate the denial. In no event will Elsevier or Copyright Clearance Center be responsible or liable for any costs, expenses or damage incurred by you as a result of a denial of your permission request, other than a refund of the amount(s) paid by you to Elsevier and/or Copyright Clearance Center for denied permissions.

LIMITED LICENSE

The following terms and conditions apply only to specific license types:

15. **Translation:** This permission is granted for non-exclusive world **English** rights only unless your license was granted for translation rights. If you licensed translation rights you may only translate this content into the languages you requested. A professional translator must perform all translations and reproduce the content word for word preserving the integrity of the article.
16. **Posting licensed content on any Website:** The following terms and conditions apply as follows: Licensing material from an Elsevier journal: All content posted to the web site must maintain the copyright information line on the bottom of each image; A hyper-text must be included to the Homepage of the journal from which you are licensing at <http://www.sciencedirect.com/science/journal/xxxxx> or the Elsevier homepage for books at <http://www.elsevier.com>; Central Storage: This license does not include permission for a scanned version of the material to be stored in a central repository such as that provided by Heron/XanEdu.

Licensing material from an Elsevier book: A hyper-text link must be included to the Elsevier homepage at <http://www.elsevier.com> . All content posted to the web site must maintain the copyright information line on the bottom of each image.

Posting licensed content on Electronic reserve: In addition to the above the following clauses are applicable: The web site must be password-protected and made available only to bona fide students registered on a relevant course. This permission is granted for 1 year only. You may obtain a new license for future website posting.

17. **For journal authors:** the following clauses are applicable in addition to the above:

Preprints:

A preprint is an author's own write-up of research results and analysis, it has not been peer reviewed, nor has it had any other value added to it by a publisher (such as formatting, copyright, technical enhancement etc.).

Authors can share their preprints anywhere at any time. Preprints should not be added to or enhanced in any way in order to appear more like, or to substitute for, the final versions of articles however authors can update their preprints on arXiv or RePEc with their Accepted Author Manuscript (see below).

If accepted for publication, we encourage authors to link from the preprint to their formal publication via its DOI. Millions of researchers have access to the formal publications on

ScienceDirect, and so links will help users to find, access, cite and use the best available version. Please note that Cell Press, The Lancet and some society-owned have different preprint policies. Information on these policies is available on the journal homepage.

Accepted Author Manuscripts: An accepted author manuscript is the manuscript of an article that has been accepted for publication and which typically includes author incorporated changes suggested during submission, peer review and editor-author communications.

Authors can share their accepted author manuscript:

- immediately via their non-commercial person homepage or blog by updating a
 - preprint in arXiv or RePEc with the accepted manuscript via their research
 - institute or institutional repository for internal institutional uses or as part of an
 - invitation-only research collaboration work-group directly by providing copies
 - to their students or to research collaborators for their personal use
 - for private scholarly sharing as part of an invitation-only work group on
 - commercial sites with which Elsevier has an agreement
- After the embargo period via non-commercial hosting platforms such as their
 - institutional repository via commercial sites with which Elsevier has an
 - agreement

In all cases accepted manuscripts should:

- link to the formal publication via its DOI bear a CC-BY-NC-ND license - this is easy to
- do if aggregated with other manuscripts, for example in a repository or other site, be
- shared in alignment with our hosting policy not be added to or enhanced in any way to appear more like, or to substitute for, the published journal article.

Published journal article (JPA): A published journal article (PJA) is the definitive final record of published research that appears or will appear in the journal and embodies all value-adding publishing activities including peer review co-ordination, copy-editing, formatting, (if relevant) pagination and online enrichment.

Policies for sharing publishing journal articles differ for subscription and gold open access articles:

Subscription Articles: If you are an author, please share a link to your article rather than the full-text. Millions of researchers have access to the formal publications on ScienceDirect, and so links will help your users to find, access, cite, and use the best available version.

Theses and dissertations which contain embedded PJAs as part of the formal submission can be posted publicly by the awarding institution with DOI links back to the formal publications on ScienceDirect.

If you are affiliated with a library that subscribes to ScienceDirect you have additional private sharing rights for others' research accessed under that agreement. This includes use for classroom teaching and internal training at the institution (including use in course packs and courseware programs), and inclusion of the article for grant funding purposes.

Gold Open Access Articles: May be shared according to the author-selected end-user license and should contain a CrossMark logo, the end user license, and a DOI link to the formal publication on ScienceDirect.

Please refer to Elsevier's posting policy for further information.

18. **For book authors** the following clauses are applicable in addition to the above: Authors are permitted to place a brief summary of their work online only. You are not allowed to download and post the published electronic version of your chapter, nor may you scan the printed edition to create an electronic version. **Posting to a repository:** Authors are permitted to post a summary of their chapter only in their institution's repository.

19. **Thesis/Dissertation:** If your license is for use in a thesis/dissertation your thesis may be submitted to your institution in either print or electronic form. Should your thesis be published commercially, please reapply for permission. These requirements include permission for the Library and Archives of Canada to supply single copies, on demand, of the complete thesis and include permission for Proquest/UMI to supply single copies, on demand, of the complete thesis. Should your thesis be published commercially, please reapply for permission. Theses and dissertations which contain embedded PJAs as part of the formal submission can be posted publicly by the awarding institution with DOI links back to the formal publications on ScienceDirect.

Elsevier Open Access Terms and Conditions

You can publish open access with Elsevier in hundreds of open access journals or in nearly 2000 established subscription journals that support open access publishing. Permitted third party reuse of these open access articles is defined by the author's choice of Creative Commons user license. See our open access license policy for more information.

Terms & Conditions applicable to all Open Access articles published with Elsevier:

Any reuse of the article must not represent the author as endorsing the adaptation of the article nor should the article be modified in such a way as to damage the author's honour or reputation. If any changes have been made, such changes must be clearly indicated.

The author(s) must be appropriately credited and we ask that you include the end user license and a DOI link to the formal publication on ScienceDirect.

If any part of the material to be used (for example, figures) has appeared in our publication with credit or acknowledgement to another source it is the responsibility of the user to ensure their reuse complies with the terms and conditions determined by the rights holder.

Additional Terms & Conditions applicable to each Creative Commons user license:

CC BY: The CC-BY license allows users to copy, to create extracts, abstracts and new works from the Article, to alter and revise the Article and to make commercial use of the Article (including reuse and/or resale of the Article by commercial entities), provided the user gives appropriate credit (with a link to the formal publication through the relevant DOI), provides a

link to the license, indicates if changes were made and the licensor is not represented as endorsing the use made of the work. The full details of the license are available at <http://creativecommons.org/licenses/by/4.0>.

CC BY NC SA: The CC BY-NC-SA license allows users to copy, to create extracts, abstracts and new works from the Article, to alter and revise the Article, provided this is not done for commercial purposes, and that the user gives appropriate credit (with a link to the formal publication through the relevant DOI), provides a link to the license, indicates if changes were made and the licensor is not represented as endorsing the use made of the work. Further, any new works must be made available on the same conditions. The full details of the license are available at <http://creativecommons.org/licenses/by-nc-sa/4.0>.

CC BY NC ND: The CC BY-NC-ND license allows users to copy and distribute the Article, provided this is not done for commercial purposes and further does not permit distribution of the Article if it is changed or edited in any way, and provided the user gives appropriate credit (with a link to the formal publication through the relevant DOI), provides a link to the license, and that the licensor is not represented as endorsing the use made of the work. The full details of the license are available at <http://creativecommons.org/licenses/by-nc-nd/4.0>. Any commercial reuse of Open Access articles published with a CC BY NC SA or CC BY NC ND license requires permission from Elsevier and will be subject to a fee.

Commercial reuse includes:

- Associating advertising with the full text of the Article
- Charging fees for document delivery or access
- Article aggregation
- Systematic distribution via e-mail lists or share buttons

Posting or linking by commercial companies for use by customers of those companies.

20. Other Conditions:

v1.10

Questions? customercare@copyright.com or +1-855-239-3415 (toll free in the US) or +1-978-646-2777.



Canadian Science Publishing - License Terms and Conditions

This is a License Agreement between Habeeb Sobanke ("You") and Canadian Science Publishing ("Publisher") provided by Copyright Clearance Center ("CCC"). The license consists of your order details, the terms and conditions provided by Canadian Science Publishing, and the CCC terms and conditions.

All payments must be made in full to
CCC.

Order Date	30-Nov-2020	Type of Use	Republish in a thesis/dissertation
Order license ID	1080957-1	Publisher	Canadian Science Publishing
ISSN	1208-6029	Portion	Image/photo/illustration

LICENSED CONTENT

Publication Title	Canadian journal of civil engineering : Revue canadienne de génie civil	Publication Type	e-Journal
Article Title	Prediction of the fracture life of a wrinkled steel pipe subject to low cycle fatigue load	Start Page	1131
Date	01/01/1996	End Page	1139
Language	English, French, French	Issue	9
Country	Canada	Volume	34
Rightsholder	Canadian Science Publishing		

REQUEST DETAILS

Portion Type	Image/photo/illustration	Distribution	Worldwide
Number of images / photos / illustrations	2	Translation	Original language of publication
Format (select all that apply)	Print, Electronic	Copies for the disabled?	Yes
Who will republish the content?	Academic institution	Minor editing privileges?	Yes
Duration of Use	Life of current edition	Incidental promotional use?	Yes
Lifetime Unit Quantity	Up to 499	Currency	CAD
Rights Requested	Main product, any product related to main product, and other compilations/derivative products		

NEW WORK DETAILS

Title	Behaviour of Wrinkled Energy Pipes Subjected to Axial Cyclic Induced Fatigue Failure	Institution name	University of Windsor
		Expected presentation date	2020-12-17
Instructor name	Sreekanta Das		

ADDITIONAL DETAILS

Order reference number	N/A	The requesting person / organization to appear on the license	Habeeb
Sobanke			

REUSE CONTENT DETAILS

Title, description or numeric reference of the portion(s)	Figures 10 and 12	Title of the article/chapter the portion is from	Prediction of the fracture life of a wrinkled steel pipe subject to low cycle fatigue load
Editor of portion(s)	Das, Sreekanta; Cheng, J J. Roger; Murray, David	Author of portion(s)	
Volume of serial or monograph	W 34	Issue, if republishing an article from a serial	Das, Sreekanta; Cheng, J J.
Page or page range of portion	1131-1139	Publication date of portion	Roger; Murray, David W 9 2007-09-01

CCC Republication Terms and Conditions

1. Description of Service; Defined Terms. This Republication License enables the User to obtain licenses for republication of one or more copyrighted works as described in detail on the relevant Order Confirmation (the "Work(s)"). Copyright Clearance Center, Inc. ("CCC") grants licenses through the Service on behalf of the rightsholder identified on the Order Confirmation (the "Rightsholder"). "Replication", as used herein, generally means the inclusion of a Work, in whole or in part, in a new work or works, also as described on the Order Confirmation. "User", as used herein, means the person or entity making such republication.

2. The terms set forth in the relevant Order Confirmation, and any terms set by the Rightsholder with respect to a particular Work, govern the terms of use of Works in connection with the Service. By using the Service, the person transacting for a republication license on behalf of the User represents and warrants that he/she/it (a) has been duly authorized by the User to accept, and hereby does accept, all such terms and conditions on behalf of User, and (b) shall inform User of all such terms and conditions. In the event such person is a "freelancer" or other third party independent of User and CCC, such party shall be deemed jointly a "User" for purposes of these terms and conditions. In any event, User shall be deemed to have accepted and agreed to all such terms and conditions if User republishes the Work in any fashion.

3. Scope of License; Limitations and Obligations.
 - 3.1. All Works and all rights therein, including copyright rights, remain the sole and exclusive property of the Rightsholder. The license created by the exchange of an Order Confirmation (and/or any invoice) and payment by User of the full amount set forth on that document includes only those rights expressly set forth in the Order Confirmation and in these terms and conditions, and conveys no other rights in the Work(s) to User. All rights not expressly granted are hereby reserved.

3.2.

General Payment Terms: You may pay by credit card or through an account with us payable at the end of the month. If you and we agree that you may establish a standing account with CCC, then the following terms apply: Remit Payment to: Copyright Clearance Center, 29118 Network Place, Chicago, IL 60673-1291.

Payments Due: Invoices are payable upon their delivery to you (or upon our notice to you that they are available to you for downloading). After 30 days, outstanding amounts will be subject to a service charge of 1-1/2% per month or, if less, the maximum rate allowed by applicable law. Unless otherwise specifically set forth in the Order Confirmation or in a separate written agreement signed by CCC, invoices are due and payable on "net 30" terms. While User may exercise the rights licensed immediately upon issuance of the Order Confirmation, the license is automatically revoked and is null and void, as if it had never been issued, if complete payment for the license is not received on a timely basis either from User directly or through a payment agent, such as a credit card company.

- 3.3. Unless otherwise provided in the Order Confirmation, any grant of rights to User (i) is "one-time" (including the editions and product family specified in the license), (ii) is non-exclusive and non-transferable and (iii) is subject to any and all limitations and restrictions (such as, but not limited to, limitations on duration of use or circulation) included in the Order Confirmation or invoice and/or in these terms and conditions. Upon completion of the licensed use, User shall either secure a new permission for further use of the Work(s) or immediately cease any new use of the Work(s) and shall render inaccessible (such as by deleting or by removing or severing links or other locators) any further copies of the Work (except for copies printed on paper in accordance with this license and still in User's stock at the end of such period).
- 3.4. In the event that the material for which a republication license is sought includes third party materials (such as photographs, illustrations, graphs, inserts and similar materials) which are identified in such material as having been used by permission, User is responsible for identifying, and seeking separate licenses (under this Service or otherwise) for, any of such third party materials; without a separate license, such third party materials may not be used.
- 3.5. Use of proper copyright notice for a Work is required as a condition of any license granted under the Service. Unless otherwise provided in the Order Confirmation, a proper copyright notice will read substantially as follows: "Republished with permission of [Rightsholder's name], from [Work's title, author, volume, edition number and year of copyright]; permission conveyed through Copyright Clearance Center, Inc. " Such notice must be provided in a reasonably legible font size and must be placed either immediately adjacent to the Work as used (for example, as part

of a by-line or footnote but not as a separate electronic link) or in the place where substantially all other credits or notices for the new work containing the republished Work are located. Failure to include the required notice results in loss to the Rightsholder and CCC, and the User shall be liable to pay liquidated damages for each such failure equal to twice the use fee specified in the Order Confirmation, in addition to the use fee itself and any other fees and charges specified.

3.6. User may only make alterations to the Work if and as expressly set forth in the Order Confirmation. No Work may be used in any way that is defamatory, violates the rights of third parties (including such third parties' rights of copyright, privacy, publicity, or other tangible or intangible property), or is otherwise illegal, sexually explicit or obscene. In addition, User may not conjoin a Work with any other material that may result in damage to the reputation of the Rightsholder. User agrees to inform CCC if it becomes aware of any infringement of any rights in a Work and to cooperate with any reasonable request of CCC or the Rightsholder in connection therewith.

4. Indemnity. User hereby indemnities and agrees to defend the Rightsholder and CCC, and their respective employees and directors, against all claims, liability, damages, costs and expenses, including legal fees and expenses, arising out of any use of a Work beyond the scope of the rights granted herein, or any use of a Work which has been altered in any unauthorized way by User, including claims of defamation or infringement of rights of copyright, publicity, privacy or other tangible or intangible property.

5.

Limitation of Liability. UNDER NO CIRCUMSTANCES WILL CCC OR THE RIGHTSHOLDER BE LIABLE FOR ANY DIRECT, **INDIRECT, CONSEQUENTIAL OR INCIDENTAL DAMAGES (INCLUDING WITHOUT LIMITATION DAMAGES FOR LOSS OF BUSINESS PROFITS OR INFORMATION, OR FOR BUSINESS INTERRUPTION) ARISING OUT OF THE USE OR INABILITY TO USE A WORK, EVEN IF ONE OF THEM HAS BEEN ADVISED OF THE POSSIBILITY OF SUCH DAMAGES.** In any event, the total liability of the Rightsholder and CCC (including their respective employees and directors) shall not exceed the total amount actually paid by User for this license. User assumes full liability for the actions and omissions of its principals, employees, agents, affiliates, successors and assigns.

6. Limited Warranties. **THE WORK(S) AND RIGHT(S) ARE PROVIDED "AS IS". CCC HAS THE RIGHT TO GRANT TO USER THE RIGHTS GRANTED IN THE ORDER CONFIRMATION DOCUMENT. CCC AND THE RIGHTSHOLDER DISCLAIM ALL OTHER WARRANTIES RELATING TO THE WORK(S) AND RIGHT(S), EITHER EXPRESS OR IMPLIED, INCLUDING**

WITHOUT LIMITATION IMPLIED WARRANTIES OF MERCHANTABILITY OR FITNESS FOR A PARTICULAR PURPOSE.

ADDITIONAL RIGHTS MAY BE REQUIRED TO USE ILLUSTRATIONS, GRAPHS, PHOTOGRAPHS, ABSTRACTS, INSERTS

OR OTHER PORTIONS OF THE WORK (AS OPPOSED TO THE ENTIRE WORK) IN A MANNER CONTEMPLATED BY USER; USER UNDERSTANDS AND AGREES THAT NEITHER CCC NOR THE RIGHTSHOLDER MAY HAVE SUCH ADDITIONAL RIGHTS TO GRANT.

7. Effect of Breach. Any failure by User to pay any amount when due, or any use by User of a Work beyond the scope of the license set forth in the Order Confirmation and/or these terms and conditions, shall be a material breach of the license created by the Order Confirmation and these terms and conditions. Any breach not cured within 30 days of written notice thereof shall result in immediate termination of such license without further notice. Any unauthorized (but licensable) use of a Work that is terminated immediately upon notice thereof may be liquidated by payment of the Rightsholder's ordinary license price therefor; any unauthorized (and unlicensable) use that is not terminated immediately for any reason (including, for example, because materials containing the Work cannot reasonably be recalled) will be subject to all remedies available at law or in equity, but in no event to a payment of less than three times the Rightsholder's ordinary license price for the most closely analogous licensable use plus Rightsholder's and/or CCC's costs and expenses incurred in collecting such payment.
8. Miscellaneous.
 - 8.1. User acknowledges that CCC may, from time to time, make changes or additions to the Service or to these terms and conditions, and CCC reserves the right to send notice to the User by electronic mail or otherwise for the purposes of notifying User of such changes or additions; provided that any such changes or additions shall not apply to permissions already secured and paid for.
 - 8.2. Use of User-related information collected through the Service is governed by CCC's privacy policy, available online here:<https://marketplace.copyright.com/rs-ui-web/mp/privacy-policy>
 - 8.3. The licensing transaction described in the Order Confirmation is personal to User. Therefore, User may not assign or transfer to any other person (whether a natural person or an organization of any kind) the license created by the Order Confirmation and these terms and conditions or any rights granted hereunder; provided, however, that User may assign such license in its entirety on written notice to CCC in the event of a transfer of all or substantially all of User's rights in the new material which includes the Work(s) licensed under this Service.

8.4. No amendment or waiver of any terms is binding unless set forth in writing and signed by the parties. The Rightsholder and CCC hereby object to any terms contained in any writing prepared by the User or its principals, employees, agents or affiliates and purporting to govern or otherwise relate to the licensing transaction described in the Order Confirmation, which terms are in any way inconsistent with any terms set forth in the Order Confirmation and/or in these terms and conditions or CCC's standard operating procedures, whether such writing is prepared prior to, simultaneously with or subsequent to the Order Confirmation, and whether such writing appears on a copy of the Order Confirmation or in a separate instrument.

8.5.

The licensing transaction described in the Order Confirmation document shall be governed by and construed under the law of the State of New York, USA, without regard to the principles thereof of conflicts of law. Any case, controversy, suit, action, or proceeding arising out of, in connection with, or related to such licensing transaction shall be brought, at CCC's sole discretion, in any federal or state court located in the County of New York, State of New York, USA, or in any federal or state court whose geographical jurisdiction covers the location of the Rightsholder set forth in the Order Confirmation. The parties expressly submit to the personal jurisdiction and venue of each such federal or state court. If you have any comments or questions about the Service or Copyright Clearance Center, please contact us at 978-7508400 or send an e-mail to support@copyright.com.



Canadian Science Publishing - License Terms and Conditions

This is a License Agreement between Habeeb Sobanke ("You") and Canadian Science Publishing ("Publisher") provided by Copyright Clearance Center ("CCC"). The license consists of your order details, the terms and conditions provided by Canadian Science Publishing, and the CCC terms and conditions.

All payments must be made in full to
CCC.

Order Date	30-Nov-2020	Type of Use	Republish in a thesis/dissertation
Order license ID	1080956-1	Publisher	Canadian Science Publishing
ISSN	1208-6029	Portion	Image/photo/illustration

LICENSED CONTENT

Publication Title	Canadian journal of civil engineering : Revue canadienne de génie civil	Publication Type	e-Journal
Article Title	Behavior of wrinkled steel pipelines subjected to cyclic axial loadings	Start Page	598
Date	01/01/1996	End Page	607
Language	English, French, French	Issue	5
Country	Canada	Volume	34
Rightsholder	Canadian Science Publishing		

REQUEST DETAILS

Portion Type	Image/photo/illustration	Distribution	Worldwide
Number of images / photos / illustrations	3	Translation	Original language of publication
Format (select all that apply)	Print, Electronic	Copies for the disabled?	No
Who will republish the content?	Academic institution	Minor editing privileges?	Yes
Duration of Use	Life of current edition	Incidental promotional use?	Yes
Lifetime Unit Quantity	Up to 499	Currency	CAD
Rights Requested	Main product, any product related to main product, and other compilations/derivative products		

NEW WORK DETAILS

Title	Behaviour of Wrinkled Energy Pipes Subjected to Axial Cyclic Induced Fatigue Failure	Institution name	University of Windsor
		Expected presentation date	2020-12-17
Instructor name	Sreekanta Das		

ADDITIONAL DETAILS

Order reference number	N/A	The requesting person / organization to appear on the license	Habeeb
-------------------------------	-----	--	--------

REUSE CONTENT DETAILS

Title, description or numeric reference of the portion(s)	Figures 6, 12 and 16	Title of the article/chapter the portion is from	Behavior of wrinkled steel pipelines subjected to cyclic axial loadings
Editor of portion(s)	Das, Sreekanta; Cheng, J.J Roger; Murray, David	Author of portion(s)	Das, Sreekanta; Cheng, J.J Roger; Murray, David
Volume of serial or monograph	W 34	Issue, if republishing an article from a serial	J.J Roger; Murray, David
Page or page range of portion	598-607	Publication date of portion	W 5 2007-05-01

CCC Republication Terms and Conditions

1. Description of Service; Defined Terms. This Republication License enables the User to obtain licenses for republication of one or more copyrighted works as described in detail on the relevant Order Confirmation (the "Work(s)"). Copyright Clearance Center, Inc. ("CCC") grants licenses through the Service on behalf of the rightsholder identified on the Order Confirmation (the "Rightsholder"). "Replication", as used herein, generally means the inclusion of a Work, in whole or in part, in a new work or works, also as described on the Order Confirmation. "User", as used herein, means the person or entity making such republication.
2. The terms set forth in the relevant Order Confirmation, and any terms set by the Rightsholder with respect to a particular Work, govern the terms of use of Works in connection with the Service. By using the Service, the person transacting for a republication license on behalf of the User represents and warrants that he/she/it (a) has been duly authorized by the User to accept, and hereby does accept, all such terms and conditions on behalf of User, and (b) shall inform User of all such terms and conditions. In the event such person is a "freelancer" or other third party independent of User and CCC, such party shall be deemed jointly a "User" for purposes of these terms and conditions. In any event, User shall be deemed to have accepted and agreed to all such terms and conditions if User republishes the Work in any fashion.
3. Scope of License; Limitations and Obligations.
 - 3.1. All Works and all rights therein, including copyright rights, remain the sole and exclusive property of the Rightsholder. The license created by the exchange of an Order Confirmation (and/or any invoice) and payment by User of the full amount set forth on that document includes only those rights expressly set forth in the Order Confirmation and in these terms and conditions, and conveys no other rights in the Work(s) to User. All rights not expressly granted are hereby reserved.

3.2.

General Payment Terms: You may pay by credit card or through an account with us payable at the end of the month. If you and we agree that you may establish a standing account with CCC, then the following terms apply: Remit Payment to: Copyright Clearance Center, 29118 Network Place, Chicago, IL 60673-1291.

Payments Due: Invoices are payable upon their delivery to you (or upon our notice to you that they are available to you for downloading). After 30 days, outstanding amounts will be subject to a service charge of 1-1/2% per month or, if less, the maximum rate allowed by applicable law. Unless otherwise specifically set forth in the Order Confirmation or in a separate written agreement signed by CCC, invoices are due and payable on "net 30" terms. While User may exercise the rights licensed immediately upon issuance of the Order Confirmation, the license is automatically revoked and is null and void, as if it had never been issued, if complete payment for the license is not received on a timely basis either from User directly or through a payment agent, such as a credit card company.

- 3.3. Unless otherwise provided in the Order Confirmation, any grant of rights to User (i) is "one-time" (including the editions and product family specified in the license), (ii) is non-exclusive and non-transferable and (iii) is subject to any and all limitations and restrictions (such as, but not limited to, limitations on duration of use or circulation) included in the Order Confirmation or invoice and/or in these terms and conditions. Upon completion of the licensed use, User shall either secure a new permission for further use of the Work(s) or immediately cease any new use of the Work(s) and shall render inaccessible (such as by deleting or by removing or severing links or other locators) any further copies of the Work (except for copies printed on paper in accordance with this license and still in User's stock at the end of such period).
- 3.4. In the event that the material for which a republication license is sought includes third party materials (such as photographs, illustrations, graphs, inserts and similar materials) which are identified in such material as having been used by permission, User is responsible for identifying, and seeking separate licenses (under this Service or otherwise) for, any of such third party materials; without a separate license, such third party materials may not be used.
- 3.5. Use of proper copyright notice for a Work is required as a condition of any license granted under the Service. Unless otherwise provided in the Order Confirmation, a proper copyright notice will read substantially as follows: "Republished with permission of [Rightsholder's name], from [Work's title, author, volume, edition number and year of copyright]; permission conveyed through Copyright Clearance

Center, Inc. " Such notice must be provided in a reasonably legible font size and must be placed either immediately adjacent to the Work as used (for example, as part of a by-line or footnote but not as a separate electronic link) or in the place where substantially all other credits or notices for the new work containing the republished Work are located. Failure to include the required notice results in loss to the Rightsholder and CCC, and the User shall be liable to pay liquidated damages for each such failure equal to twice the use fee specified in the Order Confirmation, in addition to the use fee itself and any other fees and charges specified.

3.6. User may only make alterations to the Work if and as expressly set forth in the Order Confirmation. No Work may be used in any way that is defamatory, violates the rights of third parties (including such third parties' rights of copyright, privacy, publicity, or other tangible or intangible property), or is otherwise illegal, sexually explicit or obscene. In addition, User may not conjoin a Work with any other material that may result in damage to the reputation of the Rightsholder. User agrees to inform CCC if it becomes aware of any infringement of any rights in a Work and to cooperate with any reasonable request of CCC or the Rightsholder in connection therewith.

4. Indemnity. User hereby indemnities and agrees to defend the Rightsholder and CCC, and their respective employees and directors, against all claims, liability, damages, costs and expenses, including legal fees and expenses, arising out of any use of a Work beyond the scope of the rights granted herein, or any use of a Work which has been altered in any unauthorized way by User, including claims of defamation or infringement of rights of copyright, publicity, privacy or other tangible or intangible property.

5.

Limitation of Liability. UNDER NO CIRCUMSTANCES WILL CCC OR THE RIGHTSHOLDER BE LIABLE FOR ANY DIRECT, **INDIRECT, CONSEQUENTIAL OR INCIDENTAL DAMAGES (INCLUDING WITHOUT LIMITATION DAMAGES FOR LOSS OF BUSINESS PROFITS OR INFORMATION, OR FOR BUSINESS INTERRUPTION) ARISING OUT OF THE USE OR INABILITY TO USE A WORK, EVEN IF ONE OF THEM HAS BEEN ADVISED OF THE POSSIBILITY OF SUCH DAMAGES.** In any event, the total liability of the Rightsholder and CCC (including their respective employees and directors) shall not exceed the total amount actually paid by User for this license. User assumes full liability for the actions and omissions of its principals, employees, agents, affiliates, successors and assigns.

6. Limited Warranties. THE WORK(S) AND RIGHT(S) ARE PROVIDED "AS IS". CCC HAS THE RIGHT TO GRANT TO USER

THE RIGHTS GRANTED IN THE ORDER CONFIRMATION DOCUMENT. CCC AND THE RIGHTSHOLDER DISCLAIM ALL OTHER WARRANTIES RELATING TO THE WORK(S) AND RIGHT(S), EITHER EXPRESS OR IMPLIED, INCLUDING WITHOUT LIMITATION IMPLIED WARRANTIES OF MERCHANTABILITY OR FITNESS FOR A PARTICULAR PURPOSE.

ADDITIONAL RIGHTS MAY BE REQUIRED TO USE ILLUSTRATIONS, GRAPHS, PHOTOGRAPHS, ABSTRACTS, INSERTS OR OTHER PORTIONS OF THE WORK (AS OPPOSED TO THE ENTIRE WORK) IN A MANNER CONTEMPLATED BY USER; USER UNDERSTANDS AND AGREES THAT NEITHER CCC NOR THE RIGHTSHOLDER MAY HAVE SUCH ADDITIONAL RIGHTS TO GRANT.

7. Effect of Breach. Any failure by User to pay any amount when due, or any use by User of a Work beyond the scope of the license set forth in the Order Confirmation and/or these terms and conditions, shall be a material breach of the license created by the Order Confirmation and these terms and conditions. Any breach not cured within 30 days of written notice thereof shall result in immediate termination of such license without further notice. Any unauthorized (but licensable) use of a Work that is terminated immediately upon notice thereof may be liquidated by payment of the Rightsholder's ordinary license price therefor; any unauthorized (and unlicensable) use that is not terminated immediately for any reason (including, for example, because materials containing the Work cannot reasonably be recalled) will be subject to all remedies available at law or in equity, but in no event to a payment of less than three times the Rightsholder's ordinary license price for the most closely analogous licensable use plus Rightsholder's and/or CCC's costs and expenses incurred in collecting such payment.
8. Miscellaneous.
 - 8.1. User acknowledges that CCC may, from time to time, make changes or additions to the Service or to these terms and conditions, and CCC reserves the right to send notice to the User by electronic mail or otherwise for the purposes of notifying User of such changes or additions; provided that any such changes or additions shall not apply to permissions already secured and paid for.
 - 8.2. Use of User-related information collected through the Service is governed by CCC's privacy policy, available online here:<https://marketplace.copyright.com/rs-ui-web/mp/privacy-policy>
 - 8.3. The licensing transaction described in the Order Confirmation is personal to User. Therefore, User may not assign or transfer to any other person (whether a natural person or an organization of any kind) the license created by the Order Confirmation

and these terms and conditions or any rights granted hereunder; provided, however, that User may assign such license in its entirety on written notice to CCC in the event of a transfer of all or substantially all of User's rights in the new material which includes the Work(s) licensed under this Service.

- 8.4. No amendment or waiver of any terms is binding unless set forth in writing and signed by the parties. The Rightsholder and CCC hereby object to any terms contained in any writing prepared by the User or its principals, employees, agents or affiliates and purporting to govern or otherwise relate to the licensing transaction described in the Order Confirmation, which terms are in any way inconsistent with any terms set forth in the Order Confirmation and/or in these terms and conditions or CCC's standard operating procedures, whether such writing is prepared prior to, simultaneously with or subsequent to the Order Confirmation, and whether such writing appears on a copy of the Order Confirmation or in a separate instrument.

8.5.

The licensing transaction described in the Order Confirmation document shall be governed by and construed under the law of the State of New York, USA, without regard to the principles thereof of conflicts of law. Any case, controversy, suit, action, or proceeding arising out of, in connection with, or related to such licensing transaction shall be brought, at CCC's sole discretion, in any federal or state court located in the County of New York, State of New York, USA, or in any federal or state court whose geographical jurisdiction covers the location of the Rightsholder set forth in the Order Confirmation. The parties expressly submit to the personal jurisdiction and venue of each such federal or state court. If you have any comments or questions about the Service or Copyright Clearance Center, please contact us at 978-7508400 or send an e-mail to support@copyright.com.



Special Requests > Special Request Details

Add To Cart

Decline Offer

Proceedings of the ASME International Pipeline Conference--2008 : presented at 2008 7th International Pipeline Conference, September 29-October 3, 2008, Calgary, Alberta, Canada

Article IPC2008-64039 Evaluating the Effects of Wrinkle Bends on Pipeline Integrity

GENERAL INFORMATION

Request ID	Request Date
600030036	30 Nov 2020
Request Status	Price
Accepted	0.00 CAD Special Terms

ALL DETAILS

ISBN-13:	9780791848579
Type of Use:	Republish in a thesis/dissertation
Publisher:	ASME
Portion:	Chart/graph/table/figure

LICENSED CONTENT

Publication Title	Proceedings of the ASME International Pipeline Conference--2008 : presented at 2008 7th International Pipeline Conference, September 29-October 3, 2008, Calgary, Alberta, Canada	Country	United States of America
Article Title	IPC2008-64039 Evaluating the Effects of Wrinkle Bends on Pipeline Integrity	Rightsholder	American Society of Mechanical Engineers ASME
		Publication Type	Book
		Start Page	61
		Volume	2008; Conf 7; VOL 2

Author/Editor American Society of Mechanical Engineers., International Petroleum Technology Institute., (7th : 2008 : Calgary, Alta.)(7th

Date 01/01/2009

Language English

REQUEST DETAILS

Portion Type	Chart/graph/table/figure	Distribution	Worldwide
Number of charts / graphs / tables / figures requested	2	Translation	Original language of publication
Format (select all that apply)	Print, Electronic	Copies for the disabled?	No
Who will republish the content?	Academic institution	Minor editing privileges?	Yes
Duration of Use	Life of current and all future editions	Incidental promotional use?	Yes
Lifetime Unit Quantity	Up to 499	Currency	CAD
Rights Requested	Main product, any product related to main product, and other compilations/derivative products		

NEW WORK DETAILS

Title	Behaviour of Wrinkled Energy Pipes Subjected to Axial Cyclic Induced Fatigue Failure	Institution name	University of Windsor
Instructor name	Sreekanta Das	Expected presentation date	2020-12-17

ADDITIONAL DETAILS

The requesting person / organization to appear on the license Habeeb Sobanke

REUSE CONTENT DETAILS

Title, description or numeric reference of the portion(s)	Figure 5 and 10	Title of the article/chapter the portion is from	IPC2008-64039 Evaluating the Effects of Wrinkle Bends on Pipeline Integrity
Editor of portion(s)	Kulkarni, S.; Alexander, C.	Author of portion(s)	Kulkarni, S.; Alexander, C.

12/14/2020

Manage Account


Volume of serial or monograph 2008; Conf 7; VOL 2
Page or page range of portion 61-74

Publication date of portion 2008-01-01

COMMENTS

 [Add Comment / Attachment](#)

 [Add To Cart](#)

 [Decline Offer](#)



Special Requests > Special Request Details

Add To Cart

Decline Offer

Proceedings of the 10th International Pipeline Conference 2014 : IPC2014. September 29 - October 3 2014, Calgary, Alberta, Canada

GENERAL INFORMATION

Request ID	Request Date
600030033	30 Nov 2020
Request Status	Price
Accepted	0.00 CAD Special Terms

ALL DETAILS

ISBN-13:	9780791846124
Type of Use:	Republish in a thesis/dissertation
Publisher:	ASME
Portion:	Chart/graph/table/figure

LICENSED CONTENT

Publication Title	Proceedings of the 10th International Pipeline Conference 2014 : IPC2014. September 29 - October 3 2014, Calgary, Alberta, Canada	Country	United States of America
Author/Editor	American Society of Mechanical Engineers., International Petroleum Technology Institute., International Pipeline Conference (10th : 2014 : Calgary, Alta.)	Rightsholder	American Society of Mechanical Engineers ASME
Date	01/01/2014	Publication Type	Book
Language	English		

REQUEST DETAILS

Portion Type	Chart/graph/table/figure	Distribution	Worldwide
Number of charts / graphs / tables / figures requested	2	Translation	Original language of publication
Format (select all that apply)	Electronic	Copies for the disabled?	No
Who will republish the content?	Academic institution	Minor editing privileges?	Yes
Duration of Use	Life of current and all future editions	Incidental promotional use?	No
Lifetime Unit Quantity	Up to 499	Currency	CAD
Rights Requested	Main product, any product related to main product, and other compilations/derivative products		

NEW WORK DETAILS

Title	Behaviour of Wrinkled Energy Pipes Subjected to Axial Cyclic Induced Fatigue Failure	Institution name	University of Windsor
Instructor name	Sreekanta Das	Expected presentation date	2020-12-17

ADDITIONAL DETAILS

The requesting person / organization to appear on the license	Habeeb Sobanke
---	----------------


REUSE CONTENT DETAILS

Title, description or numeric reference of the portion(s)	Fig 4 and Fig. 7	Title of the article/chapter the portion is from	STRUCTURAL INTEGRITY OF STEEL HYDROCARBON PIPELINES WITH LOCAL WALL DISTORTIONS
Editor of portion(s)	Aglaia E. Pournara	Author of portion(s)	American Society of Mechanical Engineers.; International Petroleum Technology Institute.; International Pipeline Conference (10th : 2014 : Calgary, Alta.)
Volume of serial or monograph	N/A	Publication date of portion	2014-01-01
Page or page range of portion	507-513		

COMMENTS

 [Add Comment / Attachment](#)

 [Add To Cart](#)

 [Decline Offer](#)

VITA AUCTORIS

NAME: Habeeb Sobanke

PLACE OF BIRTH: Ogun state, Nigeria

YEAR OF BIRTH: 1994

EDUCATION: University of Lagos, B.Sc., Akoka, Lagos state,
Nigeria, 2015

University of Windsor, M.Sc., Windsor, ON,
Canada, 2020